Multiwavelength Analysis of the Active Galactic Nuclei's Feedback on the evolution of Quasar host galaxies

Aishwarya Girdhar
Munich Germany, 2023

Multiwavelength Analysis of the Active Galactic Nuclei's Feedback on the evolution of Quasar host galaxies

Aishwarya Girdhar

Dissertation

at the
Faculty of Physics

of the
Ludwig Maximilians University Munich

submitted by

Aishwarya Girdhar
born at Korba, India

Munich, 01 October 2023

Multiwellenlängen-Analyse des Feedbacks der Aktiven Galaktischen Kerne zur Entwicklung der Wirtsgalaxie

Aishwarya Girdhar

Dissertation

an der
Fakultät für Physik

der
Ludwig-Maximilians-Universität München

vorgelegt von

Aishwarya Girdhar
geboren in Korba, Indien

München, den 01. Oktober 2023

Erstgutacher: Prof. Dr. Andreas Bürkert
Zweitgutachter: Prof. Dr. Daniel Grün
Tag der mündlichen Prüfung: 20 November 2023

With limitless gratitude for all that I am,

Dedicated to,

AAI & PAPA
Dr. Mukta Girdhar & Mr. Nitin Girdhar

DECLARATION

The work described in this thesis was undertaken by the author as a research student enrolled at Ludwig Maximillian University of Munich, under the supervision of Prof. Dr. Andreas Burkert.

The research presented here was carried out between October 2019 to September 2023, at the European Southern Observatory, Garching bei Munich, Germany and Newcastle University, Newcastle upon Tyne, United Kingdom, under the joint supervision of **Dr. Chris M. Harrison** and **Dr. Vincenzo Mainieri**.

Chapter

Contents

Chapter

List of Figures

Chapter

List of Tables

Chapter

Zusammenfassung

Multiwellenlängen-Analyse des Feedbacks der aktiven galaktischen Kerne zur Entwicklung der Wirtsgalaxie – Aishwarya Girdhar

Aktive galaktische Kerne (AGN) bezeichnen die Phasen, in denen *supermassereiche schwarze Löcher* in den Zentren von massereichen Galaxien durch Akkretion wachsen. AGN geben gewaltige Mengen an Energie in der Form von Strahlung und Teilchen ab. Diese Energie kann die Wirtsgalaxie durch das Entfernen von Gas durch *mehrphasige Ausflüsse*, das Herbeiführen von Turbulenzen und/oder durch die Regulierung der Gasanlagerung in die Galaxie beeinflussen. Zusammengenommen werden diese Prozesse als *AGN-Feedback* bezeichnet. Theorien der Galaxienentstehung sagen voraus, dass ohne dieses Feedback Galaxien zu massereich, zu kompakt und zu hell wären verglichen mit den Beobachtungen. Für die allerhellsten AGN, die so genannten *Quasare*, gibt es keinen Konsens bezüglich des Mechanismus, der die mehrphasigen Ausflüsse antreibt (zum Beispiel Radiojets, Akkretionsscheibenwinde, und/oder AGN-Strahlungsfelder), und dessen gesamter Einfluss auf die Sternentstehung (positives oder negatives Feedback). Dies trifft vor allem auf die Mehrheit der Quasarpopulation zu, die keine hellen Radiojets haben und als '*radioleise*' klassifiziert werden.

Diese Arbeit studiert eine Stichprobe von 9 Quasarwirtsgalaxien aus dem Quasar Feedback Survey (QFeedS), die bolometrisch hell sind, (das heißt $L_{bol} >= 10^{45}$ erg s^{-1}). Diese Galaxien werden traditionell als radioleise klassifiziert aufgrund ihrer niedrigen bis mäßigen Radiohelligkeiten ($L_{1.4GHz} = 10^{23.3-24.4}$ W Hz^{-1}). Hochqualitative Radiobeobachtungen zeigen jedoch, dass sie schwache Radiojets beherbergen ($P_{jet} = 10^{43-44}$ erg s^{-1}). Die ausgewählte Stichprobe hat den Vorteil, dass Galaxien mit AGN-Helligkeiten ähnlich der typischen AGNs zu Hochzeiten des kosmischen Wachstums ($z \sim 2-3$) beobachtet werden, wobei gleichzeitig sub-kpc Auflösungen erreicht werden durch ihre geringe Rotverschiebung ($z < 0.2$). Diese Arbeit vereint integralfeldspektroskopische MUSE-Daten um die Kinematik von Sternen und Gas zu analysieren mit interferometrischen ALMA-Daten um das kalte molekulare Gas zu studieren. Zusammen erlaubt dies eine räumlich aufgelöste Studie der Auswirkung, die AGN auf das mehrphasige galaktische interstellare Medium (ISM) haben. Dies wird mit hochaufgelösten Radiodaten vom VLA aus dem Archiv kombiniert, um kollimierte Jets nachzuvollziehen. Indem diese Daten kombiniert werden, untersucht diese Arbeit die nicht-gravitativen Bewegungen des galaktischen ISMs, um das Vorhandensein von mehrphasigen Ausflüssen und Turbulenz zu detektieren.

Zuerst werden die kinematischen Eigenschaften untersucht für ein Einzelfallbeispiel, in dem ein Radiojet beobachtet wird, der durch die gasreiche Galaxienscheibe mit einem niedrigen Inklinationswinkel pflügt. Die Interaktionen zwischen Jet und ISM verursachen erhöhte Turbulenzen in der Ebene senkrecht zur Jetachse und treiben mehrphasige Ausflüsse, die in der ionisierten Phase dreimal ausgedehnter und schneller sind als in der molekularen Gasphase. Diese Arbeit studiert dann die Interaktion von molekularem Gas mit ausgedehnten ($\geq 10\,\mathrm{kpc}$) Radiostrukturen auf großen Skalen in vier Galaxien. Zwei davon zeigen molekulare Gasstrukturen, die Radioblasen mitreißen und diese umschlingen, ähnlich denen, die man in den hauptsächlich radiolauten, hellsten Galaxien von Galaxienhaufen findet. Die Eigenschaften dieser Strukturen (Geschwindigkeitsbreiten, radiale Ausdehnung, Massenausflussrate, kinetische Wirkung) zeigen sich als sehr ähnlich zu ihren radiolauten Gegenstücken. Außerdem werden zentrale molekulare Gasausflüsse in allen vier Galaxien beobachtet. Im letzten Projekt dieser Doktorarbeit wird eine systematische Studie dieser Feedbacksignaturen auf das mehrphasige Gas der Wirtsgalaxien aller 9 Quasarwirtsgalaxien durchgeführt. Zentrale molekulare Gasausflüsse werden in allen 9 Galaxien beobachtet, doch diese scheinen sehr viel kompakter und langsamer ($2-5$ mal) zu sein als die zugehörigen ionisierten Gasausflüsse. Großskalige Interaktionen (über die Galaxienscheibe hinweg) zwischen den AGN und dem molekularen Gas werden nur gefunden, wenn es Radiojets auf diesen ausgedehnten Skalen gibt. Durchweg in dieser Arbeit wurden Beobachtungen qualitativ mit hydrodynamischen Jet-ISM Simulationen verglichen und es zeigte sich, dass die Beobachtungen konsistent sind mit den Prognosen der Simulationen zu den Interaktionen zwischen schwachen Jets und gasreichen Galaxienscheiben. Dennoch ist zusätzliche Arbeit mit größeren Stichproben nötig, um die quantitativen Voraussagen dieser Simulationen zu testen. Diese These endet mit der Diskussion solcher Zukunftspläne und beschreibt, wie die gelernten Lektionen angewendet werden könnten, um Quasare zu Zeiten des kosmischen Mittags mit astronomischen Anlagen der nächsten Generation zu studieren.

Im Gesamten zeigt diese Arbeit, dass mehrphasige Ausflüsse verbreitet sind in allen der 9 studierten Quasaren, und dass obwohl Strahlungsenergie in den Quasaren zur Genüge vorhanden ist, schwache Radiojets beobachtet werden, die einen signifikanten Einfluss auf die Wirtsgalaxie auf Skalen von sub-kpc bis $\sim 10\,\mathrm{kpc}$ nehmen.

Chapter

Abstract

Multiwavelength analysis of the Active Galactic Nuclei's Feedback on the evolution of quasar host galaxies – Aishwarya Girdhar

Active Galactic Nuclei (AGN) are phases in which the *supermassive black holes* (SMBH) residing at the centres of massive galaxies grow through accretion. AGN release a tremendous amount of energy in the form of radiation and particles. This energy may affect the host galaxy by removing gas through *multi-phase AGN outflows*, by inducing turbulence and/or by regulating the accretion of gas onto the galaxy. Together, these processes are referred as *AGN Feedback*. Without this feedback, galaxy formation theory predicts galaxies to be too massive, too compact, and too bright compared to those observed. In the most-luminous AGN, i.e., *quasars*, there is a lack of consensus on the mechanisms driving the multi-phase outflows (i.e., radio jets; accretion disk winds; and/or AGN-radiation fields) and their overall impact on the star formation (i.e., positive versus negative feedback). This is particularly true for the majority of the quasar population, which do not have luminous radio jets and are classified as '*radio quiet*'.

This thesis studies a sample of 9 quasar-host galaxies, from the Quasar Feedback Survey (QFeedS) that are bolometrically luminous, (i.e. $L_{bol} \gtrsim 10^{45}$ erg s^{-1}). These galaxies are traditionally classified as 'radio quiet' due to their low/modest radio luminosities ($L_{1.4GHz} = 10^{23.3-24.4}$ W Hz^{-1}). However, high-quality radio observations reveal that they host low-power radio jets ($P_{jet} = 10^{43-44}$ erg s^{-1}). The selected sample gives the advantage of observing galaxies with AGN luminosities representative of typical AGN at the peak epoch of cosmic growth ($z \sim 2-3$); while still having sub-kpc resolution observations, due to their low redshift ($z < 0.2$). This thesis combines integral field spectroscopic MUSE data, to obtain stellar and ionised gas kinematics, along with interferometric ALMA data to study cold molecular gas kinematics. Together this enables a spatially-resolved study of the impact of the AGN on the multi-phase galaxy interstellar medium (ISM). This is combined with the archival high-resolution radio data from VLA that help trace the collimated jets. Combining these data, this thesis studies the non-gravitational motions in the galaxy ISM to detect the presence of multi-phase outflows and turbulence.

Firstly, for a single case study, the kinematic properties are studied for a galaxy hosting a radio jet, which is observed to plough through the gas-rich galaxy disk at a low inclination angle. The jet-ISM interactions cause increased turbulence in the plane perpendicular to the jet axis and drive multi-phase outflows that are three times more extended and fast in the ionised gas phase than in the molecular gas

phase. This thesis then looks into the interaction of the molecular gas with extended ($\geq 10\,\mathrm{kpc}$) radio structures at large scales in four galaxies. Two of these reveal molecular gas structures to be entrained along, and wrapped around, the radio bubbles, similar to those seen in brightest cluster galaxies, which are predominantly 'radio loud'. The properties of these structures (velocity-widths, radial extent, mass outflow rate, kinetic power) are observed to be very similar to their 'radio loud' counterparts. Further, all four of these galaxies are observed to host central molecular gas outflows. In the final project of this thesis, a systematic study for these feedback signatures on the multi-phase host galaxy gas is performed on all 9 quasar host galaxies. The central molecular gas outflows are observed across all 9 targets but are seen to be much more compact and slower ($2-5$ times) than the corresponding ionised gas outflows. Large-scale interactions (i.e., beyond the galaxy disk), between the AGN and the molecular gas are only found when there are radio jets on these extended scales. Throughout the thesis, the observations have been qualitatively compared to hydrodynamic jet-ISM simulations finding that the observations are consistent with simulated predictions for interactions between low-power jets and gas-rich galaxy disks. However, further work on larger samples is required to test the quantitative predictions of these simulations. This thesis finishes with discussing such future plans, as well as how the lessons learnt could be applied to observing quasars at cosmic noon, with the advent of next-generation astronomical facilities.

Overall, this thesis demonstrates that multi-phase gas outflows are prevalent across all the 9 studied quasars, and despite the abundance of radiative energy available in the quasars, the low-power radio jets are seen to cause a significant impact on the host galaxy on scales ranging from sub-kpc to $\sim 10\,\mathrm{kpc}$.

Chapter

1 Introduction

Since the earliest times, the Universe has inspired curiosities about its origin and evolution. While the awareness of celestial bodies, their cataloging, and observations are known to be done since ancient times, scientific study and research into these concepts can be dated back to only the sixteenth century.

This chapter sets the scene by introducing the main concepts relevant to this thesis. Thereafter, the chapter presents a brief overview of the research in the relevant field of Active Galactic Nuclei (AGN) feedback and AGN outflows, followed by the open questions that still exist and motivate the research conducted in this thesis.

1.1 Brief History of Galaxies, AGN and Quasars

Various theories were proposed to explain the faintly glowing band, visible in the skies which later came to be known as the Milky Way. The earliest recollection associating the Milky Way with stars comes from *Democritus* ($\sim$400 BCE). In 1610, *Galileo Galilei* used a telescope to observe the night sky and concluded the Milky Way band was composed of many different stars. It was speculated by *Thomas Wright* in 1750 that the stars in the Milky Way band were bounded by gravity and seen as a band due to our perspective of being inside it. In 1755, *Immanuel Kant* suggested that the Milky Way and other 'island universes' showed flattening due to rotation and along with *Johann Lambert* in 1761, presented the first hierarchical and fractal model of the Universe (which until quite later was believed to only extend until the Milky Way galaxy).

The first observational evidence of the structure of the Milky Way came in 1785 by *William Herschel*, who counted the stars in different directions to define the structure of our Milky Way. This was improved upon by *Harlow Shapley*, who cataloged globular clusters and proposed that the galaxy was a flat disk, extending to 70 kpc in diameter, with the Sun far away from the centre (Shapley 1918). However, the effect of interstellar dust absorbing light was not taken into account and it was only in 1930 that *Julius Trumpler* studied the open clusters (see Trumpler 1930) and we arrived at our currently accepted structure of the Milky Way!

Such has been the scientific voyage of comprehending our own galaxy. From understanding our Milky Way to studying the extragalactic sources has been an incredible astronomical feat. The following section summarises this evolution of the historical concepts to our present-day definitions, followed by a systematical introduction to these definitions of Galaxies, Black Holes, Active Galactic Nuclei, and Quasars that are analyzed in quantitative detail in this thesis.

1.1.1 Galaxies in context of Extragalactic Research

A *Galaxy*, is defined today as a gravitationally-bound system of stars, the stellar remnants, interstellar multiphase gas, dust, and dark matter. Further, galaxies are generally categorised owing to their photometric properties and morphology as ellipticals, spirals, and irregulars (Sandage, 1989). While this understanding and definition of a galaxy took ~ 3 centuries to be established, the realization that galaxies other than our Milky Way existed, evolved almost simultaneously. Some of our nearest neighboring galaxies are visible also to the naked eye such as Andromeda, the Large and Small Magellanic, and the Triangulum Galaxy. The earliest documented observations of these started with Andromeda being described as a "small cloud" by a Persian Astronomer. A long time after, in the 18th century (1734), *Emanuel Swedenborg* speculated that there could be other galaxies outside our own that were formed into galactic clusters, extending far beyond those visible with the naked eye or the telescopes at that time. This was followed by many different observations and characteristics that came to define an extragalactic galaxy. To summarise a few, for e.g. nebulae-like structures; collections of stars with an extra, diffuse glow (by *Pierre Louis Maupertuis* in 1745); bright spots that were massive and flattened due to rotation (by *Johannes Hevelius*); visible nebulae in the night sky separate from the Milky Way (by *Thomas Wright* in 1750), and more. These studies led to a great momentum in this field and *Charles Messier* compiled the famous "*Messier Catalog*" consisting of about 109 brightest celestial objects visible in the night sky. Now we know that the Messier Catalog consists of galaxies, star clusters, planetary and star-forming nebulae.

Despite this early speculation, it took about two more centuries until the extragalactic nature of the other galaxies was confirmed. Early use of spectroscopy revealed that the "spiral-nebulae" (Rosse 1850) were, indeed, made up of individual stars (Huggins & Miller, 1864; Scheiner, 1899) with rotational velocities larger than any other astronomical object observed until then (Slipher, 1915, 1917b). The confirmation of these stellar systems being exterior to our Milky Way, i.e., 'extragalactic' came with the emergence of the 'Period-Luminosity' relation of the Cepheid variable stars. Also known as the "Leavitt Law", after *Henrietta Swan Leavitt*, who in 1908 showed that the luminosity of the Cepheid variable stars (or the pulsating variable stars) is proportional to their pulsation period (Leavitt 1908; Leavitt & Pickering 1912). This relation for the Cepheids hence established a benchmark for galactic and extragalactic distances scaling (e.g. the Cepheids observed in Andromeda; Hubble 1925, 1926). This understanding of inter-galactic distances enabled *Georges Lemaître* to theorize and derive that the recession of nearby galaxies could be due to 'an expanding universe' (Lemaître 1927). Shortly after, this was also observationally confirmed by *Edwin Hubble* (Hubble 1929). This brought us to the *Hubble Lemaître Law*, which states that galaxies are moving away from Earth at speeds proportional to their distances, i.e., the further the galaxy, the faster it recedes from the Milky Way galaxy.

About 60 years after, the *Hubble Space Telescope* was launched in 1990, which revealed that there are about 100 billion galaxies in the observable Universe, which resulted in a quantum leap into the modern extragalactic astronomy. With this thus also began the quest to understand the formation, assembly, and evolution of these massive extragalactic objects. The historical evolution of these concepts is

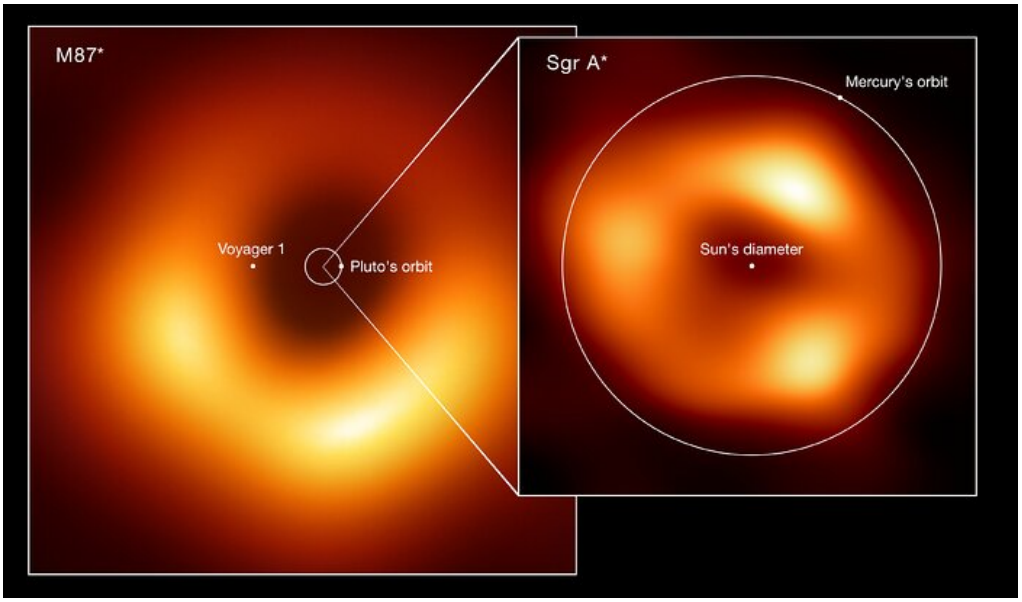

Figure 1.1: The black holes at the center of Messier 87 (left) and Milky Way (right) imaged by the Event Horizon Telescope (EHT) Collaboration with a size comparison. The black holes are respectively referred to as M87* and Sagittarius A*. These images provided a confirmed observation of super-massive black holes residing in the centre of galaxies. To appreciate the massive scales of the accretion disks of the black holes, a comparison to the orbits of the nearest planet, Mercury, and the dwarf planet, Pluto is also shown. *Image Credit: ESO Website.*

a testimony of how cognizance emerges through comprehensive and collaborative research. That it takes many people, and many techniques, and bit by bit, we connect the puzzles to our ever-evolving knowledge of the Universe. While there are a plethora of studies aimed at understanding the evolution of galaxies, this thesis focuses on the fascinating objects in their center, that is supermassive black holes, that are now gaining importance in terms of their effects on the evolution of the galaxies they reside in.

1.1.2 Active Galactic Nuclei

Active Galactic Nuclei (AGN) are compact regions in the center of the galaxy that are emitting highly energetic radiation over a broad range of wavelengths, observed in radio, microwave, infrared, optical, ultra-violet, X-ray, and gamma-ray bands. There has now been observational evidence suggesting that supermassive black holes (SMBH)[1] are present at the centers of each of the galaxies and these are the objects responsible for the AGN emission (for full review see, Kormendy & Richstone 1995; Kormendy & Ho 2013).

The first recorded observation of an AGN (which was not known back then) comes from 1908 by *Edward A. Fath* who was observing NGC 1068. However, it was in 1917 that the unusually broad, strong, and high excitation lines were noticed (Slipher, 1917a). This was followed by the radio jet in M87 being noticed and curiously described as a straight array connected with the nucleus by a thin line of matter (Curtis 1918). Over the next 25 years, various scientists started to examine galaxies

[1] SMBH are very massive BH formed at the centre of the galaxy with the mass of about 10^5–$10^{10}\,M_\odot$; unlike the stellar mass BHs that have masses of 2–20 $M_\odot$. In this thesis, every time a black hole is mentioned, it refers to an SMBH.

Figure 1.2: The image of a quasar 3C 273 observed as part of the Sloan Digital Sky Survey (SDSS). The star-like appearance of the quasar (the bright source in centre) is evident in this image when compared to a neighbouring star (to the right). The host galaxy is hardly visible in this image. Further, a faint radio jet can be seen extending towards the bottom-right of the quasar. *Image Credit: SDSS.*

with strong emission lines, and in 1943, Carl Seyfert published his work on the spectral study of the nucleus of 6 such galaxies. Consequently, such galaxies also came to be known as 'Seyfert' galaxies and two classes were established: (1) "type-1" where permitted emission lines are broader than forbidden lines and (2) "type-2" where they both have similar line-widths (definitions expanded in Section 1.2; also see Weedman 1970a; Khachikyan & Weedman 1971). Studies in the subsequent years confirmed that the Seyferts had a very bright region which was also confirmed to be compact, following variability studies.

Astronomers have now been able to peer into the centre of the M87 galaxy, our nearest neighbour with an actively accreting nuclei, and have obtained an image of its very central regions. We also now have an image of the SgrA*, the black hole at the center of our own Milky Way galaxy, however, it is not active (see Figure 1.1). These images show all the material in the immediate vicinity of the black hole covered by the 'shadow' of the black hole itself. These observations hence provide direct visual evidence for the existence of these SMBH at the centre of our Milky Way galaxy and its active counterpart in our more massive neighbor, M87, thanks to the technological advancement of the Event Horizon Telescope (EHT; for SgrA* see: Event Horizon Telescope Collaboration et al. 2022a,b,c,d,e,f; for M87 see: Event Horizon Telescope Collaboration et al. 2021a,b).

While presently astronomers are still on a quest to understand what role AGN play in the evolution of a galaxy (see Section 1.4), the understanding of what an AGN in itself is has had its own journey as summarised in the following sections.

1.1.3 Quasars

Quasars are optically very bright and powerful AGN with high bolometric luminosities. However, owing to their discovery in 1963, quasars got their name from being "quasi-stellar", since they were observed as very bright sources of light in the sky that looked like stars (see Figure 1.2). It was discovered much later that these quasi-stellar objects were the nuclei of galaxies and were so radiatively powerful that

they were shining much brighter than the entire galaxy itself. As explained below shortly, the probable mechanism that could produce such tremendous energy could be the accretion of mass onto a black hole!

Because of this star-like appearance, it was quite recently (only 60 years ago) that quasars were understood as being extragalactic objects by *Alan Sandage* in 1963 (Matthews & Sandage, 1963). He studied the spectra of the QSO 3C273 (see Figure 1.2) and found four broad lines from the Balmer series in addition to some forbidden lines. Using these lines, he estimated a cosmological redshift $z = 0.158$, which would have meant that quasars are far away. This was also supported by further studies suggesting quasars to be far (see Schmidt 1963; Greenstein 1963). While initially, this theory received quite some resistance (e.g., see Weedman 1976, 1977), eventually, it became apparent that quasars were the more distant and much more radiatively powerful versions of the Seyfert galaxies. Around this time, independent works also led to the discovery of collimated, large-scale structures (extending up to megaparsecs), originating from the nuclear regions of the galaxies; which came to be recognized as radio jets[2] later (Baade & Minkowski, 1954; Burbridge, 1963). The galaxies with these powerful radio jets hence got their reputation as powerful radio galaxies.

We now know that powerful radio galaxies, quasars, and Seyfert galaxies, all fall under the broad categorization as active galactic nuclei, since they are all associated with activity leading to strong emissions from the nuclei. For this thesis, I use the term "quasar" to refer to the most-luminous AGN (see Section 1.7). The following section discusses the different categories in which AGN are characterized.

1.2 AGN Model and Categorisation

As discussed in Section 1.1.2, when the SMBH at the centres of galaxies are seen to be "active", i.e., they are accreting matter and emitting very energetic radiation across different wavelengths, they are called the Active Galactic Nuclei. For some wavelength bands, these radiation are seen to be in excess of thermal radiation (or that expected from stellar processes) and are hence expected to come from the accretion of matter by the supermassive black holes at the centre of the galaxy. While the energy liberated from the nuclear fusion of two protons is roughly $\sim 6 \times 10^{18}\,\mathrm{erg\,g^{-1}}$, the accretion of mass m from ∞ until the Schwarzschild radius ($\mathrm{R_s}$) of a black hole (of mass M) liberates an accretion energy of $\sim 10^{20}\,\mathrm{erg\,g^{-1}}$ (following the relation, $\Delta\,\mathrm{E_{acc}} = \mathrm{G\,M\,m/R_s}$; where G is the gravitational constant; also see Salpeter 1964; Zel'dovich & Novikov 1964; Lynden-Bell 1969; Rees 1984); thereby making accretion a very efficient astrophysical energy production mechanism with $\approx 10\%$ efficiency of mass-to-energy conversion (Soltan, 1982; Marconi et al., 2004).

This magnificence is captured by Figure 1.3, which shows an observation of the Centaurus galaxy (left-panel) with an AGN at its centre emitting strong radiation and radio jets emanating from the accretion disk and reaching up to 250 kpc. The right panel of Figure 1.3 shows a model of the AGN very centrally zoomed into

[2] seen due to the strong synchrotron radio emission (Blandford & Königl 1979)

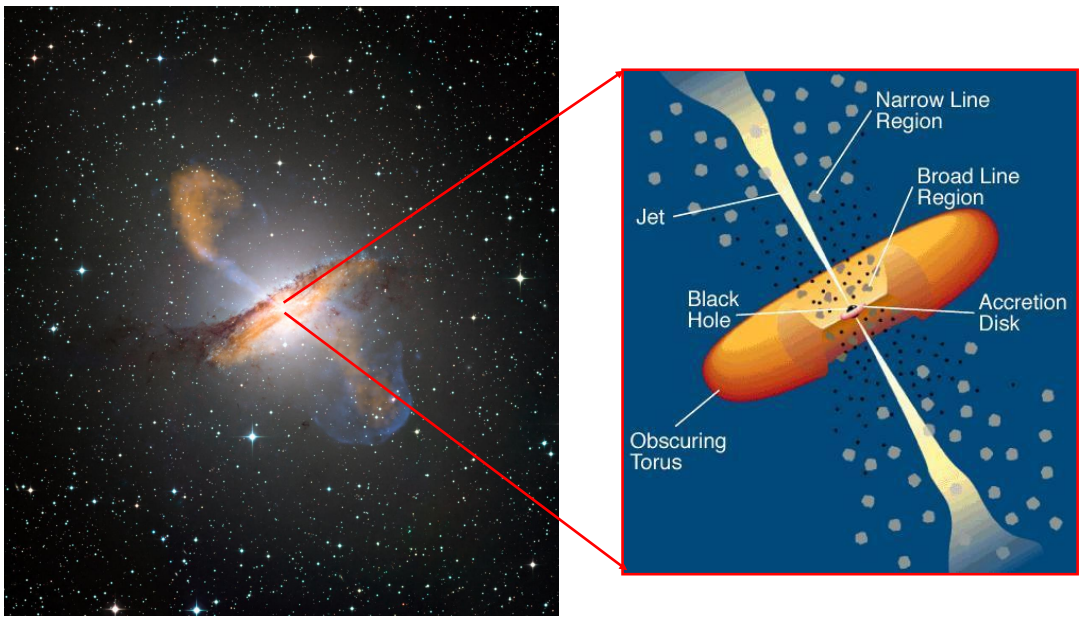

Figure 1.3: Left Panel: The colour composite image of Centaurus A with the galaxy disk shown in the centre and large radio jets emanating from the accretion disk around the active galactic nuclei, along with radio lobes seen towards the end. The radio jets span about ∼250 kpc in projected distances. *Image Credit: ESO/WFI (Optical); MPIfR/ESO/APEX/Weiß et al. 2008 (Submillimetre); NASA/CXC/CfA/Kraft et al. 2002 (X-ray).* **Right Panel:** A schematic representation of the unified model of an active galactic nucleus given by Urry & Padovani 1995 for radio loud AGNs. The model shows that the narrow and broad-line regions may correspond to different AGN orientations.

the galaxy at ∼ kpc scales. The AGN model represents some key components of an AGN which are also relevant to this thesis and are defined below (also see: Urry & Padovani, 1995; Ghisellini, 2013):

- **Accretion disk**: Cold material attracted by the gravitational pull of a black hole forms a spiraling disk around the BH and is called an accretion disk. The accretion disk transfers the matter inwards and the angular momentum outwards. These processes cause the accretion disk to heat up, which itself emits radiation over a broad range of wavelengths, peaking in the optical-ultraviolet range. The accretion disk also emits at particular wavelengths due to the excitation of the cold material in the vicinity of the black holes leading to strong emission lines.

  The standard accretion disks accrete at rates lower than or equal to the Eddington luminosity[3] and have a geometrically thin but optically thick disk which hence leads to thermal emission of the photons. The accretion disk therefore emits a thermal spectra; which can be seen as the overlap of multiple blackbody emission curves at temperatures varying from UV in the center to infrared at the outer edges. These photons emitted from the accretion disk can also be excited due to the presence of an X-ray corona, which develops as a disc of hot material above the accretion disk and causes inverse Compton scattering of the photons thereby increasing their energies up to X-ray wavelengths.

[3] *Eddington Luminosity* (L_{edd}) defines a physical limit of the black hole at which the radiation pressure from the accretion of the infalling matter balances the gravitational force of the black hole.

The two exceptions to the standard accretion disks are when the radiative efficiency is significantly lower or much higher than the Eddington luminosities. In the former case, the accretion disk is known as ADAF (advection-dominated accretion flow), and the accretion luminosity is observed to be up to 1000 times less than the Eddington luminosities. The other case is that of super-Eddington ratios, where an accretion rate higher than Eddington luminosity is achieved through loss of heat and temperature due to physical mechanisms, consequently leading to very high AGN luminosities. The latter is also often the case observed for Quasars (see Section 1.1.3).

- **Broad Line Region (BLR)**: The region very close to the black hole, $\lesssim 1\,\mathrm{pc}$, has fast-moving ($\sim 10^{3-4}\,\mathrm{km\,s^{-1}}$) and dense ($\sim 10^{10}\,\mathrm{cm^{-3}}$) gas clouds. This region produces broad emission lines due to the *Doppler broadening* of the emitted spectral lines, which is a result of the motion of the gas clouds due to their temperature (thermal motions); turbulence (non-thermal motions); or due to rotational motion; all causing the photons to be emitted at slightly varying wavelengths than the expected emission wavelength and causing the spectral line to broaden. The expected line-width due to thermal doppler broadening of $10^4\,\mathrm{K}$ gas (which is the ideal expected nebular temperature), results in a broadening of only $\sim 10\,\mathrm{km\,s^{-1}}$; and hence BLR are significantly supersonic clouds. The BLR are thus the strongly ionized regions, arising from the deep gravitational potential of the black hole. While the BLR region is quite compact, the emission lines are still observed with sufficient flux since the high-density gas is very efficient in emitting line spectra leading to broad permitted lines (detailed in Section 2.1.2 and for a full review, see Peterson 2006).

- **Narrow Line Region (NLR)**: The NLR is a more spatially-extended region ($\sim 100\,\mathrm{pc} - 1\,\mathrm{kpc}$) of comparatively less dense ($\sim 10^3\,\mathrm{cm^{-3}}$) and less fast-moving ($\leq 500\,\mathrm{km\,s^{-1}}$) gas clouds. However, the gas clouds still have speeds greater than that expected thermally. While the BLR clouds are expected to be hidden due to enshrouding dust and particles, NLR clouds often extend beyond and are hence observable in the case of many galaxies. They are a useful tracer of the physical properties of the galaxy interstellar medium and are either photo-ionized by the strong AGN radiation and/or are transferred from the more central regions with AGN-driven outflows. Either way, unlike the BLR, they are not under the strong gravitational influence of the BH. These narrower lines could be produced due to permitted as well as forbidden emission lines since the low density allows the electrons to be de-excited from metastable states by emitting a photon before it is collisionally de-excited (as further detailed in Section 2.1.2).

- **Jets**: They arise from the accretion disk, from the regions close to the black hole, carrying energetic plasma and strong radiation, as magnetically-collimated bipolar outflows. They are detected the strongest in radio waveband due to synchrotron processes producing a radio continuum emission and can be seen to extend from sub-kpc to hundreds-of-Mpc scale. They are also seen in higher wavelengths up to gamma rays due to the additional inverse Compton scattering processes at play. The direction of the jets may depend either upon the axis of the angular momentum disk or the black hole spin axis.

These different AGN components form a basis for the understanding of different AGN categories. AGN have come to be characterized into different categories based upon different classification criteria. These categories are often overlapping and the definitions continue to evolve. Below the categorizations pertinent to the work in this thesis are discussed on the basis of:

- the properties of the optical emission-line spectra: Type-1 and Type-2
- the level of radio emission: 'Radio Loud' and 'Radio Quiet'

1.2.1 Based on Orientation: Type-1 and Type-2

In the standard model of AGN (Antonucci 1993; Urry & Padovani 1995), AGN are classified as Type-1 and Type-2, which arises from the angle at which the AGN is viewed as shown in Figure 1.3; right-panel. Under the 'unified model', this is considered to be a fundamental property of the AGN depending on the viewing angle of the observer, and not different physical objects themselves. Observationally, the spectra from Type-1 AGN show broad emission lines in optical spectra indicating high densities and a rising continuum towards the blue wavelengths (owing to the accretion disk). Within the model, the viewing angle of Type-1 AGN allows the central regions (of the accretion disk/ BLR) to be visible.

On the contrary, in Type-2 AGN, the spectra have comparatively less continuum emission, which doesn't show a steep rise to blue wavelengths and broad emission lines are not seen. Within the model, the viewing angle is along the torus, thus the central regions are obscured by the dusty torus while also hiding the broad-line regions. In Type-2 AGN the Narrow-Line Region is still visible, and narrow high-intensity lines consisting of permitted as well as forbidden lines are seen.

In summary, the Type 1 AGN spectra have the presence of both the broad and the narrow emission lines. The permitted lines are often seen to be broad due to the rotational motion of the very fast-moving clouds visible in the vicinity of the black hole. In addition, the Type 1 AGN spectra also consist of some narrow forbidden lines (see Section 2.1.2). In contrast, the Type 2 AGN spectra only show the presence of narrow emission lines (permitted and forbidden), as the spectra are obtained from gas clouds much farther out from the galaxy center. This thesis focuses on a sample of Type-2 AGNs.

1.2.2 Based on Radio Emission: 'Radio Quiet' and 'Radio Loud'

Within the radio wavelength regime, the emission from different classes of AGN is seen to vary over a factor of 10^5, for the bolometric luminosity (Panessa et al. 2019). The radio loudness parameter is classically defined as the ratio of radio to optical flux density as, $\frac{f(6\,cm)}{f(4400\,\text{Å})}$, by Kellermann et al. (1989). In general, the 'radio quiet' (RQ) AGN are observed to be typically 1000 times fainter at radio wavelengths than the 'radio loud' (RL) AGN. The radio emission in RL AGN have come to be associated with powerful radio jets. In contrast, the origin of the comparatively much

lower radio emission in RQ AGN is quite unclear with possible sources being star-formation, AGN corona, AGN jets, and AGN nuclear radiative winds (see Panessa et al. 2019).

Studies have shown that this criterion of division is not a reliable method for separating AGN with and without a jet (see for e.g., Cirasuolo et al. 2003; Padovani et al. 2017; Gürkan et al. 2019). The presence of jets has been the main criterion to assign an AGN to the RL class, however, it is shown for the RQ targets that sensitive observations can reveal radio jets even in these targets (see Jarvis et al. 2019, 2021). Furthermore, traditional 'radio loud' AGN have been selected from radio surveys while 'radio quiet' AGN are generally observed in X-ray, infrared, etc. This further complicates the scenario suggesting that the two may not be different physical classes but a single continuous population (Cirasuolo et al., 2003; Gürkan et al., 2018). In this thesis, I demonstrate that the low-power radio jets are an important component of 'radio quiet' AGN and the evolution of their host galaxies. These things may evidence an evolutionary sequence of how the radio jets may affect the evolution of their own galaxy as they themselves propagate, thus again suggesting physically similar populations (Morganti et al. 2023; Talbot et al. 2021).

In this thesis, the traditional criteria of Xu et al. (1999) are used to classify type-2 as 'radio quiet' or 'radio loud'. For Type-2 AGN, the [OIII] emission-line luminosity has been used as the tracer for the optical luminosity. This criterion has been defined based on the ratio of the luminosity of the AGN in the radio wavelengths to that in optical, and precisely, [OIII] wavelengths. 'Radio quiet' quasars are expected to have their radiative energy as a more important driver. However, as the thesis expands in subsequent chapters, the jet-powered outflows and winds have also been observed to cause significant turbulences in the host galaxies.

1.3 Co-evolution of supermassive black hole and host galaxy

It is now very widely accepted that supermassive black holes reside at the centre of all massive galaxies and grow through mass-accretion events, becoming visible as AGN. Therefore, AGN are ubiquitous and each galaxy goes through at least one or multiple AGN episode(s) in its evolution (full review in Kormendy & Ho 2013). This Section discusses pieces of evidence that suggest a co-evolution scenario between the SMBH and its host galaxy.

- One of the observations that demonstrates this co-evolution is the remarkable similarity between cosmic star-formation density and the cosmic BH growth (scaled up by an arbitrary factor), with both peaking at redshift of z$\sim$1–2 (shown in Figure 1.4; also see Madau & Dickinson 2014, and the references therein). The average Eddington ratios[4] of local AGN suggest a much more rapid growth in the past (Heckman et al., 2004), further, more quasars (most luminous AGN) are seen at a z$\geq$1 than locally (Schmidt & Green, 1983; Hewett et al., 1993; Boyle et al., 2000; Richards et al., 2006).

[4] ***Eddington ratio*** is the ratio of the AGN's Bolometric Luminosity to its Eddington Luminosity, i.e., L_{bol}/L_{edd}. The *Bolometric Luminosity* (L_{bol}) can be defined as the total energy radiated per second (i.e. power or luminosity) by an AGN across all emitting wavelength ranges. L_{bol} depends on the rate of mass accretion onto the black hole and the efficiency of conversion of the gravitational energy to radiation.

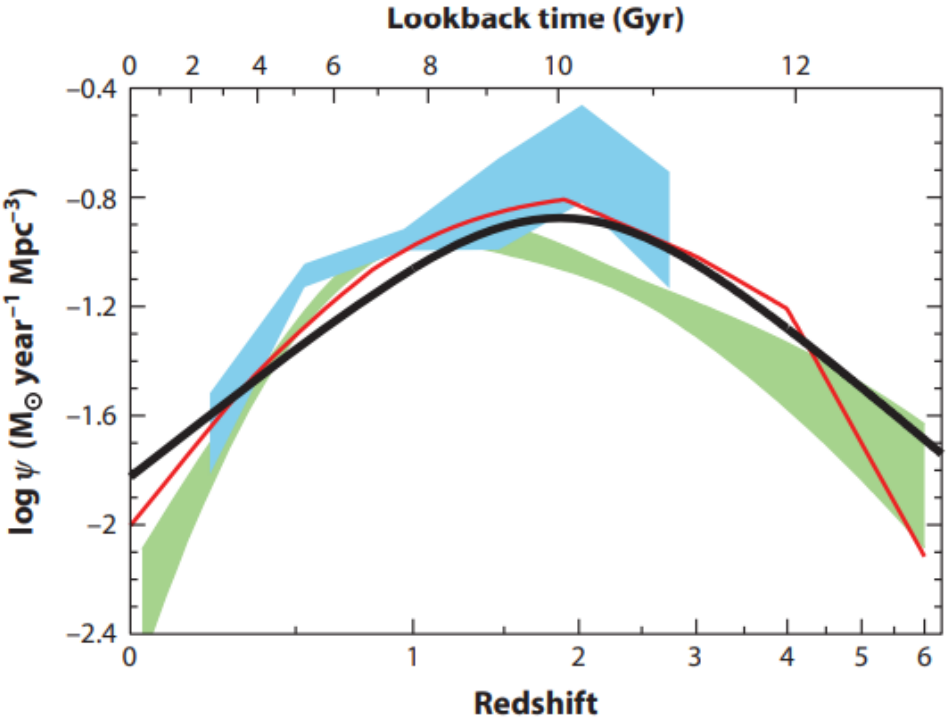

Figure 1.4: The *Madau-Dickinson Plot* showing the cosmic evolution of the star-formation rate history (black curve; from Madau & Dickinson 2014). Different methods are used to represent the SMBH accretion history, each scaled up by a factor of 3300, for example, using the X-ray data (red curve; Shankar et al. 2009 and green-shading Aird et al. 2010); and infrared data (blue-shading; Delvecchio et al. 2014). The shaded regions represent the $\pm 1\sigma$ uncertainity on the bolometric luminosity density. As can be seen from the plot, the peak of the star-formation history and SMBH accretion history are similar and around $z = (1–2)$. This is observed to reduce towards smaller redshift (more recent times).

- Another very interesting observation comes from the scaling relations between the SMBH and the properties of the host galaxies spheroid component (full review in Kormendy & Ho 2013). As shown in Figure 1.5, there is a tight correlation between the mass of the black hole and the stellar velocity dispersion in the galaxy bulge (Ferrarese & Merritt, 2000; Gebhardt et al., 2000). Further, the mass of the SMBH is also seen to be correlated to the luminosity of the galaxy bulge (Dressler, 1989; Kormendy, 1993).

The studies above suggest a co-evolution between the AGN and its host galaxy. While this co-evolution could be regulated by an external/third factor (e.g. environment, gas supply, mergers), the focus of this thesis is to investigate a causal connection if any between the host galaxy and the SMBH. Indeed a causal connection is a key component of current galaxy evolution theory (see Section 1.4). The challenging aspect to the existence of the causal connection is that the two phenomena operate on very different spatial scales, i.e., different by ~ 9 orders of magnitude[5]. In the following section, I will discuss how outflows of energy and matter powered by AGN could serve as proof of this causal connection. Despite a great spatial difference, numerical simulations commonly use these outflows to invoke the so-called AGN feedback to be able to reproduce the observed galaxy properties as discussed in the following section.

[5]Roughly, if the spatial extent of an AGN was to be approximated to the size of a coin, its host galaxy would then be about the size of the Earth!

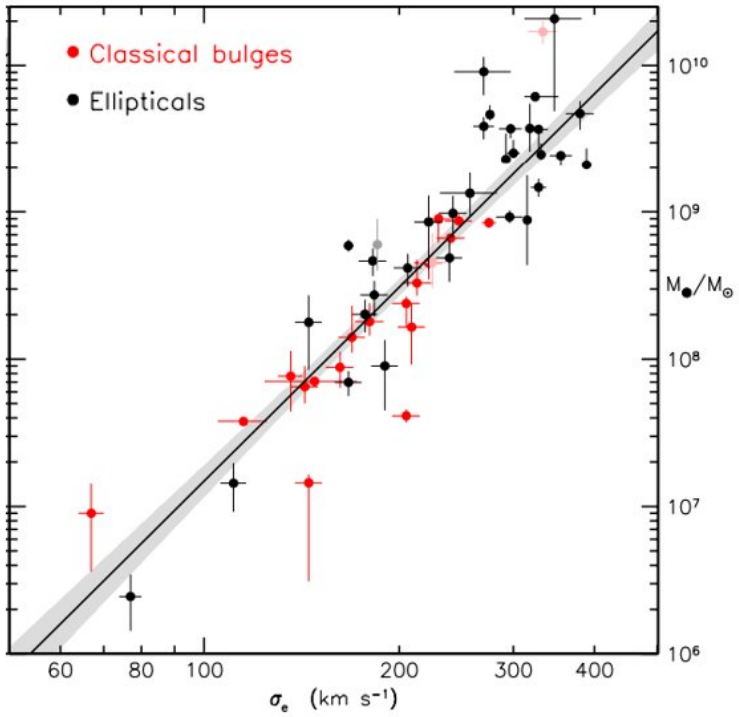

Figure 1.5: The correlation of dynamically measured black hole mass ($M_{BH}/M_\odot$; along right y-axis) with respect to the stellar velocity dispersion (σ_e; along x-axis) of classical bulges (in red) and elliptical galaxies (in black). The solid black line is the symmetric least square-fit to the galaxy points. The shaded grey region shows the 1σ error range for the fit.) *Figure from: Gültekin et al. 2009; Kormendy & Ho 2013.*

1.4 AGN Feedback

During the phase as an AGN, an SMBH releases a tremendous amount of energy. This energy may be released in the form of energetic photons (i.e., radiation), particles (i.e., winds or jets), and/or both. To understand the effect of this energy released from an AGN, the binding energy (E_{gal}) of the galaxy can be compared to the energy released by an accreting black hole (E_{BH}; also see Fabian 2012). With a mass of M_{gal} and a velocity dispersion of σ, the binding energy of the galaxy can be calculated as:

$$E_{gal} = M_{gal} \times \sigma^2 \tag{1.1}$$

The energy released by a black hole with mass (M_{BH}) and an accretion efficiency of 10 % (Soltan 1982; Marconi et al. 2004) can be computed as:

$$E_{BH} = 0.1\, M_{BH}\, c^2 \tag{1.2}$$

From observations, the mass of black hole is typically seen to be $M_{BH} = 10^{-3}\, M_{gal}$ (Kormendy & Gebhardt, 2001; Merritt & Ferrarese, 2001; Häring & Rix, 2004). For this comparison, the velocity dispersion estimate for J1316+1753 is used, which is an example quasar from the Quasar Feedback Survey (see Section 1.7) sample studied in detail in Chapter 3.

$$\frac{E_{BH}}{E_{gal}} = \frac{0.1\, M_{BH}\, c^2}{M_{gal} \times \sigma^2} = 0.1 \times 10^{-3} \times \frac{c^2}{\sigma^2} \approx 10^{-4} \times \left(\frac{3.10^5}{300}\right)^2 \approx 100$$

$$E_{BH} \approx 100 \times E_{gal}$$

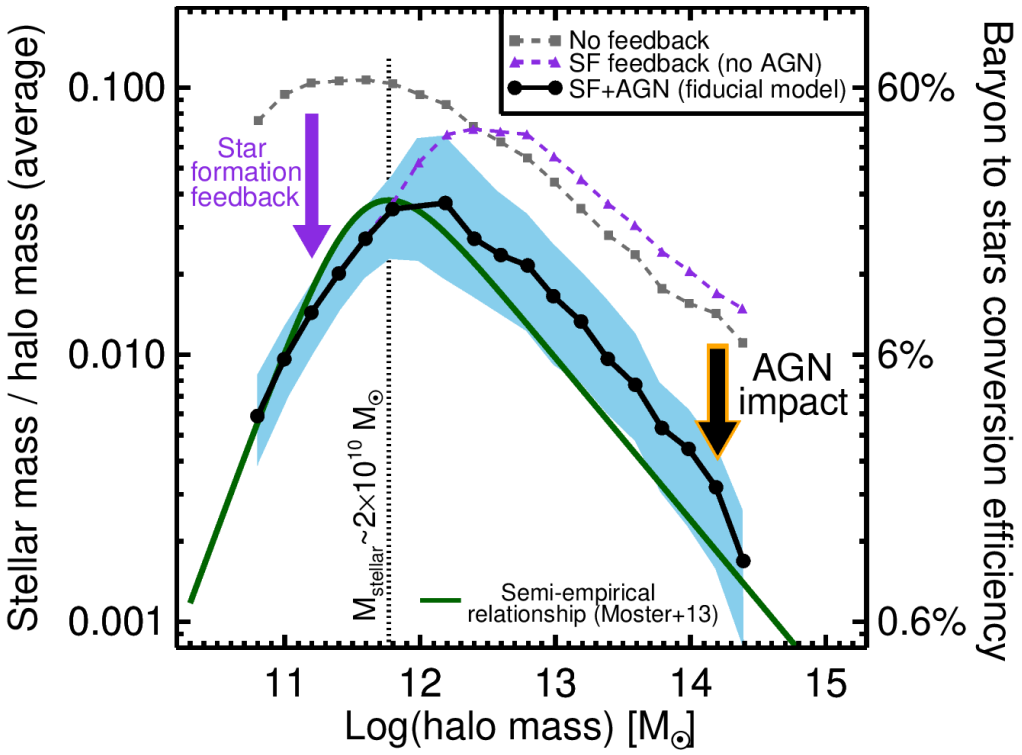

Figure 1.6: The comparison between three semi-analytical models with the semi-empirical relationship (in green), in the parameter space of stellar to halo mass vs. the halo mass. The right y-axis represents the efficiency of forming stars. The plot shows that at lower halo masses, feedback from star-formation (shown through the grey arrow) reduces the efficiency of converting baryons to stars. However, at the larger halo mass regions, without AGN feedback, the models overestimate the stellar-to-halo mass ratio. Hence, an energy injection from AGN (shown through the black arrow) becomes imperative to reduce the star-forming efficiency. *Image Credit: Harrison (2017).*

Hence, as seen in Equation 1.2, AGN accretion can lead to a tremendous energy output, which is much higher (about 2-3 orders of magnitude) than even the binding energy of the galaxy. Thus even if a small fraction of this energy couples with the interstellar medium, it can have a significant impact on the evolution of the host galaxy. For example, by removing and/or heating the material in the host galaxy; hence, regulating the rate at which the stars can form. Thus, an accreting SMBH (or AGN) has the potential to regulate the growth of the galaxy in relation to its own growth, also known as **AGN Feedback**.

Current models and simulations of galaxy evolution have emphasized the need for AGN Feedback to reproduce the galaxy observables (e.g. see, Silk & Rees 1998a; Churazov et al. 2005; Bower et al. 2006; Hopkins et al. 2006; McCarthy et al. 2010; Gaspari et al. 2011; Debuhr et al. 2012; Schaye et al. 2015; Lacey et al. 2016; Harrison 2017). Figure 1.6, shows one such formulation necessitating AGN Feedback. In Figure 1.6, the ratio of stellar mass-to-halo mass is compared with respect to the halo mass. It can be seen that in order to simulate a realistic population of galaxies (in black, from Somerville et al. 2008) to match with the empirically observed relation (in green; from Moster et al. 2013), AGN Feedback is needed especially for the high halo mass range. Without the energy injection from AGN, the simulations don't match the empirical relation with only stellar feedback[6] and without any sort of

[6]Stellar Feedback is a result of mass, energy or momentum injected into the galaxy inter-stellar medium due to the massive stars; thereby affecting the galaxy ISM and further the star-formation itself.

feedback. This shows that while stellar feedback suppresses galaxy growth in low mass halos ($< 10^{12} M_{\odot}$), AGN feedback is necessary to suppress the galaxy growth (by energy injection) at higher halo masses ($> 10^{12} M_{\odot}$; also see, Bower et al. 2006; Croton et al. 2006; Harrison 2017). AGN Feedback is also used as an explanation for more observables such as rates of gas cooling in galaxy clusters, the relation between luminosity and temperature in X-ray, the color bi-modality of galaxies, and, the evolution of cosmic star-formation density (see Figure 1.4; Quilis & Moore 2001; Churazov et al. 2002; Peterson 2003; Bower et al. 2006, 2008; Croton et al. 2006; Puchwein et al. 2008; McCarthy et al. 2010). AGN are also often required to obtain correct galaxy sizes, the distribution of metals, the properties of the intra-cluster medium, and star-formation rate distributions, to name a few (also see, Gaspari et al. 2011; Dubois et al. 2013; Hirschmann et al. 2014; Vogelsberger et al. 2014; Henriques et al. 2015; Choi et al. 2018).

However, theoretically as well as observationally, to reduce the efficiency of converting baryons to stars (right y-axis in Figure 1.6), there are different routes in which the 'Feedback' from AGN may progress - *ejective*, *preventive*, or both. For the growth of the galaxy, the cool molecular gas serves as the fuel for more star-formation thereby aiding the evolution of the galaxy. The AGN might affect the inter-stellar medium gas either by removing it through strong bursts of energy or by injecting turbulences in the medium, thereby heating/ionizing the fuel available for star-formation and reducing the efficiency of star-formation (also see Costa et al. 2020). Depending on how the energy and momentum released from the accretion disk; i.e., in the form of radiation, jets, and/or winds, forms the basis of the archaic classification of the different feedback modes as *radio mode feedback* and *quasar mode feedback*, as discussed in the following.

1.4.1 The different modes of AGN Feedback

The importance of AGN feedback in galaxy evolution is determined by if and how efficiently the available energy and momentum are transferred to the inter-stellar and circum-galactic gas. Despite cosmological and hydro-dynamical simulations being able to successfully produce the bulk properties of massive galaxies, the main physical mechanism that couples AGN energy to its surroundings is a matter of ongoing debate. The "quasar mode" and "radio mode" definitions arise from early semi-analytical models (e.g., Bower et al. 2006) differentiating the two modes based on the luminosity as discussed below.

As shown through the schematic in Figure 1.7, in the *'Quasar Mode'*, the powerful radiation from the quasars (bolometrically luminous AGN) is capable of coupling with the gas, thereby resulting in high-velocity winds (or 'superwinds') propagating through the galaxy ISM (upto galactic scales), thereby inducing turbulences and/or causing gas removal. This mode is seen in AGN with high accretion, such as in quasars. Since the initial energy originates from radiation pressure, this mode is also known as 'radiative' mode feedback (e.g. Faucher-Giguère & Quataert 2012; King & Pounds 2015; Costa et al. 2018). The other form of feedback (shown in the right panel of Figure 1.7) is called 'radio' mode or the 'maintenance' mode feedback. This case progresses through powerful radio jets, associated with radiatively-poor AGN, and are formed due to low-accretion rates. They add energy in the circum-galactic medium (CGM) and inter-galactic medium (IGM) thereby preventing the cooling of

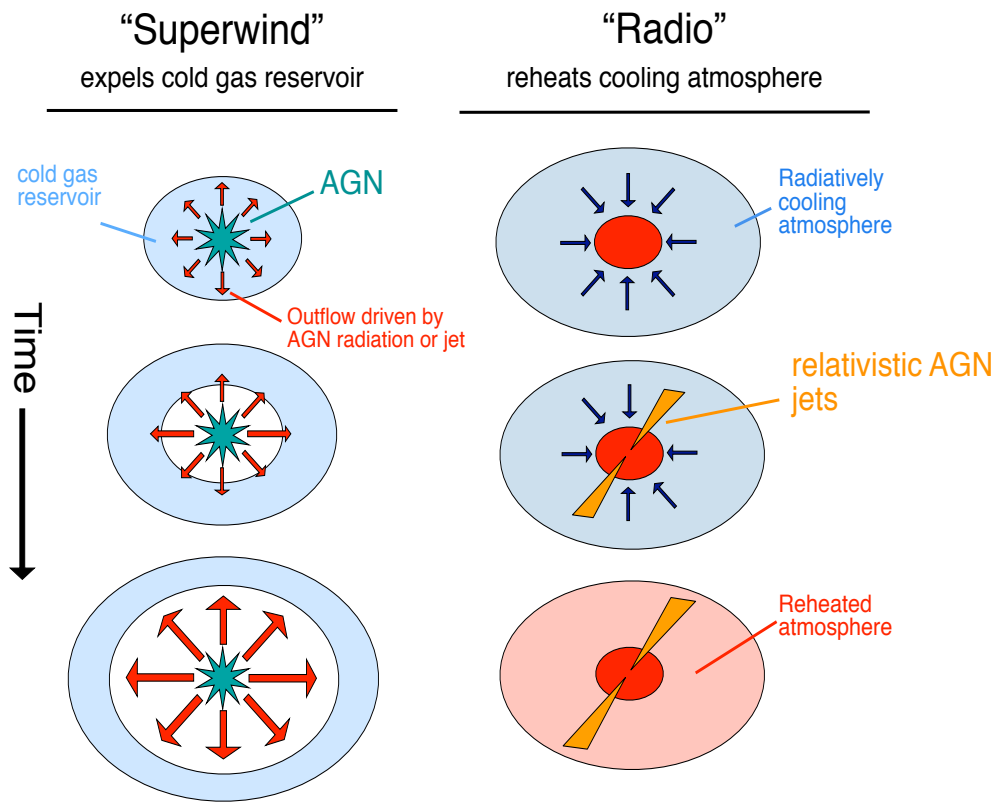

Figure 1.7: The two different feedback modes as explained by Alexander & Hickox (2012). The left panel shows the quasar mode being driven by quasars and the right panel shows the radio mode. See Section 1.4.1 for a full explanation. In this thesis, I mainly focus on understanding the feedback of the quasar mode on the quasar-host galaxies.

gas and preventing/ slowing the inflow of gas from CGM to the galaxy for further star-formation (e.g. see, Churazov et al. 2005; Alexander & Hickox 2012; McNamara & Nulsen 2012). While the maintenance mode feedback has been intensively studied in the past, the understanding of quasar mode feedback still remains very preliminary.

However, this division has now become quite obsolete with simulations (e.g., IllustrisTNG; Springel et al. 2018; Pillepich et al. 2018; Nelson et al. 2018; Marinacci et al. 2018; Naiman et al. 2018) implementing luminosity-based modes using a combination of a complex suite of variables and properties and other simulations not using any such modes at all (e.g. EAGLE; Crain et al. 2015; Schaye et al. 2015). Observations have also now come to show that the classification of the two modes is confounding, as is also discussed in detail in the following section. For quasars, particularly for those traditionally classified as 'radio quiet' (see Section 1.2.2), the origin of the connection between radio emission and outflows remains less clear, even with spatially-resolved studies (Wylezalek & Morganti, 2018). For powerful quasars, accretion disk winds and radiation pressure on dust are viable mechanisms for driving multi-phase outflows over galaxy-wide scales (e.g. Silk & Rees, 1998b; King & Pounds, 2003; King, 2005; Zubovas & King, 2012; Wagner et al., 2013; Tombesi et al., 2015; King & Pounds, 2015; Ishibashi & Fabian, 2016; Veilleux et al., 2020; Arav et al., 2020; Costa et al., 2018, 2020). Any radio emission associated with corresponding shocks in the ISM (e.g. Jiang et al., 2010; Zakamska & Greene, 2014; Zakamska et al., 2016; Nims et al., 2015; Hwang et al., 2018) or

with in-situ star-formation makes the interpretation of the emission challenging (e.g. Riffel et al., 2014; Alexandroff et al., 2016; Jarvis et al., 2019). Further analysis is required to establish the relative role of radio jets, compared to other processes, for driving outflows in quasar host galaxies. Further, recent studies have revealed that the radio jets are capable of affecting the ISM as well as the CGM, thus blurring the distinction between the two modes. This ambiguity between the two modes is discussed in detail in the following section.

1.5 Multiphase AGN Outflows

The direct observational evidence of a causal connection between the SMBH and its host galaxy comes from the observations of multiphase AGN outflows. AGN-driven outflows (or AGN outflows) are launched from the accretion disk or the dusty torus surrounding the BH due to a collimated radio jet or a wide-angled and radiatively-driven wind. Further, it could also be launched from further away, e.g., at the location of a jet-ISM interaction or by radiation pressure. While the driving mechanisms of these outflows can be different, the impact they have on the host galaxy is crucial and depends on how efficiently they couple with the ISM to remove/disturb it and sweep it up thereby causing galaxy-scale outflows. High-velocity outflows have been proposed as an efficient feedback mechanism in massive galaxies (e.g. Benson et al. 2003; McCarthy et al. 2011; Hopkins et al. 2013; Zubovas & King 2014). Observations of low-redshift AGN have identified outflows in molecular, ionized, and atomic gas phases at kpc-scales (Nesvadba et al., 2006, 2008; Fu & Stockton, 2009; Feruglio et al., 2010; Rupke & Veilleux, 2011; Alatalo et al., 2011; Nesvadba et al., 2011; Morganti et al., 2013; Veilleux et al., 2013; Liu et al., 2013; Wylezalek & Morganti, 2018; Morganti et al., 2021). Further, it has been speculated that if the kinetic powers of the outflows are even about $\sim 0.5\%$ of the AGN Eddington limit, then they could potentially remove gas from the host galaxies and quench star-formation (Hopkins & Elvis, 2010; Faucher-Giguère & Quataert, 2012).

Observations of outflows extended up to kpc-scales highlight how potentially they can impact the host galaxy. However, there are open questions on what mechanism is responsible for launching these outflows as discussed below.

1.5.1 AGN Winds

Observationally, radiatively-efficient AGN (like quasars) are seen to host a high percentage ($\sim 80\%$) of outflows in the form of high-velocity winds (up to $\sim 0.1\,c$; also see Crenshaw et al. 2003; Ganguly & Brotherton 2008; Tombesi et al. 2012). These ultra-fast outflows are usually observed in the X-ray and UV bands. These are typically associated with winds launched close to the accretion disk (full review in King & Pounds 2015; Morganti 2017; also see Costa et al. 2020). The theory states that these winds are thought to undergo growth in a bubble of entrained plasma, which undergoes an energy-conserving expansion, in which while the winds expand, they interact with and shock the ISM while still conserving the energy but losing momentum. This loss in momentum is added to the ISM which causes it to sweep up the gas and drive an outer shock (see Zubovas & King 2012; Faucher-Giguère & Quataert 2012). It could also be that the wide-angle quasar winds are due to the radiation pressure on dust launching these winds from the accretion disk or on larger

scales (as discussed in Ishibashi & Fabian 2015; Thompson et al. 2015; Bieri et al. 2017; Costa et al. 2018, 2020). The shocks produced by these radiation winds are also proposed to produce non-thermal synchrotron radio emission with luminosities in the range $L_{1.4\,GHz} \leq 10^{24}\,W\,Hz^{-1}$ (typical 'radio quiet' luminosities; see Xu et al. 1999; Jiang et al. 2010; Nims et al. 2015).

1.5.2 Radio Jets powering galactic outflows

Radio jets are another alternative mechanism causing galaxy-scale outflows and leading to the removal or heating of the gas in the galaxies (Mukherjee et al. 2016, 2018a; Mandal et al. 2021; Meenakshi et al. 2022). The shocks produced in this mechanism as well as the radio jets themselves are both a source of the radio emission seen in the case of these galaxies. The radio emission is often unambiguously associated with a radio jet, commonly seen to be driving outflows and causing turbulence within the interstellar medium (ISM; e.g. reviews in McNamara & Nulsen 2012; Hardcastle & Croston 2020). Indeed, a direct *spatial* connection between ionised gas kinematics and radio emission has also been observed in a whole suite of targets when integral field spectroscopy (IFS) or long-slit data is combined with high-resolution radio imaging. This includes studies of low-power 'radio quiet' Seyfert galaxies and powerful radio galaxies across multiple cosmic epochs (e.g. Nesvadba et al., 2006; Rosario et al., 2010; Husemann et al., 2013; Collet et al., 2016; Husemann et al., 2019; Couto et al., 2020). Such a spatially-resolved connection with the radio emission has also been observed with neutral and molecular outflows for some targets (e.g. Morganti et al., 2005; Tadhunter et al., 2014; Morganti et al., 2015; Finlez et al., 2018).

The feedback seen in the jet mode is in the form of streams of particles and radiation escaping the galaxy disk as collimated jets escape and deposit energy in the CGM and IGM thereby regulating the cooling there. However, compact jets seen in galaxies with low and modest radio emissions may also cause a significant impact on the host galaxy owing to their kinetic energy. Simulations have shown that any jet-driven impact on the ISM will be particularly significant when the ISM is clumpy, when the jets are inclined into the disk, are slow and/or have low power such that they are easily disrupted by interactions (Wagner et al., 2012; Dugan et al., 2017; Bicknell et al., 2018; Mukherjee et al., 2018b). Hence, large-scale outflows may also be generated by the interaction of these low-power jets with the surrounding ISM. Various simulations show that the interaction of a relativistic jet with the ISM is primarily dependent on the evolution of the energy bubble inflated by the jet (Sutherland & Bicknell 2007; Wagner & Bicknell 2011; Wagner et al. 2012; Mukherjee et al. 2016, 2018a). The bubble may also interact as a nuclear wind which when collides against the ISM, is decelerated through a 'reverse shock'. This in turn could also be responsible for the large-scale outflow of the shocked, swept-up ISM material as explained below briefly (also see Faucher-Giguère & Quataert 2012; Costa et al. 2014, 2020). While the jet is still confined within the galaxy disc, it expands within an energy bubble of entrained ISM and plasma. As the jet expands, this energy bubble progresses nearly spherically, strongly interacting with the galaxy's ISM. If the bubble of plasma conserves energy, it grows in size due to the increase in thermal energy. However, the momentum is then lost which is transferred through the bubble to the ISM. Depending on how efficiently this loss of momentum couples to the ISM, multi-phase outflows can be launched with a significant increase in the

momentum of the outflows. These outflows may also lead to the jet plasma being vented out. A proper understanding of this feedback requires estimates of how much energy is being transferred by the jets on the host galaxy's ISM. However, the jet could still impart enough turbulence and energy to heat the ISM gas thus inhibiting star-formation.

In this thesis, I study the targets hosting low-power radio jets and observe them to be causing multi-phase outflows and turbulences as will be discussed in further chapters.

1.6 The potential impact of multi-phase outflows

As discussed above, both radio jets and radiation-driven winds are capable of driving large-scale outflows. As described in Section 1.4.1, the different modes of feedback have also come to be associated with the 'radio quiet' and 'radio loud' nature. Further, as discussed in Section 3.2.3, the jets deposit significant amounts of energy to the galaxy ISM, thereby producing a behavior analogous to those of classical energy-driven quasar feedback models, which simulations predict to be common for high-energy winds (Costa et al. 2020). Costa et al. (2014, 2020) explains the formation of energy-driven outflows due to the collision and interaction between the small-scale winds and galaxy-ISM. It is observed that the material composed of shocked wind gas, which pushes onto the shocked ISM component from within, retains its thermal energy. However, it is also possible to see an energy-driven scenario but being powered by a jet. Even if the outflow is energy-driven, only a portion of the original nuclear jet power is expected to be seen in the kinetic form. Some fraction may also be used in doing work against the gravitational potential, the ambient pressure, and possibly, the ram pressure from the infalling gas. As in an energy-conserved propagation, the jet shocks the gas, and the momentum with which the heated plasma travels is increased to greater values. Thus, jets can produce a behavior analogous to classical energy-driven quasar feedback models. Hence, degeneracy between theoretical models could result in similar feedback outcomes where what matters mainly in the end for the feedback is the amount of energy being injected rather than the specific physical mechanism itself. However, checking this claim and determining the dominant feedback mechanism for quasars requires a multi-wavelength study of quasars, whereby both the multi-phase outflows and the origin of the radio emission can be explored. This is what is used in this thesis, where the sample comes from the Quasar Feedback Survey, which is described in Section 1.7.

AGN feedback may manifest in several forms (see Federrath & Klessen 2012; Costa et al. 2020), for example: (i) by quickly ejecting the dense gas in the nucleus, as soon as the AGN outburst begins; (ii) by gradually suppressing the halo gas accretion onto the host galaxy; which becomes more important as the star-formation proceeds to galaxy outskirts and the ejection becomes less efficient (iii) by providing additional support against collapse and thereby strongly suppressing star-formation. In order to differentiate between the various feedback scenarios, it is therefore crucial to understand how much energy and momentum is carried by the outflow. It is consequently essential to understand how the energy contained in the outflow is transmitted to the ISM of the host galaxy. While some observational studies show

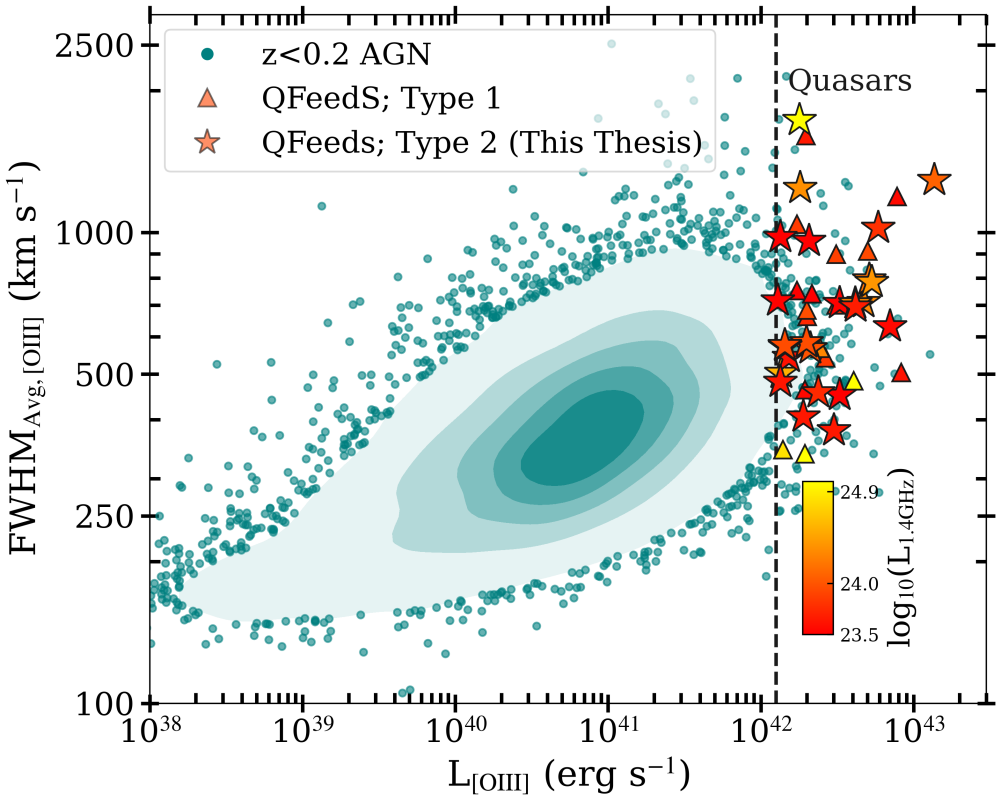

Figure 1.8: Parameter Space plot showing the Quasar Feedback Survey (QFeedS; Jarvis et al. 2021) targets in comparison to the underlying sample from Mullaney et al. (2013), of AGN at z< 0.2 (shown with teal contours and data points). The QFeedS targets are shown as triangles (Type-1) and stars (Type-2). Each of the QFeedS data points are color coded with their radio luminosity ($L_{1.4\,GHz}$). The Type-2 QFeedS targets form the primary sample for this thesis. As can be seen, these cover the range of [OIII] FWHM and all lie above $L_{[OIII]} \geq 10^{42}\,erg\,s^{-1}$, to select only the quasars.

that star-formation could be regulated or significantly suppressed by turbulences and outflows (Nesvadba et al. 2010, 2011; Alatalo et al. 2015), there is also proof for positive feedback scenario where jet-driven shocks may induce star-formation in galaxies from observations (Lacy et al. 2017; Salomé et al. 2015; Bicknell et al. 2000) and theoretical studies (Gaibler et al. 2012; Bieri et al. 2016; Fragile et al. 2017). Further, the simulations from Mandal et al. (2021) also show that there could be both local positive feedback and more global negative feedback in the same galaxy. This leaves open questions on the impact of multiphase AGN outflows on the galaxy ISM which forms the basis of this thesis.

While it has become more evident that the AGN causes feedback on the galaxy's evolution, how significant this feedback is, is determined by how efficiently the energy and momentum released by the AGN is transferred to and couples with the interstellar medium (ISM) and the circum-galactic medium (CGM) of galaxies. This efficiency is dictated by numerous processes that may operate over varying spatial and temporal scales, thereby making the understanding of AGN Feedback quite complex.

1.7 Quasar Feedback Survey

The majority of the BH growth is seen to be occurring in AGN with luminosities in the range $L_{bol} \approx 10^{44}$-$10^{46}\,erg\,s^{-1}$(which is also the quasar-regime; see Alexander & Hickox 2012). In this thesis, Quasars are defined as AGN with $L_{bol} \geq 10^{45}\,erg\,s^{-1}$(Reyes et al., 2008); where the AGN bolometric luminosity is a total of the power output of the AGN, or a total of its luminosities over the entire wavelength spectrum. This translates to an [OIII] luminosity of $L_{[OIII]} \geq 10^{42}\,erg\,s^{-1}$, which is also the selection criteria used for the parent sample of this study, the Quasar Feedback Survey. The Quasar Feedback Survey (QFeedS; Jarvis et al., 2021) comprises of 42 local ($z < 0.2$), bolometrically-luminous quasars. The survey was designed with the aim to address questions related to AGN feedback and AGN outflows as discussed in Section 1.4. This thesis utilizes a sub-sample from this, ensuring a consistent dataset for all targets in order to perform a multi-phase and hence multi-wavelength analysis as will be expanded upon in Section 1.8.

These 42 quasars have been selected from the parent sample of Mullaney et al. (2013), which consisted of 24,264 spectroscopically-identified AGN at $z < 0.4$, from the Data Release 7 of the Sloan Digital Sky Survey (SDSS). The 24,264 sources were selected using the presence of strong emission lines, namely, [OIII] λ5007, Hα, Hβ, and [N II] λ6584 emissions (all at $\geq 3\,\sigma$ significance). The Type-2 AGN were selected from this sample following their position in the 'Baldwin Phillips & Terlevich'-diagnostics diagram (BPT-diagram; Baldwin et al. 1981; Kauffmann et al. 2003; Brinchmann et al. 2004; Tremonti et al. 2004). The BPT diagnostic diagram uses the ratios of flux in [OIII] λ5007 / Hβ and [N II] λ6584 / Hα to differentiate the dominant ionization process being due to AGN, or HII regions ionised by hot, young stars in star-forming galaxies. Additionally, it was also checked that the Type-2 AGN have $FWHM_{H\alpha} < 600\,km\,s^{-1}$. The Type-1 AGN were selected as the ones with $FWHM_{H\alpha} > 600\,km\,s^{-1}$. From this parent sample, the QFeedS targets were selected using the following criteria and are shown with respect to the parent sample in Figure 1.8.

- **Redshift Cut: $z < 0.2$**
  This allows to obtain spatially resolved observations of the quasars with sub-kpc resolutions (for e.g. 1 arcsec at average z=0.1, corresponds to ~ 1.84 kpc). As an example, the spatial resolution of the CO observations from ALMA (see Chapter 2), presented throughout this thesis has an average resolution range of ~ 0.3 - 0.5 arcsec, corresponding to about $0.55 - 0.92$ kpc. Additionally, taking the luminosity cuts into account (as below), these redshift ensure reasonable integration times for the required sensitivity.

- **[O III] Luminosity cut: $L_{[OIII]} > 10^{42.1}\,erg\,s^{-1}$**
  In optically-high luminosity AGN, or quasars, radiation-driven outflows are expected to be more probable (Reyes et al., 2008; Ganguly & Brotherton, 2008). Further, these [OIII] luminosities are representative of AGN Bolometric Luminosities that are typically seen at z$\sim$1-2, i.e., $L_{bol} \gtrsim 10^{45}\,erg\,s^{-1}$, where the quasar feedback is expected to dominate (Hopkins et al., 2007; Kormendy & Ho, 2013).

- **Radio Luminosity cut: $L_{1.4GHz} > 10^{23.45} W\,Hz^{-1}$**
  This radio luminosity cut corresponds to the all-sky radio survey (NVSS) detection limit at $z \sim 0.2$ (NVSS corresponds to the NRAO VLA Sky Survey; Condon et al. 1998; Mullaney et al. 2013). Hence this provides a good parent sample for a detailed investigation of the origin of the radio emission, and the connection to outflows.

- **VLA Observable:**
  The final selection criteria was to ensure that the objects were visible in the celestial coordinate ranges that the Very Large Array (VLA) can observe in, which corresponds to a Right Ascension and Declination range of $(10-300)$ and $(24-44)$ degrees respectively. VLA or the Karl G. Jansky Very Large Array is an array of 28 antennas observing in radio frequencies ($1.0-50$ GHz; Thompson et al. 1980; Condon et al. 1998).

All the 42 QFeedS targets have a high bolometric luminosity, $L_{bol} \geq 10^{45}$ erg s^{-1}, with moderate radio luminosities. It is worth noting that all of the QFeedS sources (except 5) are classified as 'radio quiet' quasars, following the traditional criteria based on the radio vs. [OIII] luminosity from Xu et al. 1999. While the overview of the 42 quasars can be found in Jarvis et al. (2021), several other pilot studies have analyzed subsets of QFeedS targets (e.g. see, Harrison et al. 2014; Lansbury et al. 2018; Jarvis et al. 2019, 2020). Extended radio structures are seen in two-thirds of the sample, however, the origin is less clear, and only 57% of the quasars are confirmed to have radio emission associated with the AGN (see Jarvis et al. 2021). These radio structures range from $1-60$ kpc. Further, in addition to the jetted morphology, using additional criteria such as brightness temperature and spectral index of the radio cores, and FIR-radio correlation, Jarvis et al. (2021) confirms 24/42 quasars to have radio emission associated with the AGN. This highlights the need to incorporate additional parameters to characterize the radio emission. All this evidence highlights the unclear difference between the jet and the wind mode of feedback. Following this work on the QFeedS targets, this thesis aims to study the feedback of these compact radio jets on the multiphase ISM and star formation in the host galaxies.

To characterize multi-phase outflows requires spatially-resolved multi-wavelength observations, and directly comparing these to the radio emission for which this work uses a combination of the radio data from `VLA` with integral field spectroscopic data from MUSE at the Very Large Telescope (`VLT`) and interferometric data from Atacama Large Millimeter/submillimeter Array (`ALMA`). While MUSE aids in obtaining stellar and ionized gas kinematics, ALMA helps understand the molecular gas properties of the outflows as well as the galaxies. Each of these will be discussed in detail in the next Chapter.

1.8 Overview of the objectives of this thesis

Despite four decades of extensive research in this field, there still remain many open questions, those relevant to this thesis are listed below:

- What is the dominant source of the radio emission in radio quiet quasars?

- Which is the dominant mechanism for driving the outflows/turbulences in the interstellar medium of the quasar host galaxies (e.g. jets/disk winds/radiation)?

- What impact do these multiphase outflows have on their host galaxies?

Spatially-resolved spectroscopy contains rich and crucial diagnostic information on how rapidly growing supermassive black holes, i.e., quasars, interact with their host galaxies. Using the observations from ESO's integral field spectroscope, MUSE, as part of our Quasar Feedback Survey (QFeedS) of z<0.2 quasars I present the findings in this thesis from a sub-sample of QFeedS. I use spatially-resolved ionised gas kinematics and stellar kinematics in the quasar's host galaxy, combined with multi-wavelength information in terms of molecular gas traced with CO (3–2) from the interferometric data obtained with the ALMA telescope, along with the radio continuum emission at 6 GHz and 1.4 GHz as observed from the Very Large Array (VLA). I am assessing: (1) the properties of galactic multi-phase outflows driven by low-power and compact radio jets; (2) what impact these have on the star-formation properties of the host galaxies; (3) how the jet-ISM interactions are causing multi-phase outflows; (4) what is the impact of the multi-phase outflows on the galaxy's interstellar medium; (5) how is the impact at different spatial scales of the host galaxy; (6) how does the AGN Feedback on the host galaxy vary with the properties of the radio jet.

Here, I briefly summarize the content of the following chapters:

- **Chapter 2:** This chapter introduces the telescopes and the associated instruments used to obtain the data for this study. It also explains the interpretation of the data structure obtained using these facilities.

- **Chapter 3**: This chapter presents a case study of the bolometrically-luminous quasar with moderate-radio brightness, called J1316+1753 at $z = 0.15$. The chapter presents the use of the unprecedented sensitivity of MUSE, to measure ionized gas and the stellar kinematics, and isolated non-gravitational motions caused by the small-scale (~ 1 kpc) radio jet that is found to be ploughing at an inclined angle into the galaxy disk. The analysis for the J1316+1753 was done at the galaxy scale with an overall view of the kinematic properties, followed by an in-depth look at the nuclear scales, closer to the jets, to ascertain the properties at that spatial scale. This is extended to a multi-phase analysis using the molecular gas data. I report some findings that are attributed to possible jet-ISM interaction at the nuclear scales of the galaxy owing to the low-angle jet; possibly causing a positive AGN feedback. Further, I report the observation of multi-phase outflow caused by the jet-ISM interaction and discuss its effect on the host galaxy.

- **Chapter 4**: This chapter selects 4 quasars from the QFeedS sample with the largest projected radio sizes ($\mathrm{LLS_{radio}} \geq 10$ kpc) along with available 12-m ALMA data for CO (3–2) transition which traces the molecular gas. These targets are also observed to host compact low-power radio jets that are seen to be causing broad central outflows observed in molecular gas for all four targets. Further in 2/4 targets, extended molecular gas structures are observed, away from the main galaxy disk that are interestingly seen to entrain around the

radio lobes. The properties of the filamentary structures are compared with similar structures observed around the brightest cluster galaxies and are found to be quite similar. This chapter shows a multi-scale impact of the radio jet causing broad gas outflows at central scales and gentle pushing of molecular gas by radio lobes at larger scales.

- **Chapter 5**: Chapter 5 builds upon the previous two chapters by performing a multi-wavelength study on 9 quasars from the QFeedS sample. All these quasars have available ionised gas and stellar data available from MUSE, molecular gas data from ALMA, traced through CO (3–2) transition, and radio continuum data at 1.4 and 6 GHz from VLA. All the targets also host compact low-power radio jets which forms an excellent base for the study. The chapter combines this data to understand the main drivers and the main impacts caused to the host galaxy at the central as well as the spatially extended scale. Further, the chapter explores what are the main factors contributing to the feedback effect and if and how they evolve with the properties of the radio jets and the host galaxy.

- **Chapter 6**: This chapter outlines the summary of the thesis and the main conclusions from each aspect of the analyses. Further, the chapter discusses the ongoing research and gives an onward view of the future possibilities in the context of upcoming astronomical advances and their potential for this branch of research.

Chapter

Primary Instruments and Methods

2

The majority of the work in this thesis uses a combination of data utilising the techniques of (i) integral field spectroscopy (IFS), and (ii) interferometry. These data are used in Chapter 3, Chapter 4, and Chapter 5 to trace the stellar and ionised gas kinematics from IFS data obtained from the Multi-unit spectroscopic explorer (MUSE; see Section 2.1), and molecular gas kinematics from interferometric data obtained from the Atacama Large Millimeter/sub-millimeter Array (ALMA; see Section 2.2.1). This thesis also makes heavy use of archival radio images, obtained primarily with the radio interferometer, the Karl G. Jansky Very Large Array (VLA; Thompson et al. 1980; Condon et al. 1998). These data were processed and imaged in previous works (i.e., Jarvis et al. 2019, 2021); therefore, I do not describe the VLA data in detail here. However, the basic information on interferometry relevant for interpreting these images is provided in Section 2.2. This chapter aims to provide a broad overview of these techniques and the benefits of these approaches. Additionally, in order to appreciate the properties of the data obtained using these techniques, the chapter also presents a brief introduction to the MUSE instrument and the ALMA facility, and how the data is obtained using each of these.

2.1 Integral Field Spectroscopy

The main principle behind spectroscopy is to:

(i) collimate the incoming electromagnetic radiation using a collimator/lens;

(ii) split it into its constituent wavelengths using a disperser such as prisms/gratings;

(iii) pass the spectrally-dispersed but still collimated beams through a converging lens so it can be imaged; and

(iv) collect the variation of brightness intensity over different wavelengths (a spectrum) on a detector.

This spectrum then helps us to understand the different distributions of intensity in terms of emission and absorption of the associated light over different wavelengths which is key to understanding various astronomical processes by using just radiation!

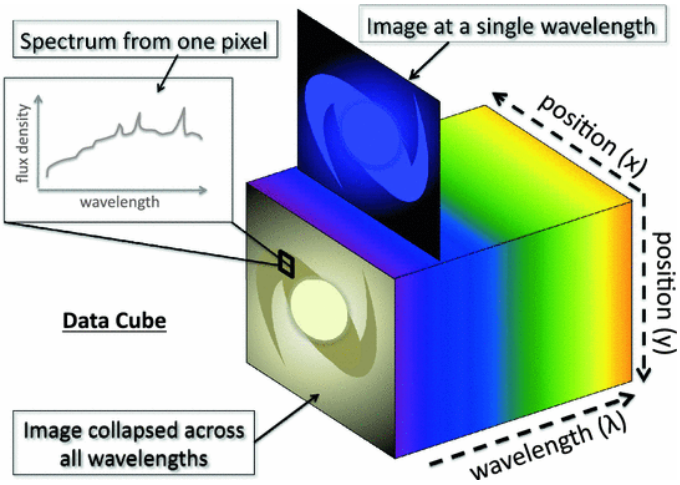

Figure 2.1: Schematic Diagram of a MUSE datacube, with two spatial dimensions [x,y] and one spectral dimension (λ). As can be seen from the schematic, each spatial pixel (spaxel) also has associated spectra, hence one can obtain an image at every wavelength channel, or across all wavelengths (by collapsing along the spectral dimension). Further, one can also obtain spectra from either each spaxel or over the entire spatial extent of the datacube by collapsing over the spatial (x and y) dimensions. *Image Credit: PhD Thesis from C.M.Harrison.*

Depending on the aperture and type of the input slit and the disperser, various forms of spectroscopic approaches have come to be used. Traditional spectroscopic approaches obtained a single spectrum from the source being observed, for example in long-slit spectroscopy. However, this does not give spatially-resolved information for the target in consideration, which leads to a loss of information in cases of spatially-extended sources. In *long-slit spectroscopy*, a narrow and long slit aperture is used for the incoming light and the image of the slit is dispersed. Depending on how and where the slit is aligned on the extragalactic source, one can obtain information along the source in one direction only. This approach limits the amount of light being analyzed to only the slit dimensions and the rest of the light from the source is lost. Depending upon the angular size of the target under analysis, numerous long-slit observations may be needed to obtain observations over different regions and orientations for the source.

The advent of *Integral Field Spectroscopy* (IFS) has marked a big leap in extragalactic research, by resolving the above-mentioned issues. IFS is a technique that uses instruments called integral field spectrographs to provide 3D information for the target being observed. The data is obtained in terms of a 'datacube', corresponding to 2 dimensions of spatial information (in terms of [x, y] or [RA, Dec]) and 1 dimension of spectral information (i.e., λ for wavelengths, or ν for frequencies; see Figure 2.1). Figure 2.1 shows a schematic representation of a 3D datacube of a galaxy. Due to the third spectral dimension a spectrum can be obtained for each spectral pixel, or spaxel). Likewise, due to the spatial information at every wavelength, different images can be obtained for different velocity ranges (or slices). The result is a rich dataset, where both the spatial and spectral information can be obtained across the full field of view on the instrument.

Integral field spectrography (IFS) can be performed in optical as well as infrared wavelengths, by using an integral field unit (IFU) that samples the light in multiple spatial components. This light is passed through an integral field spectrograph

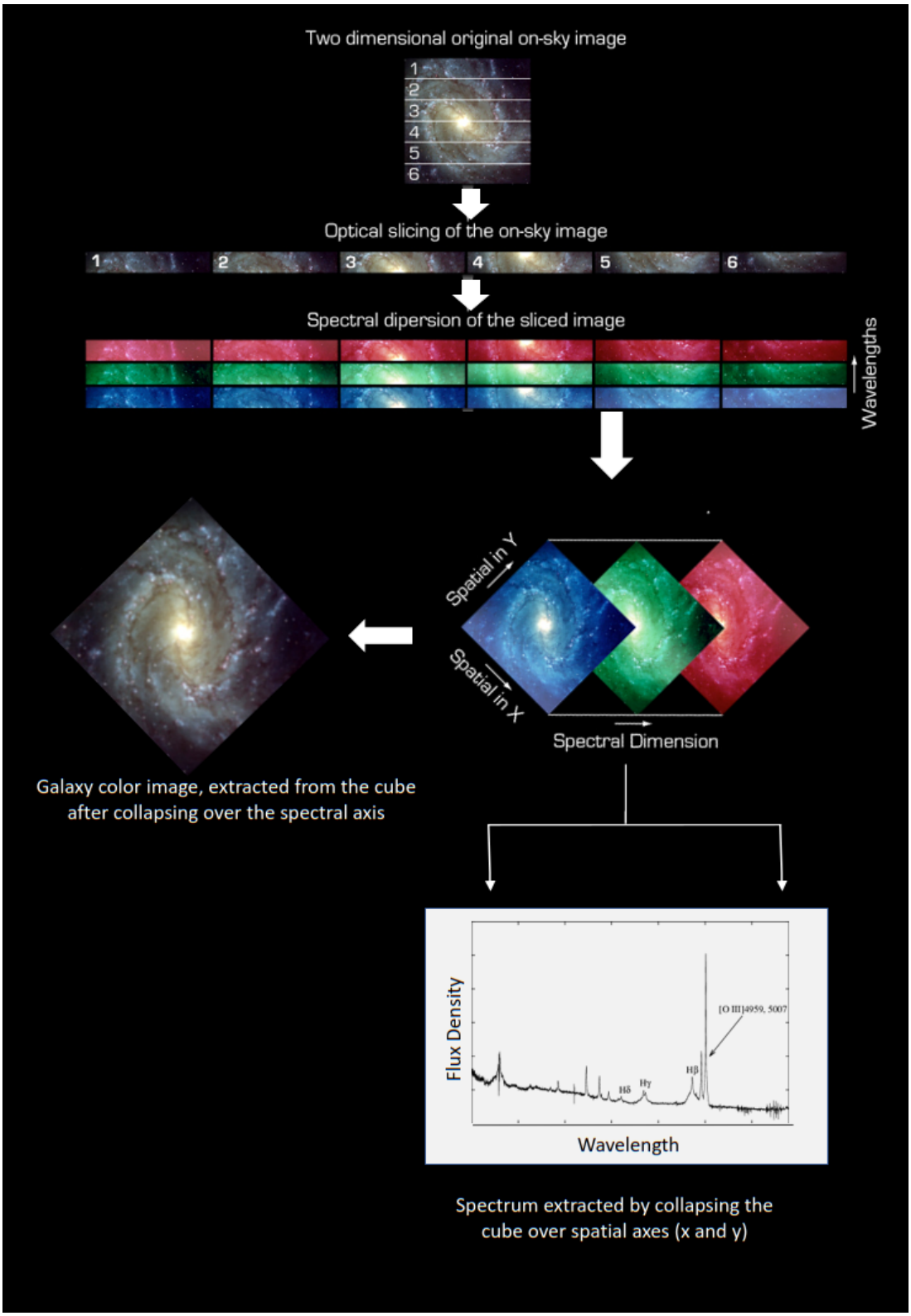

Figure 2.2: A schematic representation explaining the main principles of integral field spectroscopy. The full explanation is in Section 2.1.1 *Image Credit: ESO Website and example AGN spectra used from Kovacevic-Dojcinovic & Popovic (2012).*

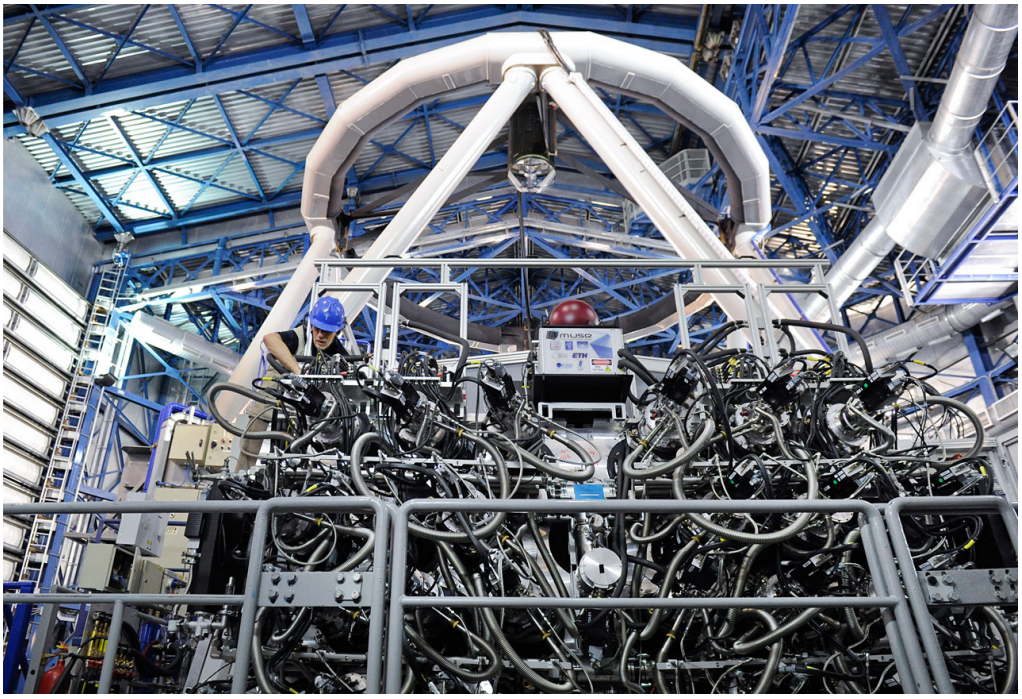

Figure 2.3: The MUSE at UT4 of the Very Large Telescope in Paranal, Chile. Each of the 24 spectrographs is associated with a detector. Each of the 24 detectors requires its own continuous cooling flow systems and hence the immense number of pipes. *Image Credit: ESO Website.*

which disperses the light. The primary methods through which IFUs can sample the incoming light are summarised below, and Figure 2.2 shows a particular combination of the techniques used in the IFS instrument most relevant to this work, MUSE (more in section 2.1.1):

- *Lenslet arrays* divide the image of the observed target into several points where light is concentrated. Each of these is then dispersed by the spectrograph. This ensures contiguous sampling of the input image. In order to avoid the overlapping of the spectra, the dispersed light is tilted.

- *Fibres* can either be used in combination with the lenslet array or by themselves. When used with the lenslet array, the bundle of optical fibres is placed behind a lenslet array, while when used alone, the optical fibres can sample the image directly. The light from the fibres is then aligned to create a "pseudo-slit", corresponding to each fibre. This is then passed to the spectrograph.

- *Image-slicers* split the input image using horizontal stripes of segmented mirrors that are oriented in slightly different directions. A second set of mirrors then formats the prior slices together to create multiple pseudo-slits which are thereafter passed to the spectrograph.

The light obtained through the above formatting methods is then collimated and dispersed by the spectrograph, which is then finally recorded by the detector as the spectrum. During the data reduction process, each individual spectrum can then be reformatted to a three-dimensional datacube as shown in Figure 2.1.

2.1.1 MUSE

MUSE (Figure 2.3; Bacon et al. 2010) is an integral-field spectrograph on the Nasmyth B focus of the Yepun (Unit Telescope 4) of the Very Large Telescope (VLT) in Paranal, Chile. MUSE consists of 24 IFU (integral field unit) modules that make up one contiguous field of view, and work in the visible wavelength range (4650 – 9300 Å). In the narrow-field-mode (NFM), MUSE observes in a 7.5 arcsec × 7.5 arcsec region, with a spatial sampling of 0.025 arcsec. This thesis uses data from the wide-field-mode (WFM) of MUSE, which covers a field of view (fov) of 1 arcmin × 1 arcmin with a spatial sampling of 0.2 arcsec. In WFM, since each spaxel (of size 0.2 arcsec) of MUSE corresponds to one spectrum, every MUSE datacube with a fov of 1 arcmin × 1 arcmin comprises of roughly 90,000 spectra! The spectral sampling is done with an average spectral resolution[1] (R) of ∼2.6Å (R = 1750 at 4650 Å and 3750 at 9300 Å) and a spectral sampling of 1.25Å pixel^{-1}.

A schematic representation of how MUSE works is shown in Figure 2.2. In WFM, the 1 arcmin × 1 arcmin field of view is split into 24 image segments or channels by the first field-splitter (for simplicity, Figure 2.2 shows only 6 image segments). Then a group of mirrors and lenses sends each of these beams to the 24 IFUs. Each IFU then has the second field-splitter which is known as the *slicer*, which further arranges each slice into 48 slitlets or mini-slices (15 arcsec × 2 arcsec), giving a total of 1152 mini-slits. The light reflected from each of the 48 mini-slits then enters the spectrograph. The spectrograph disperses the entering light as per its wavelength and produces spectra of each of the mini slits and images these onto the detector. The detector then registers the spectrum of a small part of the galaxy until this process is repeated for all 48 beams after which the detector is completely illuminated. This same process happens in each of the 24 spectrographs. The light exiting each of the 24 spectrographs is then sent to a CCD with 4x×4k pixels (where the physical size of each pixel is ∼15 µm).

MUSE implements Adaptive Optics (AO) through the ESO-designed module called GALACSI (Ground Layer Adaptive Corrector for Spectroscopic Imaging; Hubin et al. 2004; Stuik et al. 2005), using 4 artificial laser guide stars (LGS) and 1 natural guide star (NGS). In the NFM, the 4 LGS probe atmospheric turbulence at 10 arcsec off-axis, along with the infrared light of the 1 NGS star that aids in measuring the atmospheric tip-tilt and defocus. In the WFM, the 4 LGS are at 64 arcsec off-axis to correct for atmospheric turbulence combined with the 1 NGS star in visible light for the remaining atmospheric tip-tilt. This is used in combination with a deformable secondary mirror to obtain a wavefront corrected for the turbulent atmospheric ground layer of our planet.

In the Quasar Feedback Survey (see Section 1.7), 17/42 targets are classified as Type-2 quasars and have been observed using the wide-field adaptive optics mode (WFM-AO) of MUSE under the program code 0103.B-0071 (PI: Chris M. Harrison). 9/17 targets have been used in this thesis for Chapters 3, 4, 5[2].

[1] *Spectral resolution* (R) is measured as $R = \lambda / \Delta\lambda$, where λ is the observation wavelength and $\Delta\lambda$ is the width of spectral sampling.

[2] Some of the targets also had available archived data from other observing programs. These have been mentioned in the relevant chapters.

2.1.2 Ionised Emission-Line Analysis with MUSE

MUSE is used in a broad range of astrophysical research from spectroscopic monitoring of the solar system's outer planets to studying kinematics of very high-redshift galaxies. This thesis uses the observations of the 9/17 QFeedS targets observed with MUSE for various purposes such as: (1) creating emission-line images (for example, see Figure 2.4); (2) tracing the velocity structure of absorption and emission lines in different directions and orientations; (3) extracting the emission-line flux ratios for emission-line ratio diagnostics; (4) searching and looking for the outflowing or inflowing gas; (5) characterizing the ionised gas kinematics of the outflowing gas if any with respect to the host galaxy kinematics; (6) characterizing the stellar kinematics likewise. While the detailed methods are mentioned in the respective chapters, here a few of these approaches are broadly presented as follows.

For the QFeedS targets at z<0.2 (see Section 1.7), the spectra covering some of the brightest emission lines produced by AGN can be obtained. Using the MUSE rest-frame wavelength range, I focus on *permitted emission lines* of H$\beta\,\lambda\,4861\,$Å, H$\alpha\,\lambda\,6563\,$Å, and *forbidden emission lines* of [O III] $\lambda\lambda\,4959, 5007\,$Å, [O I] $\lambda\lambda\,6300$, $6363\,$Å, [N II] $\lambda\lambda\,6548,\ 6584\,$Å and [S II] $\lambda\lambda\,6717, 6731\,$Å (hereafter H$\beta$, H$\alpha$, [O III], [O I], [N II], [S II], respectively). In spectroscopic terms, *permitted lines* are seen as the ones with a high transition probability, which corresponds to a very short ($\approx 10^{-8}\,$s) decay time of the particles by resulting in a photon emission of equivalent energy-fall. Permitted lines are hence produced when the radiative de-excitation is faster than a probable collision. These lines can be produced in both high- and low-density environments. In contrast, *forbidden lines* are transitions from meta-stable states with a very long decay time (≈ 0.001–$1\,$s) thus being highly improbable. Hence if a particle excites to a meta-stable state (through any of the physical processes), in a low-density environment, a collision is less likely to happen and hence the radiative de-excitation from the meta-stable state will occur thus producing the emission of the forbidden line radiation (since the particle density is too low for a collision to de-excite it). On the other hand, if the density is high, then the particle will de-excite following a collision with another particle and an emission line won't be seen. This also explains why broad line regions of AGN (see Section 1.2) only show permitted lines, due to their high densities ($n\sim10^{9-10}\,cm^{-3}$). On the contrary, the narrow-line regions also show forbidden lines along with permitted lines due to their comparatively lower density ($n\sim10^{3-6}\,cm^{-3}$).

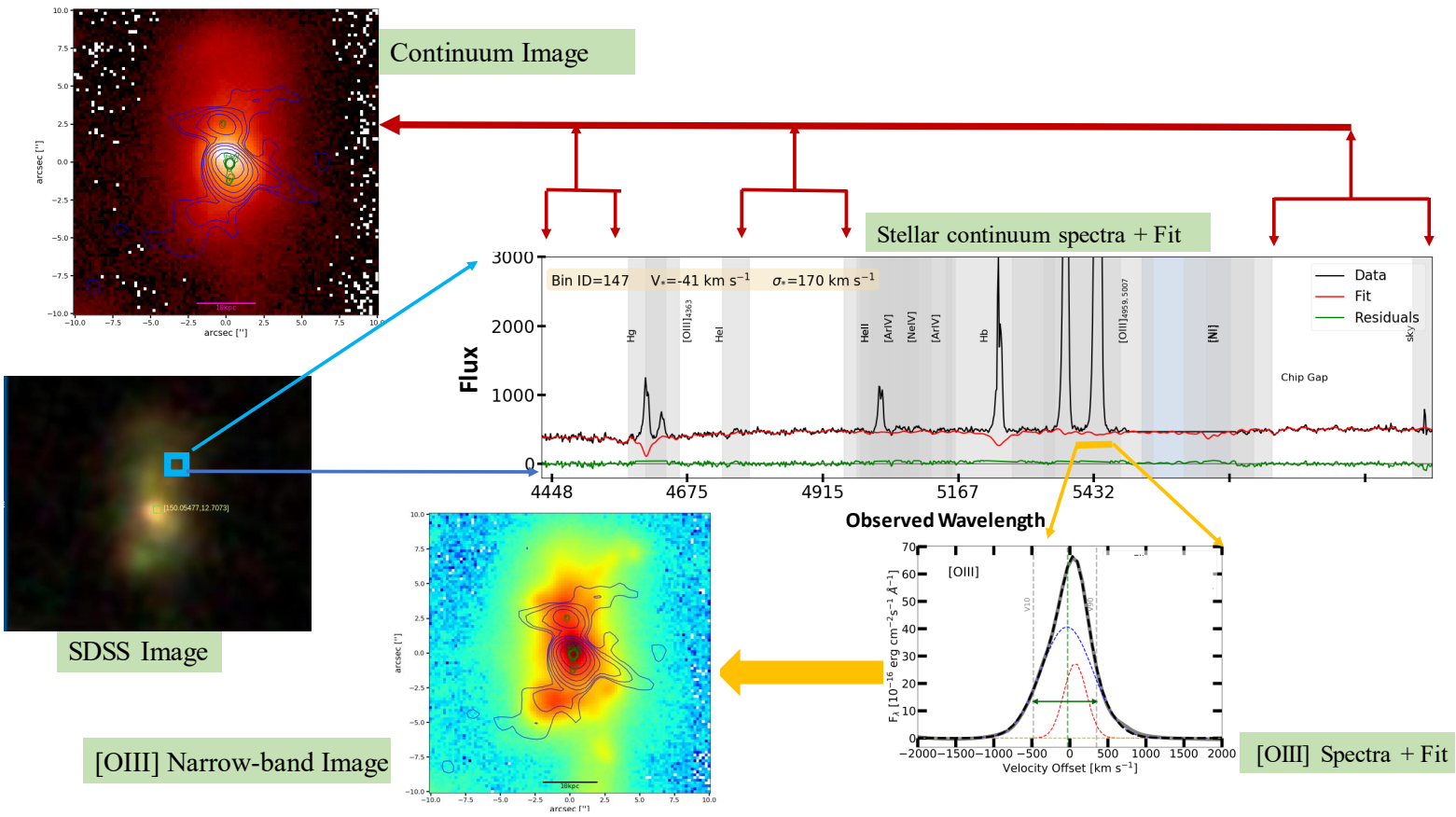

Figure 2.4: A representation of the MUSE data from QFeedS sample, using J1000+1242 quasar. The bottom left image shows an SDSS image from which a small region (greater than a pixel for illustration) is selected to extract the spectrum as shown on the right. This spectrum is fit for the stellar continuum regions (fit shown in red) while masking the emission lines (in grey). Using these line-free continuum regions, an image of the continuum is generated, as shown in red on the top-left. In the bottom, a close-up of the [OIII] emission line is shown along with its two Gaussian components. Next to it, on the left is an image of the galaxy collapsing the cube over only the wavelength range of the [OIII] spectral line to create a narrow-band map. Both this and the continuum images are overlaid with 6 GHz radio continuum contours in blue (this radio data is described in Chapter 5).

[OIII] to analyse the ionised gas kinematics

To derive the ionised gas kinematics of the outflow, I used the [OIII] emission line. This is because [OIII]λ5007 Å is a particularly bright line and is not blended with other emission lines. Further, since [OIII] is a forbidden line, it cannot be produced in the BLR and therefore is an ideal tracer for the kinematics on the galaxy scales, not being contaminated by unresolved emission (as opposed to for e.g. Hα and Hβ). Indeed it is used as a common diagnostic to identify the outflowing ionised gas over large scales if it shows an asymmetric emission line profile with a high velocity and a broad component (i.e., emission line widths exceeding that expected from galaxy dynamics). It has been used extensively in the literature to identify galactic-scale outflows in local and low-redshift galaxies in small and big galaxy samples (e.g. see: Weedman 1970b; Stockton 1976; Veron 1981; Heckman et al. 1981, 1984; Feldman et al. 1982; Vrtilek 1985; Whittle et al. 1988; Veilleux et al. 1995; Boroson & Green 1992; Nelson & Whittle 1996; Boroson 2005; Komossa et al. 2008; Zhang et al. 2011; Wang et al. 2011; Mullaney et al. 2013). In general, quasar-host galaxies are seen to show quite complex [OIII] line profiles, especially in regions close to the nucleus of the galaxy. Using the emission lines, it was possible to estimate the size of the emission-line regions, and spatially resolve the ionised gas kinematics in the host galaxy.

Various studies in the past years have used IFS data to study high-velocity outflows on kpc scales (e.g. see, Nesvadba et al. 2006, 2008, 2010; Alexander et al. 2010; Rupke & Veilleux 2011; Harrison et al. 2012; Liu et al. 2013; Harrison et al. 2014; Brusa et al. 2015; Cresci et al. 2015; Carniani et al. 2015; Harrison et al. 2015; Husemann et al. 2016; Kakkad et al. 2017; Wylezalek & Morganti 2018). The emission line profiles in type-2 AGN are often found to be complex, with multiple narrow and broad components, as was also the case observed for the galaxies studied in this thesis. Due to these complexities seen in emission-line fitting, I opted to use the non-parametric definitions (Harrison et al. 2014) to characterize the gas kinematics by analyzing the widths and velocities from each pixel. The *non-parametric approach* helps reduce the degeneracy of results, by approximating the complex line profile to a non-parametric model. As described in detail in the individual science chapters, the emission-line profiles are modeled by a set of multiple Gaussian components, and then parametric values are measured using these models as below. The aim is to characterize both the bulk velocity and the velocity dispersion of the ionised gas.

- For the bulk velocity, V_{50} is used, which is defined as the 50^{th} percentile of the velocity profile. V_{50} is a tracer of bulk velocity of the gas, but can be complicated in the presence of outflowing material.

- For the velocity dispersion of the gas, W_{80} is used, which is defined as the velocity-width of the emission line profile that encloses 80% of the integrated flux of the emission line. It is obtained as the difference of the 10th and 90th velocity percentiles, as, $W_{80} = v_{90} - v_{10}$. For a single Gaussian component, it roughly translates to the full-width-at-half-maximum, i.e., $W_{80} = 1.088 \times \text{FWHM} = 1.088 \times (2.354 \times \sigma) \approx 2.6 \times \sigma$.

Hence these values are used as a proxy for the median velocity and velocity-width in gas for different regions of the galaxy. These are then compared to the stellar velocity and stellar velocity dispersion to understand the deviation in the galaxy kinematics due to non-gravitational processes.

In summary, this thesis uses the [OIII] emission observed with the MUSE to trace the ionised gas kinematics in Chapter 3 and Chapter 5. Additionally, in Chapter 3, [SII] $\lambda\lambda\,6717, 6731\,\text{Å}$ line ratios are also used to obtain the electron density; and all the emission lines covered by MUSE's spectral range are used to obtain ionisation-line-ratio diagrams to understand the dominant ionisation process. Both these approaches are detailed in the relevant sections in Chapter 3.

2.1.3 Stellar kinematics

The emission-line free regions of the MUSE spectra are used to extract the stellar motions. This is done by using the stellar absorption features to identify the host galaxy's line-of-sight velocity shift and stellar velocity dispersion by comparing it to a set of stellar templates. In this way, stellar kinematics can be obtained which helps us to study gas kinematics free of any gravitational effects. This is a critical step to identify potential non-gravitational kinematic anomalies in the gas of the host galaxy, which could be due to AGN outflows and/or mergers, etc. I utilize a pipeline that implements the spectral fitting from pPXF routine (Cappellari & Emsellem 2004; Cappellari 2017) which combines stellar spectra from a source library of choice to obtain the best fit to the observed stellar continuum. The full stellar fitting details can be found in Section 3.4.3.

2.2 Interferometry

The molecular gas kinematics is studied using the carbon monoxide gas transition, CO (3–2) (detailed in Section 2.2.2), observed with the sub-mm and mm interferometer, ALMA (see Section 2.2.1). Hence, in this Section, I am describing the underlying methods, in the context of interferometric observations from ALMA.

Interferometry is a technique used to combine observations from different telescopes into an equivalent large telescope with an angular resolution equivalent to the largest separation between the individual telescopes. The basic principle behind the working of the interferometer is using the interference of super-imposed light wave-fronts to obtain information. This mainly comes from the *Double Slit Experiment* (Young, 1804), in which interference is obtained by combining two wave-fronts from the same source, but with a difference in path length which also leads to a difference in phase shift. This principle of interferometry finds its use in sub-mm/mm Astronomy by replacing the slits with individual telescope antennas and applying interferometry to combine the signals from each antenna to obtain an angular resolution equivalent to that from a virtual antenna with a diameter equal to the spatial separation (or 'baseline') of the farthest individual antennas (i.e., an equivalent giant virtual telescope). Following the Rayleigh Criterion for the limits of resolution for a telescope (Hecht 2001), at an observing wavelength of λ and for a baseline separation of

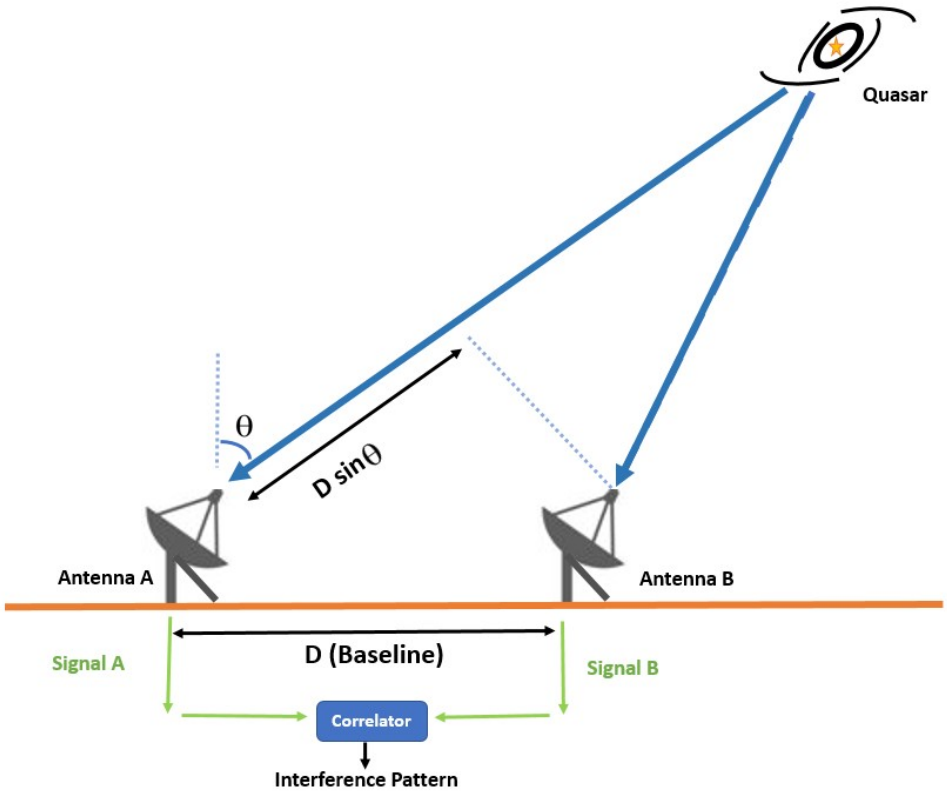

Figure 2.5: This is a schematic representation of how interferometry is used in radio astronomy. When observing a distant quasar in the centre of a galaxy (shown through a yellow star to represent its brightness), the two shown radio antennas are at a distance of D which introduces a path difference of $D\sin\theta$ between the paths of the light rays coming to both the antennas. This path difference then leads to interference.

diameter, $D_{baseline}$, the angular resolution θ (in radians) can be obtained as:

$$\theta = 1.22 \times \frac{\lambda}{D_{baseline}} \tag{2.1}$$

As an example, let us estimate the telescope size needed for obtaining sub-arcsec angular resolution at a wavelength of $\sim 870\,\mu m$ (roughly corresponding to the wavelength of interest for tracing the CO (3–2) emission line). Applying the relation above, to achieve $\theta \sim 1\,\text{arcsec} = \frac{1}{3600}\frac{\pi}{180}\,rad$, would require a $D_{baseline}$ of $\sim 200\,m$! Clearly, a single-dish telescope to achieve this resolution would be highly impractical (for comparison, the most ambitious astronomical telescope to date with the largest mirror size is ESO's Extremely Large Telescope[3] (which will have a primary mirror of 39 m; Gilmozzi & Spyromilio 2007; Liske et al. 2008). Hence, interferometry is an extremely useful technique for longer wavelengths in astronomy.

Figure 2.5 illustrates the use of interferometry in a radio telescope array made of multiple radio antennas. Considering only two of these radio antennas for simplicity, each receives radiation from the same astrophysical source under observation, in this case, a distant quasar, at an observing angle θ from the zenith. Since the antennas are at different locations, the radiation from the source has to travel slightly different

[3] https://elt.eso.org/

distances to reach the different antennas. Another way of looking at it is the distance (D) between these antennas results in a path difference of $D \sin\theta$ between the two incoming wavefronts. This path difference translates into a phase shift which results in interference. Hence increasing the distance between the antennas can lead to increased resolution, comparable to 'zooming-in' on the distant extragalactic source. These observations are then passed on to the interferometer which produces the final dataset as a set of interference patterns from each pair of antennas (also called visibilities). The method of combining signals from different antennas is called aperture synthesis.

While the area of the antennas can help improve the sensitivity, the long baselines help improve the resolution of the observations. Hence, if there are only a few small antennas, the sensitivity will be limited (due to limited light collecting area). Therefore, the availability of large antennas increases sensitivity. Furthermore, having multiple antennas also helps to use different baselines during the final image creation depending on the science goals. This gives different benefits as explained in the following. Each baseline is only sensitive to emissions in the sky on scales smaller than $\sim \frac{1}{\mathrm{D_{baseline}}}$. As a result, any emission structures that are larger than this limit can not be 'seen' by the antenna with this baseline (also known as being 'resolved-out'). In this sense, the combinations of smaller baselines will be the most sensitive to large-scale structures.

Since this thesis focuses on the study of galactic-scale AGN outflows and also explores the effect of large-scale radio structures on the host galaxy and the outflows, recovering the large-scale structures was imperative for the scientific goals. This explains how smaller baselines are also essential to capture these extended emissions. The data-reduction steps used to obtain the image with a good balance of the baselines are explained in the subsequent chapters as the decisions were inspired by the different science goals.

Since ALMA data is used extensively for this thesis, the next section briefly describes the features of the ALMA telescope and the data obtained through it.

2.2.1 ALMA

ALMA, shown in Figure 2.6, is a single, very powerful telescope located at the Chajnantor plateau of the Atacama Desert, at an altitude of 5000 m above sea level in Chile. As an interferometer, ALMA combines millimeter and sub-millimeter observations from an array of 66 radio telescopes, each of which is high-precision antennas, observing in the range of (0.32–3.6) mm. The main 12-m array consists of 50 antennas, with each being 12 m in diameter that act like a combined interferometer (or telescope). ALMA antennas are designed to be movable which means the $\mathrm{D_{baseline}}$ in the main 12-m array of ALMA can be varied between 150 metres to 16000 metres (16 km), thus providing a powerful zoom up to 0.02 arcsec scales in the galaxies.

Figure 2.6: This is an image of the antennas of the Atacama Large Millimeter/submillimeter Array (ALMA) at the Chajnantor Plateau, Chile, as photographed in 2013.*Image Credit: ESO Website.*

ACA, or the Atacama Compact Array is a subset of ALMA, utilizing 16 antennas to observe. Of these 16, four antennas are 12-meter in diameter, similar to the antennas used in ALMA configuration and 4 are 7-meter antennas. Together, ACA complements ALMA to obtain observations of molecular clouds at a large angular size.

The working of the ALMA observatory can be briefly summarised as: each antenna collects radiation from the sky which is measured by receivers (initially cooled down to $\sim -269^\circ$ C) and digitized before being transmitted through 16 kilometers of optical fibers. The ALMA correlators combine the signals from all the antennas.

With its increased sensitivity and unprecedented resolutions, ALMA has been a tremendous development in the study of molecular gas and dust in extragalactic sources. Since radiation at this wavelength corresponds to cold interstellar clouds at temperatures slightly over absolute zero, carefully capturing these can give a deep insight into the physical and kinematical structure of the clouds. While these clouds are often dark and obscured in visible light, they are strongly emitting in mm and sub-mm ranges. However, as compared to visible lights these signals are still quite faint, and excellent light-gathering powers are needed to capture these. With a combination of its 66 antennas, ALMA has a combined surface area of 6500 square metres. ALMA is hence designed to be sensitive to these emissions, and its location at one of the driest places on Earth aids it in obtaining highly resolved and scientifically viable observations of these molecular clouds.

2.2.2 Molecular Emission Analysis with CO(3-2)

In addition to imaging, ALMA also serves as a spectroscopic instrument. Each receiver is capable of splitting the light to generate a spectra over 7 bands (Band 3-10). This thesis makes use of Band-7 observations from Cycle 6 under the proposal

code ADS/ JAO.ALMA#2018.1.01767.S (PI : A.P. Thomson) for 7 quasars of the Quasar Feedback Survey. Additionally, for 2 quasars (J1430+1339 and J1356+1026), the archival Band-7 observations are used and detailed in subsequent chapters. To trace the molecular gas distribution and kinematics, I use the ^{12}CO *J=(3–2)* transition at a central frequency $\nu_{\rm obs} = 345.795990\,\rm GHz$.

Since the main constituents of molecular gas clouds (molecular hydrogen and atomic helium) do not emit radiation at low gas temperatures, we need to resort to different tracers. Carbon Monoxide (CO) is a luminous tracer of similar environments where we expect to find molecular Hydrogen (H_2), which is the fuel for star-formation in galaxies. The use of CO as a tracer has a clear advantage to be abundantly present in galaxies being the second-most abundant molecule after H_2. Further, it readily emits at lower temperatures, and the specific intensity distribution between the different rotational states ($\boldsymbol{J}$) are sensitive to the temperature and gas density of the H_2 gas, thus making it a good tracer (Solomon & Vanden Bout, 2005). Additionally, the formation of CO molecule in the interstellar medium involves H_2 as a key ingredient thus suggesting that a dearth of CO would also mean a dearth of H_2 (Glover et al., 2010). The *J=(3–2)* transition is specifically used in this thesis since it has been found to be a reliable tracer of the excitation temperatures typically found in AGN outflows (García-Burillo et al. 2014). Hence, the CO(3–2) serves as a reliable tracer for the molecular gas kinematics even in regions disturbed by AGN outflows.

For measuring the kinematic properties of the CO (3–2) emission line profiles, similar approaches are used as described for fitting the IFS data (in Section 2.1.2). Broadly, the non-parametric approach is used to estimate velocity and velocity dispersion of the molecular gas in the form of V_{50} and W_{80}, with more specific details given in each science chapter as necessary.

This thesis uses the ALMA data to study the following molecular gas properties which will be expanded upon in the related Chapters later:

- to morphologically and spectroscopically assess which of the molecular gas is associated with the host galaxy or with the outflowing gas;
- to measure the emission-line fluxes, velocities, and line widths in the outflowing regions, which can then be used to estimate the mass, the mass-outflow rate, and kinetic power of the outflowing molecular gas;
- to study the feedback from the AGN on the molecular gas in the ISM by spatially mapping the distribution of the molecular gas, with respect to the radio jets and outflows.

Chapter

Jet-ISM interactions and feedback in a z∼0.1 quasar

3

Multi-phase outflows, turbulence and evidence for feedback caused by low power radio jets inclined into the galaxy disk

We present a study of a luminous, $z = 0.15$, type-2 quasar ($L_{[OIII]}=10^{42.8}$ erg s^{-1}) from the Quasar Feedback Survey. It is classified as 'radio-quiet' ($L_{1.4\,GHz}=10^{23.8}$ W Hz^{-1}); however, radio imaging reveals $\sim$1 kpc low-power jets ($P_{jet}= 10^{44}$ erg s^{-1}) inclined into the plane of the galaxy disk. We combine MUSE and ALMA observations to map stellar kinematics and ionised and molecular gas properties. The jets are seen to drive galaxy-wide bi-conical turbulent outflows, reaching $W_{80} = 1000$ - 1300 km s^{-1}, in the ionised phase (traced via optical emission-lines), which also have increased electron densities compared to the quiescent gas. The turbulent gas is driven perpendicular to the jet axis and is escaping along the galaxy minor axis, reaching 7.5 kpc on both sides. Traced via CO(3–2) emission, the turbulent material in molecular gas phase is one-third as spatially extended and has 3 times lower velocity-dispersion as compared to ionised gas. The jets are seen to be strongly interacting with the interstellar medium (ISM) through enhanced ionised emission and disturbed/depleted molecular gas at the jet termini. We see further evidence for jet-induced feedback through significantly higher stellar velocity-dispersion aligned, and co-spatial with, the jet axis ($< 5°$). We discuss possible negative and positive feedback scenarios arising due to the interaction of the low-power jets with the ISM in the context of recent jet-ISM interaction simulations, which qualitatively agree with our observations. We discuss how jet-induced feedback could be an important feedback mechanism even in bolometrically luminous 'radio-quiet' quasars.

3.1 Introduction

Active galactic nuclei (AGN) are the sites of growing supermassive black holes at the centre of galaxies (Kormendy & Ho 2013). They can produce enough energy, through accretion of matter, to exceed the binding energy of their host galaxies (Cattaneo & Best 2009; Bower et al. 2012). With this tremendous amount of energy available, if it can efficiently couple to the gas extending from the vicinity of the AGN to galactic scales, the AGN could cause significant impact (known as 'feedback') on their host galaxies by either facilitating or suppressing the star-formation (see e.g., Binney & Tabor 1995; Ciotti & Ostriker 1997; Alexander & Hickox 2012; Fabian 2012; Harrison 2017). This 'AGN feedback' has become an imperative ingredient in cosmological galaxy formation simulations for them to reproduce key observables of galaxy populations and intergalactic material (e.g., Bower et al. 2006; McCarthy et al. 2010; Gaspari et al. 2011; Vogelsberger et al. 2014; Hirschmann et al. 2014; Schaye et al. 2015; Henriques et al. 2015; Taylor & Kobayashi 2015; Choi et al. 2018).

This chapter is based on the publication Girdhar et al. 2022 in the Monthly Notices of the Royal Astronomical Society journal and the supplementary appendix can be found in Appendix 7.

However, understanding how this process occurs in the real Universe, particularly in the case of the most powerful AGN (i.e., quasars; $L_{\rm bol} \geq 10^{45}\,{\rm erg\,s^{-1}}$), remains a challenge of extragalactic research.

One way that AGN are known to be capable of interacting with their host galaxy's multi-phase interstellar medium (ISM) is through driving galaxy-wide (≥ 0.1 - $10\,{\rm kpc}$) energetic outflows and turbulences (e.g., Nesvadba et al. 2011; Liu et al. 2013; Cicone et al. 2018; Veilleux et al. 2020; Davies et al. 2020; Fluetsch et al. 2021; Venturi et al. 2021a; Roy et al. 2021). Theoretically, these outflows may be driven by radiation pressure, jets or AGN-driven winds and could occur over scales from the accretion disc ($\leq 10^{-2}\,{\rm pc}$) through to galaxy-wide scales, where they could affect the properties of the gas in the ISM and beyond (Ishibashi et al. 2018; Mukherjee et al. 2018b; Costa et al. 2018, 2020; Morganti et al. 2021). However, from an observational perspective, whilst these multi-phase outflows are now seen to be common in quasar host galaxies, controversy remains over the relative role of the different possible driving mechanisms (Hwang et al. 2018; Wylezalek & Morganti 2018; Jarvis et al. 2019; Somalwar et al. 2020). In particular, in this work, we are interested in the relative importance of radio jets in driving multi-phase outflows (see e.g., Morganti et al. 2005; Nesvadba et al. 2006, 2008; Mullaney et al. 2013; Jarvis et al. 2019; Molyneux et al. 2019; Liao & Gu 2020; Venturi et al. 2021a; Ramos Almeida et al. 2021).

Also from a theoretical perspective, AGN can regulate black hole growth and star-formation, (i.e., causing a 'negative feedback' effect) by expelling gas through outflows, preventing gas from cooling and/or destroying star-forming ISM (e.g., Silk & Rees 1998a; Benson et al. 2003; Granato et al. 2004; Hopkins et al. 2006; Booth & Schaye 2010; Faucher-Giguère & Quataert 2012; King & Pounds 2015; Costa et al. 2018, 2020). On the contrary, AGN may also induce a 'positive feedback' effect due to the compression of the gas from outflows or jets, which induce localised enhancement of star-formation (e.g., Zubovas et al. 2013; Ishibashi et al. 2013; Fragile et al. 2017; Lacy et al. 2017; Wang & Loeb 2018; Gallagher et al. 2019). However, from an observational perspective, the impact of the most luminous AGN on their host galaxies' ISM and star-forming properties is a matter of ongoing debate (e.g., Husemann et al. 2016; Villar-Martín et al. 2016; Maiolino et al. 2017; Harrison 2017; Kakkad et al. 2017; Cresci & Maiolino 2018; Perna et al. 2018; Rosario et al. 2018; do Nascimento et al. 2019; Bluck et al. 2020; Yesuf & Ho 2020; Scholtz et al. 2021).

Understanding the drivers of outflows and the impact of AGN on their host galaxies requires multi-wavelength observations. Since outflows are multi-phase, different diagnostics are required to study their properties and impact on their host galaxy. For example, spatially-resolved observations in a small number of systems observed with both integral-field spectroscopy (IFS) and interferometers have shown that the ionised gas and molecular gas kinematics could be completely decoupled (Shih & Rupke 2010; Sun et al. 2014). This further highlights the need to study multiple gas phases at comparable resolutions to fully understand the impact of the feedback. In this work, we will trace warm ($\sim 10^4\,{\rm K}$) ionised gas kinematics using optical emission-lines, mostly [O III], which has long been used as a diagnostic to search for non-gravitational gas kinematics in AGN host galaxies (e.g., Weedman 1970b; Stockton 1976; Heckman et al. 1981; Vrtilek 1985; Boroson & Green 1992; Veilleux

et al. 1995; Harrison et al. 2014; Jarvis et al. 2019; Scholtz et al. 2021). For tracing cold (i.e., tens of Kelvin) molecular gas, following many other works, we will make use of the CO emission-line, specifically the ^{12}CO J = 3 – 2 transition as a tracer (e.g., Combes et al. 2014; Sun et al. 2014; Cicone et al. 2021; Circosta et al. 2021).

This work is part of the Quasar Feedback Survey (QFeedS; Figure 3.1; Jarvis et al. 2021). This survey aims to address the challenges outlined above by studying the spatially-resolved multi-wavelength properties of 42 relatively low redshift ($z < 0.2$) quasar host galaxies. Using this redshift range allows us to obtain sensitive, high spatial resolution observations (typically $\lesssim$1 kpc), whilst also yielding a reasonable sample of powerful quasars ($L_{\rm bol} \gtrsim 10^{45}\,{\rm erg\,s^{-1}}$) representative of $L_\star$ at the peak cosmic epoch of growth, where quasar feedback is expected to dominate (Kormendy & Ho 2013). Several pilot studies have been conducted on a subset of the QFeedS targets (Harrison et al., 2014, 2015; Lansbury et al., 2018; Jarvis et al., 2019, 2020), whilst an overview of the full sample can be found in Jarvis et al. (2021). Spatially-resolved radio observations form the basis of QFeedS, which provides important insights into the prevalence and properties of radio jets in what is a representative and predominantly 'radio-quiet' quasar sample (Jarvis et al., 2019, 2021). Here we define radio-quiet using the criterion of Xu et al. 1999 that compares the radio to [O III] emission-line luminosity. For a detailed discussion in the context of the QFeedS sample see Jarvis et al. 2021.

In this work, we study one target from QFeedS for which we combine published radio observations with new observations from the integral field spectrograph Multi Unit Spectroscopic Explorer (MUSE; Bacon et al. 2010, 2017) and from the Atacama Large Millimeter/submillimeter Array (ALMA). The former enables us to map the stellar kinematics and ionised gas properties and the latter enables us to map the molecular gas properties. In Section 3.2, we introduce the target, observations and data reduction. In Section 3.3 we estimate radio jet properties from existing data. In Section 3.4 we describe the approaches employed to fit the spectra and map the stellar kinematics and gas properties. In Section 3.5 and Section 3.6, we present our results and discussion, respectively. Finally, in Section 3.7, we summarise our conclusions.

We have adopted the cosmological parameters to be $H_0 = 70$ km s^{-1} Mpc^{-1}, $\Omega_M = 0.3$ and $\Omega_\Lambda = 0.7$, throughout. In this cosmology, 1 arcsec corresponds to 2.615 kpc for the redshift of $z = 0.15$ (i.e., the redshift of the galaxy studied here). We define the radio spectral index, α, using $S_\nu \propto \nu^\alpha$.

3.2 Target, Observations and Data Reduction

In Section 3.2.1 we describe the target investigated in this study in the context of the parent Quasar Feedback Survey and summarise its basic radio properties. We describe the details of the observations and data reduction for the MUSE and ALMA data in Section 3.2.2 and 3.2.3, respectively. A summary of the data used throughout this work is presented in Figure 3.2, with the central panel showing an optical continuum image from the MUSE data (∼62×62 kpc); the right panel showing a closer look (∼10×10 kpc) of the pseudo-narrow-band [O III] image (from MUSE) with CO (3–2) emission (from ALMA) overlaid as contours in purple; and

the left panel with a zoom-in (∼26×26 kpc) of the continuum image, focused on the central regions of the galaxy. A description of how these images were created is described in the following sub-sections and Section 3.4.1.

3.2.1 J1316+1753 in the context of the Quasar Feedback Survey

This paper focuses on a single target, J1316+1753, with an optical right ascension (RA) of $13^{h}16^{m}42^{s}.90$ and declination (DEC) of $+17^{\circ}53'32''.5$ (J2000, ICRS). It is selected from QFeedS and this target illustrates the rich information gained on outflows and AGN feedback from our high-resolution multi-wavelength QFeedS dataset, comprising of radio, optical and sub-mm data. QFeedS was originally constructed using the emission-line selected AGN from Mullaney et al. (2013). Figure 3.1 presents the 16,680 $z < 0.2$ AGN from Mullaney et al. (2013) in the [O III] full-width-half-maxima ($FWHM_{Avg}$) versus [O III] luminosity parameter space. The QFeedS targets are indicated with stars in the figure. We note that the $FWHM_{Avg}$ values plotted in Figure 3.1 are the flux-weighted average of the FWHMs of the two emission-line components fitted by Mullaney et al. (2013). QFeedS targets were selected to have quasar-level [O III] luminosities (i.e., $L_{[OIII]} > 10^{42.1}$ erg s^{-1}; Jarvis et al. 2021). As described in Jarvis et al. (2021), a radio luminosity selection of $L_{1.4GHz} > 10^{23.45}$ W Hz^{-1} is also applied to obtain the final QFeedS sample of 42 targets. This radio cut was set to be above the NVSS detection limit (Mullaney et al. 2013; Molyneux et al. 2019). Despite their moderate radio luminosities, the QFeedS sample still consists of 88 % 'radio-quiet' sources, based on the criteria of Xu et al. (1999) (see Jarvis et al. 2021), which is consistent with the 'radio-quiet' fraction of the overall quasar population (i.e. ∼90 %; Zakamska et al. 2004). Furthermore, the QFeedS targets cover a representative range of emission-line widths of the parent population.

The target of this study, J1316+1753, is highlighted with a circle in Figure 3.1. A comprehensive summary of the target's properties and its previous studies can be found in the supplementary material of Jarvis et al. (2021). However, briefly, J1316+1753 has a type-2 spectra; it has an optical emission-line redshift of $z = 0.150$ (see Jarvis et al. 2019); it is one of the most optically luminous sources in the QFeedS sample (with $L_{[OIII]} = 10^{42.8}$ erg s^{-1}); and it exhibits a broad [O III] emission-line profile ($FWHM_{Avg} = 1022$ km s^{-1}). The one-dimensional [O III] emission-line profile consists of two bright narrow emission-line components, in addition to a strong broad emission-line component (see Jarvis et al. 2019) and we investigate this emission using our spatially-resolved MUSE data in Section 3.4. Based on the spectral energy distribution (SED) fitting from the *UV* to *FIR*, J1316+1753 is a star-forming galaxy with star formation rate $= 30 \pm 10\,M_{\odot}\,yr^{-1}$, and stellar mass $= 10^{11}\,M_{\odot}$ (see Jarvis et al. 2019 for these estimates).

Importantly, J1316+1753 has a modest radio luminosity of $L_{1.4GHz} = 10^{23.8}$ W Hz^{-1} and, although it is confirmed to host a radio AGN, it is classified as 'radio-quiet', as per the traditional criteria (Xu et al., 1999; Best & Heckman, 2012; Jarvis et al., 2021). Compared to some of the other QFeedS sources, J1316+1753 has relatively simple radio morphology (Jarvis et al., 2019, 2020). The 6 GHz radio image of this target from the Very Large Array (VLA) data was produced by Jarvis et al. (2019) (with a synthesised beam of 0.33×0.28 arcsec; root-mean-square (RMS) noise of 8 μJy beam^{-1}) and the morphology reveals three components, which are most likely

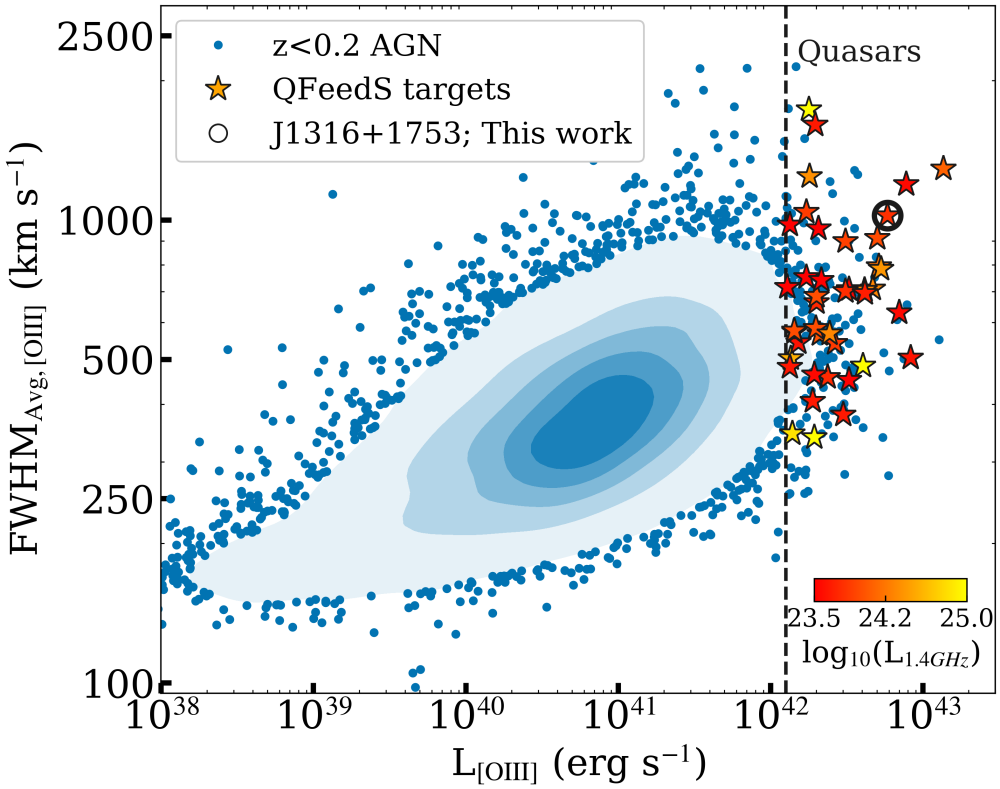

Figure 3.1: [O III] FWHM versus $L_{[OIII]}$ for $z < 0.2$, spectroscopically-selected AGN from Mullaney et al. (2013), represented as blue data points and density contours. Stars represent the 42 QFeedS targets, with $L_{[O\ III]} > 10^{42.1}$ erg s^{-1} (dashed line), from which the quasar of this study was selected (highlighted with a black circle). The QFeedS targets are colour-coded by their radio luminosities ($L_{1.4GHz}$). The quasar in this study has a modest, representative radio luminosity ($L_{1.4GHz}$=$10^{23.8}$ W Hz^{-1}) and it is classified as 'radio-quiet' using traditional criteria (see Section 3.2.1).

attributed to a radio core and two hot spots associated with radio jets. These were labelled as HR:A, HR:B and, HR:C in Jarvis et al. (2019) respectively, and we continue with this nomenclature in this work. The hot spots HR:B and HR:C are located at a projected distances of 0.91 kpc and 1.40 kpc from the central component, respectively. The central radio component, HR:A, has a flatter 1.5–7 GHz spectral index of $\alpha \sim -0.3$, compared to the two hot spots, which have $\alpha \sim -1$ and $\alpha \sim -1.2$ (for HR:B and HR:C, respectively; Jarvis et al. 2019). Overall, the properties of J1316+1753 provide a cogent case to investigate the impact of low luminosity and compact radio jets on the multi-phase ISM in a 'radio-quiet' quasar host galaxy.

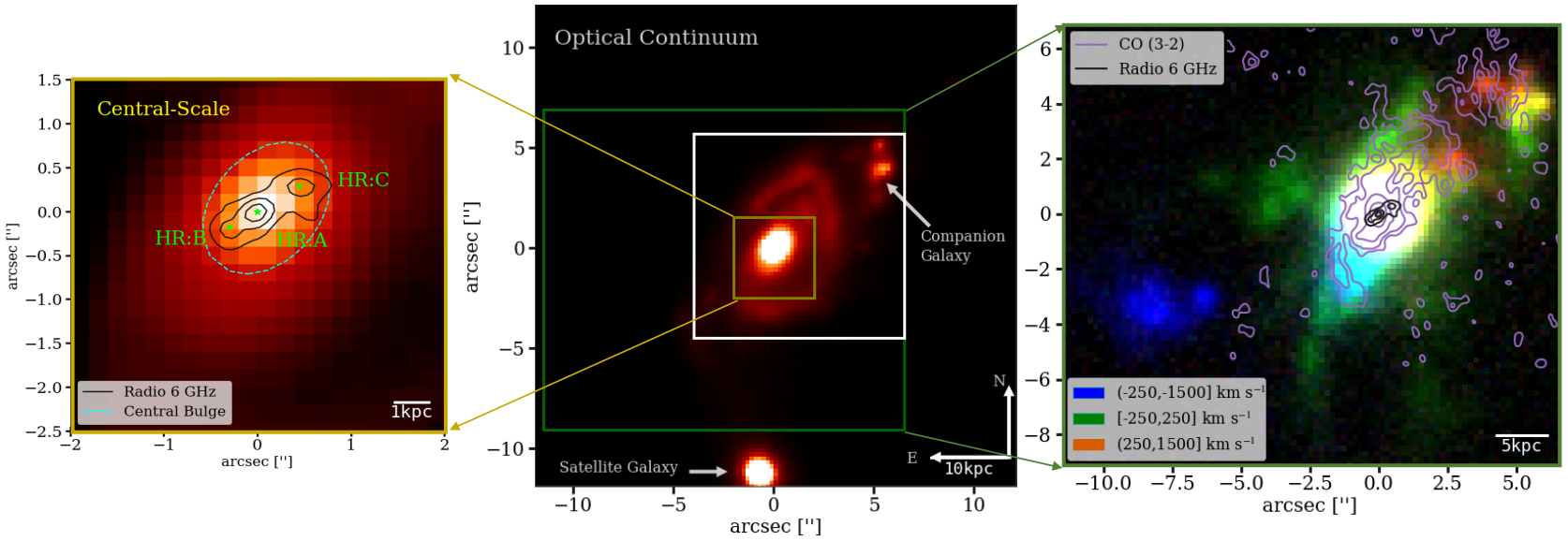

Figure 3.2: A multi-wavelength and multi-scale view of our target galaxy. *Centre:* An optical continuum image from the MUSE data showing the local, 24×24 arcsec (∼62×62 kpc), environment of J1316+1753. The primary target galaxy is centered at a position (0,0) with two clear spiral arms. To the north-west is an associated companion galaxy and to the south one passive satellite galaxy can be seen. *Right:* A closer look (18×16 arcsec; ∼47×42 kpc) showing the pseudo narrow-band [O III] image (from MUSE) with CO (3–2) emission (from ALMA) overlaid as contours in purple (with levels [16,8,4,2,1] $\mathrm{RMS}_{\mathrm{CO(3-2)}}$). The three colours are obtained by dividing the [O III] emission-line profile in three velocity slices as indicated in the legend. *Left:* A zoom-in of the continuum image in the central regions of the galaxy (4×4 arcsec; ∼10×10 kpc). The black contours are the VLA 6 GHz radio emission, at the levels [128,64,32] $\mathrm{RMS}_{\mathrm{radio}}$. In light green we show three dots to highlight the positions of the radio core (HR:A) and the two radio jet hotspots (HR:B and HR:C), as defined in Jarvis et al. (2019). The central panel also shows the 'galaxy-scale' (white inset; 10×10 arcsec; ∼26×26 kpc) within which the kinematic analysis is done. North is up and East is left in all panels and for all plots throughout this paper.

3.2.2 Observation and reduction of the MUSE data

J1316+1753 was observed with the Multi Unit Spectroscopic Explorer (MUSE; Bacon et al., 2010) on ESO's Very Large Telescope (VLT) as part of proposal ID: 0103.B-0071 (PI: Harrison). MUSE is an optical and near-IR integral-field spectrograph at the VLT, housed at the European Southern Observatory's Paranal Observatory. The observations were carried out in wide field mode, with adaptive optics, in a single observing block on the night of 2019 April 29-30. The observations consisted of 4 science exposures (of 550 s each) and 1 sky exposure (of 100 s), rotated by 90° and dithered within a ∼4 arcsec box. The spectra ranges from 4750 to 9350 Å with a spaxel size of about 1.25 Å . The field-of-view is about 1×1 arcmin, with a pixel size of 0.2 arcsec.

The raw data were reduced using the standard ESO MUSE pipeline version 2.6 (Weilbacher et al., 2014, 2020). The flow of the pipeline includes bias-subtraction, correction for flat-field, illumination and geometry, and calibration in wavelength and flux. The sky emission was estimated using the sky exposure and subtracted from the science data. The datacubes were resampled onto a 0.2 arcsec × 0.2 arcsec × 1.25 Å grid. For the flux scaling, the relative offsets between the four exposures were computed using an average of 12 sources in the white-light images of each datacube. The final datacube was obtained by average-combining the four exposures corrected for their offset.

To estimate the seeing point spread function (PSF) for our cube, we used two point-like sources in our field of view. We estimated the PSF to be ∼0.75 arcsec, in the wavelength range around the $[\mathrm{O\ III}]_{5007}$ emission, using the `MoffatModel2` function from the `mpdaf` package (Bacon et al. 2016). We corrected for the wavelength-dependent line-spread function (LSF), introduced by MUSE, during the line-profile fitting procedure, as described in Section 3.4.4.

3.2.3 Observation and reduction of the ALMA data

J1316+1753 was observed with ALMA in Band 7 in 3 × 1 hour epochs between 2019 April 29 - 2019 May 03 under ALMA project 2018.1.01767.S (PI: A. P. Thomson). Our chosen correlator setup comprises of three spectral windows, with one having a central frequency $\nu_{\rm obs} = 345.795990$ GHz, corresponding to the redshifted CO(3-2) line at $z_{\rm opt} = 0.15$ (Jarvis et al., 2019), and the others overlapping this spectral window with central frequencies of 344.7 GHz and 347.0 GHz used for baseline subtraction. Each of the three spectral windows has a bandwidth of 1875 MHz (1870 km s^{-1}) and a spectral resolution of 31.25 MHz (31.17 km s^{-1}), recorded in dual polarization (XX,YY). In total, our three overlapping spectral windows provide 4.17 GHz (∼ 3600 km s^{-1}) of spectral coverage centred on the CO(3-2) line. Our science goals of mapping the galaxy-scale molecular gas kinematics and looking for jet-ISM interactions in the region of the radio jet, lead to using the C43-4 array, providing an angular resolution of $\theta_{\rm res} \sim 0.5$ arcsec and a largest angular scale $\theta_{\rm LAS} \sim 4$ arcsec (corresponding to linear scales of ∼ 1.3 kpc and ∼ 11 kpc, respectively, at the source redshift $z = 0.15$).

We obtained the raw data from the ALMA science archive and pipelined the data in CASA v5.4.0-68 using the reduction script supplied by ALMA user support. Following the successful completion of the ALMA CASA pipeline, the phases and amplitudes were visually inspected as functions of frequency and time using the CASA tool PLOTMS, during which a small percentage ($\lesssim 1\%$) of outliers were flagged from the calibrated data.

The reduced *uv* data were imaged in CASA TCLEAN. A spectral line datacube was created, using natural weighting (ROBUST=2.0), on-the-fly primary beam correction (PBCOR=True) and multi-scale clean at a pixel scale of 0.05 arcsec pix^{-1}, across an image of $\sim$ 51 arcsec, (or 135 kpc) on a side. The resulting naturally-weighted images have a synthesized beam which well-resembles a two-dimensional Gaussian of width $0.54'' \times 0.45''$ at a position angle of 8°, with an rms sensitivity of $\sigma_{\rm rms} = 347\,\mu$Jy beam^{-1} channel^{-1}.

3.2.4 Alignment of the MUSE, ALMA and VLA data

To perform a multi-wavelength analysis we need to be sure that all the data are registered on the same astrometric solution. To do this, we followed the same procedure as in Jarvis et al. 2019, who demonstrated that the astrometric solutions of Sloan Digital Sky Survey (SDSS) images were accurate enough to align datacubes to VLA data, for 9 targets from QFeedS including J1316+1753, with a median accuracy of 0.13 arcsec (i.e., ∼0.3 kpc). This is sufficient for the multi-wavelength comparison that we perform in this work (Section 3.4). Briefly, we created pseudo broad-band images from the MUSE IFS cubes over the same wavelength range as the *g*-band images from SDSS. The peak emission in the pseudo-broad band image was identified to be located 0.6706 arcsec from the peak radio emission and 0.6709 arcsec from the peak CO(3–2) emission (see Figure 3.2; Section 3.4.1). Then we used the `find_peaks` function of the `photutils` (Bradley et al. 2020) python package to identify the pixel associated to the peak emission in the MUSE pixel and anchored the coordinate values of this pixel to match the associated position from the image peak in SDSS. This resulted in a global astrometric shift of $\sim$ 2.5 arcsec to the MUSE cube.

Since, after this shift, the peak continuum and the radio core were well aligned (i.e., within $\sim$ 0.1 arcsec) this provides confidence in the alignment process, although we note that a priori these different emissions may not by physically aligned. Ultimately we chose the HR:A position of the radio core (introduced in Section 3.2.1; RA of $13^{\rm h}16^{\rm m}42^{\rm s}.8$ and DEC of 17°53'32".3) as our 'nucleus' position, indicated with a (0,0) in all relevant figures. All distances are measured with respect to this position as the reference point.

3.3 Estimated jet properties

In this section, we estimate the properties of the radio jets obtained from empirical relations and existing radio data for the target. These estimated properties are used to help interpret our new observations in terms of the effects of the jets on the quasar host galaxy in Section 3.2.3.

3.3.1 Jet Kinetic Power ($P_{\rm jet}$)

To estimate the kinetic jet power ($P_{\rm jet}$), we use the empirical relation of Merloni & Heinz 2007, obtained from a sample of low-luminosity radio galaxies, as below:

$$\log P_{\rm jet} = (0.81 \pm 0.11) \times \log L_{5\,\rm GHz} + 11.9^{+4.1}_{-4.4} \quad (3.1)$$

From the VLA data in Jarvis et al. 2019, the 5.2 GHz flux density of the radio core (HR:A) is 1.1 mJy (spectral index $\alpha = -0.3$). This corresponds to 5 GHz luminosity of $6.5 \times 10^{39}\,\rm erg\,s^{-1}$ for the radio core. Using the relation above we estimate a jet power of $7.8 \times 10^{43}\,\rm erg\,s^{-1}$. However, since the empirical relation is derived from lower resolution data than ours, we also calculate the jet power using the total 5 GHz flux density (i.e., over HR:A, HR:B and HR:C), which is 2.7 mJy (spectral index $\alpha = -0.85$; Jarvis et al. 2019). Using this flux density, we estimate a jet power that is only higher by a factor of 2.5 (i.e., $1.7 \times 10^{44}\,\rm erg\,s^{-1}$). Hence, for our order-of-magnitude estimate, we assume the jet power to be, $P_{\rm jet} = 10^{44}\,\rm erg\,s^{-1}$ during our discussion in Section 3.2.3.

3.3.2 Jet inclination angle (θ)

Since AGN jets experience bulk relativistic motions (Blandford & Königl 1979; Ghisellini et al. 1993), the apparent brightness of the different AGN sub-components can be used as an estimator of their inclination angle with respect to line of sight (los). The radio core prominence parameter is a measure of the core-to-extended radio flux density [$R_{\rm C} = S_{\rm core}/S_{\rm ext} = S_{\rm core}/(S_{\rm tot} - S_{\rm core})$], and is a known statistical indicator of inclination angle, with respect to los, as discussed in detail in Orr & Browne 1982 (also see Saikia & Kapahi 1982; Kharb & Shastri 2004). We used the flux density estimates from the 5.2 GHz VLA data from Jarvis et al. 2019, which estimates the $S_{\rm core} = 1.1$ mJy and $S_{\rm tot} = 2.7$ mJy. Using these values we estimated the $R_{\rm C}$ to be $= 0.7$, which gives $log_{10}(R_{\rm C}) = -0.16$. The $log\,R_{\rm C}$ values are seen to vary from -4 to +4 for a sample of randomly oriented radio galaxies and blazars, corresponding to inclination angles from 90° to 0° (see Kharb & Shastri 2004). Therefore, the estimated $logR_C \sim 0$, value for J1316+1753 corresponds to an inclination angle of $\sim 45°$ for the jet in this source, with respect to our line of sight. Hence, based on these statistical arguments, a projected inclination of ~ 45° with respect to our los, is assumed for the jets in the rest of the paper. Since we estimated our galaxy's inclination angle to be 46° (see Section 3.4.2), we conclude that the jets are seen to be in the plane of the galaxy disk.

3.3.3 Jet Speed (β)

The relativistic doppler beaming effects in jets enable us to estimate which is the approaching and which is the receding jet, and to also estimate a jet speed (Ghisellini et al. 1993; Urry & Padovani 1995). Using the 5.2 GHz VLA image from Jarvis et al. 2019, we measured the surface brightness (SB [µ Jy / beam]) values at equal distances from the peak surface brightness point (i.e., the radio core, HR:A) on both sides along the jet axis. We define the ratio of these surface brightness values as $J = SB_{\rm HR:B}/SB_{\rm HR:C}$, and repeated these measurements at 7 different distances ranging from 0.07-1.2 arcsec. A range of J estimates was obtained from 1.1 to 2.6. On

average, the south-eastern jet (HR:B) was measured with ~ 2 times higher surface brightness than the north-western jet (HR:C). Hence it was concluded that HR:B is the approaching side of the jet.

Furthermore, the ratio, J was used to estimate the jet speed, $V_{\rm jet} = \beta\, c$, using equation A10 from Urry & Padovani 1995 as follows:

$$\beta \cos \theta = \frac{\mathrm{J}^{1/p} - 1}{\mathrm{J}^{1/p} + 1} \tag{3.2}$$

We assumed the value of $p = 3.0$ (as defined for a continuous, non-blobby jet, with α=−1; Urry & Padovani 1995)[1]. Using our estimate of the jet inclination angle ($\theta = 45\,^{\circ}$; see Section 3.3.2), we estimate the jet speed to be in the range $0.04\,c$–$0.2\,c$. This seems to be a reasonable value, since for a typical low-luminosity AGN, jet speeds would be expected to be around $0.15\,c$ (Ulvestad et al. 1999). A limitation of the jet speed and jet inclination estimates is that this relation is defined for radio-loud AGNs, in contrast to our radio-quiet source. However, we mainly use these values for a qualitative comparison to simulations and order-of-magnitude estimates in Section 3.2.3.

3.4 Analysis

In this section, we describe our analysis methods to: (1) produce the continuum and emission-line images shown in Figure 3.2 (Section 3.4.1); (2) estimate the structural parameters of the galaxy (Section 3.4.2); (3) map the stellar kinematics using the MUSE data (Section 3.4.3); (4) model the optical and CO(3–2) emission-line profiles from the MUSE and ALMA data, respectively (Section 3.4.4); (5) estimate the non-parametric properties of the emission-lines and produce their maps (Section 3.4.5). As illustrated in Figure 3.2, we perform the analyses on two spatial scales, firstly over the whole 'galaxy-scale' (for which we map the stellar and gas properties using bins following Voronoi tesellation, see Section 3.4.3) and, secondly, focusing on the inner 'central-scale' region around the jets (for which we map the gas properties only).

3.4.1 Environment and central-regions of J1316+1753

We present pseudo-broadband and narrow-band (emission-line) images of J1316+1753 in Figure 3.2. We note that for all images in this paper, North is up and East is to the left, as indicated in the central panel of this figure. The central panel shows the stellar continuum image of the galaxy inside a 24×24 arcsec (62×62 kpc) region. To make the image, we median-collapsed the data cube (masking all the emission-lines) across the same wavelength range as that used for the stellar continuum fitting (see Section 3.4.3 for a detailed explanation and Figure 3.3 for a representation). The figure clearly reveals the galaxy morphology, with a central bulge and two prominent spiral arms extending over ~ 21 kpc. Within this image we identify, in addition to our main target, one passive satellite galaxy to the south (without any emission-lines). However, based on the regular morphology and kinematics (discussed in Section

[1]We note that Urry & Padovani 1995 use the opposite sign convention for spectral index (α) in their study compared to this analysis.

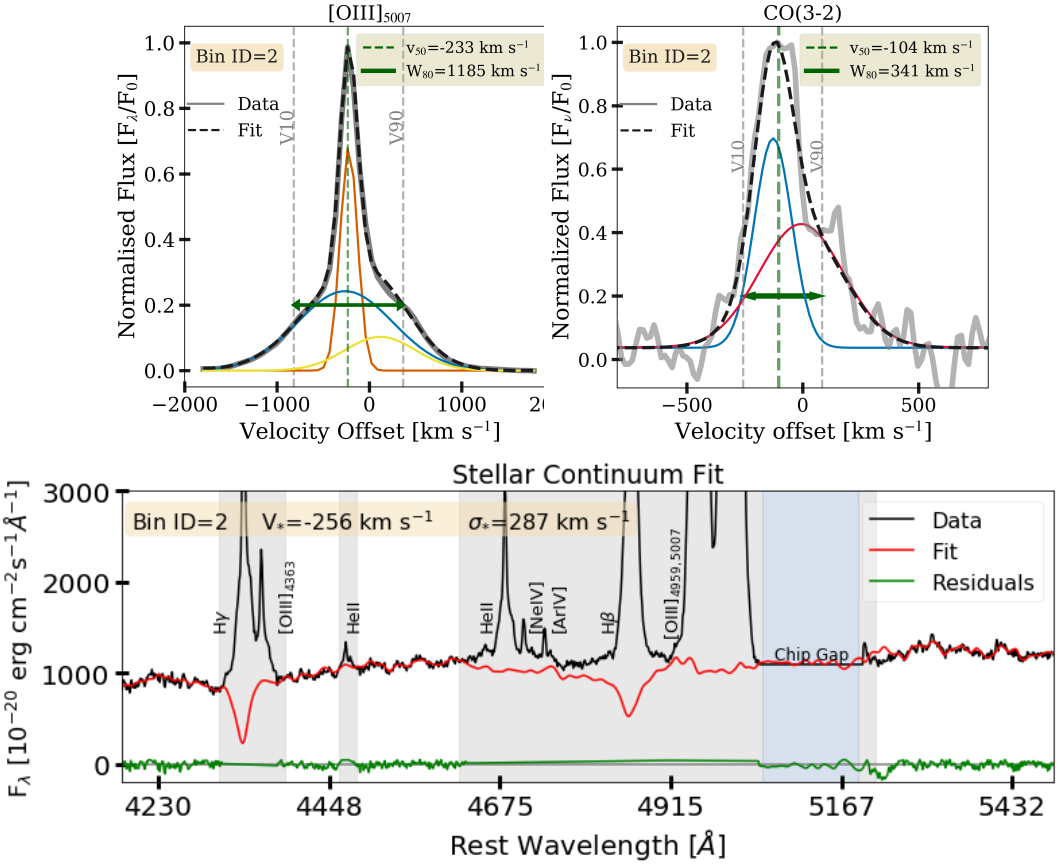

Figure 3.3: Examples of our emission-line and stellar continuum fits to the MUSE and ALMA data. *Upper-left:* [O III] emission-line profile (grey curve) and our best fit (dashed black curve), as well as the three individual Gaussian components used to construct the total fit (yellow, blue and orange curves). *Upper-right:* CO(3–2) emission-line profile (grey curve), with the best fit (dashed black curve) and the two Gaussian components that make up the total fit (blue and red curves). In both upper panels we indicate the non-parametric values obtained from our analyses: V_{50} (dashed green line) to trace the bulk velocity and W_{80} (green arrows) to trace the velocity-dispersion, which is the velocity width between V_{10} and V_{90} (vertical dashed grey lines). Both emission-line profiles are extracted from Voronoi Bin no. 2, as defined in Section 3.4.3. *Lower panel:* Spectra (black curve), presented across the wavelength range used to obtain the stellar continuum fits (red curve) for estimating the stellar kinematics (see Section 3.4.3). Wavelength regions excluded from the fits (due to strong emission-lines and the instrumental chip gap) are highlighted with shaded regions. The fit residuals are shown as green curves.

3.5.2), we do not see any clear disturbances in the galaxy dynamics caused by it that could affect our conclusions and hence they are not discussed henceforth in this work. We make particular note of the bright and clumpy continuum structure located $\sim$17 kpc to the north-west of the primary galaxy nucleus. For identification purposes only, we label this as the 'companion galaxy'. We note that this is identified in emission lines at the same redshift as our target galaxy, meaning that it is also physically associated. The kinematic anaysis in Section 3.5.2 is done within the region indicated through the white box. We refer to it as the 'galaxy-scale' region (10×10 arcsec or 26×26 kpc).

The right panel of Figure 3.2 covers a spatial region of 18×16 arcsec (i.e., 47×42 kpc), chosen to show the extent of the [O III] gas we identified in and around the main galaxy. The three-colour image shown is comprised of three pseudo narrow-band [O III] images, collapsed over the velocity slices indicated in the legend. The overlaid

contours in purple represent the CO(3–2) image, created by collapsing the ALMA cube over a frequency range of $\pm 700\,\mathrm{km\,s^{-1}}$. The black overlaid contours are from the 6 GHz VLA image (see Section 3.2.1; Jarvis et al. 2019).

In the left-panel of Figure 3.2 we show a zoom-in of the continuum image, as indicated by the yellow box in the main panel, extending over ~ 4 arcsec (i.e., 10 kpc). We use this region as the 'central-scale' to perform our spaxel-by-spaxel kinematic analyses in Section 3.5.3. The three light-green color dots indicate the position of the radio core (HR:A) and the two jet hotspots (HR:B and HR:C; discussed in detail in Section 3.2.1). The cyan color ellipse shows an isophote fit to the stellar bulge profile, and is discussed later in Section 3.4.2.

3.4.2 Position angle, inclination angle and sizes

To aid the discussion on how the jets and gas interact, it is useful to constrain some basic properties of the host galaxy stellar emission, specifically the size, major axis position angle and inclination angle. We used the high spatial resolution continuum image (Figure 3.2; middle panel) to make measurements of half-light radii ($R_{1/2}$), morphological axes (PA) and inclination angle (θ). We fitted a two-dimensional Gaussian model to our galaxy's continuum image to obtain a morphological position angle $= 152 \pm 2°$, an axis ratios (b/a) $= 0.71 \pm 0.04$, and $R_{1/2} = 6.10 \pm 0.12$ kpc. We note that all quoted position angles are defined as going East of North. The half-light radius estimate was further verified by fitting an exponential Sersic profile to the surface brightness of the galaxy disc. Furthermore, following the works of Tully & Fisher (1977); Weijmans et al. (2014), we used the axis ratios (b/a) to estimate the inclination angle (θ) using the following relation:

$$\cos^2\theta = \frac{(b/a)^2 - q_0^2}{1 - q_0^2} \tag{3.3}$$

where q_0 is the intrinsic axial ratio of an edge-on galaxy (Tully & Fisher 1977). We assumed $q_0 = 0.2$, which is appropriate for thick disks, however, for our axis ratio values, a change in q_0 by a factor of 2 would result in a $< 9\,\%$ change in the inclination angle (θ). Using the above relation, we estimated a galaxy inclination angle of $46 \pm 2°$. We would like to note that the reported uncertainties are purely from the fitting function, and do not take into account the intrinsic uncertainties arising due to the choice of a simple model.

In Section 3.2.3, we are interested in the relative position angle between the radio jets and the observed stellar bulge. Therefore, we followed a similar approach for the stellar bulge (Figure 3.2; left-panel) and fitted a 2D Gaussian (cyan ellipse) to obtain a position angle of $139 \pm 4°$.

3.4.3 Stellar kinematics from MUSE

The gas kinematics in centres of galaxies can be a good tracer of the AGN-driven outflows and the consequent jet-ISM interactions. However, the effect of the underlying stellar kinematics needs to be quantified to de-couple gravitational-motions from

gas dynamics arising due to other processes. We use the MUSE data to map the stellar kinematics over the full extent of the stellar emission, i.e., the 'galaxy-scale' indicated by the white box in Figure 3.2.

We fitted the stellar continuum using the modular analysis framework of `GIST` pipeline[2] (Galaxy IFU Spectroscopy Tool; Bittner et al., 2019). As a brief overview, the `GIST` pipeline works directly on the science-ready MUSE datacubes, performs a Voronoi tesellation (Cappellari & Copin 2003), fits spectral templates to the observed spectra and outputs a best-fit estimate of stellar velocity and stellar velocity-dispersion for each Voronoi bin. A complete overview of the pipeline is presented in Bittner et al. (2019).

The spectra were de-redshifted to the rest-frame using an initial estimate of the systemic redshift ($z = 0.15$). The spaxels below an isophote level with an average signal-to-noise-ratio (SNR) of 5 per spectral bin, as measured within the rest-frame wavelength range of 4452 to 4630 Å (range devoid of any bright emission-lines), were excluded from the fits. Then, the remaining galaxy spaxels were spatially binned to achieve a minimum SNR using the adaptive Voronoi tesellation routine of Cappellari & Copin (2003). We set the minimum SNR per Voronoi bin to be 30, which resulted in stable measurements of the stellar kinematics, but still provided a good spatial sampling (see Section 3.5.2). As a result of this procedure, the galaxy was divided in 41 Voronoi bins over the galaxy-scale frame. We show the shape and location of these bins in the Appendix, Figure 3.9. Of these, 38 bins (Bin No. 0-37) were contiguous and represented the main galaxy under investigation, while 3 bins (Bin No. 38, 39, 40) were associated with the minor companion galaxy (as discussed in Section 3.5.1, and indicated in Figure 3.2).

The actual wavelength range used to fit the stellar continuum was restricted to 4185–5500 Å in the rest-frame. This wavelength range covers sufficient emission-line free regions of prominent stellar absorption features, whilst avoiding the redder wavelength range of MUSE that is more strongly affected by sky line residuals (also see e.g., Falcón-Barroso et al., 2006; Bittner et al., 2019).

The stellar continuum fitting with `GIST` requires the preparation of a spectral template library. We required a spectral template library that is compatible with sufficient wavelength range and the spectral resolution for our MUSE data. Following these requirements, we selected the second data release (DR2) of the X-Shooter Spectral Library (`XSL`; Arentsen et al., 2019; Gonneau et al., 2020). The `XSL` is a stellar spectral library covering the wavelength range from 3000-25000 Å, at a resolution of about R $\sim$ 10000. We used the ultra-violet to blue (UVB) set of the DR2 of `XSL` that covers 813 observations of 666 stars. The parametrisation from Bacon et al. (2017) was adopted as the MUSE line-spread function to broaden all the template spectra to the resolution of our observed spectra before any fits were conducted. This process corrects the velocity-dispersion measurements for the spectral resolution of MUSE.

The stellar kinematics were derived by performing a run of the `pPXF` routine (Cappellari & Emsellem, 2004; Cappellari, 2017). To account for small differences between the MUSE spectra and the templates, we included an additive Legendre polynomial

[2] `http://ascl.net/1907.025`

of the order 8 (following literature, see Pinna et al. 2019; Gadotti et al. 2020; Bittner et al. 2020)[3]. Before the fitting, care was taken to mask wavelength ranges covered by the broad and bright emission-lines. We adopted a conservative approach and used broad masks with a width of up to 200 Å for the broadest emission-lines (e.g., NeIV, [Ar IV], Hβ, [O III]$_{4959}$, [O III]$_{5007}$, etc.; see Figure 3.3) in order to ensure that these lines were masked even for the central spaxels with the broadest emission-lines. This ensured that no contamination from the emission-lines affected the analysis of the stellar kinematics, but still left sufficient stellar absorption features to obtain stable solutions for the stellar kinematics. We note that on reducing the masking width to 100 Å for the strongest emission lines, the velocity measurements are consistent in the outer Voronoi bins where the strongest emission lines are much narrower, giving us confidence the fitting wavelength coverage is sufficient. In addition, the wavelength range from 5820-5970 Å is masked, to avoid the contamination of the spectra from the laser guide stars of the adaptive optics facility. The stellar fits were visually inspected for each bin and were seen to closely follow the observed spectra in each case. As an example illustration, the observed spectra and the fits to the stellar continuum are shown in the lower panel of Figure 3.3 (see supplementary material for the fits from all other Voronoi bins). In Section 3.5, we discuss the resulting stellar kinematics. The median of errors, across all Voronoi bins, on the stellar kinematics were $\pm\,16\,\mathrm{km\,s^{-1}}$ for stellar velocities and $\pm\,18\,\mathrm{km\ s^{-1}}$ for stellar dispersion estimates, where the errors are formal errors (1σ) uncertainties estimated from `pPXF`.

We used the redshift estimate from the stellar fits of each Voronoi bin and estimated a flux-weighted mean redshift of $z = 0.15004$. This value has then been used as the systemic redshift, for all of the analysis in this paper.

3.4.4 Emission-line profile fitting procedure

In this work, we characterise the spatially-resolved kinematics and flux ratios of strong optical emission-lines (using the MUSE data) and the CO(3–2) emission-line (using the ALMA data). We take the same overall approach for fitting all emission-lines, which we describe first, before giving details that are specific to fitting individual emission-lines. All of the line profiles and velocity maps displayed in this work have been shifted to the rest frame, using the stellar systemic redshift described in Section 3.4.3. A set of emission-line profiles and fits from across the whole galaxy are shown in the supplementary material.

We fitted the profiles using the χ^2 minimisation procedure CURVE_FIT (Virtanen et al. 2020b) and the most appropriate number of Gaussian components (detailed below) were selected using the Akaike Information Criteria (AIC; Akaike 1974). Due to the complexities of the optical emission-line profiles, we primarily use these fits to obtain an overall non-parametric characterisation of the line profiles (see Section 3.4.5) and largely refrain from assigning physical significance to individual

[3]We note that we tried the fit for two different cases, one with only an additive Legendre polynomial and the other with only a multiplicative Legendre polynomial (both with order 8). We find no qualitative difference in the kinematic estimates and only a moderate variation in absolute measured velocity values of about $6\,\mathrm{km\,s^{-1}}$ (median value).

components (following e.g., Liu et al., 2013; Harrison et al., 2014). However, we verified that the non parametric results on the gas kinematics provide qualitatively the same conclusions as investigating 'broad' and 'narrow' components separately.

For our primary tracer of the ionised gas kinematics we use the [O III]λ5007 emission-line. We fitted the spectral region around the [O III]$\lambda\lambda$4959,5007 emission-line doublet using the rest-frame air wavelengths in the range [4940, 5040] Å. We attempted to fit the [O III]λ5007 profile using one, two or three Gaussian components (selected based on the AIC). An example [O III]λ5007 (hereafter [O III]) emission-line profile and the best-fit solution is shown in Figure 3.3. We used the same Gaussian component parameters to fit simultaneously the [O III]λ4959 emission profile, by using the same line width, a fixed wavelength separation and a fixed intensity ratio of [O III]λ4959/[O III]λ5007 = 0.33 (e.g., Dimitrijević et al., 2007).

For the purpose of obtaining estimates of electron densities (see Appendix, section 3.8.2), we followed a similar procedure to fit other optical emission-lines (in all cases using rest-frame air wavelengths). We note that we used a simple first-order polynomial to characterise the local continuum around all the optical emission-lines. This is typically appropriate for the strong emission-line dominated spectra that we have and hence will not affect the inferred ionised kinematics.

To trace the molecular gas kinematics, the CO(3–2) line (with a rest frame frequency of 345.7960 GHz) was extracted from the ALMA data cube around a spectral window of $\sim \pm 700$ km s^{-1}. Based on visual inspection and an AIC estimate, a maximum of two Gaussian components were required to characterise the CO(3–2) emission-line profile over the whole galaxy. The local baseline continuum was well characterised with a constant value. An example CO(3–2) emission-line profile and the best fit solution is shown in Figure 3.3 and a set of emission-line profiles and fits from across the whole galaxy are shown in the supplementary material.

3.4.5 Non-parametric velocity definitions

The complexities and degeneracies of the emission-line fits exhibited in powerful quasars lead us to favour non-parametric definitions of bulk velocity shifts and velocity-dispersion (also see Harrison et al., 2014; Jarvis et al., 2019, for a kinematic study of other QFeedS targets). Therefore, we used the best-fit models of the emission-line profiles from Section 3.4.4 to calculate the following:

- V_{50}, which is the median velocity of the overall emission-line profile, and is a tracer of the bulk gas velocity.

- W_{80}, which is the velocity-width of the emission-line that contains 80 per cent of the integrated flux and is a tracer of the velocity-dispersion. This is defined as, $W_{80} = V_{90} - V_{10}$, where V_{10} and V_{90} are the 10th and 90th percentiles of the emission-line profile, respectively. For a single Gaussian profile, W_{80} is equivalent to 1.083×FWHM or 2.6×σ.

- Peak SNR ratio, which is simply the ratio of the peak flux density in the emission-line profile to the noise in the spectra. The noise is calculated by taking the standard deviation of the continuum spectra, in windows of ~ 30 Å, on both sides of the emission peak.

We note that we corrected the W_{80} values by first subtracting, in quadrature, the line-spread function (LSF) $\sigma_{\rm LSF}$, from each of the component gaussians. The wavelength-dependent $\sigma_{\rm LSF}$ of the MUSE data was estimated using equation 8 from `udf-10` parametrisation of Bacon et al. (2017).

In addition to tracing these non-parametric values, we also attempted to trace the properties of the individual broad and narrow components. Although these results are more subject to degeneracies, and therefore provided noisier results, we found that we draw the same conclusions on the spatial distribution of the high velocity-dispersion gas and positions of bulk velocity offsets discussed in Section 3.5.2 and Section 3.5.3. This can be visually verified by looking at the individual Gaussian components of the fits shown in the supplementary material.

To map the ionised and molecular gas kinematics and the emission-line flux ratios on the galaxy-scale, we use the same spatial Voronoi bins as obtained for the stellar kinematics maps described in Section 3.4.3. This approach is sufficient for our goal of establishing a broad description of the galaxy kinematic structure and performing a like-for-like comparison between the stellar kinematics and the two gas phases (see Section 3.5.2). Furthermore, we find that the gas is predominantly located within the extent of the stellar emission (see Figure 3.2; Section 3.5.1). We note that for the CO(3–2) gas, some bins had low SNR (i.e., < 3; see Figure 3.8.1), and are hence not shown for the ALMA maps. A study of any additional faint gas in the circumgalactic medium is deferred to future work. To plot the values extracted from the fits in the maps, on the galaxy-scale, we required a signal-to-noise ratio (SNR$\geq$3). However, this only affected the galaxy-scale maps of CO(3–2) where the SNR was found to be lower than this threshold in three bins. Maps of V_{50} and W_{80} for [O III] and CO(3–2) are discussed in Section 3.5.2 and 3.5.3. A visual inspection of the data reveals that our maps provide a reliable and meaningful representation of the underlying data.

We also produced maps of the emission-line properties on the central-scale around the jets (see yellow box in Figure 3.2). For the central-scale maps, we performed the emission-line profile fits, following Section 3.4.4, in spatial regions of 0.2×0.2 arcsec. Again, we required a SNR$\geq$ 3 to plot the derived quantities in these maps. Central-scale maps of SNR, V_{50} and W_{80} for both [O III] and CO(3–2) are presented and discussed in Section 3.5.3. We note that we lack sufficient SNR to map the stellar kinematics using these smaller spatial bins on this scale. For all the fitted parameters, we obtained the one standard deviation errors as $\sqrt{diag(pcov)}$, where pcov is the estimated covariance of each parameter. To estimate the uncertainty in W_{80}, we used the error in the FWHM of the broadest gaussian component and for the uncertainty in V_{50} we used the error in the velocity estimate of the narrowest gaussian component.

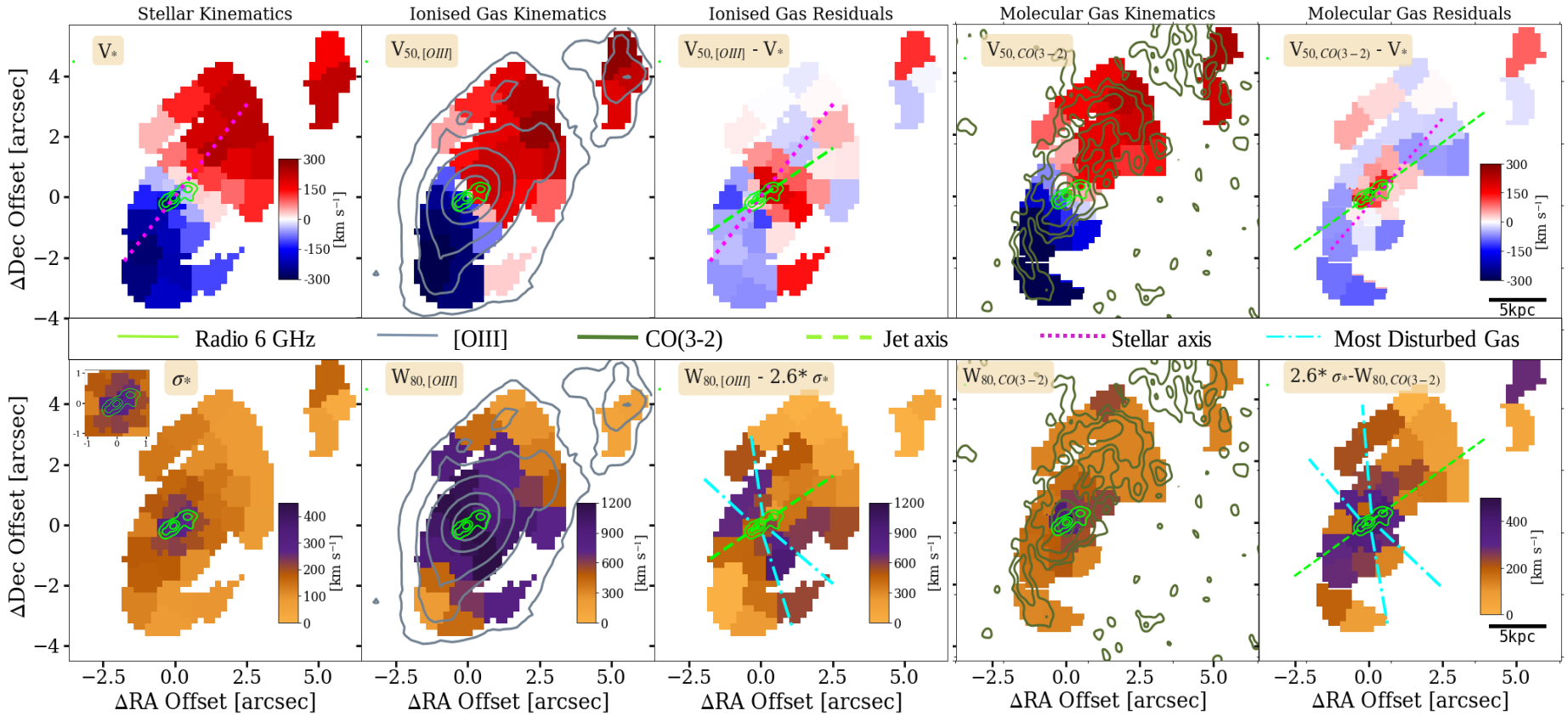

Figure 3.4: Caption continued on the next page.

Figure 3.4: (*Caption continued from the plot on the previous page*) A comparison of the stellar and multi-phase galaxy-scale kinematics using the Voronoi bins. *Top row:* bulk velocity maps ($V_\star$ for the stellar and V_{50} for the gas). *Bottom row:* velocity-dispersion maps ($\sigma_\star$ for the stellar kinematics and W_{80} for the gas). In both rows, *from left-to-right:* stellar kinematics, ionised gas kinematics (from [O III]), residual ionised gas kinematics (i.e., the velocity difference between the stellar and ionised gas maps; see Section 3.5.2), molecular gas kinematics (from CO(3–2)), and residual molecular gas kinematics. In all panels, the light-green contours represent the 6 GHz radio emission at levels [32,16,4] $\mathrm{RMS_{radio}}$. Grey contours (in second column) trace the [O III] emission at [64,16,4,2,1] $\mathrm{RMS_{[OIII]}}$. The dark-green contours trace the CO(3-2) emission at levels of [16,8,4,2,1] $\mathrm{RMS_{CO(3-2)}}$. The dashed green and dotted pink lines trace the projected jets and stellar kinematic axis, respectively. A scale bar representing a length of 5 kpc is shown in both the right-most panels. The bulk of the gas follows the stellar velocities at the galaxy scale as seen in both the phases, except for the central bins, around the jet region, which show strong velocity residuals (top-row: third and fifth column). The highest dispersion values are seen perpendicular to the jets for ionised gas (bottom-row, third column), indicated by the cyan-lines (traced from the cones of highest velocity-dispersion identified in Figure 3.5).

3.5 Results

In this section we present our results from the analysis of MUSE and ALMA data for the $z = 0.15$, type-2 quasar, J1356+1753, selected from QFeedS (see Figure 3.1). Specifically, we present: (1) the distribution of stellar emission, ionised gas and molecular gas (Section 3.5.1); (2) the galaxy-scale stellar and multi-phase gas kinematics (Section 3.5.2) and (3) the central-scale gas kinematics and emission-line properties close to the jets (Section 3.5.3).

3.5.1 Overview of the stellar and gas distribution

Figure 3.4 presents the galaxy-scale stellar kinematics (first column), ionised gas kinematics (second column), residuals by subtracting the stellar and ionised gas kinematics (third column), the molecular gas kinematics (fourth column) and the residuals from subtracting the molecular and stellar kinematics (fifth column). In all columns, the upper-row presents the bulk velocity maps ($\mathrm{V}_\star$ or V_{50}) and the lower-row presents the velocity-dispersion maps ($\sigma_\star$ or W_{80}) maps. We note that while computing residuals, the stellar dispersion values were scaled by a factor of 2.6, to make the values more directly comparable to W_{80}, which we used to characterise the velocity width of the gas (see Section 3.4.5 for the estimation methods).

As can be seen in Figure 3.2, J1316+1753 is a spiral galaxy extending over ~ 20 kpc ($R_{1/2} = 6.1$ kpc) from the north spiral arm to the south spiral arm. [O III] emission is our tracer of the ionised gas. The [O III] image shown in the left-most panel of the figure reveals that the ionised gas broadly covers the same spatial regions as the stellar continuum emission in both the primary galaxy and the minor companion galaxy to the north west (also see the second column of Figure 3.4). However, we also observe an ionised gas cloud (i.e., with no corresponding stellar continuum emission), at a distance of ~ 17 kpc south-east of the galaxy nucleus, with a blue-shifted velocity of - 250 $\mathrm{km\,s^{-1}}$. Although not the focus of this work, we speculate that this cloud may be a tidal debris or the result of an historic outflow (see Lintott et al. 2009; Keel et al. 2012, 2019 and the references therein).

CO(3–2) emission is our tracer of the molecular gas (see Section 3.2.3). The CO(3–2) contours shown in the right-most panel of Figure 3.2 and in the fourth column of Figure 3.4 reveal that the molecular gas broadly follows the distribution of the

stellar continuum emission, including tracing the northern and southern spiral arms. However, at the sensitivity of our observations, the molecular gas is less extended than both the [O III] and continuum emission. Specifically, CO(3–2) emission is not detected towards the outer edges of the spiral arms. Nonetheless, for this work we only aim to qualitatively describe the galaxy-scale molecular gas kinematics, for which the data is sufficient.

3.5.2 Kinematics on the galaxy-scale

As a first investigation of the stellar and multi-phase gas kinematics, we look at the entire galaxy-scale (i.e., across a 26×26 kpc region; see Figure 3.2) using the Voronoi bins defined in Section 3.4.3 (also see Figure 3.9). By using the same spatial bins, we are able to directly compare the stellar, [O III] and CO(3–2) kinematics without having to rely on a particular dynamical model with the associated uncertain assumptions. We note that for the following results, we are only concerned with the contiguous Voronoi bins of the central galaxy and we exclude the minor companion galaxy when presenting quantitative values. Our goal here is to qualitatively assess if the multi-phase gas follows the host galaxy's gravitational motions, before performing a deeper investigation of the kinematics and distribution of the gas in the central region of the galaxy in Section 3.5.3.

Stellar kinematics

The stellar velocity and stellar velocity-dispersion maps, presented in Figure 3.4, clearly suggest the presence of a smoothly rotating stellar galaxy disk. We obtain an approximate major kinematic axis of 140 ° by connecting the Voronoi bins with the highest values of projected velocities (i.e., $-268\pm18\,\mathrm{km\,s^{-1}}$ and $+240\pm14\,\mathrm{km\,s^{-1}}$) through the galaxy nucleus. This major kinematic axis is well aligned with the morphological axis of 150 °, which we measured in Section 3.4.2. Accounting for the 46° inclination angle of the galaxy (see Section 3.4.2), we estimated the de-projected maximum rotation velocities of $-360\,\mathrm{km\,s^{-1}}$ and $+330\,\mathrm{km\ s^{-1}}$. These high rotation velocities are consistent with previous work suggesting that this galaxy has a very high mass (i.e., the inferred stellar mass from SED fitting is $= 10^{11\pm0.3}\,\mathrm{M_\odot}$; Jarvis et al., 2020).

The observed stellar velocity-dispersion ranges from $81\pm22\,\mathrm{km\,s^{-1}}$ in the outer spiral arms to much higher values between $290-360$ km s^{-1} in the very central regions, with a median value of $326\pm27\,\mathrm{km\,s^{-1}}$ (see small inset in Figure 3.4). We discuss the interesting origin of the highest central stellar velocity-dispersion, and the remarkable spatial alignment with the radio jets in Section 3.6.

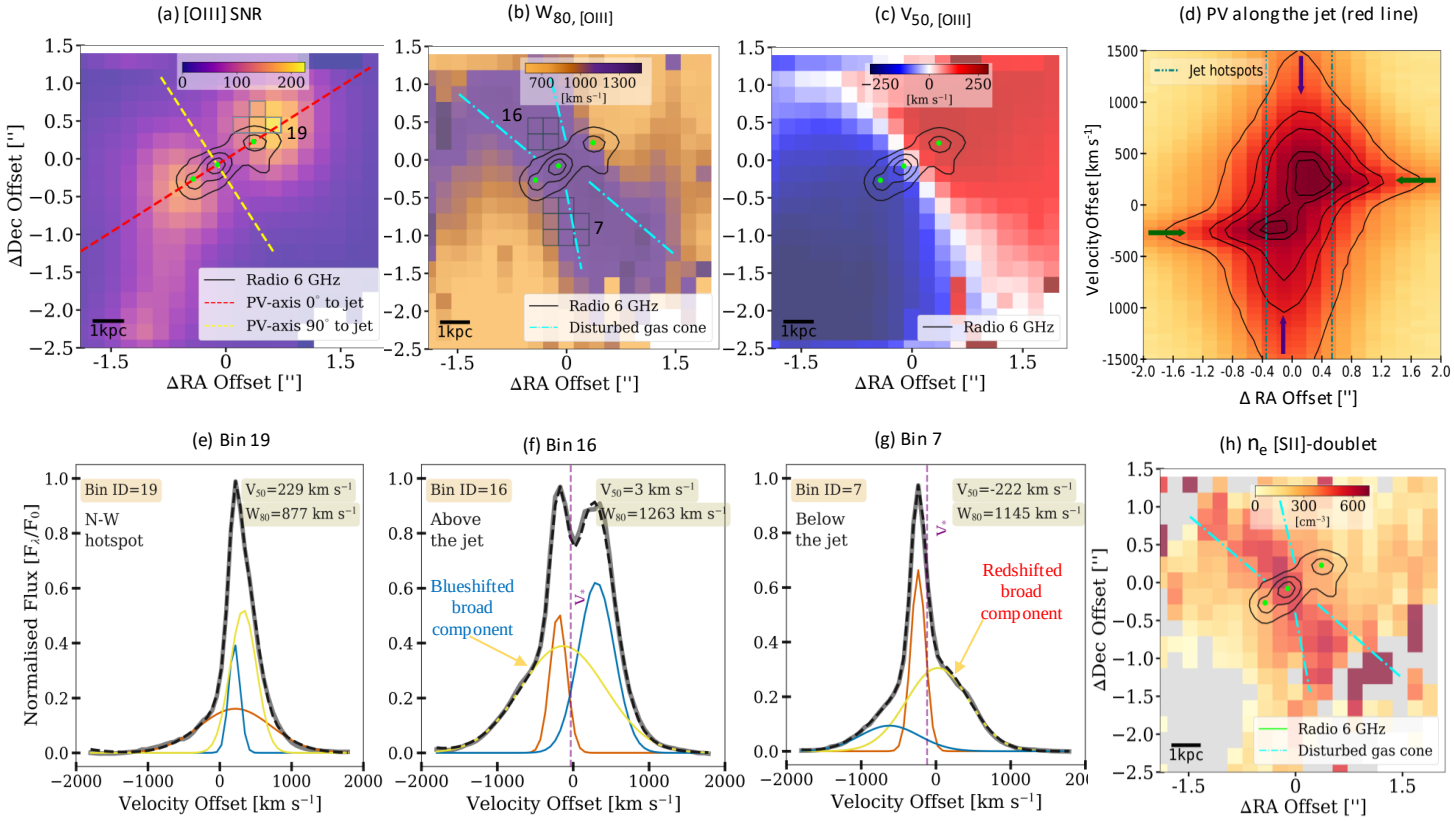

Figure 3.5: Kinematic analysis of the ionised gas in the region around the central jet, using maps of the non-parametric values of the [O III] emission-line fits and position velocity diagrams around the [O III] emission-line (see Section 3.5.3). The black contours in each map represent the 6 GHz radio emission at levels of [32,16,4] $\mathrm{RMS_{radio}}$. The three cyan dots represent the HR:A (core) and jet hot spots (HR:B and HR:C), as in Figure 3.2. A 1 kpc scale bar is shown in each of the maps. **Panel a:** Peak-SNR map; **Panel b:** W_{80} map; **Panel c:** V_{50} map; **Panel d:** PV diagram extracted along the jet axis (as shown through the dashed red axes in panel *Panel a:*), with the position-offset along x-axis and velocity-offset along y-axis, and the vertical lines indicate the locations of the radio jet hot spots; **Panel e:** the [O III] line profile from regions of highest peak-SNR values; **Panel f and Panel g:** the [O III] line profiles from regions of disturbed gas, above (Voronoi bin 16) and below (Voronoi bin 7) the jet, respectively, and **Panel h:** electron density map from [SII] doublet. The gaussian components (in *panels, e, f, and g*) are as described in Figure 3.3. In *Panel b*, the emission corresponding to an enhanced velocity-dispersion (W_{80} ≥1000 km $\mathrm{s^{-1}}$), suggests a bi-conical structure in the region perpendicular to the jets (indicated by the dash-dotted cyan lines). The PV diagram in *Panel d*, reveals enhanced velocities behind the jet hot spots, as highlighted by the purple vertical arrows. Narrow velocity components, highlighted with horizontal darkgreen arrows in *Panel d*, are observed to propagate roughly from the radio hotspots and extend for 0.8 arcsec (2.1 kpc) in each direction.

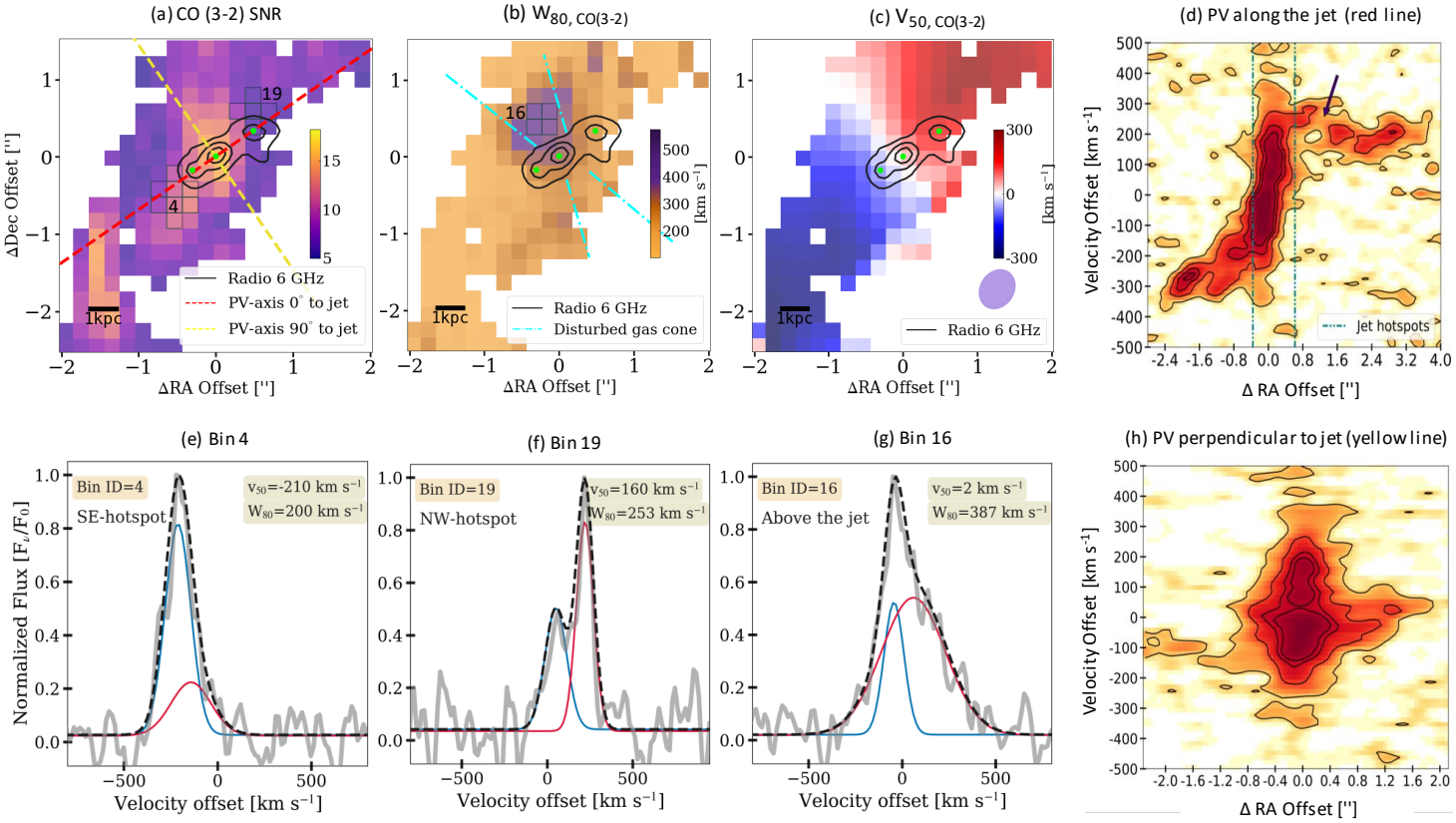

Figure 3.6: Kinematic analysis of the molecular gas in the region around the jet, using maps of the non-parametric values of the CO(3–2) emission-line fits and position velocity (PV) diagrams around the CO(3–2) emission-line (see Section 3.5.3). The black contours in each of the maps represent the 6 GHz radio emission at levels of [32,16,4] RMS_{radio}. **Panel a:** Peak-SNR map; **Panel b:** W_{80} map; **Panel c:** V_{50} map; **Panel d:** PV diagram extracted along the jet axis (see red dashed axes in *Panel a:*), with the position-offset along x-axis and velocity-offset along y-axis, and the vertical lines indicate the hot spots of the radio jets; **Panel e:** and **Panel f:** CO(3–2) line-profiles from the locations of the jet hotspots (Voronoi bin 4 and 19); **Panel g:** CO(3–2) line-profile from region of the broad disturbed gas just above the jet (Voronoi bin 16) and **Panel h:** PV diagram extracted along an axis perpendicular to the jets (see yellow dashed axis in *Panel a:*). The components in the line-fit plots are as described in Figure 3.3. *Panel b:* shows the presence of disturbed molecular gas in a localised region perpendicular to the jet (Voronoi bin 16). The PV diagram in Panel d, reveals a break in the velocity profile at the north-west jet hotspot (HR:C, highlighted with an arrow).

Ionised gas kinematics

In Figure 3.4 (second column) the kinematic structure of the bulk ionised gas velocity on large scales, i.e. $V_{50,[\mathrm{OIII}]}$, can be seen to broadly follow the stellar velocity structure. Indeed, the residuals (third column) created by subtracting the stellar kinematic values from $V_{50,[\mathrm{OIII}]}$, reveals only modest residuals in the majority of the bins outside of the central regions, with $|V_{50,[\mathrm{OIII}]} - V_\star| \leq 50\,\mathrm{km\,s^{-1}}$ in the spiral arms. We therefore infer that on large scales the [O III] emission is broadly following the gravitational motions of the host galaxy. In contrast, the residuals between $\mathrm{V}_{50,[\mathrm{OIII}]}$ and $\mathrm{V}_\star$ are much larger in the central, $\lesssim$10 kpc regions of the galaxy, reaching values of up to $-105\,\mathrm{km\,s^{-1}}$ and $+260\,\mathrm{km\,s^{-1}}$. We note that the bin at the tip of both spiral arms also shows a large velocity residual of $=139\,\mathrm{km\,s^{-1}}$ that we attribute to disturbed ionised gas extending as far as these locations (see below).

A comparison between the stellar velocity-dispersion and velocity-dispersion of the [O III] emission further confirms non-gravitational ionised gas motions (Figure 3.4). The $W_{80,[\mathrm{OIII}]}$ map reveals extreme ionised velocity widths over very large scales. With the exception of the outermost north west and south east regions, the majority of the bins have [O III] velocity widths much greater than the local stellar velocity-dispersion. Most dramatically, perpendicular to the jet axis, high velocity dispersion is seen with $\mathrm{W}_{80} >> 2.6\,\sigma_\star$ (with residuals of typically $740\,\mathrm{km\,s^{-1}}$). The velocity-dispersion in these bins ranges from 1000-1300 km $\mathrm{s^{-1}}$, and hence we identify this as the most disturbed gas with $\mathrm{W}_{80} \geq 1000\,\mathrm{km\,s^{-1}}$. This disturbed gas is seen to extend as far as the outer Voronoi bins which are located 7.5 kpc each side of the nucleus. While the disturbed gas may be extending beyond this distance, we take a conservative estimate of 7.5 kpc, obtained from the Voronoi bins defined at a SNR > 5 (as explained in Section 3.4.3). Therefore we conclude that, whilst the [O III] gas follows the large-scale rotation of the host galaxy, we see significant non-gravitational motions around the jets that is detected to a projected distance of 7.5 kpc along the minor axis of the host galaxy.

For an estimate of the outflow velocities, we obtained the maximum (terminal) velocities following Heckman et al. (2004), as $V_{\mathrm{max}} = \Delta V - FWHM_{\mathrm{broad}}/2$, where $\Delta V = V_{\mathrm{broad}} - V_\star$ (also see e.g., Rupke et al. 2005; Veilleux et al. 2005). We found these velocity estimates[4] in the terminal bins (precisely, Voronoi bin 28 and 33) to be similar to our non-parametric estimate of W_{80}[5] in the same location and hence we decided to use the W_{80} values for our estimate of the outflow velocity in Section 3.2.3 (also see e.g., Liu et al. 2013; Harrison et al. 2014). This analysis of the galaxy scale ionised gas kinematics reveals non-gravitational motions in and around the nuclear radio jets in J1316+1753, with high velocity-dispersion gas extending to a distance of 7.5 kpc each side of the nucleus. We investigate the velocity structure of the central regions in more detail in Section 3.5.3. We note that the spatially-resolved emission-line ratio diagnostic for the dominant ionising source reveals AGN to be the dominant ionising source across all galaxy bins (except in the companion galaxy), however, we defer the detailed discussions to future works.

[4] $\mathrm{V}_{\mathrm{max,Bin28}} = 480 \pm 17\,\mathrm{km\,s^{-1}}$; $\mathrm{V}_{\mathrm{max,Bin33}} = 650 \pm 10\,\mathrm{km\,s^{-1}}$

[5] $\mathrm{W}_{80,\mathrm{Bin28}} = 880 \pm 19\,\mathrm{km\,s^{-1}}$; $\mathrm{W}_{80,\mathrm{Bin33}} = 820 \pm 26\,\mathrm{km\,s^{-1}}$

Molecular gas kinematics

Using the kinematics of CO(3-2) as a tracer in Figure 3.4, we find that the molecular gas shows a similar, but less extreme, behaviour than the ionised gas. The bulk velocity of the molecular gas on large scales broadly follows that of the stellar velocity. The peak projected velocities of the CO(3–2) are similar to the peak stellar velocities and furthermore, the major kinematic axes are found to be around 140 ° for both the molecular and stellar kinematics. The $|V_{50,CO(3-2)} - V_\star|$ residuals are small (i.e., $\leq$70 km s^{-1}) in all but the central 6 Voronoi bins[6], which on average have residuals of 190 km s^{-1}. Therefore, the bulk velocity of the molecular gas is even closer to the stellar kinematics than found for the ionised gas, but still shows significant non-gravitational motion in regions around the radio jets. This is investigated further in Section 3.5.3.

Figure 3.4 shows that, similar to the ionised gas, the molecular gas has a velocity-dispersion comparable to the stellar kinematics in the outer bins, but with much higher residuals (i.e., 110 km s^{-1}) in the central bins. However, whilst the central 7 Voronoi bins[7] show the highest velocity widths of $W_{80,CO(3-2)}$ = 380-500 km s^{-1}, these are on average, a factor of 3 less than those seen in [O III] at the same location. The most distant spaxel where this disturbed molecular gas is observed (i.e., with W_{80} >380 km s^{-1}) in Figure 3.4 has a projected distance from the radio core of 2.5 kpc. Therefore, the spatial extent of the high velocity-dispersion molecular gas is seen to be approximately a third of that seen in the ionised gas, i.e. 2.5 kpc (Figure 3.4). We investigate this further by zooming into the central regions in the following subsection.

3.5.3 Kinematics on the central-scale

Following the identification of non-gravitational gas motions identified in the central region of J1316+1753, presented in the previous sub-section, we were motivated to map the ionised and molecular gas properties in more detail in this region. To do this, we mapped ionised and molecular gas kinematics across the central, 10×10 kpc region (see Section 3.2) using smaller spatial bins, and with a SNR cut of $\geq$ 3. For the central-scale maps, we performed the emission-line profile fits, in spatial regions of 0.2×0.2 arcsec, i.e., in individual spaxels for the MUSE data and in bins of 4×4 pixels for the ALMA data to have a comparable resolution as MUSE. The results are described below and are illustrated in Figure 3.5 for ionised gas and in Figure 3.6 for the molecular gas. As discussed in Section 3.4.3 we lack the sensitivity to fit the stellar continuum with finer binning; however, in Section 3.2.3 we discuss the remarkable alignment between the jets and stellar emission and kinematics in this region using the larger spatial bins.

Ionised gas around the jet

In Figure 3.5, we show maps of SNR, W_{80}, V_{50} and n_e, along with some line-profiles for the [O III] emission (see Figure caption for detail). Contours of radio emission are overlaid, showing the relative location of the radio jets. Particularly striking is the high levels of velocity-dispersion running perpendicular to the jet axis, apparent

[6] Specifically, the Voronoi bins 0, 1, 2, 13, 17, 19 (see Figure 3.9)
[7] Specifically, the Voronoi bins 0, 1, 2, 3, 13, 16, 17 (see Figure 3.9)

in the W_{80} maps shown in panel (b). The high velocity-dispersion in the ionised gas is further supported by the position-velocity (PV) diagram shown in panel (d), which was constructed by summing over a 0.6 arcsec-wide pseudo-slit, along the jet axis. It is quite clear that these central regions show a broad velocity component with maximum velocities of around $\pm 1500\,\mathrm{km\,s^{-1}}$.

Indeed, a visual inspection of the [O III] emission-line profile just north and just south of the jets (see panel (f) and (g), respectively), reveals a very broad component in these regions, with FWHM $= 980 \pm 46\,\mathrm{km\,s^{-1}}$ and $1310 \pm 18\,\mathrm{km\,s^{-1}}$, respectively. North of the jet, this component is blueshifted by $100\,\mathrm{km\,s^{-1}}$ with respect to the local stellar velocity and south of the jet this component is redshifted by $140\,\mathrm{km\,s^{-1}}$. We note that this shows the opposite red- and blue-shifts with respect to the galaxy rotation. This highest velocity-dispersion emission (with $\mathrm{W_{80}} \geq 1000\,\mathrm{km\,s^{-1}}$) starts from just behind the jet hot spots (highlighted with green dots in the W_{80} map and vertical dot-dot-dashed lines in the PV-diagram).

All of these observations suggest outflowing, high velocity-dispersion gas that originates from behind the jet hot spots and expands, in what appears to be a bi-cone structure. We trace the outer-edges of these cones by drawing straight dot-dashed lines, on the W_{80} map for spaxels along the axis perpendicular to the jet and identified with $W_{80} \geq 1000\,\mathrm{km\,s^{-1}}$ to identify the morphology of the most extreme gas kinematics (see Section 3.5.2). These cones have opening angles of $\sim 40\,^{\circ}$. To understand how this translates to the observations we made on the galaxy scales (Section 3.5.2), we overlaid them onto Figure 3.4. Re-reassuringly, this gives a consistent picture because the highest velocity-dispersion gas seen on the galaxy-scale in Figure 3.4 (i.e., out to 7.5 kpc each side of the nucleus), is located within these cones.

In panel (h) we show the electron density in the individual spaxels as estimated by using the ratio of the [S II] doublet (see Appendix 3.8 for more details and caveats). This reveals that the spaxels with the highest inferred electron density (i.e., 500-600 $\mathrm{cm^{-3}}$) are co-spatial with the cones of highest velocity-dispersion ionised gas. We verified that this behaviour continues onto the galaxy scale by creating a map with electron density for each of the Voronoi bins and present the results in Appendix 3.8.2. The spaxels outside the cones of highest velocity-dispersion regions have more modest electron densities (≤ 150 $\mathrm{cm^{-3}}$). We discuss the implications of these observations in Section 3.6.1.

Another key observation of the [O III] emission in the central regions, presented in Figure 3.5, is that the highest SNR emission is concentrated in two regions; one around each of the two radio jet hot spots. A visual inspection of the emission-line profiles demonstrates that this is due to two narrow emission-line components that are particularly strong in each of these locations. These narrow emission-line components, which can be seen in the emission-line profiles shown in panel (e) and panel (g) of Figure 3.5, are separated in velocity by $441 \pm 14\,\mathrm{km\,s^{-1}}$. Indeed, the V_{50} map, shown in panel (c) of Figure 3.5, highlights this further; we observe a strong velocity gradient *directly* along the jet axis. We note that this is offset by $20\,^{\circ}$ from the galaxy kinematic axis and we have already shown that the gas in these regions is not dominated by gravitational motions (Section 3.5.2). The PV diagram in panel (d) of Figure 3.5 shows that these two strong narrow emission-line components, which are highlighted with horizontal arrows on the panel, are emanating with velocities of

$+206 \pm 15\,\mathrm{km\,s^{-1}}$ and $-235 \pm 1.3\,\mathrm{km\,s^{-1}}$ from the location of the two jet hot spots. These jet hot spot locations are highlighted with vertical lines in the panel. We discuss these ionised gas velocity components in the context of jet-ISM interactions in Section 3.6.1.

Molecular gas around the jet

In Figure 3.6, we present a similar set of figures for the CO(3–2) emission in the vicinity of the radio jets, as we did for the [O III] emission in Figure 3.5, namely, maps of SNR, W_{80}, and V_{50}, along with some line-profiles for the CO(3–2) emission (see Figure caption for detail). We observe the presence of molecular gas with high velocity-dispersion perpendicular to the jet axis (Figure 3.6; panel (b)). A visual inspection of the emission-line profile of this region (see panel (g)), shows that there is a broad CO(3–2) emission-line component (FWHM of $404 \pm 10\,\mathrm{km\,s^{-1}}$) responsible for the high W_{80} values seen in this location. Furthermore, Panel (h) shows a PV diagram extracted along a 0.6 arcsec slit perpendicular to the jet axis, which further confirms a region of high velocity-dispersion along this axis.

The disturbed molecular gas is located within the same cone identified in the ionised gas phase (see dot-dashed lines on panel (b) of Figure 3.5), but, this time, only in the northern side of the jet. Furthermore, the disturbance appears to be less extreme. Specifically, the FWHM of the broad [O III] emission-line component in the same region is 3× higher than that observed in CO(3-2) at the same location. Additionally, the disturbed molecular gas is seen to extend to 2.5 kpc, which is only a third the extension of the disturbed ionised gas.

In the PV diagram of CO(3–2), created using a 0.6 arcsec pseudo-slit running along the jet axis (panel (d) in Figure 3.6), we observe a small velocity jump of around $100\,\mathrm{km\,s^{-1}}$ at the location of the northern radio hot spot (highlighted with an arrow in the Figure). Further evidence for irregular kinematics in this region comes from a visual inspection of the emission-line profile (see panel (f) in Figure 3.6) which shows that the profile is split into two components separated by $169 \pm 9\,\mathrm{km\,s^{-1}}$. Finally, there is some evidence for a deficit of CO(3–2) emission close to the northern hot spot of the jet, as indicated by a black arrow in the figure. From the PV-diagram, we estimate the SNR of the CO flux to be 11-14 times higher before and after this cavity and about 90 % less flux is seen in the cavity as compared to the surroundings. These observations coupled with the strong narrow emission-line components seen in the ionised gas profile, serve as evidence of possible jet-ISM interactions happening in this region.

3.6 Discussion

We have presented new MUSE and ALMA data for a type-2, $z = 0.15$ quasar, J1316+1753, selected from the Quasar Feedback Survey (Figure 3.1). Based on the previous radio data, this source contains low-power ($P_{\mathrm{jet}} = 10^{44}\,\mathrm{erg\,s^{-1}}$) ∼1 kpc radio jets. These jets are confined within the galaxy disc and inclined at $\lesssim 5^\circ$ with respect to the plane of the galaxy disc, with the south-east jet (HR:B) as the approaching side (see Section 3.3.2 and Figure 3.2). We summarise our key observations on the stellar, warm ionised gas and cold molecular gas kinematics with a schematic representation

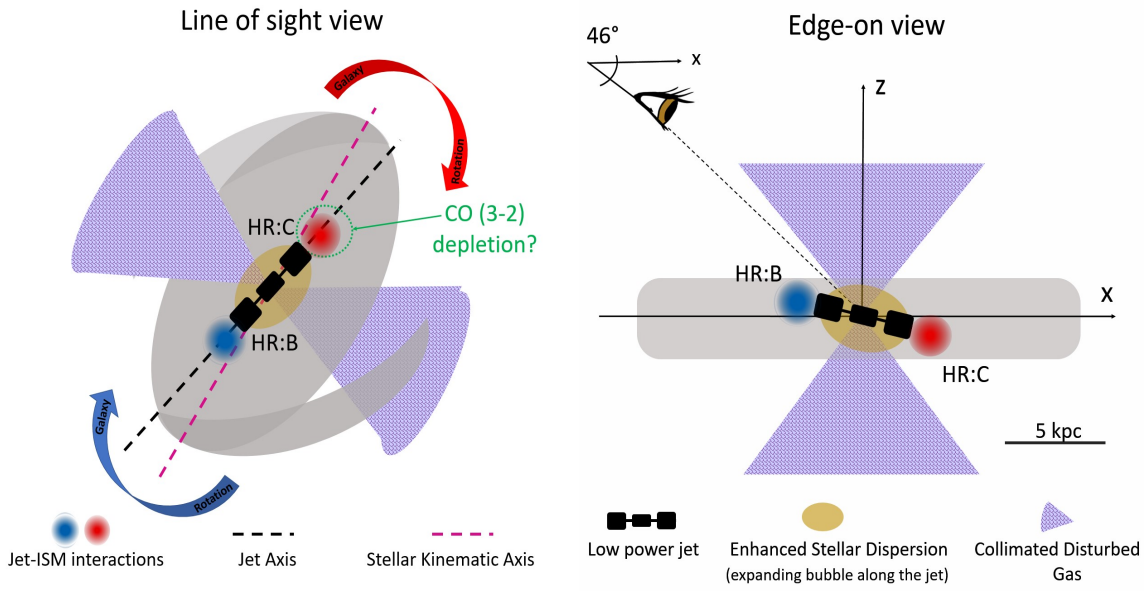

Figure 3.7: A schematic view of the galaxy J1316+1753 to highlight the key observations identified in this work. *Left:* The line-of-sight view (where North is up and East is to the left); *Right:* Our inferred edge-on view. A legend shows the different symbols used to represent the main features of interest and an approximate scale bar is shown in the right panel at the bottom. A detailed description of the features in this schematic is presented in Section 3.6.1.

in Figure 3.7. This is presented both from the line-of-sight point of view (*left-panel*) and an edge-on view (*right-panel*). Below, we discuss the observational features that appear to be tracing the interaction of the jets with the host galaxy's ISM (Section 3.6.1), before discussing the possible evidence for feedback effects on the host galaxy (Section 3.6.2) and then discussing the results in the context of the overall AGN population (Section 3.6.3).

3.6.1 Turbulent outflows and jet-ISM interactions

Here we describe how our observations are consistent with the low power jets, which are highly inclined into the galaxy disk, are interacting with the ISM and driving large scale turbulent outflows.

We see evidence for jet-ISM interactions on the multi-phase gas at the jet termini (highlighted with blue/red regions in Figure 3.7). Strong velocity enhancements in the warm ionised gas are seen, with two high velocity offset ionised gas components, separated by $441\,\mathrm{km\,s^{-1}}$, that are brightest in the regions of the jet termini and appear to propagate away along the jet axis (Figure 3.5). In the molecular gas phase, a $-100\,\mathrm{km\,s^{-1}}$ change in the molecular gas velocity is observed just beyond the HR:C radio hot spot (Figure 3.6). This is consistent with previous work that has found velocity jumps in multiple phases of gas at the locations of jet termini (e.g., Morganti et al. 2013; Riffel et al. 2014; Tadhunter et al. 2014; Morganti et al. 2015; Ramos Almeida et al. 2017; Finlez et al. 2018; Jarvis et al. 2019; Husemann et al. 2019; Ruffa et al. 2019; Santoro et al. 2020; Morganti et al. 2021). Furthermore, our results confirm that the strongly double peaked [O III] emission-line profile, seen in the SDSS spectrum of J1316+1753, is not the result of the presence of a dual AGN despite it being such a candidate (Xu & Komossa 2009; Smith et al.

2010; Lyu & Liu 2016; Baron & Poznanski 2017). Indeed, studies have also shown that double-peaked emission-lines could mostly be an indication of the existence of (jet-driven) galaxy-wide outflows (see Rosario et al. 2010; Kharb et al. 2015; Nevin et al. 2018; Kharb et al. 2019, 2021; Ramos Almeida et al. 2021).

We also observe tentative evidence for depleted CO (3–2) emitting gas at the location of the brightest jets (see Figure 3.6). We indicate this with a green-dashed circle in the schematic in Figure 3.7 (also see top-right panel, Figure 3.6). This is the same region where we see a bright warm ionised gas component in the [OIII] (Figure 3.5). Possible explanations for this include molecular gas removal or an interaction between the radio jets and the ISM that suppresses CO emission (e.g., through excitation or dissociation) while boosting the emission of the warm ionised gas (e.g., Rosario et al. 2019; Shimizu et al. 2019). Obtaining more molecular gas tracers, such as multiple CO lines and rotational and vibrational H_2 lines would help to verify this observation and differentiate between these scenarios (e.g., Rigopoulou et al. 2002; Dasyra et al. 2016).

Further evidence for an impact of the jets on the host galaxy ISM comes from the very high velocity-dispersion ionised gas ($W_{80} \geq 1000\,\mathrm{km\,s^{-1}}$; i.e., $\sigma \sim 400\,\mathrm{km\,s^{-1}}$) originating from just behind the jet hot spots, and outflowing in an apparent bi-cone, in a perpendicular direction as far as project distance of 7.5 kpc (see Figure 3.4 and Figure 3.5). The regions of this high velocity-dispersion ionised gas are highlighted as the purple hatched regions in the schematic diagram in Figure 3.7. This disturbed gas can be seen to be moving along the galaxy minor axis and due to the orientation of the galaxy is seen to be moving towards us (and hence blue-shifted) above the galaxy plane and moving away from us (and hence red-shifted) below the galaxy plane. We also observe that this turbulent gas has a three times higher electron density than the rest of the galaxy disk (see Figure 3.5). Such high electron densities within outflowing components have also been seen in previous studies (e.g, Villar Martín et al., 2014; Perna et al., 2017; Mingozzi et al., 2019; Davies et al., 2020; Fluetsch et al., 2021). A possible explanation for this could be due to the compression of the gas expelled in the outflow (e.g., Bourne et al., 2015; Decataldo et al., 2019).

In the molecular phase, we also see enhanced velocity-dispersion in the same direction as the turbulent ionised gas, but only in the regions north of the jet (not indicated in Figure 3.7 for simplicity) and extends to about a distance of 2.5 kpc. A possible explanation for the less extreme kinematics observed in CO, compared to [O III], could be that the low velocity gas has cooled more efficiently, as the higher velocity gas has a higher post-shock temperature (e.g. Costa et al. 2015). The densest material in the ISM will also naturally be driven to lower velocities, which would also result in a smaller spatial extent of the turbulent/outflowing cold molecular gas compared to the less-dense warm ionised gas (see Nayakshin & Zubovas 2012; Mukherjee et al. 2016, 2018a). Furthermore, it is interesting to see the asymmetry (i.e., unipolar nature) of the CO(3–2) cones. One of the possible reasons could be that the galaxy disk maybe optically thicker to the CO(3–2) emission, thus hiding the other side of the turbulence, or the molecular gas could itself be intrinsically asymmetric as predicted by simulations at higher redshifts (Gabor & Bournaud 2014) and observations at lower redshifts (Lutz et al. 2020).

Our results are in qualitative agreement with recent hydro-dynamical simulations showing that when a radio jet propagates through an inhomogenous medium, its impact can go beyond the radio-jet axis. This happens because as the jets progress, they launch outflows close to them which disturb the local velocity flows and kinematics. However, they also inflate a spherical bubble of jet plasma that can lift the multi-phase gas and cause turbulence, which would naturally be collimated along the minor axis of the host galaxy disk (Sutherland & Bicknell 2007; Wagner & Bicknell 2011; Wagner et al. 2012; Mukherjee et al. 2016, 2018a; Talbot et al. 2021). This would mean the disturbed gas would be extended beyond the radio emission (also see Zovaro et al. 2019). Mukherjee et al. (2018a,b) further predict a stronger impact on the host-galaxy's ISM when low power jets are inclined into the plane of the galaxy disk and have only moderate power, which matches the characteristics of the jets in J1316+1753. Within these simulations, as the jets flood through the inter-cloud galaxy disk, they cross and interact more with the inter-stellar medium due to their lower inclination. We thus attribute the turbulent, high velocity-dispersion gas being vented out perpendicular to the galaxy disk in J1316+1753 to be originating as a consequence of the jets propagating through the ISM. Our observations are less consistent with a model where a quasar-driven shocked wind propagates through the ISM and causes both the radio emission and the turbulence (e.g., Hwang et al. 2018).

3.6.2 Feedback effects on the host galaxy

While the effect of radio jets is well studied and established at the scales of galaxy halos, particularly for massive early-type galaxies and in cluster environments (McNamara & Nulsen 2012, hardcastle20), it is less clear to what extent galaxies can be directly affected by low power jets confined within the ISM. Recent simulations show that, while on one hand density enhancements near the jet axis can make gravitational collapse of clouds more probable, thereby *supporting* star-formation; an overall increase in turbulent kinetic energy may also *lower* the star-formation rate (Mandal et al. 2021). From an observational perspective, studies have shown how jets could potentially suppress or regulate the star-formation in the host galaxy by introducing turbulence in the ISM or causing multi-phase outflows (e.g., Nesvadba et al. 2010, 2011; Alatalo et al. 2015). On the contrary, studies have also shown a jet-induced positive feedback being driven by the shocks from the jets causing the gas to compress and thus inducing star-formation (e.g., Bicknell et al. 2000; Salomé et al. 2015; Lacy et al. 2017). Hence, a jet may cause both a positive and a negative feedback on its host galaxy. Since we observe significant jet-ISM interactions and outflowing material in our observations we now investigate the possible feedback effects arising from these on the host galaxy.

Impact of the jets on the molecular star-forming gas

To understand the impact of the jets in J1316+1753, we first quantify how much energy has been available from the jets over the lifetime of the observed outflows, using order-of-magnitude estimates. We assume a single jet episode, since we lack any evidence of multiple jet episodes. Under the assumption that the turbulent outflowing ionised gas is launched by the jet, we use it's kinematics to estimate the lifetime. The outflow velocity in the ionised gas is estimated to be $V_{\rm out} = 800\,{\rm km\,s^{-1}}$,

at a distance of $R_{\rm out} = 7.5\,$kpc (see Section 3.5.2).[8] If we then estimate the outflow lifetime as:

$$t_{\rm out} \approx R_{\rm out}/v_{\rm out}, \tag{3.4}$$

we obtain $t_{\rm out}$ ∼9 Myr. Using the value of the jet power ($P_{\rm jet} = 10^{44}\,{\rm erg\,s^{-1}}$) estimated in Section 3.3, we estimate the total energy from the jet over this period as:

$$E_{\rm jet} = P_{\rm jet} \times t_{\rm out} \sim 3 \times 10^{58}\,{\rm erg}. \tag{3.5}$$

Next, we estimate the kinetic energy, $E_{\rm mol,gas}$ in the molecular gas phase (traced via CO) of the galaxy disk following Nesvadba et al. 2010, i.e., using the relationship between molecular gas mass, $M_{\rm mol,gas}$ and velocity-dispersion:

$$E_{\rm mol,gas} = 0.5 \times M_{\rm mol,gas} \times \sigma^2_{\rm mol,gas}. \tag{3.6}$$

We focus on the molecular gas phase since the molecular gas reservoirs play a determining role in the AGN-galaxy co-evolution, as it is this gas that is redistributed to promote the star-formation in the galaxy and also for fuelling the black-hole growth in the AGN (Carilli & Walter 2013; Vito et al. 2014). To determine the molecular gas mass, we first convert our measured CO fluxes into a CO (3–2) emission-line luminosity ($L'_{\rm CO(3-2)}$ [K km s^{-1} pc^{-2}]), following Solomon et al. 1997 and then into $L'_{\rm CO(1-0)}$, by adopting two different values for the line brightness temperature ratio, $r_{31} = 0.5$ and r_{31}=1 (following Weiss et al. 2007; Riechers et al. 2011; Bolatto et al. 2013; Sargent et al. 2014). The former value is more consistent with quiescent star-forming gas, while the latter is for disturbed gas affected by the AGN. Finally, the molecular mass was estimated by using two values of the H_2-to-CO conversion factor of $\alpha_{\rm CO} \approx 4\ {\rm M_\odot/(K\ km\ s^{-1}\ pc^{-2})}$ and $\alpha_{\rm CO} \approx 0.89\ {\rm M_\odot/(K\ km\ s^{-1}\ pc^{-2})}$. The choice of the former $\alpha_{\rm CO}$ is justified in Jarvis et al. (2020) and is consistent with that found in the Milky Way and assumed for quiescient gas. The latter choice is for typical high-redshift, high star-forming, quasar host galaxies, following (Solomon et al. 1987; Solomon & Vanden Bout 2005; Carilli & Walter 2013; Bolatto et al. 2013). Although uncertain, these conversion factor choices are sufficient for our order-of-magnitude estimates (see further discussion in Jarvis et al. 2020). If we focus on the pixels inside the 2.5 kpc region showing the disturbed outflowing molecular gas (i.e., pixels with $W_{80} \geq 400\,{\rm km\,s^{-1}}$, shown in Figure 3.6), the range of molecular mass in the broad component was estimated to be $\sim 3.1 \times 10^7\,{\rm M_\odot} - 2.8 \times 10^8\,{\rm M_\odot}$ (using the different conversion factors). Hence, this broad component is seen to consist ∼1 % of the total CO(3–2) flux. Furthermore, using the measured velocity, $\sigma_{\rm mol,gas} = 230\,{\rm km\,s^{-1}}$, the total kinetic energy was estimated to be $E_{\rm mol,gas} \sim 1.6 \times 10^{55}\,{\rm erg} - 1.4 \times 10^{56}\,{\rm erg}$.

Hence, with a jet power higher by two orders of magnitude than the molecular kinetic energy, the jets are sufficient to drive the observed outflow. However, comparing the outflowing molecular gas mass to the total molecular mass in the galaxy, which is estimated as $\sim 10^{10}\,{\rm M_\odot}$ (see Jarvis et al. 2020), we conclude that only a very small fraction of the total molecular gas mass is residing in this turbulent, outflowing material. This suggests little in-situ disruption to the overall molecular gas disk (also see Ramos Almeida et al. 2021).

[8] We note that if we use the properties of the CO gas instead of the [O III] we would obtain an estimated lifetime of $t_{\rm out} \sim 6\,$Myr, which is sufficiently close to that derived from [O III] for our order-of-magnitude estimates

We further explore the possible fate of the molecular gas by comparing this energy to the galaxy binding energy. We used the stellar mass estimate of $M_\star = 10^{11}\,M_\odot$ from Jarvis et al. 2019 and the stellar velocity-dispersion of $\sim 300\,\mathrm{km\,s^{-1}}$ (computed as an average value for the central bins in Figure 3.4). Hence, the binding energy of the galaxy is estimated as[9],

$$E_\star = M_\star \times \sigma_\star^2 \approx 10^{59}\,\mathrm{erg}. \tag{3.7}$$

Comparing the jet power with the binding energy of the galaxy, we thus conclude that the current jet episode will be limited in its ability to completely unbind the molecular gas from the host galaxy. However, negative AGN feedback may still manifest in several forms (see Federrath & Klessen 2012; Costa et al. 2020; Mandal et al. 2021), for example: (i) by quickly ejecting the dense gas from only the nuclear regions, as soon as the AGN outburst begins; (ii) by gradually suppressing the halo gas accretion onto the host galaxy; (iii) by inducing turbulence that provide additional support against the collapse, thereby strongly suppressing star-formation. Indeed, recent jet-ISM simulations do not predict a complete unbinding of host galaxy star-forming material, but rather a suppression of star-formation at the global galaxy scales by a factor of a few due to the ablation and fragmentation of the clouds (Mukherjee et al. 2018b; Mandal et al. 2021).

Evidence for feedback from stellar kinematics

We now focus on the possible signatures of feedback on the stellar properties of J1316+1753. We can clearly see a bright elongated bulge-like structure in the stellar continuum emission (Figure 3.2, left-panel). Following Section 3.4.2, we fitted a two-dimensional gaussian to the surface brightness profile of this bulge-shape, and estimated a position angle of 130 °, which is remarkably close to the position angle of the jet axis, at 120 ° (red dashed line in Figure 3.5 and 3.6). In addition, the regions with highest stellar dispersion (i.e., ∼290–360 $\mathrm{km\,s^{-1}}$) follow, almost exactly, the jet axis (see the left-bottom panel of Figure 3.4 and the galaxy schematic Figure 3.7). We discuss two possible explanations of these observations.

We have seen clear signatures of jet-ISM interactions. A compression of the ISM gas caused by the jets could therefore trigger episodes of star-formation, i.e. positive feedback. Stars formed during feedback will initially have motions which are significantly perturbed from regular circular stellar kinematics, and hence they may contribute to increasing the stellar velocity-dispersion and could alter the stellar structure of the host galaxy. This could be due to either directly induced positive feedback by jets or outflows, or because of stars that have formed in outflowing/turbulent material (see Ishibashi et al. 2013; Zubovas et al. 2013; Dugan et al. 2014; Maiolino et al. 2017; Gallagher et al. 2019). This may explain the increased velocity disperion along the jet axis from our observations. Furthermore, at the jet termini, we can see gas velocities of -235 ± 1.3 and 206 ± 15 $\mathrm{km\,s^{-1}}$, which entails to the jets pushing the gas with this velocity (the velocities seen in the two regions of enhanced [O III] SNR, or regions of jet-ISM interactions in Figure 3.5). Interestingly, this roughly matches the higher stellar velocity-dispersion seen in these regions (-268 ± 18 and

[9] We note that if we estimate the binding energy following the universal relationship between stellar mass and binding energy presented in Shi et al. (2021) we obtain the same order-of-magnitude result.

$240 \pm 14\,\mathrm{km\,s^{-1}}$, see Figure 3.4). Detailed analyses of the stellar populations found in the different stellar kinematic components would be required to further test this scenario.

Another possible reason for this high stellar dispersion could be due to the sudden removal of gas in the very central regions, thereby causing a decrease in the local gravitational potential that may lead to ballistic orbits of central stars (see van der Vlugt & Costa 2019), thereby causing an apparent increase in the stellar velocity-dispersion. However, it is not immediately clear why this would cause enhanced stellar velocity-dispersion along the jet axis and detailed dynamical modelling (accounting for the relative mass in stars, dark matter and gas) would be required to test this scenario further.

3.6.3 Implications of our results for 'radio-quiet' AGN feedback

Jet-ISM interaction similar to the one reported here have been identified in several other radio-quiet AGN host galaxies. We compare our source to a list of 13 targets, compiled by Venturi et al. (2021a), which show a similar observation of high velocity-dispersion gas in the perpendicular direction (Section 3.6.1). In Figure 3.8, we demonstrate this comparison of J1316+1753 in the $L_{\rm bol}$ - $P_{\rm jet}$ plane. We derived the $P_{\rm jet}$ from the 5 GHz radio luminosities[10] in literature, following Equation 3.1. This approach is sufficient for our order-of-magnitude investigation of the parameter space in Figure 3.8. We used the $L_{\rm Bol}/L_{\rm [OIII]} = 3500$ ratio following Heckman et al. (2004) to obtain the $L_{\rm Bol}$ values from the $L_{\rm [OIII]}$ values in literature[11].

It can be clearly seen that the target we study here has a higher bolometric luminosity than those typically identified to have these type of jet-ISM interactions. Although J1316+1753 is at the upper end of jet powers, with $\mathrm{P_{jet}}{=}10^{44}\,\mathrm{erg\,s^{-1}}$ compared to the comparison sample in Figure 3.8 (which reach $\mathrm{P_{jet}}{<}10^{44}\,\mathrm{erg\,s^{-1}}$), our target still lies in the radio-quiet regime. However, in contrast to the other sources, this target is a quasar, with $L_{\rm [OIII]} \geq 10^{42.1}\,\mathrm{erg\,s^{-1}}$ (shown as dashed vertical line in the figure). Therefore, we would like to stress that for quasars and in general if $L_{\rm Bol} >> P_{\rm jet}$, jets could still be present as strong sources of feedback and hence should not be ignored (also see Villar-Martín et al. 2017). Indeed with the increasing availability of deep, high resolution imaging, an increasing number of systems are also showing the presence of jets (e.g., Jarvis et al. 2019; Pierce et al. 2020; Villar Martín et al. 2021).

In summary, we have shown that for J1316+1753, low power jets are the dominant mechanism for the central AGN to have an impact on the host galaxy's ISM, even when the system is bolometrically powerful. Interestingly, by comparing the hydrodynamical simulations of individual galaxies that invoke a jet (Mukherjee et al. 2018b; Mandal et al. 2021) with those that invoke a quasar-wind (Costa et al. 2014,

[10] For three of the sources where 5 GHz values were not available, we used 1.4 GHz values and converted them using a simple power law and an average spectral index $\alpha = -0.7$ to calculate 5 GHz luminosities. References used for radio luminosities: Jarvis et al. 2019; Griffith et al. 1994; Gallimore et al. 2006; Bicay et al. 1995; Griffith et al. 1995; Disney & Wall 1977; Whiteoak 1970; Wright & Otrupcek 1990

[11] We note that since we could not obtain the $L_{\rm [OIII]}$ values for two of the sources, they are excluded from Figure 3.8. This does not affect our results since the two excluded sources have X-ray flux emission that might be rather associated to X-ray binaries than with accretion on a SMBH. References used for $L_{\rm [OIII]}$: Jarvis et al. 2019; Muñoz Marín et al. 2007; Schmitt et al. 2003; Whittle 1992.

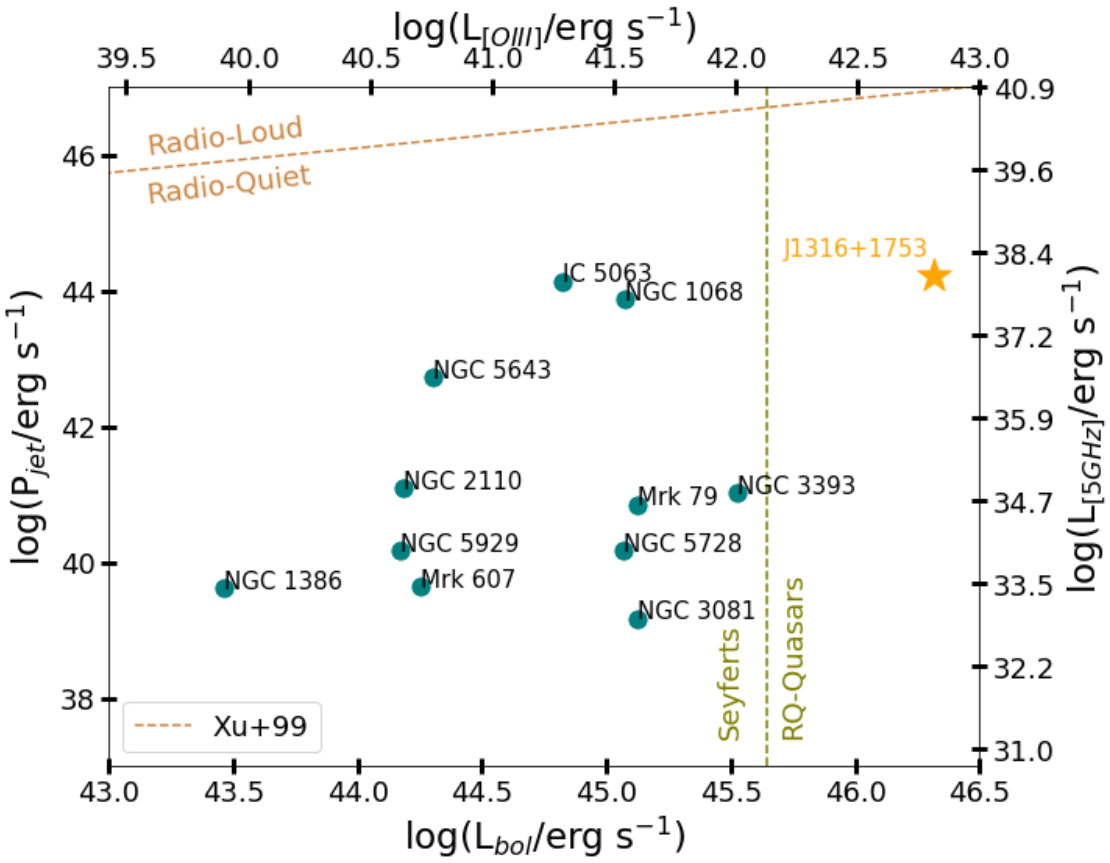

Figure 3.8: A comparison of jet power ($P_{\rm jet}$; scaled directly from 5 GHz radio luminosity) versus $L_{\rm Bol}$ for radio-quiet AGN-host galaxies from literature, which show high velocity-dispersion gas, perpendicular to radio jets (see Section 3.6.3). Although this effect has been seen numerous times in the Seyfert-luminosity regime, J1316+1753 target clearly lies in the quasar regime as identified using our definition ($L_{\rm [OIII]} \geq 10^{42.1}$ erg s^{-1}, dashed line). The dashed orange line traces the division between 'radio-quiet' and 'radio-loud' AGN from Xu et al. 1999.

2020), suggests that both mechanisms may have a very similar impact on the host galaxy (also see Faucher-Giguère & Quataert 2012; Talbot et al. 2021); specifically, both localised enhanced star-formation (due to compression of gas) and more global, gradual suppression of star-formation. Understanding which of these modes dominate for quasar host galaxies, and how representative J1316+1753 is across the quasar population, will require further studies combining high quality radio imaging with spatially-resolved measurements of the multiphase gas. We plan such a study across the wider QFeedS sample, where it will become possible to investigate trends with jet power and jet inclination angle, which are two crucial parameters according to simulations (Mukherjee et al. 2018b). Further careful studies of the role of *low power jets* for AGN feedback is important because lower power jets are very common, compared to their more powerful counterparts, in high mass galaxies (including quasars) even if it is harder to decouple their radio emission from that produced by star-formation (Gürkan et al. 2019; Sabater et al. 2019; Macfarlane et al. 2021).

3.7 Conclusions

We present MUSE and ALMA data of J1316+1753, a luminous $z = 0.15$, type-2 quasar selected from the Quasar Feedback Survey (Jarvis et al., 2021). This target represents one of the most [O III] luminous sources from the survey ($L_{[\mathrm{OIII}]}$=$10^{42.8}\,\mathrm{erg\,s^{-1}}$) and exhibits a broad [O III] emission-line profile (FWHM$\sim$1300 $\mathrm{km\,s^{-1}}$; Figure 3.1; Figure 3.3). Radio imaging of this source reveals low-power radio jets ($P_{\mathrm{jet}} \sim 10^{44}\,\mathrm{erg\,s^{-1}}$) that are compact, reaching only 1 kpc in projected distance from the core. Furthermore, the jets are inclined into the plane of the host galaxy disk (see Section 3.3 and Figure 3.2).

Our data enables us to map the stellar kinematics (traced with stellar absorption features), warm ionised gas properties (traced with optical emission-lines) and the cold molecular gas properties (traced with the CO(3–2) emission-line; see Figure 3.3). On galaxy scales, both the molecular gas and ionised gas broadly follow the stellar gravitational motions (Figure 3.4). However, across the central few kiloparsecs, both gas phases reveal high velocity non-gravitational motions and we observe evidence of jet-induced feedback. Specifically:

1. **Jet-ISM interactions**
   We observe two bright and high velocity offset ionised gas components (separated by 441 $\mathrm{km\,s^{-1}}$) concentrated at the positions of the jet hot spots and that appear to propagate away from the jets, along the jet axis (see Figure 3.5). Furthermore, a $-100\,\mathrm{km\,s^{-1}}$ change in the molecular gas velocity is observed just beyond the brighter radio hot spot, with tentative evidence for depleted CO (3–2) emitting gas at the same location (see Figure 3.6).

2. **Multi-phase turbulent gas, driven perpendicular to the galaxy**
   Ionised gas with very high velocity-dispersion (i.e., $W_{80} = 1000 - 1300\,\mathrm{km\,s^{-1}}$) is seen to propagate outwards in a bi-cone from just behind the radio hot spots, travelling perpendicular to the galaxy disk and seen in projection as extending to at least 7.5 kpc from the nucleus (see Figure 3.4 and 3.5). The highest inferred electron densities of the ionised gas are found within these bi-cones (as inferred from the [S II] doublet; Figure 3.5). This turbulent gas is also seen in the molecular gas phase. However, it is 3 times less extended (and only in one direction) with 3 times lower velocity-dispersion (i.e., $\mathrm{W_{80}} \sim 400\,\mathrm{km\,s^{-1}}$) compared to ionised gas phase (see Figure 3.4 and 3.6).

3. **Strong spatial connection between the jets and stellar properties**
   We see a close alignment of the position angle of the stellar bulge with the radio-jet axis ($< 5°$; see Figure 3.2, left-panel). Furthermore, the regions with the highest stellar velocity-dispersion (i.e., $\sigma_\star$ are seen to be lagging behind the jets, following the jet axis (see Figure 3.4, bottom-left panel).

Our observations provide strong evidence for low power radio jets, inclined into the galaxy disk, having a direct impact on the multi-phase ISM inside the host galaxy of this type-2 quasar. Our observations are qualitatively consistent with the simultaneous positive and negative feedback effects observed in hydrodynamics

simulations of jet-ISM interactions (Mukherjee et al., 2018a,b; Talbot et al., 2021; Mandal et al., 2021). Specifically: (1) as the inclined, lower power jets move through the galaxy, they strongly interact with the ISM; (2) highly turbulent material is stripped and escapes above and below the galaxy disk, removing gas from the host galaxy and; (3) as the jets propagate, they compress the gas in the disk also causing new stars to form in these regions, contributing to the formation of the stellar bulge (see Section 3.2.3). Although we only have indirect evidence, this final factor may be the cause of the high velocity-dispersion stars located behind the jets we have observed.

Interestingly, the same qualitative behaviour of outflows and positive feedback in the inner few kiloparsecs of galaxies is predicted by simulations invoking quasar-driven disk winds (Costa et al. 2020). Whilst jets have been seen to be dominant in lower power AGN (See Figure 3.8 and Section 3.6.3), our observations reveal that jets can be the dominant feedback mechanism, even for this bolometrically luminous source, i.e., for an AGN currently in a 'quasar mode'. To understand the relative role and impact of jets and winds in all quasars requires a similar multi-wavelength study of the wider population.

3.8 Appendix to the Chapter

3.8.1 Voronoi Binning Map

In Figure 3.9, we show a map with the spatial distribution and numbering system of the Voronoi bins, produced from the Voronoi tesselation routine, as explained in Section 3.4.3.

3.8.2 Electron Densities

We estimated the spatial variations in electron density by using the ratio of the [S II]$\lambda\lambda$6716,6731 emission-line doublet, assuming a temperature of $T_e = 10^4$ K (Osterbrock & Ferland 2006). As described in Section 3.4.4, we fit the [S II] doublet with Gaussian components: three components for each line, as shown in the left-panel in Figure 3.10 for two example bins. We note that the [S II] emission line fits were fit independently for their flux, velocity and linewidths, without any influence of the [O III] parameters obtained in Section 3.4.4. The right-panel of Figure 3.10 shows a map of the estimated electron density values on the galaxy-scale using the Voronoi bins that were defined on the stellar continuum in Section 3.4.3. We further perform this analysis on the central-scale using individual MUSE spaxels, the results of which are shown in the bottom-right panel of Figure 3.5. We note that the [S II] doublet is only sensitive to electron densities in the range $50 \lesssim n_e \lesssim 5000\,\mathrm{cm}^{-3}$ (Osterbrock & Ferland 2006). Therefore beyond this range, we indicate the electron densities are unconstrained in these regions through grey pixels in Figure 3.5 and we discuss this limitation further below.

Interestingly, both the central-scale (10 kpc) and the galaxy-scale analyses (26 kpc) reveals that higher electron densities (i.e., ∼500–600cm^{-3}) are observed perpendicular to the radio jets. Furthermore, the regions of the highest inferred electron densities are remarkably co-spatial with the most disturbed ionised gas (see Section

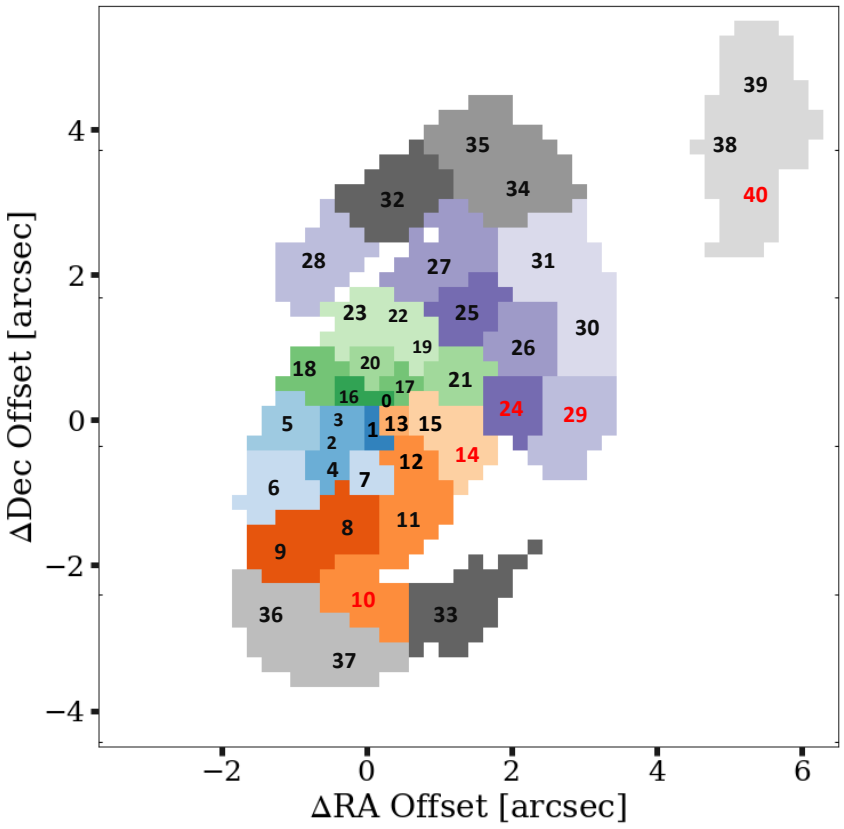

Figure 3.9: A map of the 41 Voronoi Bins obtained using a SNR of 5, as described in the Section 3.4.3. The same Voronoi mapping is used for the analysis of the MUSE and ALMA data at the galaxy-scale, as summarised in Section 3.5.2 and 3.5.2, respectively. Five of the bins (no. 10, 14, 24, 29, 40) that were excluded from the analysis of the molecular gas due to low SNR are labeled in red. Also, it can be seen here that the bins 38, 39, 40 correspond to the companion galaxy while the rest belong to the main galaxy as labeled in Figure 3.2.

3.5.3), whilst the spaxels outside of this cone exhibit more modest electron densities (i.e., ~ 150 cm^{-3}). This has also been observed by other studies (e.g.; see Fluetsch et al. 2021; Davies et al. 2020; Mingozzi et al. 2019). However, we urge caution in interpreting the absolute values of the electron densities inferred using this approach. For example, the [S II] doublet is limited in its diagnostic power for tracing electron densities and may give results that are about 1-2 orders lower in magnitude than the electron densities derived using trans-auroral [O II] and [S II] lines (for details, see Harrison et al. 2018a). A recent study by Davies et al. 2020 also found significantly lower electron densities using this method as compared to the auroral and trans-auroral lines (also see, Rose et al. 2018; Harrison et al. 2018a; Shimizu et al. 2019; Baron & Netzer 2019).

Supplementary Plots for each Voronoi Bin of the galaxy can be found at the end of the thesis under the supplementary plots chapter 7.

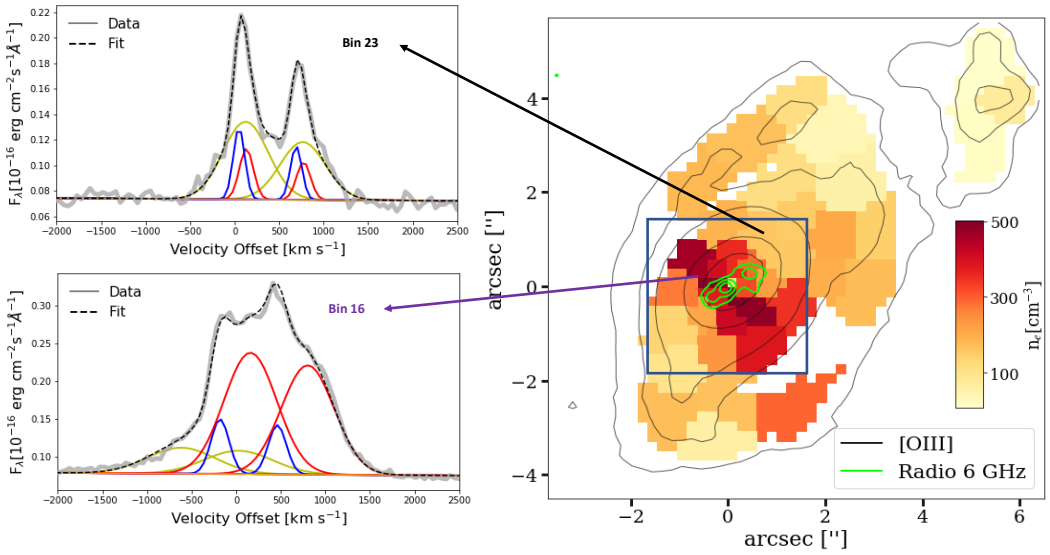

Figure 3.10: A representation of the spatial distribution of electron densities (n_e) using the [S II] doublet method. *Right panel:* A map colour-coded by n_e, estimated for each of the Voronoi bins, mapped over the entire galaxy. The contours are same as described in Figure 3.2. The small inset box shows the central-scale, for which the map is presented in Figure 3.5. *Left panels:* Example [S II]-emission-line profiles and their fits are shown for regions of low (Bin 23) and high (Bin 16) electron densities. The data and fitting-components are displayed using the same convention as for Figure 3.3.

Acknowledgements

The authors would like to thank the referee for their comments which helped improved the quality of the manuscript. PK and SS acknowledge the support of the Department of Atomic Energy, Government of India, under the project 12-R&D-TFR-5.02-0700. DMA and ACE acknowledge support from STFC (ST/T000244/1). We would like to acknowledge the valuable insights from Dimitri Gadotti in helping us with the stellar spectral fits. This research made use of Astropy,[12] a community-developed core Python package for Astronomy (Astropy Collaboration et al., 2013, 2018).

This paper makes use of the following ALMA data: ADS/JAO.ALMA#2018.1.01767.S. ALMA is a partnership of ESO (representing its member states), NSF (USA) and NINS (Japan), together with NRC (Canada), MOST and ASIAA (Taiwan), and KASI (Republic of Korea), in cooperation with the Republic of Chile. The Joint ALMA Observatory is operated by ESO, AUI/NRAO and NAOJ.

Data Availability

The MUSE and ALMA data presented in this analysis were accessed from the ESO archive (`http://archive.eso.org/scienceportal/home`) under the proposal ids: 0103.B-0071 and 2018.1.01767.S, respectively. The VLA image used in this work is available at Newcastle University's data repository (`https://data.ncl.ac.uk`) and can also be accessed through our Quasar Feedback Survey website.

[12] http://www.astropy.org

Chapter

AGN feedback on molecular gas in quasars

4

Molecular gas around radio lobes and in central outflows reveals dual feedback effects in 'radio quiet' quasars

We present a study of the molecular gas, traced via CO (3–2) from ALMA data, of four z<0.2 luminous, 'radio quiet', type 2 quasars ($L_{bol} \sim 10^{45.3-46.2}$ erg s^{-1}; $L_{1.4\,GHz} \sim 10^{23.7-24.3}$ W Hz^{-1}). These targets were selected since they had extended radio lobes ($\geq$10 kpc). They also host compact and low-power radio jets (1–10 kpc; $P_{jet} \sim 10^{43.9-44.4}$ erg s^{-1}). In all four targets, we observe evidence of central molecular outflows, or injected turbulence, within the gas disks traced via wing components in CO emission-line profiles. The inferred velocities (V_{out}=250–440 km s^{-1}) and spatial scales (0.6–1.6 kpc), are consistent with the CO wing components traced for other samples of luminous low redshift AGN. In two of the targets, we observe extended molecular gas structures beyond the central disks, which constitute 9 – 53 % of the total molecular gas mass. These structures tend to be elongated, radially extended from the core, and wrap-around (or along) the radio lobes. Their properties are similar to the molecular gas filaments observed around the radio lobes in (the mostly 'radio loud') Brightest Cluster Galaxies. They have: projected distances of 5 – 13 kpc; bulk velocities of 100 –340 km s^{-1}; velocity dispersion of 30–130 km s^{-1}; inferred mass outflow rates of 4 – 20 $M_\odot$ yr^{-1}; and estimated kinetic powers of $10^{40.3-41.7}$ erg s^{-1}. Our observations are consistent with simulations that suggest low-power jets can have a direct (but modest) impact on molecular gas on small scales, through direct jet-cloud interactions, and also on larger scales by jet-cocoons pushing gas aside. Both these processes can contribute to the long-term regulation of star formation.

4.1 Introduction

Active Galactic Nuclei (AGN) are observed as sites of growing black holes (Kormendy & Ho 2013) and are capable of converting the energy from accreted material into intense episodes of emitted energy in the form of radiation, accretion disk winds, and jets of relativistic particles. This energy can be extremely high, also exceeding the binding energy of the galaxy itself (Cattaneo & Best 2009; Bower et al. 2012) and is theoretically capable of affecting the host galaxy through regulation of star-formation (McNamara & Nulsen 2012; Fabian 2012). Depending on how the available energy couples to the interstellar medium (ISM), the gas could be driven due to wide-angled accretion disk winds, radiation pressure on dust, and/or due to the acceleration by radio jets (e.g., Sijacki et al., 2007; Fabian, 2012; King & Pounds, 2015; Ishibashi & Fabian, 2016; Mukherjee et al., 2016; Costa et al., 2018, 2020; Tanner & Weaver, 2022; Almeida et al., 2023). These processes can also influence the fuel available for feeding the black hole itself, thereby giving this process a self-limiting nature, and thus earning the name 'AGN feedback'.

This chapter is based on the publication Girdhar et al. 2023 in the Monthly Notices of the Royal Astronomical Society journal and the supplementary appendix can be found in Appendix 4.6.

Direct evidence of the influence of AGN on the ISM comes from observations that have confirmed the presence of galactic-scale AGN outflows over different phases, including ionized, neutral, and molecular forms (e.g., Morganti et al. 2005; Nesvadba et al. 2008; Feruglio et al. 2010; Alexander et al. 2010; Harrison et al. 2012; Rupke & Veilleux 2013b; Liu et al. 2013; Cicone et al. 2014; Villar Martín et al. 2014; King & Pounds 2015; Fiore et al. 2017; Rupke et al. 2017; Cicone et al. 2018; Harrison et al. 2018b; Förster Schreiber et al. 2019; Davies et al. 2020; Roy et al. 2021; Venturi et al. 2021b; Ramos Almeida et al. 2021; Girdhar et al. 2022; Kakkad et al. 2022, 2023). While each of these phases are crucial in forming a complete understanding of galaxy evolution, understanding the impact of AGN on molecular gas is particularly popular because: (i) most of the mass in galactic outflows is seen to reside in the molecular gas phase; (ii) molecular gas is the main reservoir for fuelling star-formation and the growth of supermassive black holes. It is hence important to understand the effect of powerful quasars on the molecular gas in their host galaxy (e.g., Feruglio et al., 2010; Mainieri et al., 2011; Alatalo et al., 2011; Cicone et al., 2014; Morganti et al., 2015; Harrison, 2017; Fiore et al., 2017; Mainieri et al., 2021; Ward et al., 2022; Dall'Agnol de Oliveira et al., 2023).

For the brightest AGN, with high accretion rates, the dominant feedback mechanism is typically expected to be due to accretion disk winds (which can propagate into the host galaxies) or directly due to radiation pressure. This can lead to the disturbance or removal of inter-stellar gas (e.g., Costa et al., 2018, 2020). Many of the observational studies focusing on high accretion rate AGN have looked at starburst and highly luminous quasar targets. Specifically, there is a class of observational work searching for underlying wing components in CO emission-line profiles, as a tracer of molecular gas outflows, and then investigating these outflow properties as a function of star formation rates, stellar masses, and AGN luminosities (Cicone et al. 2014; Fiore et al. 2017; Fluetsch et al. 2019). Another class of observational studies have focused on massive, radio-luminous Brightest Cluster Galaxies (BCGs), located in cool-core clusters, revealing molecular gas entrained in filamentary structures along with the large radio lobes and X-ray cavities in the systems (Salomé & Combes 2004; David et al. 2014; McNamara et al. 2014; Tremblay et al. 2016; Vantyghem et al. 2016; Russell et al. 2017, 2018; Tremblay et al. 2018; Russell et al. 2019; Olivares et al. 2019; Tamhane et al. 2022). Therefore, these classes of studies appear to investigate different types of feedback effects on the molecular gas, with the former assuming a dominant role of AGN winds/radiation (at least for driving the most powerful molecular outflows) and the latter finding a dominant role of radio jets.

One might conclude a simple overall picture of two feedback modes on the molecular ISM; one acting on larger scales, caused by powerful radio jets (e.g., in the BCGs) and one acting within the molecular gas disks, due to the radiative output of high accretion rate AGN. However, recent observational studies have come to highlight the importance of low-power radio jets ($P_{jet} \sim 10^{45}\,erg\,s^{-1}$) in galaxies, which are traditionally classified as "radio quiet" (because their radiative output dominates over that from jets). Low-power jets in these systems have been observed to be driving turbulence, outflows, and excitation of the molecular gas (e.g., Morganti et al. 2015; Rosario et al. 2019; Girdhar et al. 2022; Audibert et al. 2023; Morganti et al. 2023), which have an impact which is, at least qualitatively, expected from jets in simulations (Mukherjee et al. 2016; Meenakshi et al. 2022; Tanner & Weaver

2022; Morganti et al. 2023). This all motivates an observational study to search for the impact on molecular gas, on multiple spatial scales, in systems that contain both radio jets and high luminosity AGN. With this goal in mind, we make use of the spatially resolved, multi-wavelength data from the Quasar Feedback Survey (Jarvis et al., 2021).

The Quasar Feedback Survey (QFeedS; Jarvis et al. 2021)[1], includes 42 quasars that were selected from the parent population of AGN at z≤0.2. The redshift provides the advantage to obtain spatially-resolved, sensitive observations of powerful quasars ($L_{bol} \gtrsim 10^{45}\,erg\,s^{-1}$). These luminosities are representative of the peak of the luminosity function, L_*, at the peak of the cosmic epoch of growth when quasar feedback is also expected to dominate (i.e., $z \sim 1$). The QFeedS dataset is being used to extract information on: the origin of radio emission in 'radio quiet' quasars; multi-phase outflows; and the impact of AGN on the host galaxies (e.g. see Harrison et al. 2015; Lansbury et al. 2018; Jarvis et al. 2019, 2020, 2021; Girdhar et al. 2022; Silpa et al. 2022).

One benefit of QFeedS, for exploring different feedback mechanisms, is the availability of sensitive and high-resolution radio imaging provided by the Karl G. Jansky Very Large Array (VLA) (Jarvis et al., 2021). In this work, we explore the feedback on the molecular gas of these quasar-host galaxies by comparing the radio emission with respect to the spatial distribution and kinematics of the molecular gas, traced with CO (3–2) transition, with data from the Atacama Large Millimeter/submillimeter Array (ALMA). The main focus of this work is to compare with the prior feedback studies performed in BCGs, which look for molecular structures associated with radio lobes (Russell et al. 2019; Tamhane et al. 2022); and to also simultaneously search for the presence of CO emission-line wings (as a tracer of molecular outflows), as performed for a compilation of z< 0.2 AGN and starburst galaxies by Fluetsch et al. (2019).

This paper is structured as follows. In Section 4.2, we discuss the sample selection and the different observations and their reduction used for this analysis. In Section 4.3, we describe the approach for the emission-line fits to extract the molecular gas kinematics, followed by the stellar kinematics (using data obtained on the Very Large Telescope's Multi Unit Spectroscopic Explorer; VLT/MUSE) and the methods used to extract morphological and kinematic properties of the molecular gas. In Section 4.4, we present the results and a discussion of these results, in the context of previous observations and simulation studies. Finally, in Section 4.5, we present our conclusions.

We have adopted the cosmological parameters to be $H_0 = 70$ km s^{-1} Mpc^{-1}, $\Omega_M = 0.3$ and $\Omega_\Lambda = 0.7$, throughout. In this cosmology, 1 arcsec corresponds to 2.47 kpc for the redshift of $z = 0.14$ (i.e., the average redshift of the galaxies studied here). When referred to, we define the radio spectral index, α, using $S_\nu \propto \nu^\alpha$.

[1] https://blogs.ncl.ac.uk/quasarfeedbacksurvey/

Table 4.1: Study targets and their properties: (1) quasar name; (2) redshift; (3) and (4) optical Right Ascension and Declination positions from SDSS (DR7: Abazajian et al. 2009) in the format hh:mm:ss.ss and dd:mm:ss.s, respectively. Values in (5)-(7) are from Jarvis et al. 2019: (5) bolometric AGN luminosity; (6) [O III] luminosity; (7) 1.4 GHz radio luminosity; and (8) largest linear size measured for the radio structures (LLS_{radio}; Jarvis et al. 2021).

Quasar	z	RA	Dec	$\log(L_{bol})$	$\log(L_{[O\ III]})$	$\log(L_{1.4GHz})$	LLS_{radio}
	(SDSS)	(J2000)	(J2000)	[erg s^{-1}]	[erg s^{-1}]	[W Hz^{-1}]	[kpc]
(1)	(2)	(3)	(4)	(5)	(6)	(7)	(8)
J0945+1737	0.128	09:45:21.30	+17:37:53.2	45.70	42.66	24.3	11
J1000+1242	0.148	10:00:13.14	+12:42:26.2	45.30	42.61	24.2	21
J1010+1413	0.199	10:10:22.95	+14:13:00.9	46.20	43.13	24.0	10
J1430+1339	0.085	14:30:29.88	+13:39:12.0	45.50	42.61	23.7	14

4.2 Targets, Observations and Ancillary Data

We select our targets for this work from QFeedS (Jarvis et al. 2021), a survey of 42 sources that were originally selected from the parent population of emission-line AGN at z≤0.2 (Mullaney et al. 2013), with quasar-like [O III] λ 5007 Å luminosities ($L_{[O\ III]} > 10^{42.1}$ erg s^{-1}). A moderate radio luminosity criteria of $L_{1.4GHz} > 10^{23.45}$ W Hz^{-1} is also applied to obtain the QFeedS sample; however, the sample still consists of 88 % 'radio quiet' sources, based on the criteria of Xu et al. (1999) (see Jarvis et al. 2021 for full details). This is consistent with the 'radio quiet' fraction of the overall quasar population (i.e. ∼90 %; Zakamska et al. 2004).

Figure 4.1 shows the [O III] luminosities and the projected largest linear radio sizes, LLS_{radio}, of the 42 quasars from QFeedS. The LLS_{radio} measurements were calculated in Jarvis et al. (2021) from a set of 1.5–6 GHz VLA images, with a resolution ranging from 0.3–1 arcsec. It is defined as the distance between the farthest radio emission peaks in the lowest resolution image where the source shows radio structures. If the source shows no morphological features beyond the core in any image, LLS_{radio} is defined as the beam de-convolved size of the core. The sample exhibits a wide range of radio sizes (∼0.1 kpc to ∼60 kpc). Section 4.2.1 gives an overview of the sources selected from QFeedS for this study, followed by a description of the data used from ALMA, VLA, and VLT/MUSE (Section 4.2.2-4.2.4).

4.2.1 Sample Selection

Following our goal to analyze the molecular gas, we identified 9/42 targets from the QFeedS sample which have available CO 12-m array ALMA data (highlighted by the empty black circles in Figure 4.1). For all 9 of these, CO(3–2) data is available in ALMA Band 7 observations; therefore, we decided to use this as our tracer of molecular gas for this work.[2] To clearly separate CO emission related to galaxy disks from any extended emission outside the disks, which could be associated with extended radio lobes, we further only selected the sources with LLS_{radio} ≥10 kpc (from VLA data, see Section 4.2.3). As shown in Figure 4.1, 4/9 sources with ALMA data meet this criteria; namely, J0945+1439, J1000+1242, J1010+1413, and J1430+1339. Table 4.1 lists the basic properties of these four targets. The CO maps and radio images are shown for these four targets in Figure 4.2 (center-panel; see Section 4.2.2 and Section 4.2.3 for details).

[2]We note 2/9 also have CO(2–1) data and 1/9 has CO(1–0) data which are presented in (Ramos Almeida et al., 2021; Audibert et al., 2023) and (Sun et al., 2014).

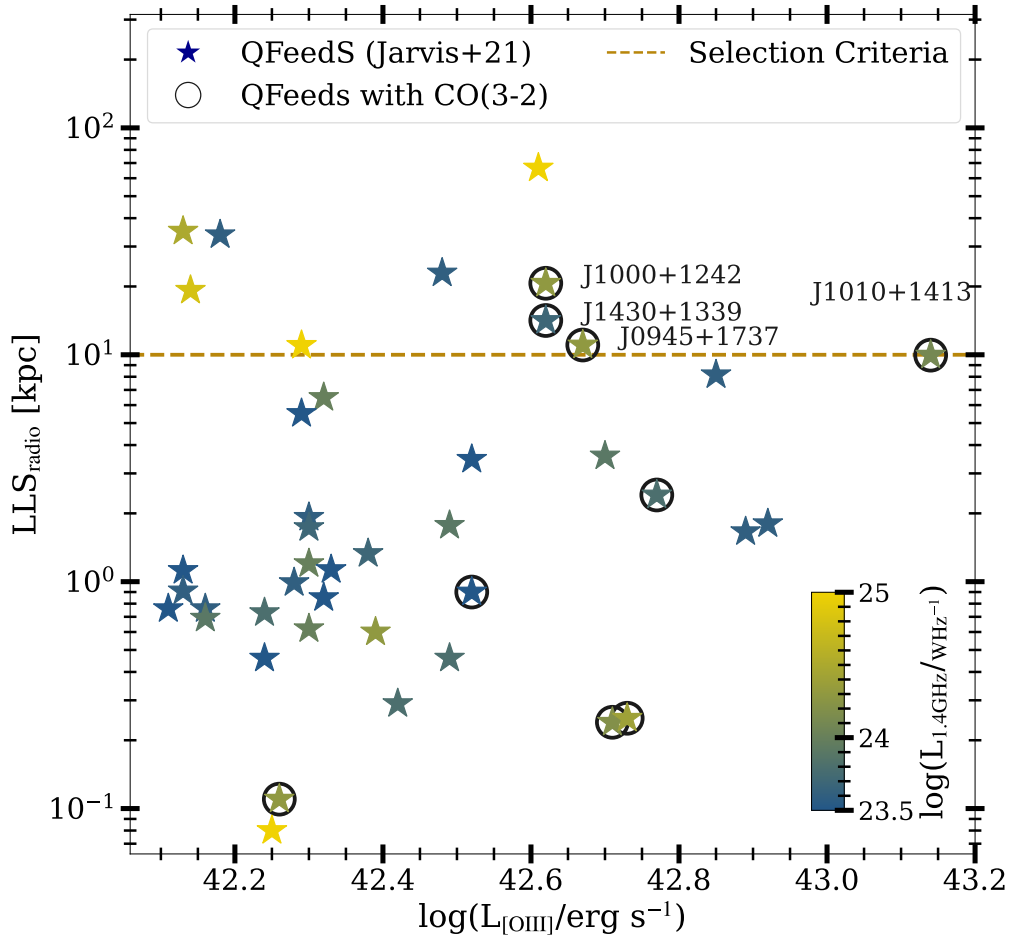

Figure 4.1: Largest linear size of radio structures (LLS_{radio}) versus [O III] luminosity for the parent sample of 42 QFeedS targets, colour-coded by their 1.4 GHz radio luminosity (Jarvis et al. 2021). The 9/42 QFeedS targets with the required CO(3–2) ALMA data are highlighted with a black circle. A selection criteria of $LLS_{radio} \geq 10$ kpc was then applied (dashed line) to select the four targets for this work (labeled with their names, see Section 4.2.1).

All four targets are bright AGN with high, quasar-like bolometric luminosities of $\log(L_{bol}/\mathrm{erg\ s^{-1}}) = 45.3-46.2$ (from the fitting of the spectral energy distributions; Jarvis et al. 2019). These four targets are all classified as 'radio quiet' based on the $L_{[OIII]}$ versus $L_{1.4GHz}$ criteria of Xu et al. (1999). However, despite their modest radio luminosities of $\log(L_{1.4GHz}/\mathrm{W\ Hz^{-1}}) = 23.7-24.3$, all four of these targets have been confirmed to have an excess of radio emission over that expected from star-formation from their radio imaging (see Jarvis et al. 2019, 2021). High-resolution VLA data at 1.4 GHz (see Jarvis et al. 2021) reveals collimated structures along with the presence of hotspots consistent with a jet morphology. Furthermore, the imaging and study of the polarization data of these four galaxies suggests a jet origin of the radio emission (see Silpa et al. 2022).

These targets also have known central AGN-driven outflows and/or high levels of turbulence identified in ionized gas, as traced via broad emission line widths (W_{80}>600 km s^{-1}) of the [O III] emission, extending over the central few kiloparsecs. In all cases, the interactions of radio jets with the ISM seem to be a significant driver with possible contributions from disk winds (Harrison et al., 2014; Jarvis et al., 2019; Venturi et al., 2023, Ulivi et al. in prep). Near-infrared spectroscopy of

J1430+1339 and J0945+1737 further reveals multiple ionized outflow components through different gas tracers (Ramos Almeida et al., 2021; Speranza et al., 2022). Furthermore, for J1430+1339, there is evidence that the small scale inner $\sim$1 kpc jet influences both the kinematics and excitation state of the cold molecular gas, as traced with CO (2–1) kinematics and CO (3–2)/CO (2–1) emission-line ratios (Ramos Almeida et al., 2021; Audibert et al., 2023).

In summary, these targets are well aligned with our goal to understand the impact of low-power radio jets on the molecular gas on small ($\sim$1 kpc) and large ($\gtrsim$10 kpc) scales in 'radio quiet' quasars.

4.2.2 Observation and reduction of the ALMA data

We use 12-m array ALMA Band 7 observations to obtain the spatially-resolved molecular gas emission, traced by the CO(3–2) transition. Three of the four targets (J0945+1737, J1000+1242, and J1010+1413) were observed in three, one-hour epochs under the ALMA project 2018.1.01767.S (PI: A.P. Thomson); using the C 43 - 4 array configuration. The chosen correlator setup comprises three spectral windows, with one spectral window covering the central frequency $\nu_{\rm obs} = 345.795990$ GHz, corresponding to the CO (3–2) line, and the other two windows partially overlapping the former spectral window for an enhanced signal. The fourth target, J1430+1339 was observed under the program code 2016.1.01535.S (PI: G. Lansbury) in the C40-3 configuration. The observation has a single pointing on-source integration time of 30.3 minutes. The spectral window has a bandwidth of 1.875 GHz and was centered at the CO (3–2) line, with the same frequency as mentioned above. The resulting angular resolutions of the observations are $\theta_{\rm res} \sim 0.33 - 0.65$ arcsec (corresponding to linear scales of 0.75 – 1.09 kpc for the respective source redshifts) and a largest angular scale $\theta_{\rm LAS} \sim 4$ arcsec (i.e., 4.6 – 6.4 kpc) for the former three and $\sim$ 19 arcsec ($\sim$ 30 kpc), for J1430+1339.

The data for the four galaxies were reduced and calibrated using the Common Astronomy Software Applications (CASA; McMullin et al. 2007). Using CASA v6.4.3, the imaging of the cubes was made with the task `tclean`. The cleaning was performed in a mask centered in the peak luminosity pixel of each galaxy, with a radius varying between 5 arcsec and 8 arcsec to make sure all the resolved emission was included. A channel width of 25 km s^{-1} was selected, and a pixel scale of 0.05" was used to sample all the synthesized beams. The `Högbom CLEAN` algorithm was run to a flux density threshold of 2 times the root mean square of each of the cubes. Different weightings of the Briggs mode were compared: a robustness = 2.0 (close to natural weighting), a robustness = 0.5 (between uniform and natural weighting), and applying a tapering of the visibilities in the u-v plane. We decided to use the robustness = 2.0 to maximize the recovery of the extended emission without losing significant flux, or the central source small-scale structures. For this work, we use cubes with the continuum and allow a line component to fit the continuum (see Section 4.3.2). The final beam sizes of the observations were an average of 0.37 arcsec $\times$ 0.28 arcsec for the first three targets and 0.7 arcsec $\times$ 0.6 arcsec for J1430+1339.

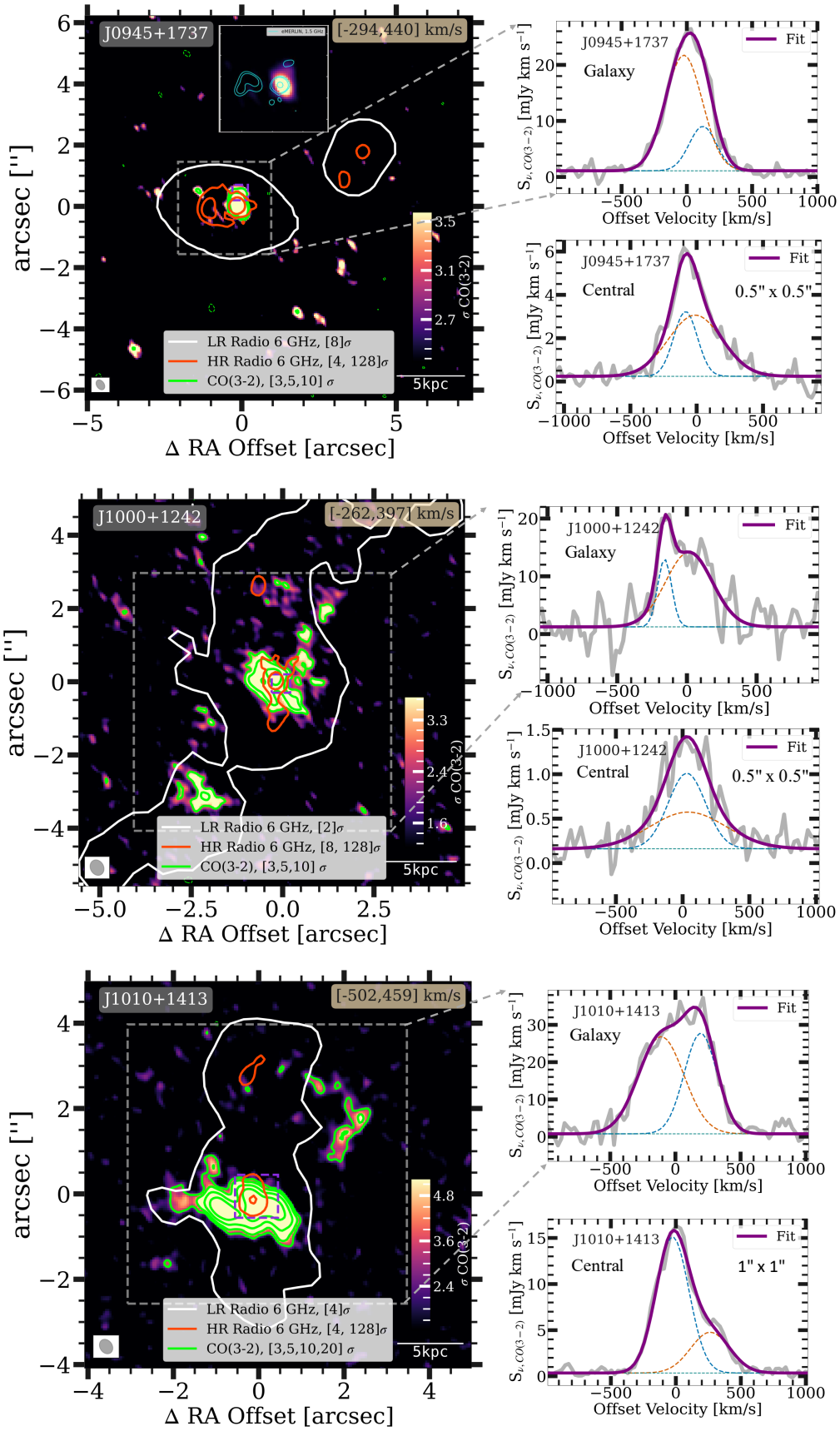

Figure 4.2: Plot and Figure caption continued on the following page.

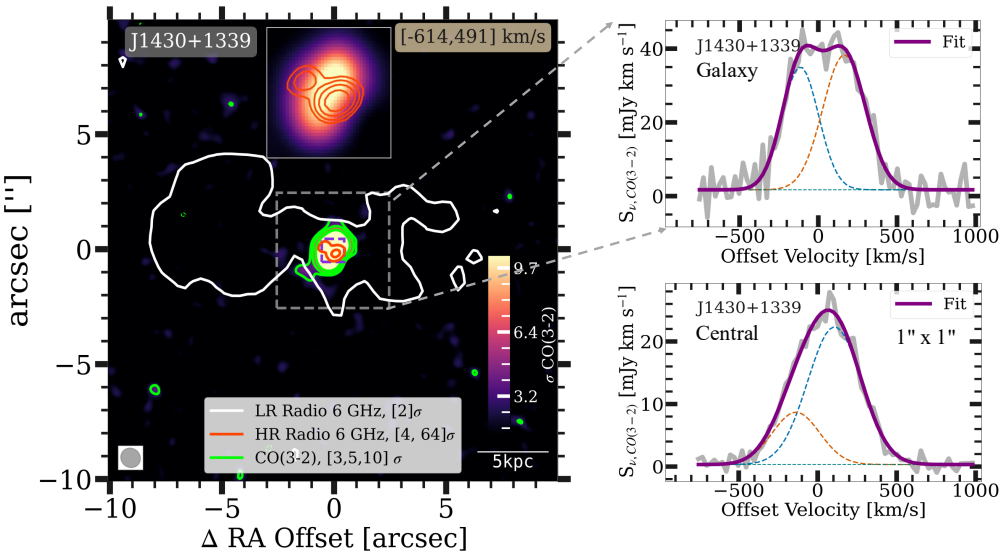

Figure 4.2: *Plot and Figure caption continued from the previous page.* The *bigger left panels* show CO (3–2) flux (moment 0) maps for the four targets selected following Section 4.2.1. The CO(3–2) images are created by integrating over the velocity ranges annotated in the top-right of each panel. The green contours show CO emission corresponding to levels indicated in the individual legends, and the dashed green contours show the $-3\,\sigma$ level of CO emission. The red and the white contours show the radio emission from the high- and low-resolution 6 GHz images, respectively. The contour levels are mentioned in the individual panel legends and are chosen to highlight the important structures in each target. Zoom-ins of the central emission are shown at the top for J1430+1339 and J0945+1737 (where the e-MERLIN image is used and shown through cyan-blue contours). A 5 kpc scale bar is shown in each panel at the bottom-right and the ALMA beams are shown at the bottom-left of the panel. The dashed-grey boxes show the region over which the galaxy-integrated spectra are extracted and are shown in the *top-right panels* with the properties listed in Table 4.2. The dashed purple boxes show the central outflow regions with the spectra shown in *bottom-right panel* and properties listed in Table 4.5. The purple curve shows the combined fit while the blue and orange dashed curves represent the individual Gaussian components. In the case of central spectra, we use the orange curves as the "broad" Gaussian component.

4.2.3 Summary of the radio images

For our investigation of the relationship between the CO emission-line properties and radio morphology, we use the 6 GHz (C-band) VLA radio images from Jarvis et al. (2019). We use both the 'low-resolution' (LR) and 'high-resolution' (HR), images described in that work, which are constructed from a combination of A- and B-configuration VLA data. These images were obtained by optimizing the imaging parameters and weighting schemes to enhance the extended morphological features for each source. We note that this is why we use these images and not those presented in Jarvis et al. (2021), where a simpler but uniform set of imaging parameters was applied to the whole QFeedS sample. The LR images have major axis beam sizes of $\sim$1.0 – 1.2 arcsec (i.e., $\sim$ 2 kpc resolution for z = 0.1) , whilst the HR images have beam sizes of $\sim$0.2 – 0.3 arcsec (i.e, $\sim$ 0.5 kpc resolution for z = 0.1). In each of the figures in this work, we use the contours from these two images to show the range of radio structures seen on the different spatial scales (e.g., Figure 4.2). Further, for J0945+1737, we also make use of the 1.5 GHz e-MERLIN image from (Jarvis et al., 2019), which has a beam size of 0.2 – 0.3 arcsec. This image highlights the bent jet-like $\sim$ 2.1 kpc structure in this source.

Table 4.2: Measured global galaxy properties using the spectra shown in Figure 4.2 (left-panel) and extracted from the dashed-grey regions shown in the central panels: (1) quasar name; (2-3) stellar redshift and stellar velocity dispersion, respectively, measured from the stellar kinematics following Section 4.2.4; (4-7) measurements following Section 4.3.2, namely, (4) mean velocity (V_{50}); (5) velocity width (W_{80}); (6) velocity dispersion estimated as $\sigma = W_{80}/2.56$; (7) flux; (8) molecular gas mass; (9) jet kinetic power

Quasar	z_*	σ_* [$km\,s^{-1}$]	$V_{50,CO,gal}$ [$km\,s^{-1}$]	$W_{80,CO,gal}$ [$km\,s^{-1}$]	$\sigma_{CO,gal}$ [$km\,s^{-1}$]	$S_{CO(3-2),gal}$ [Jy]	$\log(M_{mol,gal})$ / [$M_\odot$]	$\log(P_{jet})$ [$erg\,s^{-1}$]
(1)	(2)	(3)	(4)	(5)	(6)	(7)	(8)	(9)
J0945+1737	0.12840	171 ± 30	0 ± 5	398 ± 13	156 ± 5	9.39 ± 1.29	9.6	44.35
J1000+1242	0.14787	174 ± 18	-54 ± 26	438 ± 102	171 ± 40	6.89 ± 0.29	9.6	44.35
J1010+1413	0.19877	272 ± 20	22 ± 10	583 ± 18	228 ± 7	19.86 ± 0.17	10.4	44.19
J1430+1339	0.08507	182 ± 29	29 ± 13	511 ± 39	200 ± 15	22.20 ± 0.19	9.3	43.86

4.2.4 Stellar velocities and velocity dispersion from MUSE data

For this analysis, we are interested in measuring the stellar redshift (z_*) and stellar velocity dispersion (σ_*), integrated over the spatial extent of the galaxies. To do this, we use the available MUSE data for these targets and follow the procedure outlined in Girdhar et al. (2022) for another QFeedS target, making use of spectral fitting of stellar templates. Full details of the MUSE data and its reduction for these, and other QFeedS targets, is deferred to future works (e.g., Venturi et al. 2023; Ulivi et al. in prep.). Therefore, we only provide brief details here.

Briefly, the four targets have been observed with MUSE, in wide-field mode. This provides a field of view of 1×1 arcmin and a pixel sampling of 0.2 arcsec. Observations of these targets were taken under proposal IDs 0103.B-0071 (PI: C. Harrison), 0102.B-107 (PI: Sartori) and 0104.B-0476 (PI: G. Venturi). We combine the data from these multiple programs to construct deep final stacked cubes, following the data reduction steps described in Girdhar et al. (2022).

We obtained stellar kinematics by employing the GIST pipeline (Bittner et al. 2019), following the detailed methodology and parameters described in Girdhar et al. 2022. Briefly, GIST performs a Voronoi tessellation routine (Cappellari & Copin 2003) to divide the galaxy into regions with significant signal-to-noise-ratio (SNR) for stellar fits. Following this, for each Voronoi region, GIST obtains the best-fit to the stellar continuum, exploiting the pPXF routine (Cappellari & Emsellem 2004; Cappellari 2017), with a combination of stellar templates from XSL Library (Arentsen et al. 2019; Gonneau et al. 2020). This results in an accurate measure of the stellar velocity and stellar velocity dispersion in each Voronoi bin. We used flux-weighted averaging over all the Voronoi bins for the systemic redshift (z_*) and the stellar velocity dispersion (σ_*) of the galaxy. These systemic redshifts are used to shift all the molecular gas emission profiles to the rest frame (see Section 4.3.2). The errors in the values are determined as a median of the formal errors across all the Voronoi bins for each target, where formal errors are 1σ uncertainties as obtained by pPXF fitting. For the four targets, we obtain stellar velocity dispersion values between $170 - 270\,km\,s^{-1}$. All values for z_* and σ_* are listed in Table 4.2.

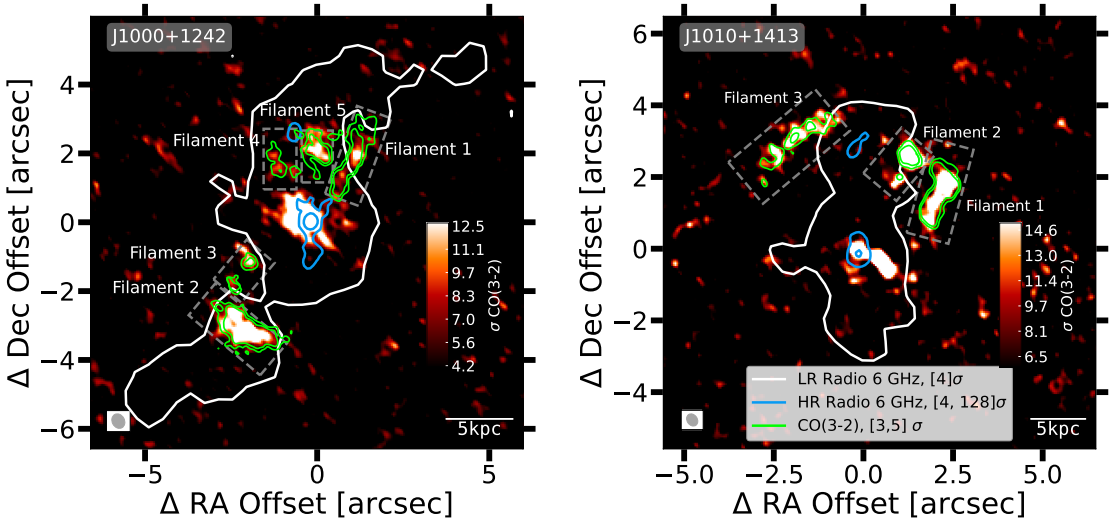

Figure 4.3: CO(3–2) emission-line maps, integrated over specific velocity ranges (quoted in Table 4.3; column (3)), to highlight the identified filamentary structures (in 2 of the 4 targets; see Section 4.2.1). The filament regions are highlighted with the labeled, dashed-grey boxes. The green contours are the CO(3–2) emission in associated velocity ranges, at the 3 and 5σ level. The radio contours are the same as in Figure 4.2 but shown here in blue and white colours for high- and low-resolution, respectively. A legend is shown in the right panel. The individual velocity ranges over which the filaments were detected are listed in Table 4.3 and the narrow-band images are in Appendix 4.6.1.

4.3 Analysis of the CO emission

In this Section, we present our analysis steps to obtain the observed and derived properties of the molecular gas on different scales; for the whole galaxy, and for various spatially-resolved scales. In Section 4.3.1, we formalize our approach to identify any molecular gas structures outside of the central galaxy disks. In Section 4.3.2 we describe our emission-line fitting procedure to characterize the kinematics of the CO emission. In Section 4.3.3 we evaluate the properties of the molecular gas structures (velocity, velocity dispersion, projected extent, and estimated masses). Finally, in Section 4.3.4, we present a brief analysis of the broad CO emission-line components, which are observed in the central regions.

Table 4.3: Measured properties for the filamentary molecular gas structures (see Section 4.3.3) extracted from within the dashed-white regions shown in Figure 4.3. The individual spectra are shown in appendix Figures 4.11 and 4.12. The properties listed here are namely: (1) quasar name; (2) filament name (see Figure 4.3); (3) velocity range used to identify the filaments (see Figure 4.3 and Section 4.3.1); (4) filament axis ratio; (5) radial extent of the filament (R_{fil}); (6) filament velocity ($V_{50,fil}$); (7) filament velocity width ($W_{80,fil}$); (8) filament velocity dispersion (σ_{fil}); (9) flux

Quasar	Filament	Velocity range [km s^{-1}]	Axis ratio	R_{fil} [kpc]	$V_{50,fil}$ [km s^{-1}]	$W_{80,fil}$ [km s^{-1}]	σ_{fil} [km s^{-1}]	$S_{CO(3-2);fil}$ [Jy]
(1)	(2)	(3)	(4)	(5)	(6)	(7)	(8)	(9)
J1000+1242	1	[93,220]	6.51 ± 0.12	10.43 ± 0.16	134 ± 13	242 ± 25	95 ± 10	0.93 ± 0.32
	2	[-262,-109]	2.39 ± 0.03	10.97 ± 0.16	-177 ± 12	239 ± 24	94 ± 9	1.16 ± 0.72
	3	[-211,-160]	2.96 ± 0.11	5.76 ± 0.16	-193 ± 15	82 ± 12	32 ± 5	0.27 ± 0.06
	4	[-185,-109]	2.04 ± 0.08	9.12 ± 0.16	-189 ± 42	340 ± 190	133 ± 74	0.63 ± 0.20
	5	[-160,-33]	1.15 ± 0.03	8.15 ± 0.16	-96 ± 19	170 ± 28	67 ± 11	0.68 ± 0.11
J1010+1413	1	[-401,-274]	3.02 ± 0.06	13.24 ± 0.13	-228 ± 6	143 ± 10	56 ± 4	0.96 ± 0.08
	2	[-477,-401]	1.25 ± 0.02	12.45 ± 0.13	-332 ± 9	223 ± 22	87 ± 9	0.51 ± 0.17
	3	[-502,-426]	3.47 ± 0.07	13.17 ± 0.13	-342 ± 14	119 ± 15	47 ± 6	0.30 ± 0.05

Table 4.4: Derived properties for the filamentary molecular gas structures(see Section 4.3.3) extracted from integrated spectra within dashed-white regions shown in Figure 4.3. The properties listed here are namely: (1) quasar name; (2) filament name; (3) molecular gas mass in filaments; (4) mass outflow rates; (5) kinetic power; (6) jet kinetic power; (7) jet coupling efficiency; (8) radiative coupling efficiency

Quasar	Filament	$\log(M_{fil})$ / $[M_\odot]$	$\log(\dot{M}_{mol,fil})$ / $[M_\odot\,yr^{-1}]$	$\log(\dot{E}_{kin})$ / $[erg\,s^{-1}]$	$\log(P_{jet})$ / $[erg\,s^{-1}]$	η_{jet} [%]	$\eta_{radiative}$ [%]
(1)	(2)	(3)	(4)	(5)	(6)	(7)	(8)
J1000+1242	1	8.77	7.77	40.67	44.35	0.02	3×10^{-4}
J1000+1242	2	8.86	10.98	40.97	44.35	0.04	7×10^{-4}
J1000+1242	3	8.22	3.64	40.26	44.35	0.01	1×10^{-4}
J1000+1242	4	8.60	7.92	40.92	44.35	0.04	6×10^{-4}
J1000+1242	5	8.63	5.46	40.28	44.35	0.01	1×10^{-4}
J1010+1413	1	9.04	19.58	41.53	44.19	0.2	8×10^{-4}
J1010+1413	2	8.77	15.49	41.72	44.19	0.3	11×10^{-4}
J1010+1413	3	8.54	9.10	41.53	44.19	0.2	7×10^{-4}

Table 4.5: Measured central outflow properties in CO(3–2) following Section 4.3.4 and spectra from the region shown through dashed-blue boxes in right-panel of Figure 4.2: (1) quasar name; (2) velocity (V_{out}); and (3) radial extent (R_{out}) of the observed central outflow.

Quasar	V_{out} $[km\,s^{-1}]$	R_{out} [kpc]
(1)	(2)	(3)
J0945+1737	249 ± 27	0.60 ± 0.13
J1000+1242	376 ± 236	0.65 ± 0.15
J1010+1413	441 ± 57	1.64 ± 0.13
J1430+1339	313 ± 146	0.80 ± 0.23

4.3.1 Identification of molecular gas structures

In Figure 4.2, we show CO (3–2) emission-line images, collapsed over the full observed velocity width of the emission-line profiles (the velocity limits are indicated at the top-right of each panel). Overlaid on these images are contours of the 6 GHz radio emission for both the low-resolution and high-resolution images (shown as white and red contours, respectively; see Section 4.2.3). In two of the galaxies, J0945+1737 (first panel) and J1430+1339 (fourth panel), we see that the CO emission is only observed in a central, contiguous region. However, for the other two galaxies, J1000+1242 and J1010+1413, in addition to the central molecular gas, we see molecular CO structures outside of the central regions.

To discern extended molecular gas structures in a systematic way, we formalized the following procedure, which is motivated by the qualitative methods used by Russell et al. (2019) and Tamhane et al. (2022) to search for extended molecular gas structures around BCGs. These two works will serve as our primary comparison sample (see Section 4.4.2). Firstly, we define the central molecular gas disks as central, contiguous CO structures with smooth velocity gradients centered on the systemic galaxy velocities. By inspecting the individual velocity channel images, we then search for additional CO structures that meet all of the following criteria:

1. Emission with a clear morphological and/or kinematic separation from the central molecular gas disk.

2. Emission detected at a $\geq 5\sigma$ significance level in individual velocity channels of the data cube, but also seen in more than one consecutive velocity channel.

3. Structures extending to ≥ 1 kpc in projected size.

Using this systematic approach, for J0945+1737 and J1430+1339, we do not identify any extended molecular gas structures away from the central emission. This confirms the observation made from the total CO emission-line images shown in Figure 4.2. These two quasars are hence not included in our analysis pertaining to the extended CO gas structures.

For J1000+1242 and J1010+1413, we identified 5 and 3 molecular gas structures, respectively, using the above method. We created narrow velocity slice CO images by collapsing over the consecutive velocity channels where any emission $\geq 5\,\sigma$ was seen associated with these structures. These are shown in Figure 4.10. A combined overview of the molecular gas structures is shown in Figure 4.3. For this figure, to distinctly visualize each of these molecular gas structures, we performed a weighted combination of the narrow velocity slices of each filament shown in Figure 4.10, with higher weights to the structures with lower surface brightness. Each filament is labeled and highlighted with a surrounding dashed grey box. These boxes cover the full observed extent (at $\geq 3\,\sigma$) of the structures, where the $3\,\sigma$ CO emission contours are also shown in green for each galaxy. In Section 4.3.3, we evaluate the properties of each of the identified extended gas structures.

For all 8 identified gas structures, we estimated an axis ratio by fitting a 2D Gaussian over the surface brightness images of each. The quoted uncertainty in the axis ratio of the filaments is taken as the ratio of the respective beam axes. These values are listed in Table 4.3. The axis ratios range from $1.2-6.5$, with a median of 2.7, and all but two have an axis ratio >2. Furthermore, most of these structures tend to extend radially from the galaxy centers. Therefore, following the terminology adopted for the molecular gas structures seen in BCGs, which show a similar range in morphology across the samples (e.g., Russell et al., 2019; Tamhane et al., 2022), we refer to each of the identified molecular gas structures as 'filaments'.

We note that our approach of selecting these structures may not uniquely select physically distinct 'filaments'. For example, the identified structures may be part of a larger connected 'flow', and/or each 'filament' can contain sub-structures. Indeed, the contours in Figure 4.3 do show sub-structure. However, we prefer to follow the systematic approach to identify these structures, outlined above, and note that this does not affect our scientific goals, which are primarily to compare the properties of these overall structures to those seen in BCGs (which were identified and analyzed using a very similar approach and definitions). We discuss the origin and properties of these structures in Section 4.4.

4.3.2 Emission-line fitting procedure

We evaluate the molecular gas velocity and velocity dispersion by performing fitting to the CO emission-line profiles. We studied the properties on various spatial scales from the datacubes: (1) in individual spatial pixels to produce maps; (2) from a

region covering the entire CO emitting region for the full galaxies (shown through dashed-grey boxes in Figure 4.2); (3) and regions covering each of the individual filaments (shown through dashed-white boxes in Figure 4.3).

We used the SCIPY CURVE FIT routine (Virtanen et al. 2020b) to obtain the best fit to the data, within the velocity range of $\pm 700\,\mathrm{km\,s^{-1}}$. We modeled the emission-line profiles using one and two Gaussian components; in addition to a linear component for characterizing any underlying continuum emission. To statistically select the best fit to the data, we used the difference in the BIC values (Bayesian Information Criterion; Schwarz 1978), i.e., the model with the lowest BIC value was selected.

While we use multiple Gaussian components, to characterize the emission-line profiles, we adopt a non-parametric approach for most of our analysis (following e.g., Harrison et al., 2014; Girdhar et al., 2022). The bulk velocity is measured in terms of the median velocity of the line profile, V_{50}; and the velocity dispersion is measured through velocity width in terms of W_{80}, i.e., the width containing 80% of the emission-line flux. For a single Gaussian, W_{80} is approximately related to the full-width-at-half-maxima (FWHM) as $W_{80} = 1.088 \times \mathrm{FWHM}$; where the FWHM itself can be related to σ as $\mathrm{FWHM} = 2.35\,\sigma$.

All line profiles and velocity maps presented in this work are shifted from the observed to the rest-frame using the stellar systemic redshift as listed in Table 4.2 (following Section 4.2.4). The application of this emission-line fitting process to different spatial scales is explained in detail below.

- **For the entire galaxy-scale**:
  For the total CO emission, we extract the spectrum over the region shown through a grey-dashed box in Figure 4.2 for all four targets. The obtained emission-line spectra along with the best fit following the fitting procedure above is shown in the respective left panels in the figure.

- **For individual spatial pixel fits**:
  To apply the emission-line fitting routine on individual spaxels, we first regrided the ALMA cubes from an initial spatial resolution of 0.05×0.05 arcsec^2 to 0.15×0.15 arcsec^2, to increase the SNR of each spatial-unit. We first compared the single Gaussian fit, to a simple straight line fit using ΔBIC, and if the line fit had a lower BIC value, the spaxel was discarded from the kinematic analysis. We additionally required that $\mathrm{SNR} \geq 3$ for the emission line to be considered as detected. After these checks for a detected emission line, the line fitting routine continued as above. For the two targets that show the filamentary molecular gas structures, the resulting kinematic maps are illustrated in Figure 4.4 and Figure 4.5 for J1000+1242 and J1010+1413, respectively.

- **For individual molecular gas structures**:
  To quantify the kinematic properties of the molecular gas structures (the 'filaments'), we fit the integrated spectra from the region shown through dashed,

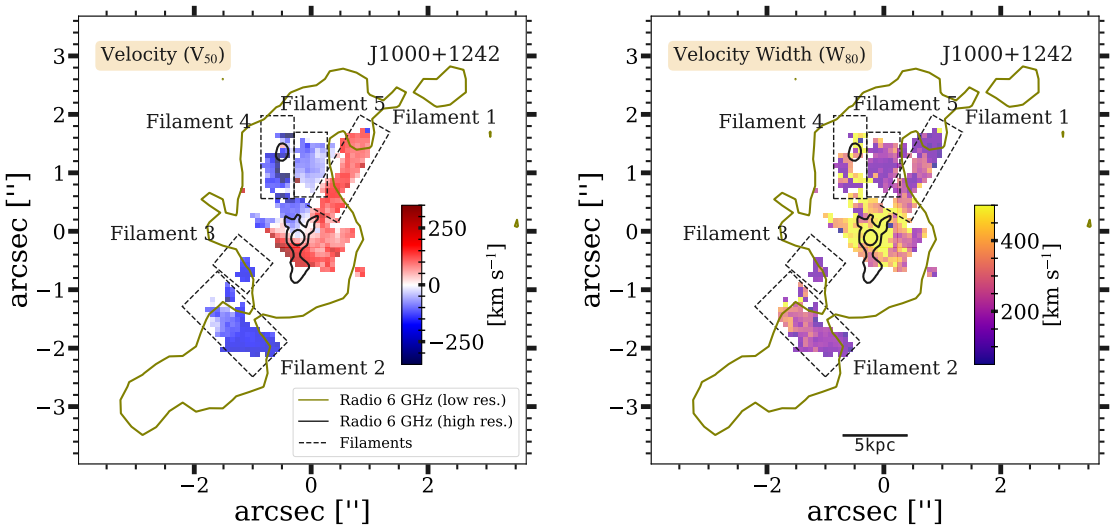

Figure 4.4: Kinematic analyses of the CO(3–2) emission line for J1000+1242 (see Section 4.3.2). The *left panel* is a velocity map (V_{50}), the *right panel* is a map of velocity width (W_{80}). Overlaid on each map, the black and olive-green contours correspond to the high- and low-resolution 6 GHz radio images, same as in Figure 4.2. The black, dashed boxes highlight the filamentary regions identified in Figure 4.3. A legend is shown in the left panel and a 5 kpc scale bar in the right panel.

gray boxes in Figure 4.3. Kinematic maps for the individual structures, along with the extracted CO emission-line profiles and fits, are shown in the Appendix Figures 4.11 and 4.12.

4.3.3 Molecular gas properties

In this section, we measure the properties of the CO filaments seen in our sources. To compare the properties to similar structures seen in the BCGs at comparable redshifts ($z \lesssim 0.2$); we closely follow the methods employed in Russell et al. (2019) and Tamhane et al. (2022). These works have performed an extensive study of the morphology and kinematics of the filaments for 14 unique BCGs (across both samples). The measured CO properties for the whole galaxy measurements are listed in Table 4.2. For the individual filaments, the properties are provided in Tables 4.3 and 4.4.

Molecular gas velocity

To measure the bulk velocities in the molecular gas, we utilize the median velocity V_{50} (see Section 4.3.2) derived from the emission-line profiles depending on the spatial level in consideration, i.e., at the galaxy-level, the velocity will be $V_{50,gal}$ (or V_{gal} for simplicity), where the median velocity is calculated from the fit to the galaxy-level spectra as shown in the top-right panels of Figure 4.2. The velocity maps for J1000+1242 and J1010+1413 are shown in the left panels of Figure 4.4 and 4.5, respectively. For the filamentary molecular gas structures, the velocity of the filaments (or V_{fil}) is obtained from the spectra extracted from the filamentary regions (see appendix figures 4.11 and 4.12). To estimate the uncertainties for our velocity values, we performed Monte Carlo (MC) simulations. For this purpose, multiple simulated representations of the CO emission-line data were obtained by adding random Gaussian noise to our best-fit model (on the scale of the residual

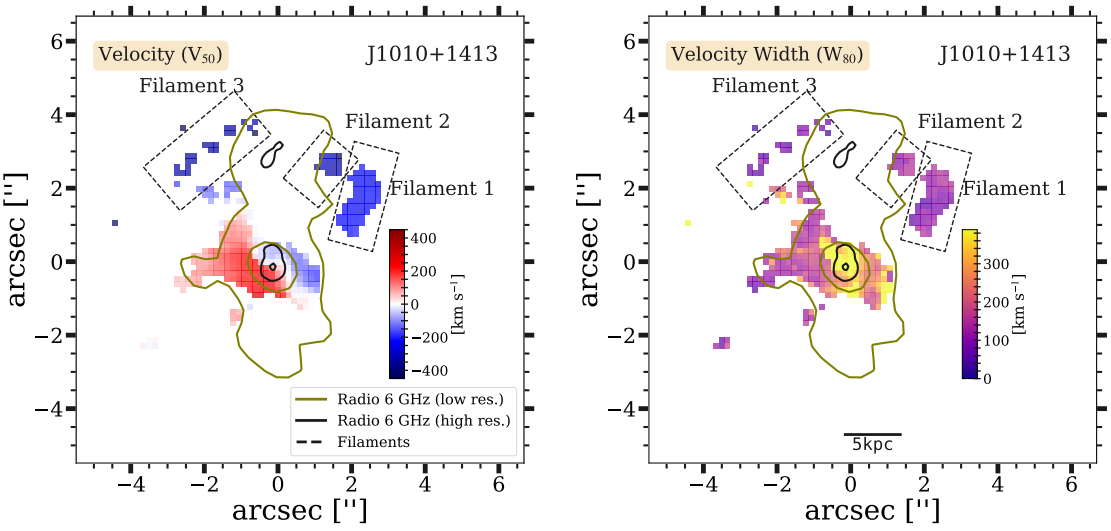

Figure 4.5: Kinematic analyses of the CO(3–2) emission line for J1010+1413 (see Section 4.3.2). The *left panel* is a velocity map (V_{50}), the *right panel* is a map of velocity width (W_{80}). The rest is the same as mentioned in Figure 4.4.

noise in the continuum). A fit was obtained for each of these simulated spectra with V_{50} measured each time. The standard deviation of the distribution of the measured V_{50} values was then used as the uncertainty. We also compared our method with that used by Tamhane et al. (2022), where filament velocities are defined as 'flow velocities' (V_{flow}). They obtain their value from a flux-weighted average, over the filament regions, from a velocity map, and always use a single Gaussian component for their fits. Following this approach, we find the values to be very similar, within $\leq 5\%$. We also note that in the case of more than one filament for a galaxy, Tamhane et al. (2022) only provides an average value over all the filaments.

Molecular gas velocity dispersion

To obtain the velocity dispersion, we refer to the analysis of Russell et al. (2019). They define the molecular velocity dispersion σ_{gal} (σ_{mol} in Russell et al. 2019) as the σ width of a single Gaussian component, fitted to the CO line emission over the entire galaxy. They also separately estimate the CO line velocity dispersion of the filaments, σ_{fil}, by fitting a single Gaussian for the emission-line profiles obtained only over the individual filamentary regions. We follow the same process to obtain the CO velocity dispersion for the total galaxy spectrum and for each of the extended filamentary structures in our sample. While we allow for multiple Gaussian fits, for consistency, we obtain an equivalent σ value from the non-parametric values of velocity width, following $\sigma = W_{80}/2.6$. To obtain the uncertainty in the obtained values, we perform MC simulations as described for estimating the molecular gas velocity (see Section 4.3.3).

Radial extent of filaments

We quantify the maximum projected radial extent, R_{fil}, of the filamentary structures as the maximum projected distance from the nucleus to the most distant part of each filament. This was done following the same method as Tamhane et al. (2022)

(defined as R_{flow} in their work) and by using the images that are collapsed over the velocity range of the individual filaments (see Figure 4.10). We estimate the uncertainty on these values as the equivalent size of the beam's major axis.

Molecular gas mass estimates

To obtain the total molecular gas mass in the galaxy (M_{tot}), we first estimated the integrated line flux for the CO (3–2) emission from the galaxy spectra. Likewise, for the filament mass (M_{fil}), we used the integrated flux from the spectra extracted from filamentary regions. The uncertainty in flux values is obtained from the emission line fitting routine as the square root of the diagonal of the covariance matrix of each free parameter used for the emission line fit.

To estimate the molecular mass, we used the same conversion factors as Tamhane et al. (2022), for a consistent comparison. We first converted CO (3–2) fluxes to CO (1-0), by using integrated line flux ratios of 7.2 (Vantyghem et al. 2016). We then converted the integrated flux density of CO(1–0) line ($S_{CO}\,\Delta\,v$) to molecular gas mass (M_{mol}) using the following relation (Solomon & Vanden Bout 2005; Bolatto et al. 2013):

$$M_{mol} = 1.05 \times 10^4 \, \frac{X_{CO}}{[X_{CO,Gal}]} \, \frac{1}{1+z} \, \frac{S_{CO}\,\Delta\,v}{[Jy\,km\,s^{-1}]} \, \frac{{D_L}^2}{[Mpc^2]} \, M_\odot \tag{4.1}$$

where z is the redshift of the galaxy, D_L is the luminosity distance, and X_{CO} is the CO-to-H_2 conversion factor, with $X_{CO,Gal} = 2{\times}10^{20}\,cm^{-2}\,(K\,km\,s^{-1})^{-1}$ (Solomon et al. 1987; Solomon & Vanden Bout 2005). This relation is the corollary of the relation $M_{mol} = \alpha\,L'_{CO(1-0)}$, where X_{CO} and α_{CO} are both referred to as "CO-to-H_2" conversion factor. For $X_{CO} = 2{\times}10^{20}\,cm^{-2}\,(K\,km\,s^{-1})^{-1}$, the corresponding $\alpha_{CO} = 4.3\,M_\odot\,(K\,km\,s^{-1}\,pc^2)^{-1}$. It is a caveat that this exact $X_{CO,Gal}$ factor may not apply to our galaxies (and also neither to BCGs), and there may be significant variation, pertaining to environmental variations (reviewed by Bolatto et al. 2013). However, we use these factors for a consistent comparison between these different studies, and we assume a systematic uncertainty of ~ 0.5 dex on any derived quantities related to molecular gas masses, throughout (following Tamhane et al., 2022).

4.3.4 Spatially mapping CO wing components

We are also interested in central molecular outflows, which are often traced with underlying wings in the CO emission-line components (e.g., Fluetsch et al. 2019). Although a detailed kinematic analysis of molecular outflows is beyond the scope of this work (following e.g., Ramos Almeida et al. 2021), we wish to compare the CO properties to previous works that investigate such CO components, under the assumption that they are tracing outflows (e.g., Fluetsch et al. 2019; Tamhane et al. 2022). Specifically, motivated by the methods of Fluetsch et al. (2019), which were also considered in the analyses of Tamhane et al. (2022), we wished to measure the spatial extent of the region over which CO emission-line wings (assumed to be outflows) are identified.

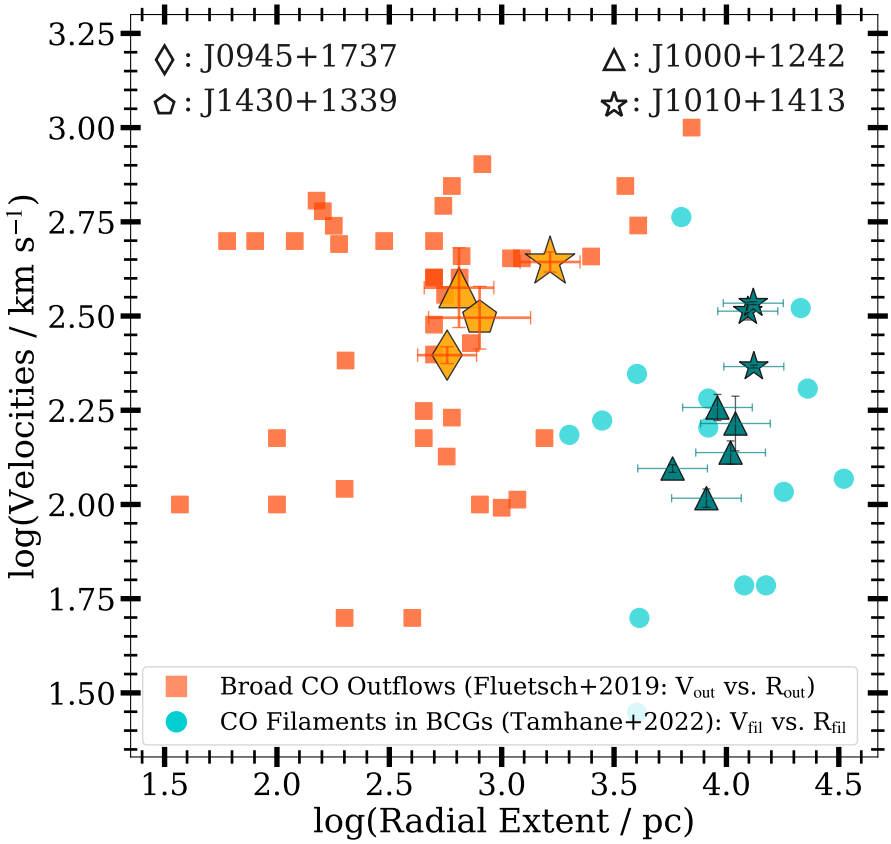

Figure 4.6: Velocity (V_{fil}) versus radial extent (R_{fil}) of the filamentary structures identified in this work. Small teal triangles and stars represent the filaments in J1000+1242 and J1010+1413, respectively, and the measurements for BCGs are represented with light-blue circles (Tamhane et al. 2022). The larger orange symbols, now including J1430+1339 and J0945+1737 plotted as a pentagon and diamond, respectively, represent V_{out} and R_{out} of the central broad outflows identified using CO (3–2) emission (see Section 4.3.4). A comparison is shown with the AGN and star-burst galaxies sample as orange squares (from Fluetsch et al. 2019).

Following Section 4.3.2, we mapped the CO emission in the central regions, identifying pixels where two emission-line components were required. The velocity width maps within the central regions reveal broad velocity widths across all four galaxies (i.e., $\gtrsim 400\,\mathrm{km\,s^{-1}}$). This motivated us to undertake a more comprehensive analysis to identify any disturbed gas in the central regions of the four targets. Due to the complexities of the emission-line kinematics, in addition to the BIC-based selection, we visually inspected the fits in the individual spaxels over these regions, to ensure that the emission-line profiles show clear signs of secondary, underlying emission-line wing components. The regions over which broad CO wings are clearly identified, through two Gaussian components, are shown as dashed purple boxes in the central panels of Figure 4.2. Using these regions, we extracted the spectral profile for studying the properties of the central broad outflows (shown in the right panels of Figure 4.2). We measured R_{broad} as the projected distance between the farthest spaxel from the central spaxel over these regions. The uncertainty in the projected distance was taken as the major axis of the respective beams.

We use the CO emission-line profiles from these central regions to obtain the velocities of the outflowing gas as: $V_{out} = FWHM_{broad}/2 + V_{broad}$, i.e., the same definition as Fluetsch et al. (2019). For the uncertainty in the velocity values, we combined

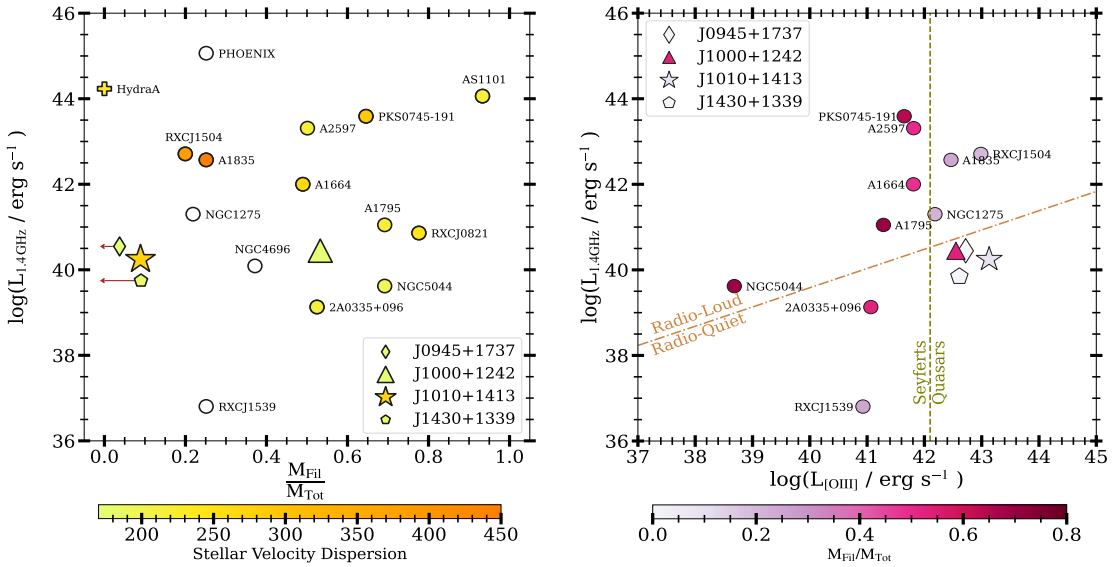

Figure 4.7: *Left*: Ratio of molecular gas in filaments to the total molecular gas as a function of 1.4 GHz radio luminosity of the respective target for both the samples: symbols as in the legend, and the 14 BCGs from Tamhane et al. 2022, represented as circles. Hydra A is also shown which has no identified filaments, through a plus symbol (Rose et al. 2019). The data points are colour-coded by stellar velocity dispersion of the galaxies, except where these data were not found (shown as empty circles). *Right*: 1.4 GHz radio luminosity versus [O III] luminosity for the same targets as in the left panel, but for the entire galaxy (excluding 4 BCGs for which $L_{[OIII]}$ was not available), and colour-coded by the ratio of molecular mass found in filaments to the total. The dot-dashed line separates radio-loud and 'radio quiet' sources (following Xu et al. 1999) and the vertical dashed line is the 'quasar' luminosity threshold used to select our sample (i.e., $L_{[OIII]} \geq 10^{42.1}\,\mathrm{erg\,s^{-1}}$; see Section 4.2.1).

the uncertainties in FWHM and V_{broad} (see Section 4.3.3). The central outflow properties are listed for all four targets in Table 4.5 and plotted in Figure 4.6. We discuss these properties later in Section 4.4.3. We note that when we employ the same methods used by Fluetsch et al. (2019) (which involves a simplified approach of producing CO images over the high-velocity wings of the profiles), we obtain very similar values, and our derived values are also close to the previous studies of the CO emission for the case of J1430+1339 (see Audibert et al. 2023). In summary, our values are sufficient for the simple parameter-space comparison of CO emission-line profile properties presented in Figure 4.6.

4.4 Results and Discussion

In this section, we present our results, and discuss their interpretation, from our analysis of the molecular gas (traced via CO (3–2) emission) of four quasars from the QFeedS (Figure 4.1). Specifically, in Section 4.4.1, we summarise the properties of the identified extended molecular gas structures in terms of their morphology, radial extent, and kinematics. In Section 4.4.2 we make a comparison to similar structures found in BCGs. Finally, in Section 4.4.3, we discuss the evidence for two feedback mechanisms acting on the molecular gas, in the same targets, and discuss possible implications for an evolutionary sequence of feedback via low-power radio jets in 'radio quiet' quasars.

4.4.1 Properties of the molecular gas structures

Figure 4.2 reveals molecular gas in the form of radially-extended filamentary structures for two of the four galaxies. As presented in Section 4.3.1, these structures have morphologies that are typically elongated (with a median axis ratio of 2.7; see Table 4.3). Following the terminology used for similar morphological structures seen in BCGs, we refer to these gas structures as filaments. As shown in Figure 4.3, we identify five filaments for J1000+1242 and three for J1010+1413. Figures 4.4 and 4.5 show the velocity and velocity-width maps (in terms of W_{80}) over the entire CO emitting regions. A zoomed-in version of these maps, and corresponding CO (3–2) emission-line profiles extracted from these regions, are provided for the individual filaments in Appendix 4.6.2. The observed filament properties are listed in Table 4.3.

We present values of filament velocity and radial extent in Figure 4.6, as teal-coloured triangles for J1000+1242 and stars for J1010+1413. For J1000+1242, across the 5 filaments, there is a radial extent range of $R_{fil} = 5-11$ kpc and velocities of $V_{fil} = |100-190|\,km\,s^{-1}$. In case of the 3 filaments in J1010+1413, we see a radial extent range of $12-13$ kpc with comparatively higher velocities of $220-340\,km\,s^{-1}$. This gives us an average radial extent of 8 kpc and 12 kpc; and an average velocity of $\sim 150\,km\,s^{-1}$ and $\sim 280\,km\,s^{-1}$ for J1000+1242, and J1010+1413, respectively.

In Figure 4.8, we compare the molecular velocity dispersion of the filaments (σ_{fil}) with the stellar velocity dispersion (σ_*) of the host galaxies. The filaments show velocity dispersion values in the range of $30-130\,km\,s^{-1}$ for J1000+1242 and $47-90\,km\,s^{-1}$ for J1010+1413. In general, the velocity dispersion of the filaments is much lower than the stellar velocity dispersion values, with a median ratio of $\sigma_{fil}/\sigma_* = 0.32$ across all 8 filaments.

In the left panel of Figure 4.7, we present the fraction of total molecular gas mass located in the filaments, with respect to the radio luminosity ($L_{1.4GHz}$), where the colour-scaling corresponds to the galaxy's stellar velocity dispersion. These ratios are simply the ratio of CO (3–2) flux across all filaments, divided by the total CO (3–2) flux for each galaxy. That is, we are assuming the same CO flux to the mass conversion factor for both the filaments and total gas mass. J1000+1242 is observed to have the highest value, with 53%. J1010+1413 has only 9% of the CO(3–2) emitting gas located in these structures. For J0945+1737 and J1430+1339, where no filaments were detected, we estimated upper limits for the molecular gas mass of the filaments of 4%, and 9% respectively.[3] We note that these mass ratio measurements can be affected by the sensitivity to structures on different scales, depending on the distribution of the CO (3–2) emitting gas. For example, we may be missing low surface brightness CO (3–2) emission (either contained in filaments or the central galaxy). Towards this, we compared our total CO flux measurements from the 12 m ALMA observations with single-dish observations of the three targets detected in CO (3–2) in APEX data (i.e., all but J0945+1737; Molyneux et al. in prep). We found that ALMA/APEX flux ratios range from 0.53–1.3. Although

[3]For estimating the upper limits, we used the flux ratio of the faintest detected filament (i.e., filament 3 of J1010+1413) to total galaxy flux and scaled it by the noise in the respective cubes of J0945+1737 and J1430+1339.

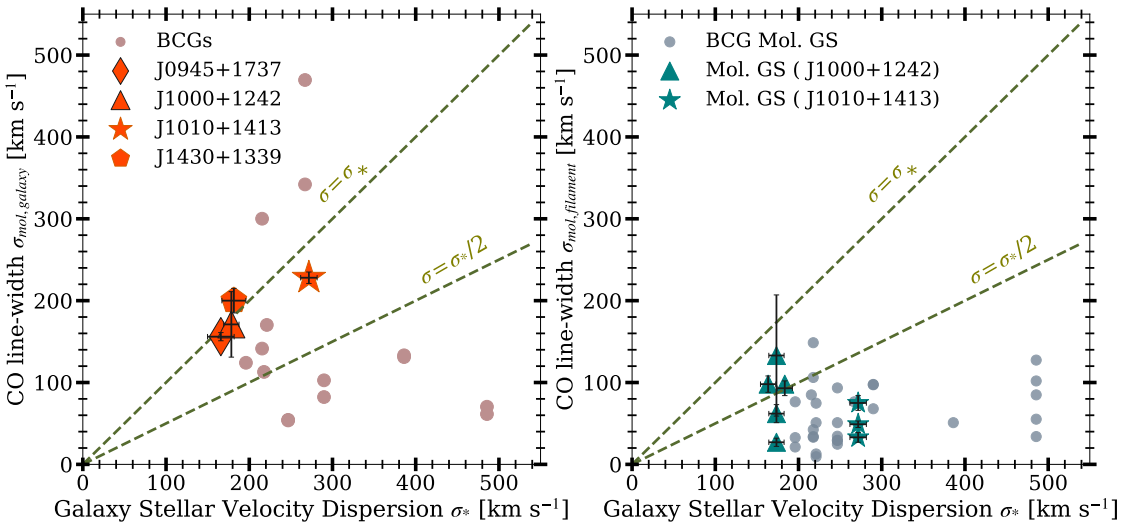

Figure 4.8: *Left:* CO velocity dispersion from the galaxy-wide emission-line profile ($\sigma_{\rm mol,galaxy}$; as in Figure 4.4) and *Right:* from the individual filaments ($\sigma_{\rm mol,filament}$; see spectra in Figures 4.11 and 4.12) versus stellar velocity dispersion (σ_*), for our targets (different symbols, as in legend) compared to the 12 BCGs sample (from Russell et al. 2019; shown as small circles). The two dashed lines in each panel show a 1:1 and 1:0.5 relationship of $\sigma_{\rm mol}$:σ_*. For stellar velocities, we obtain values from the stellar template fits for the whole galaxy (see Section 4.2.4). The σ values are obtained following the method summarised in Section 4.3.3.

this adds some additional uncertainty (at the ∼0.3 dex level on these mass ratios), our measurements are sufficient for a broad comparison to the values for similar structures, obtained using similar datasets, seen in BCGs (Section 4.4.2).

The CO (3–2) emitting molecular gas seen as elongated structures in the two galaxies, appear to be entrained along or around the radio bubbles seen in these targets (see Figure 4.3; Figure 4.4; and Figure 4.5). The surface brightness and velocity maps of the filaments reveal some clumpy sub-structures, but the velocity gradients across the filaments are relatively smooth, and are typically small ($30-100\,{\rm km\,s^{-1}}$), following the major axes of the structures. Further, the more clumpy molecular gas is seen to be coincident with bends in the radio bubbles. Qualitatively, all of these morphological and kinematic structures, and their spatial connection to expanding bubbles, are similar to those we see associated with BCGs, hosted in cool core clusters that are rich in molecular gas (e.g., see Tremblay et al. 2018; Balmaverde et al. 2018; Russell et al. 2019; Tamhane et al. 2022; Capetti et al. 2022). Therefore, it is warranted to make a more quantitative comparison between the structures observed in our new observations of 'radio quiet' quasars, with those seen in BCGs.

4.4.2 Comparison with BCGs

We compare our observations of molecular gas structures with a sample of 14 BCGs (at $z \leq 0.2$) compiled from Tamhane et al. (2022) in terms of their radial extent, velocity, and mass. For comparing in terms of velocity dispersion, we use the velocity dispersion data for the 10 BCGs from Russell et al. (2019), that are in common over both the samples[4]. Additionally, we also add Hydra-A to this comparison list (studied

[4]We also note that the filament properties from Russell et al. (2019) are provided as individual filaments, whilst for Tamhane et al. (2022), they are often an average over all the filaments. When referred to, we make this clear for each comparison.

in Rose et al. 2019), making the total a sample of 15 BCGs. These works make use of ALMA to make measurements of gas structures observed via low CO transitions (i.e., CO (3–2), CO (2–1), and CO (1–0)), similar to our observations and approaches. The stellar velocity dispersion, the radio fluxes, and the [O III] luminosities for the BCGs are taken from Hogan et al. (2015, 2017) and Pulido et al. (2018)[5]. These BCGs are typically more massive than our sample (with $\sigma_\star$ $\sim$200–500 $\mathrm{km\,s^{-1}}$; see Figure 4.8) and are typical 'radio loud' galaxies (see Figure 4.7; right-panel). In contrast, our sample is purely made up of 'radio quiet' quasars (see Section 4.2.1; Figure 4.7). The BCGs, with known strong 'radio-mode' feedback and large reservoirs of molecular gas ($10^9 - 10^{11} \mathrm{M_\odot}$) serve as an interesting comparison for our targets. This helps to explore the feedback processes across different populations.

In comparison to the BCGs, the CO filaments observed in our targets have comparable properties in the $\mathrm{V_{fil}}$ vs. $\mathrm{R_{fil}}$ parameter space (Figure 4.6). Across the comparison sample 15 BCGs, they show a significant spread in the filament mass fraction from 0% in Hydra-A (disk-dominated) to $\sim$90% in AS1101 (filament-dominated; see Figure 4.7). Three of the four galaxies from our sample lie towards the lower end of this filament mass-fraction, with J1000+1242 lying towards the middle at 53%. Due to the archival and inhomogeneous nature of the BCG sample, and the small sample of 'radio quiet' quasars investigated here, it is not yet possible to rigorously assess if the distribution of filament-to-total molecular mass fractions of the two populations is consistent. A more complete, systematic survey of the two populations is required.

In the right panel of Figure 4.8, we see that the CO filaments in BGGs have velocity dispersion values of $\sim 10-160\,\mathrm{km\,s^{-1}}$, which is the same as seen in the two 'radio quiet' quasars, with detected filaments, in our work. Furthermore, the vast majority of BCG filaments fall significantly lower than half of the stellar velocity dispersion, as is also seen for those in our sample.

In Figure 4.7, we look for trends in the observed filament-to-total molecular gas fractions, with respect to radio luminosity ($\mathrm{L_{1.4GHz}}$), [O III] luminosity ($\mathrm{L_{[OIII]}}$), and stellar velocity dispersion (σ_*) for the combined sample of BCGs plus our sample. In the left panel of Figure 4.7, we see no clear trends with radio luminosity, nor with stellar velocity dispersion (represented by the colour-scaling). In the right panel of Figure 4.7, we compare our targets to the BCG sample in the $\mathrm{L_{1.4GHz}}$ vs. $\mathrm{L_{[OIII]}}$ plane; with the colour-scaling corresponding to the filament mass fraction. While we see no obvious trend with respect to the radio-luminosity, the BCG sources with a higher [O III] luminosity ($\mathrm{L_{[OIII]}} \geq 10^{42.1}\,\mathrm{erg\,s^{-1}}$; in the quasar regime) have a typically lower mass-fraction of gas in the filaments ($\sim 22\%$), as opposed to a higher average mass-fraction of ($\sim 52\%$) seen for those with low [O III] luminosities. The average filament mass-fraction for luminous [O III] sources reduces further when our targets are also included ($\leq 16\%$). This appears to indicate that higher radiative power does not result in higher fractions of mass involved in these filaments. However, we reiterate,

[5]When radio flux and [O III] luminosities were not available in these work, we obtained these values using NASA/IPAC Extragalactic Database (Helou et al. 1991). However, for 5/15 BCGs we didn't obtain either the radio flux or the [O III] luminosities, and hence these are excluded from the Figure 4.7 (right panel). For 4/15 BCGs, we could not recover the stellar dispersion values and hence these are represented as empty symbols in Figure 4.7 (left panel), and discussed later.

a more homogeneous and complete investigation across both samples is required to confirm any such trend (or lack thereof) between radiative power and the fraction of molecular gas located in filamentary structures.

4.4.3 Radio-driven dual feedback effects and evolutionary sequence for 'radio quiet' quasars

With a goal to understand the relative importance of feedback processes in different populations, a recent study by Tamhane et al. (2022) compared the properties of molecular filaments (located around radio bubbles) in $z \leq 0.2$ BCGs with the properties of high-velocity wings observed in CO emission lines (as a tracer of central molecular outflows) in a sample of $z \leq 0.2$ AGN and starburst galaxies in Fluetsch et al. (2019). They conclude that radio feedback is generally more effective at lifting the gas in galaxies compared to the AGN and starburst winds. However, as acknowledged by Tamhane et al. (2022), there is not a systematic investigation of possible 'radio feedback' in the Fluetsch et al. (2019) sample. We have searched for both types of molecular gas features (extended filaments and central outflows) in our sample of four 'radio quiet' quasars. In Section 4.4.1 and Section 4.4.2 we showed that two of the four targets show molecular gas filaments located around radio lobes, with similar properties to those seen in BCGs. In this section, we first discuss signatures of central outflows, traced by high-velocity wings in the CO emission-line profiles, and seen in all four galaxies. Thereafter, we discuss the implications for the observed feedback effects on multiple scales.

Central multi-phase outflows

All four quasars are already known to contain central ionized gas outflows (traced by broad emission-line components) from previous work (see Harrison et al. 2014, 2015; Ramos Almeida et al. 2021; Speranza et al. 2022; Audibert et al. 2023; Venturi et al. 2023; Ulivi et al. in prep.), with velocities reaching $1000\,\mathrm{km\,s^{-1}}$, and extending to spatial extents of $\gtrsim$1–10 kpc. In all cases, the jet-ISM interactions have been proposed as an important driving mechanism of outflows and turbulence, with possible additional contributions from quasar-driven winds being an important driving mechanism for these outflows.

As reported in Section 4.3.4, we have found evidence of high-velocity wings in the CO (3–2) emission lines profiles in the central regions of the galaxies. Such signatures are attributed to outflowing molecular gas in Fluetsch et al. (2019); and following their definition (also see Section 4.3.4), we observe the velocities of the central disturbed gas to be around $V_{out} = 249$, 376, 441, and 331 $\mathrm{km\,s^{-1}}$ respectively for J0945+1737, J1000+1242, J1010+1413, and J1430+1339. We measure the projected radial extent of this outflowing phase to be $R_{out} = 0.60$, 0.65, 1.64, 0.80 kpc, for these same targets. In Table 4.5, we summarise all the properties, along with the measured uncertainties of the central outflows. We note that for J1430+1339, similar properties of outflowing molecular phase using the CO (3–2) and CO (2–1) emitting gas were presented in Ramos Almeida et al. (2021) and Audibert et al. (2023), which is attributed to the inner radio jet seen in this source (Harrison et al., 2015; Jarvis

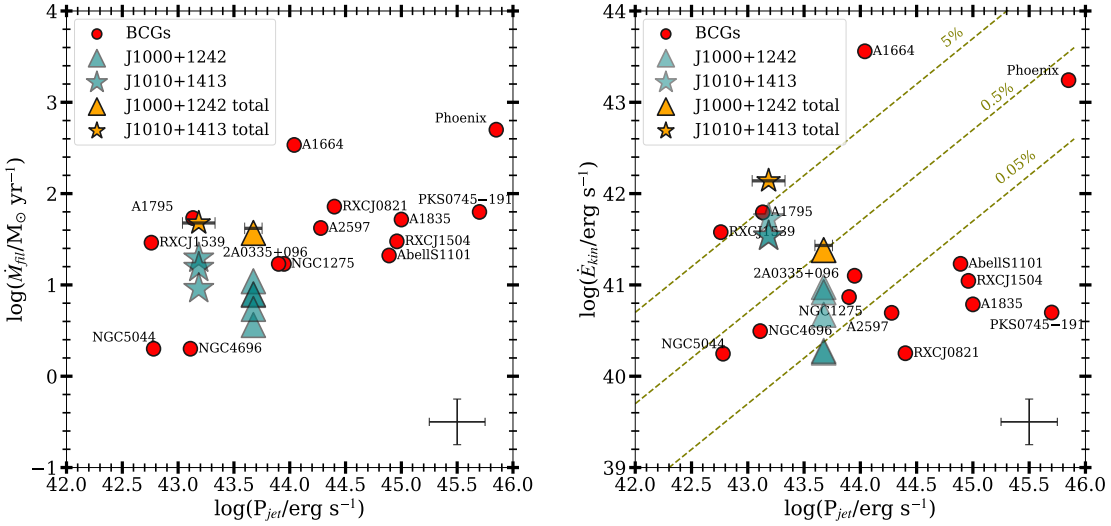

Figure 4.9: *Left panel:* Rate of Molecular Mass Outflow vs. the Jet Kinetic Power (P_{jet}) for our filaments and the 14 comparison BCG. *Right panel:* The rate of kinetic energy vs. the jet kinetic power (P_{jet}). The teal symbols show the individual filaments for our targets. The yellow symbols show the total rates over all the filaments for each galaxy and the red circles show the values for the BCG sample (which are averaged over multiple filaments). The black error bar shows the variation in the jet power depending on whether the core or total radio luminosity was used. The dashed olive lines on the right correspond to coupling efficiencies of 5%, 0.5%, and 0.05%. In the bottom-right the average systemic error assumed for each derived value is shown.

et al., 2019). These molecular outflow components are less extreme in both velocity and spatial extent than seen in the corresponding ionized gas, in agreement with the multi-phase study of Girdhar et al. (2022) for a different QFeedS target.

Our goal here is not to provide a detailed kinematic analysis of CO outflows but to compare the parameters of CO wings, following a similar approach to Fluetsch et al. (2019). Indeed, Figure 4.6 reveals that the velocities and radial extents of molecular outflow properties estimated by Fluetsch et al. (2019) (shown as orange squares) lie closely in the parameter space to our observed central outflow properties (yellow symbols).

Radio lobes impact on ∼10 kpc scale molecular gas

Possible explanations of the molecular gas structures seen around the radio bubbles (which contain radio jets; see Figure 4.3), is either a thin cover of clumpy molecular gas, expanding along with the expanding radio bubbles, or molecular gas that is in-situ condensed in the updrafts (e.g., McNamara et al., 2014, 2016; Russell et al., 2019). The gas is then expected to appear the brightest around the edges of the bubbles, aligned with the line of sight, thus giving a filamentary appearance. In general, the filaments are observed to have slow velocities and narrow velocity widths (Figure 4.6, 4.8; and also in Russell et al. 2019; Tamhane et al. 2022). This could be because they retain the velocity structure of the rising bubbles which themselves may be relatively cool, and not shock-heated (McNamara et al. 2000; Fabian et al. 2000) as opposed to the typically energetic jet-ISM interactions. The lower molecular gas velocities as compared to the stellar velocity dispersion (Figure 4.8) could indicate that these filamentary structures are in their youth or are transient or both, as they have not yet settled in the galaxy's gravitational potential (Russell et al., 2016, 2019).

Whilst we can not be conclusive about the origin of the molecular gas structures observed, following Tamhane et al. (2022), we assume the off-nuclear molecular gas structures as a flow, noting that some of this gas may be flowing towards the central galaxies as opposed to a pure outflow (see Russell et al. 2016; Balmaverde et al. 2022). Tamhane et al. (2022) noted that these molecular flows in BCGs are 1–3 orders of magnitude larger than the central outflows found in Fluetsch et al. (2019). In two of our sample, we find evidence of both types of molecular gas structures in the same sources. We find that those molecular gas structures identified around the radio lobes are roughly an order of magnitude larger in size. However, it is important to note the approaches taken to search for these types of flows are very different and are somewhat biased by the requirement to have large radio bubbles outwith the central molecular gas disks.

Again, following Tamhane et al. (2022), we compute the mass flow rate for the filaments ($\dot{\mathrm{M}}_{\mathrm{fil}}$) as the molecular mass in the filament ($\mathrm{M}_{\mathrm{fil}}$) divided by the time ($\mathrm{t}_{\mathrm{fil}}$) it would have taken the filament to reach the projected radial extent ($\mathrm{R}_{\mathrm{fil}}$) at the velocity of the filament ($\mathrm{V}_{\mathrm{fil}}$); which is computed as $\mathrm{t}_{\mathrm{fil}} = \mathrm{R}_{\mathrm{fil}}/\mathrm{V}_{\mathrm{fil}}$. We compute the kinetic power of the filament as: $\dot{\mathrm{E}}_{\mathrm{kin}} = 1/2\,\dot{\mathrm{M}}_{\mathrm{fil}}\,\mathrm{V}_{\mathrm{fil}}^2$. For all these derived quantities, we assume a systemic error of 0.5 dex on our computed values (following Tamhane et al. 2022). These derived values for the filaments are listed in Table 4.4.

In Figure 4.9, we compare the filaments in our targets to BCGs in terms of their mass outflow rates (left panel) and kinetic powers (in the right panel) in relation to estimated jet powers. The jet power, $\mathrm{P}_{\mathrm{jet}}$ is obtained using the Merloni & Heinz (2007) relation, for which the radio luminosity values at 1.4 GHz were converted to 5 GHz following the relation $S_\nu \propto \nu^\alpha$. For all conversions, a standard value of $\alpha = -0.7$ was used following Jarvis et al. (2021). In Figure 4.9, individual filaments are shown as triangles for J1000+1242 and as stars for J1010+1413, and the total for all filaments is represented using hatched symbols.

It can be seen that the mass outflow rates in the filaments for our targets (4–$20\,\mathrm{M}_\odot\,\mathrm{yr}^{-1}$) are comparable to the BCGs. At the same time, the kinetic power in the filaments ($10^{40-42}\,\mathrm{erg\,s}^{-1}$) also seems to be comparable to the BCGs. However, similar to the case of the BCGs, the kinetic energy transferred in the filaments is a significantly smaller fraction of the energy available in the radio jet. The rate of energy transferred to the filaments, under these assumptions, is observed to be lower than 1 % percent of the jet kinetic power (consistent with all but 3 of the BCGs). Summing over all filaments, this suggests a jet coupling efficiency of $0.1-0.9\,\%$ for our sample, which is significantly higher than if we were to assume the AGN bolometric luminosity was responsible for driving these flows, i.e., $\dot{E}_{\mathrm{kin}}/L_{\mathrm{bol}} \sim 10^{-3}\,\%$ (see Table 4.4).

This brings us to the conclusion that Figure 4.6 does not necessarily always correspond to two different galaxy populations for different feedback mechanisms on the molecular gas, i.e., where radiative energy ('quasar') drives central CO outflows in luminous, high accretion rate AGN, and radio jets drive molecular flows in typically 'radio loud', low accretion rate sources. In our sample, we see both central outflows and turbulence (in all four galaxies) and large-scale filamentary structures (in two).

Furthermore, despite the high radiative output, it appears that radio jets and lobes also have a significant role in the impact caused on the molecular gas on multiple scales.

Dual feedback effects and evolution of low power radio jets

We have found two different types of impact on molecular gas in 'radio quiet' quasars, acting on different scales. Indeed, theoretical studies do show that specific AGN physical mechanisms are expected to result in distinct concomitant forms of AGN feedback, operating on different spatial and temporal scales for example: a) ultra-fast outflows/small-scale winds (Costa et al. 2014, 2020), (b) jets (Talbot et al. 2022, 2023), (c) radiation pressure (Costa et al. 2018) and even the more phenomenological AGN feedback models used in state-of-the-art cosmological boxes (e.g. Zinger et al. 2020).

In the case of radio jets, even low-power jets, have gained recognition as potentially causing significant disturbance through direct jet-ISM interactions from observations (Alatalo et al. 2011; Tadhunter et al. 2014; Morganti et al. 2015; Venturi et al. 2021b; Girdhar et al. 2022; Morganti et al. 2023). Hydrodynamic simulations of jets (see Sutherland & Bicknell 2007; Wagner et al. 2012; Mukherjee et al. 2016, 2018b; Mandal et al. 2021; Talbot et al. 2022, 2023; Tanner & Weaver 2022; Talbot et al. 2022) have studied the progression of a jet through a clumpy interstellar medium to understand its impact on the ISM.

Through these works comes a possible evolutionary sequence of jet-ISM interactions as motivated by both simulations and observations. On small spatial scales (and shorter timescales), the jet directly interacts with the ISM causing turbulence, and as the jet propagates, it grows along with the cocoon of shocked and heated gas and ISM plasma, that takes over at larger scales. This may cause the molecular gas to couple and rise in the wake of this growing radio bubble to greater radial extents. On larger scales ($\sim 5-10\,\mathrm{kpc}$), the feedback may hence be moderated by the jet-cocoon which heats or disperses the molecular gas causing cavities and pushing it aside, which is then observed as filaments. However, we cannot be certain about the origin of the filaments and it could also be possible they were cooled in situ around the radio bubbles (see Section 4.4.3). Furthermore, a single radio event can continue to drive gas outwards for a long time after a quasar of similar power has shut down (see discussion in Tamhane et al. 2022). We may be seeing both effects in our targets, which have ongoing accretion activity, and the impact of the larger-scale radio bubbles may take over as the dominant mechanism on longer timescales, as is also observed to be the dominant feedback mechanism in more evolved BCGs.

Our observations stem from a small number of objects and need to be confirmed by a larger sample. One significant step towards this would be to quantify the feedback from jets depending on their properties of inclination, power, and evolutionary stage. Additionally, it will be important to establish the relative importance of jets, quasar-driven winds, and radiation pressure for driving multi-phase outflows and turbulence across a homogenous sample. Further, obtaining observations of other resolved CO transitions could be crucial for deriving their excitation and physical properties and will also help unveil the full "population" of filaments.

4.5 Conclusions

We present the study of the molecular gas properties in four z<0.2 luminous, 'radio quiet' type 2 quasars from QFeedS ($L_{bol} \sim 10^{45.5-46.7}\,erg\,s^{-1}$; $L_{1.4\,GHz} \sim 10^{23.7-24.3}\,W\,Hz^{-1}$), namely, J0945+1737, J1000+1242, J1010+1413, J1430+1339. These targets were selected based on the availability of high spatial-resolution ALMA data, to trace the CO(3–2) emission, and their projected radio linear sizes of $LLS_{radio} \geq 10\,kpc$ (see Figure 4.1, and Table 4.1 for an overview of properties). We explored the kinematics and spatial distribution of the CO (3–2) emission with ~ 0.33 - $1.09\,kpc$ spatial resolution. This was compared to the morphology seen in 6 GHz radio images, previously obtained from the VLA (see Figure 4.2 for a data overview). Our main findings are summarised below:

1. We identify filamentary molecular gas structures in and around ∼10 kpc radio lobes in two out of the four 'radio quiet' quasars (Figure 4.3, 4.4, and 4.5).
Both J1000+1242 and J1010+1413 show filamentary molecular gas structures that appear to wrap around the radio lobes. They have maximal radial extents of $5-13\,kpc$, velocities of $V_{fil} = |\,100-340\,|\ km\,s^{-1}$ and velocity dispersion values of $\sigma_{mol,filament} = 30-135\,km\,s^{-1}$. We observe that ∼53% and ∼9% of the total molecular gas mass is contained within these structures for J1000+1242 and J1010+1413, respectively. For J0945+1737 and J1430+1339, we do not see any such structures, but estimate a maximum of 4% and 9% of the total CO (3–2) emitting gas could be contained in such structures (see Figure 4.7; left-panel). Our observations of radial extents and mass fractions are in close agreement to simulations of low-power radio jets predicting the relation between the radial extent and the mass of molecular gas being driven (see Figure 20 in Mukherjee et al. 2016).

2. The molecular gas filaments in these 'radio quiet' quasars have properties comparable to those seen driven by radio jets in, predominantly radio-loud, BCGs (Figures 4.6, 4.7, 4.8, and 4.9).
The velocities, velocity dispersion and maximal radial extent of the molecular filaments from our 'radio quiet' quasars show very similar values to those seen in BCGs, for which similar analyses have been performed (see Figures 4.6 and 4.8).

The inferred mass outflow rates ($4-20\,M_\odot\,yr^{-1}$) and kinetic powers ($10^{40-42}\,erg\,s^{-1}$) are also comparable to those seen in the BCGs (Figure 4.9). Combining our sample with the BCGs, we observe no obvious trends with stellar velocity dispersion or radio luminosity and the fraction of mass found in filaments. Although limited by source statistics, there is tentative evidence that less [O III] luminous sources (i.e., $L_{[OIII]} \leq 10^{42}\,erg\,s^{-1}$) tend to show higher fractions of the molecular mass in filaments, with an average filament mass-fraction of 55 %, while the higher-[O III] luminous sources, including our targets, have an average filament mass-fraction of <16 % (see Figure 4.7; right-panel). This may tentatively suggest that kinetic power might be a more compelling driver of these molecular filaments than radiative power at larger scales (∼10 kpc).

3. Evidence for both central molecular outflows and large-scale radio feedback on the molecular gas in 'radio quiet' quasars (Figure 4.4, 4.5, and 4.6).
In all four quasars, we see evidence for central (0.6 – 1.6 kpc), outflows traced by high-velocity wings ($V_{out} = 250 - 440\,km\,s^{-1}$) of the CO(3–2) emission-line profiles (see Figure 4.4 and 4.5). These have properties comparable to those seen for the archival AGN and starburst galaxies (of typically lower L_{bol}; Fluetsch et al. 2019). This adds to the evidence for central multi-phase outflows in these systems, likely caused by an interaction between low-power radio jets and the ISM.

We have shown that both central molecular outflows, typically associated with luminous AGN, and molecular gas filaments around radio lobes on ∼10 kpc-scales (analogous to those found in BCGs), can also be found in 'radio quiet' quasars. This implies that both feedback mechanisms can act within the same systems. Our observations are consistent with recent simulations and observations (e.g., Talbot et al. 2022; Morganti et al. 2023) that suggest that two feedback effects can take place due to low-power radio jets ($P_{jet} \leq 10^{45}\,erg\,s^{-1}$). On the smaller scales, jet-ISM interactions can drive turbulence and central outflows. On larger scales, radio lobes have penetrated beyond galaxy disks and cause a more gentle pushing aside of molecular gas. Unlike high-power jets that escape swiftly, low-power jets are seen to be trapped for longer in simulations. Their effect is amplified due to the development of an energy bubble which is basically a cocoon of a shocked ISM and plasma. This interaction leads to the constant stirring of the ISM with the energy bubble, thus inhibiting the star formation (see Mukherjee et al. 2016).

Our results underscore that the availability of higher radiative energy as we see in quasars, does not necessarily imply that it would also be the dominant feedback mechanism on all spatial scales. A radio jet, even if low in power, has considerable potential to couple with the galaxy ISM and lead to a significant impact on the host galaxy gas (Mukherjee et al. 2016, 2018b; Meenakshi et al. 2022). We acknowledge that all four studied targets are different to some extent and the two targets showing the presence of filaments are themselves quite unalike. To draw firm conclusions about the population as a whole, calls for a larger study, across a wider sample, to understand: how common each of these different mechanisms are; the relative importance of radio jets compared to radiative processes; and what AGN or galaxy properties determine the amount of molecular mass associated with both central outflows and larger-scale radio lobe interactions.

4.6 Appendix to the Chapter

4.6.1 Individual Filament Narrow-band Images

To identify the filaments following our approach in Section 4.3.1, we created narrow velocity slice CO images by collapsing over the consecutive velocity channels where any emission $\geq 5\,\sigma$ was seen associated with these structures. These are shown in Figure 4.10. For J1000+1242, we identified 5 filaments and for J1010+1413, we identified 3 filaments, as shown in each of the panels below. The velocity windows used for collapsing each image are labeled on the top-right of each panel, and each filament is highlighted with a surrounding dashed white box. These boxes cover the

full observed extent (at $\geq 3\,\sigma$) of the structures, where the $3\,\sigma$ contours are also shown. A combined overview figure for each of the targets can be seen in Figure 4.3.

4.6.2 Kinematic Maps of the Filamentary Molecular Gas Structures

The velocity and velocity width maps obtained following the methods outlined in Section 4.3.3, are shown in Figure 4.11 and Figure 4.12 for each of the filaments of J1000+1242 and J1010+1413, respectively. From left to right, each of the panels in the figure represents (a) CO(3–2) emission narrow band image; (b) a map of the median velocity values in a group of (3×3) spaxels; (c) a map of the velocity width (W_{80}); and (d) emission-line profile extracted over the entire filamentary regions. The CO (3–2) emission map in panel (a) shows a zoom-in of each of the filaments identified following the definition in Section 4.3.1 and shown in Figure 4.3. The green and cyan contours show the emission at 3σ and 5σ respectively. The two subsequent panels (b) and (c) represent the spatially resolved kinematics for each of the filaments with the 5σ contour highlighting the edges and the colour bars at the bottom. The final panel (d) shows the integrated emission line profile over the entire filamentary region enclosed within the 5σ contour.

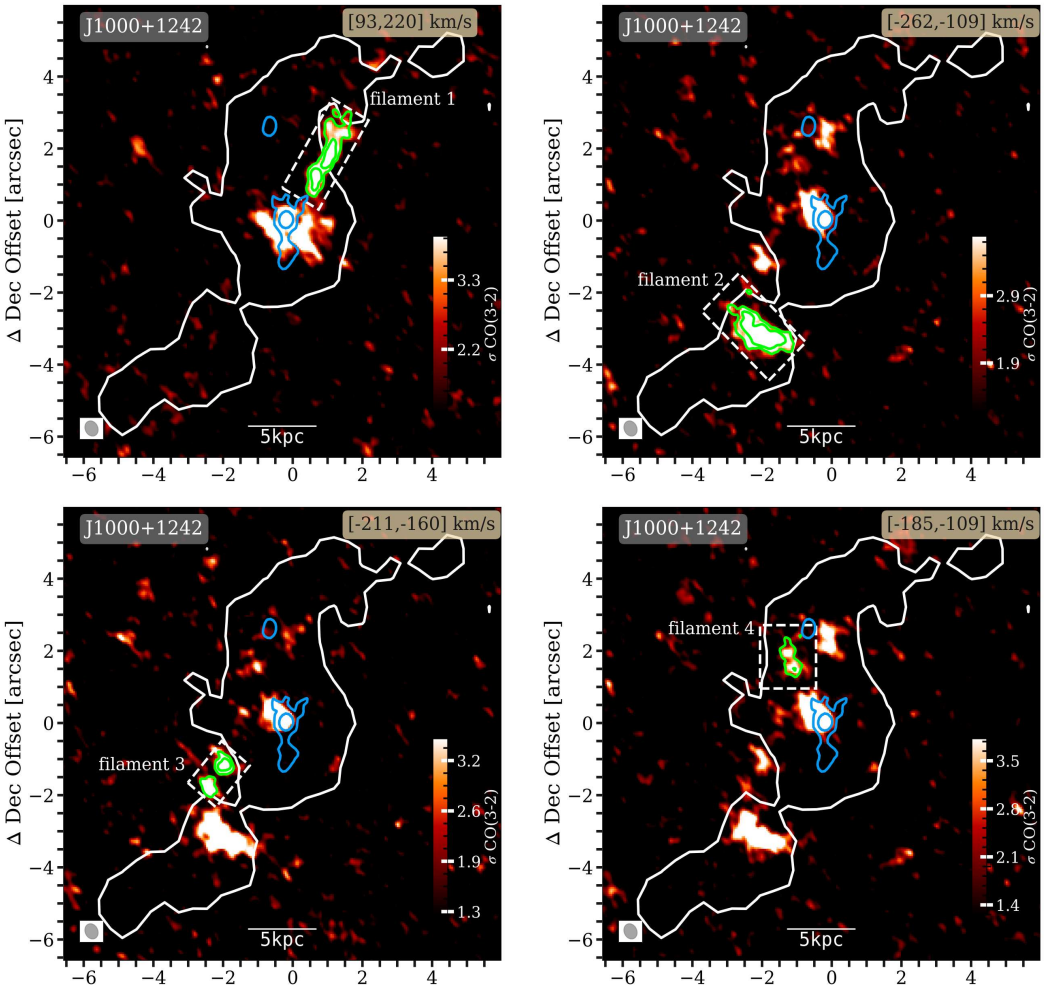

Figure 4.10: Figure and caption continued on the following page.

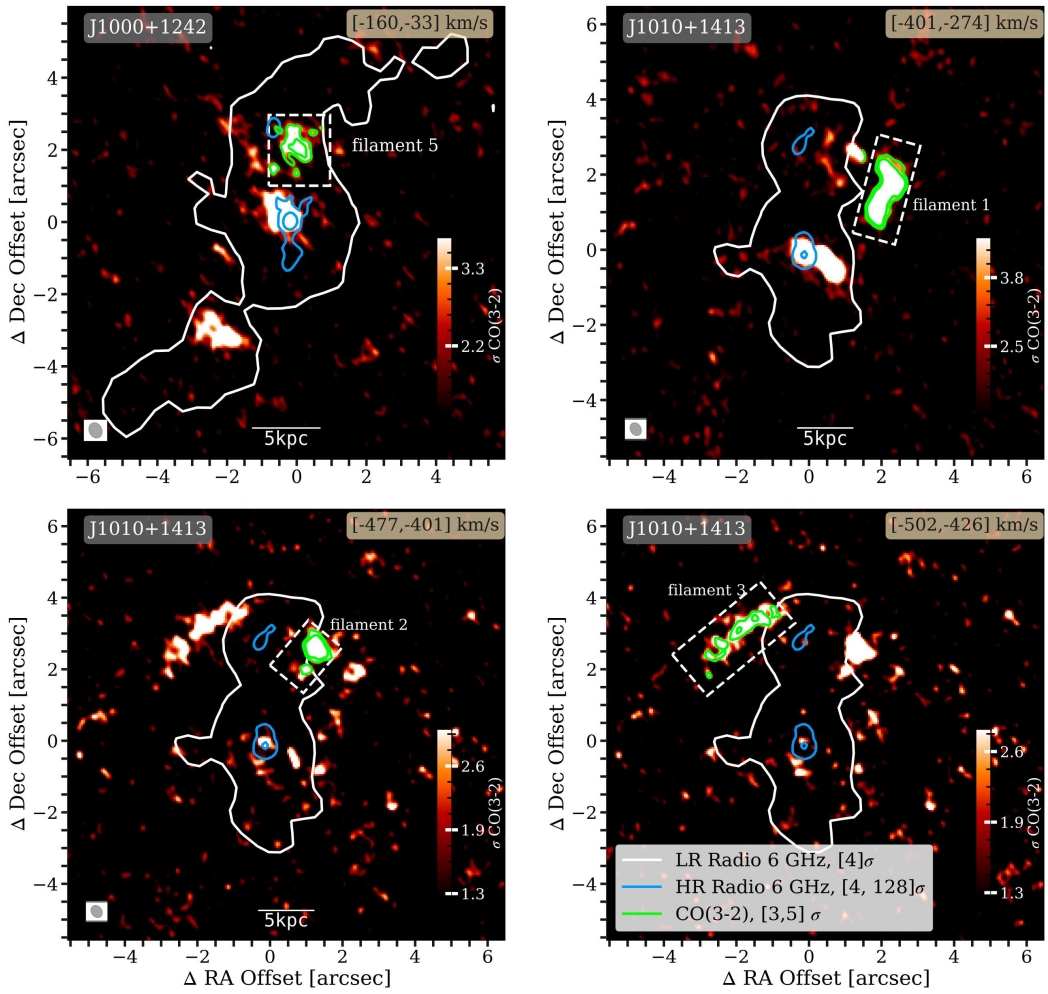

Figure 4.10: CO(3–2) emission-line maps, integrated over specific velocity ranges (quoted in the top-right of each panel), to highlight the identified filamentary structures (see Section 4.2.1). The filament regions are highlighted with the labeled, dashed-white boxes. The green contours are the CO(3–2) emission inside these boxes, at the 3 and 5σ level. The radio contours are the same as in Figure 4.2 just shown here in blue and white colours for high- and low-resolution at 6 GHz respectively. A legend is shown on the bottom-right panel.

Acknowledgements

We thank the referee for their valuable comments. CMH & AN acknowledge funding from the United Kingdom Research and Innovation grant (code: MR/V022830/1). ACE acknowledges support from Science and Technology Facilities Council (STFC) grant ST/P00541/1. EPF is supported by the international Gemini Observatory, a program of NSF's NOIRLab, which is managed by the Association of Universities for Research in Astronomy (AURA) under a cooperative agreement with the National Science Foundation, on behalf of the Gemini partnership of Argentina, Brazil, Canada, Chile, the Republic of Korea, and the United States of America. MB acknowledges funding support from program JWST-GO-01717, which was provided by NASA through a grant from the Space Telescope Science Institute, which is operated by the Association of Universities for Research in Astronomy, Inc., under NASA contract NAS 5-03127. PK & SS acknowledges the support of the Department of Atomic Energy, Government of India, under the project 12-R&D-TFR-5.02-0700. SS acknowledges financial support from Millenium Nucleus NCN19_058 (TITANs).

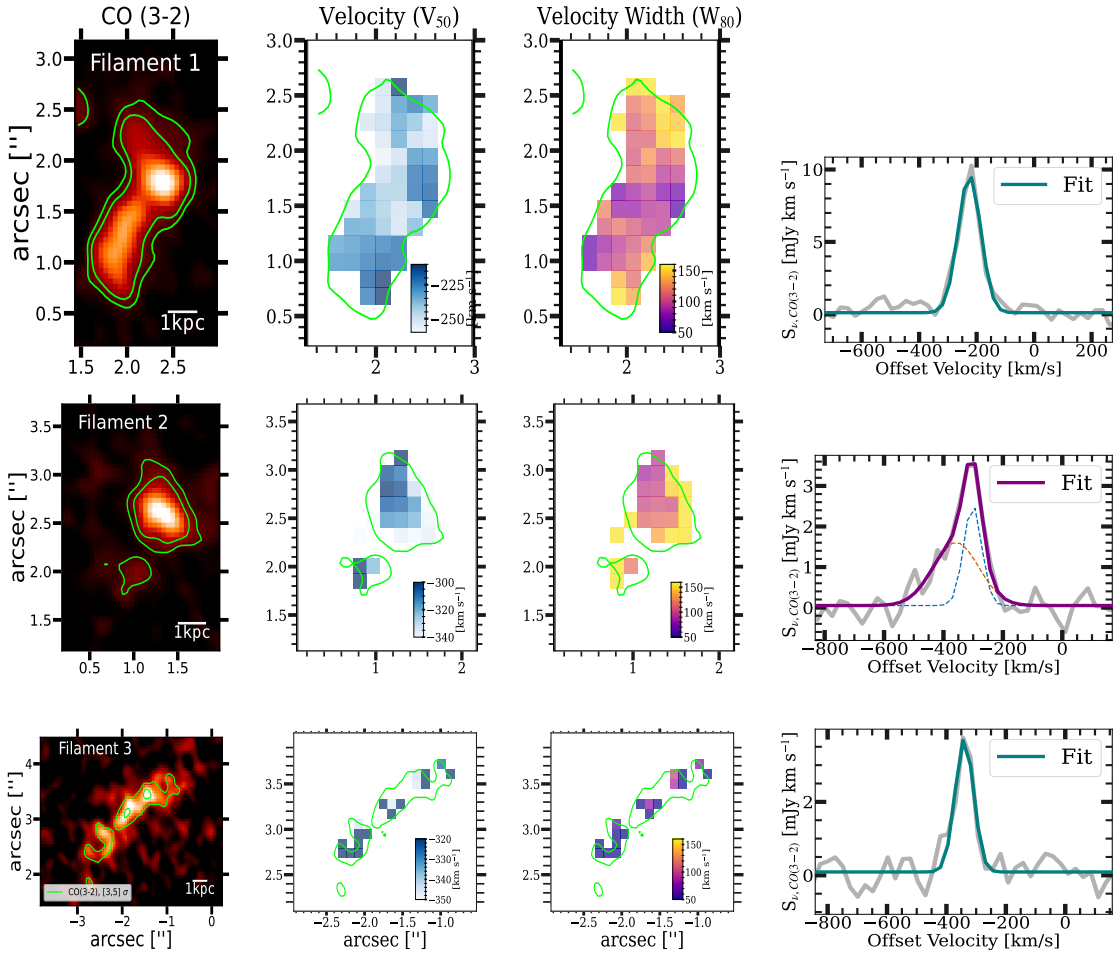

Figure 4.11: Kinematic analyses of the filamentary molecular gas structures in J1010+1413. Each row corresponds to a single filament, numbered 1−3, as shown in Figure 3. *(From Left to Right:)* (1) CO(3–2) emission-line map, collapsed over the velocity range of the filament (see Section 3.1); (2) velocity map (V_{50}); (3) velocity width map (W_{80}); (4) CO(3–2) emission-line profile obtained over the entire filament region. The CO(3–2) emission is highlighted with 3σ and 5σ contours in the first column and overlaid on the kinematic maps the same 3σ contour is shown. In the final row, the coloured solid curves show the emission-line fits, and the dashed curves show the individual Gaussian components (when more than one).

We thank Helen Russell for helping us obtain the values for the CO velocity widths. This paper makes use of the following ALMA data: ADS/JAO.ALMA#2016.1.01535.S and ADS/JAO.ALMA#2018.1.01767.S. ALMA is a partnership of ESO (representing its member states), NSF (USA) and NINS (Japan), together with NRC (Canada), MOST and ASIAA (Taiwan), and KASI (Republic of Korea), in cooperation with the Republic of Chile. The Joint ALMA Observatory is operated by ESO, AUI/NRAO and NAOJ. This research has made use of the NASA/IPAC Extragalactic Database (NED), which is funded by the National Aeronautics and Space Administration and operated by the California Institute of Technology. This research mainly uses the Python packages: Astropy,[6] a community-developed core Python package for Astronomy (Astropy Collaboration et al., 2013, 2018); SciPy (Virtanen et al. 2020a); NumPy (Harris et al. 2020); Matplotlib (Hunter 2007).

[6] http://www.astropy.org

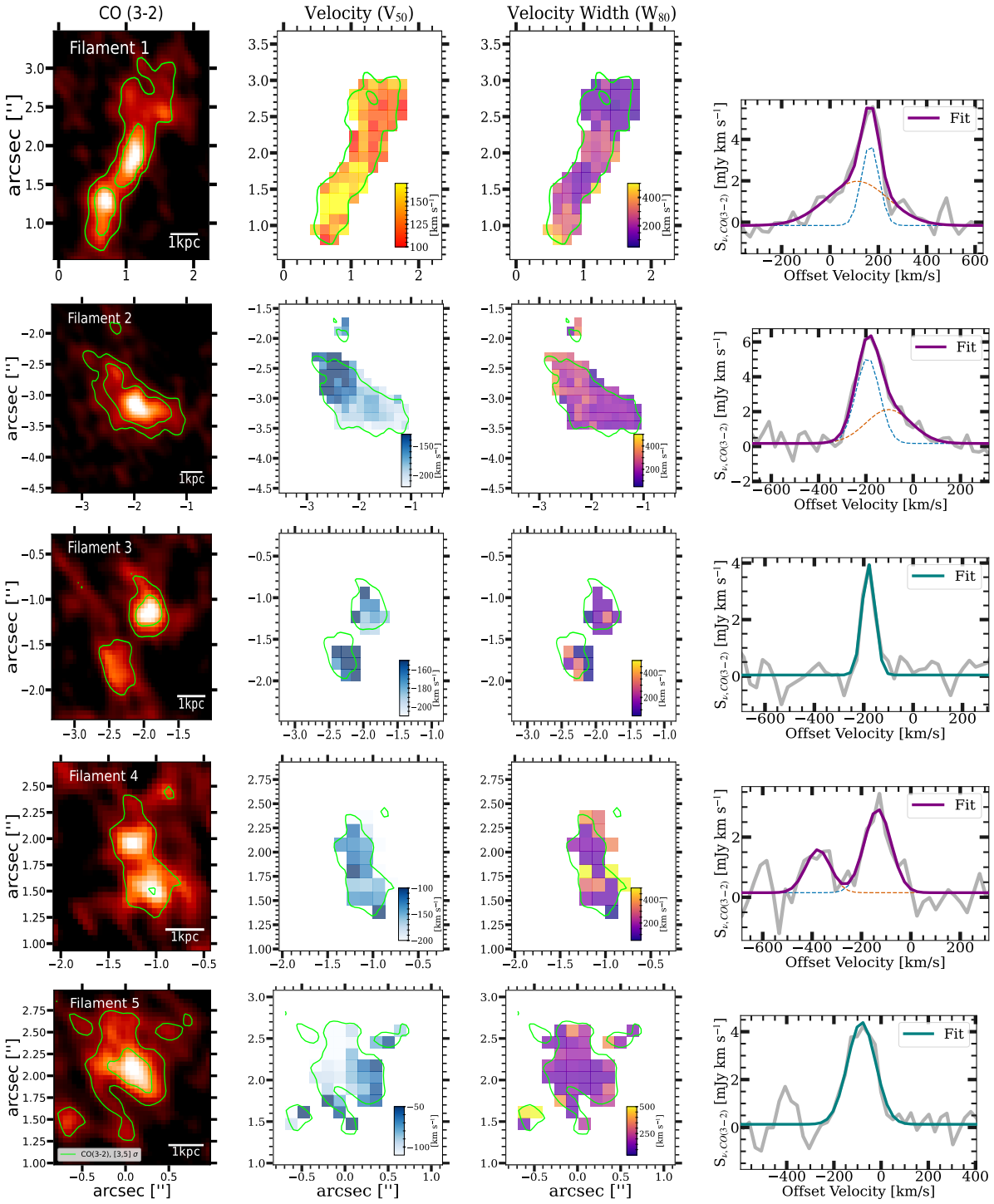

Figure 4.12: Same as Figure **4.11** but for J1000+1242 with its 5 identified filamentary molecular gas structures.

Data Availability

The MUSE and ALMA data presented in this analysis were accessed from the ESO and ALMA archives under the proposal ids: 0103.B-0071, 0102.B-107, and 0104.B-0476 for the MUSE data and ADS/JAO.ALMA#2016.1.01535.S and ADS/JAO.ALMA#2018.1.01767.S for the ALMA data. The VLA images used in this work are available at Newcastle University's data repository (`https://data.ncl.ac.uk`) and can also be accessed through our Quasar Feedback Survey website.

Chapter 5

Multi-phase quasar analysis

Understanding the dependency of quasar feedback on the radio jet properties

This work presents the study of 9 $z \leq 0.2$ type 2 luminous ($L_{bol} >= 10^{45}$ erg s^{-1}) quasars. These quasars are classified as 'radio quiet' with their modest radio luminosities ($L_{1.4GHz} = 10^{23.3-24.4}$ W Hz^{-1}), but host compact low-power jets ($P_{jet} = 10^{43-44}$ erg s^{-1}). Using high-resolution ALMA data for tracing the molecular gas with the CO (3–2) emission, and MUSE data for ionised gas with [OIII] emission, a systematic study reveals the presence of multi-phase AGN outflows in all 9 targets. The stellar morphologies and kinematics reveal a range of host galaxy types (ordered spiral galaxies, elliptical galaxies, and on-going mergers with irregular morphologies). The AGN outflows are observed to be 2 – 5 times slower, and at least 5 times less extended in the molecular phase as compared to the ionised phase. However, when the analysis is limited to the regions with molecular outflows, the fractional flux contribution across both the phases is observed to be comparable ($\sim 50-90\%$). The work also undertakes a systematic study of the interaction of the radio jets on different spatial scales. On the central scales ($\sim 1.5-3$ kpc, i.e., within the molecular gas disks), jet-ISM interactions are seen to be causing multi-phase outflows in all targets. On extended scales (≥ 10 kpc), the molecular gas is observed to be entrained along the radio bubbles only in three targets. These molecular gas structures are seen only for the 3/5 targets in which radio lobes are also observed to extend beyond the molecular gas disks. However, no such structures are observed for the cases where the radio structures are compact. These results are qualitatively similar to predictions of low-power jets interacting on small and large scales in gas-rich galaxy disks. However, this small sample does not reveal clear trends between the strength of the observed outflows and the relative location of the jets with respect to the galaxy disks (extent and inclination angle) predicted by these simulations.

5.1 Introduction

AGN are fundamental in galaxy formation simulations to explain the properties of massive galaxies and their central black holes (Schaye et al. 2015; Pillepich et al. 2018; Davé et al. 2019). However, the impact of the AGN on its host galaxy, or AGN-feedback, is particularly unclear for the case of the galaxies hosting the most luminous AGN, i.e., quasars. In simulations, as well as observations, AGN-driven outflows have become a significant diagnostic tool to search for AGN feedback (see Harrison et al. 2018a for a full review). AGN-driven multi-phase gas outflows have been observed and are seen to influence the interstellar medium (ISM) of the host galaxy and have the potential to regulate its star formation. (McNamara & Nulsen 2007, 2012; Alatalo et al. 2011; Fabian 2012; Combes et al. 2013; García-Burillo et al. 2014; Morganti et al. 2015; Mukherjee et al. 2018b; Costa et al. 2020).

A complete understanding of AGN-driven outflows can be a challenging process as they are observed to cover a broad range of morphologies and multiple phases; as is also predicted by simulations (An & Baan 2012; Morganti et al. 2013; Rupke &

Veilleux 2013a; Harrison et al. 2014; Fiore et al. 2017; Husemann et al. 2019; Herrera-Camus et al. 2020; Comerón et al. 2021). This hence underlines the requirement of a multi-phase overview for a comprehensive understanding of the feedback processes at play in a galaxy. Additionally, it is highly debated which mechanism drives the outflows, with possible candidates being AGN-driven central winds, radio jets, and/or radiation pressure (e.g. see, Ishibashi et al. 2018; Mukherjee et al. 2018b; Costa et al. 2020). This is especially unclear for the 'radio quiet' quasars (e.g. Zakamska et al. 2016; Wylezalek & Morganti 2018; Fischer et al. 2023) and forms the motivation of this study. For example, molecular gas outflows have been observed in a variety of AGN-luminosity systems such as Seyferts, Quasars, and ULIRGS (e.g. see, Cicone et al. 2014; Pereira-Santaella et al. 2018; Fluetsch et al. 2019, 2021; Herrera-Camus et al. 2020). Studies of these molecular outflows in high-luminosity systems such as quasars are helping in understanding the role of AGN luminosity in driving these outflows. On the other hand, studies have also observed that the molecular gas outflows in galaxies hosting jets were seen to be more extreme, i.e., faster and more massive; tentatively hinting at the role of jets in launching and/or accelerating these molecular gas outflows (see García-Burillo et al. 2014, 2019; Morganti et al. 2015; Wylezalek & Morganti 2018). Recent studies have further highlighted the impact low-power jets can have in driving nuclear molecular outflows (e.g. see Aalto et al. 2016; Fernández-Ontiveros et al. 2020; Girdhar et al. 2022; Ramos Almeida et al. 2021; Audibert et al. 2023). Hence, the specific properties of the driving mechanism and host galaxy ISM might be crucial to appreciate the level of impact the AGN can have.

This calls for a systematic study to investigate the responsible physical feedback mechanisms at different scales and assess the prevalence of these processes. The Quasar Feedback Survey[1](QFeeds; see Section 3.2.1) provides a multi-phase data sample suitable for this objective. QFeedS consists of a sample of 42 quasars at $z \leq 0.2$, which provides spatially-resolved multi-phase observations of powerful quasars ($L_{bol} \gtrsim 10^{45}\,erg\,s^{-1}$; see Jarvis et al. 2021; Girdhar et al. 2022). These quasar luminosities are similar to the peak luminosities at the cosmic epoch of growth thereby enabling the study of quasars with luminosities similar to those seen in quasars with dominant gas outflows. For the analysis here, I study 9, $z \sim 0.1$, type-2 quasars from QFeedS. In Chapter 3, a case study from the QFeedS sample revealed low-power inclined jets launching multi-phase gas outflows. This was observed in both ionised and molecular gas but the former phase was seen to be comparatively faster and extended. This is in agreement with simulations that show that a radio jet inclined into a disk of clumpy ISM is likely to have a more direct impact on the host than a jet orientated along the minor axis of a disk (Mukherjee et al. 2016; Tanner & Weaver 2022; Meenakshi et al. 2022). However, we lack systematic observational tests of these predictions. Subsequently, the molecular gas analysis performed on 4 of these 9 targets in Chapter 4, using CO (3–2) data obtained from ALMA (Girdhar et al. submitted), revealed that 2/4 targets showed molecular gas structures associated with the expanding radio lobes on large scales; and 4/4 targets showed high-velocity CO outflows in the central regions. These targets were, however, selected to have known radio structures extending beyond 10 kpc, i.e., with $LLS_{radio} > 10\,kpc$.

[1] https://blogs.ncl.ac.uk/quasarfeedbacksurvey/

In this chapter, I aim to extend the work in the previous two chapters by, (i) removing the $\mathrm{LLS_{radio}} > 10\,\mathrm{kpc}$ criteria and additionally exploring the [OIII] emission to supplement the understanding of how the radio emission affects the host galaxy disk properties; (ii) methodically looking for the interaction of the radio emission at different spatial scales. Hence, for the sample of these 9 quasars, the focus will be to put in context which of the processes are relevant in which galaxies and if, and how, this depends on the host galaxy and/or the radio jet properties.

The chapter is outlined as follows. In Section 5.2, the sample selection methods are described, followed by the process to obtain science-ready data products. Section 5.3 presents a qualitative multi-phase overview of the selected targets and the associated methods. In Section 5.4 the interaction of the radio lobes on the molecular gas at large scales is analyzed and discussed. Firstly, the methods are described to identify the molecular gas structures at these scales and thereafter their properties and the impact observed on them are discussed in this section. In Section 5.5, the interaction of the radio jets on the small scales is studied (i.e. $\sim$kpc scales). The section describes the methods followed to observe the presence of any gas outflows and discusses their properties over the molecular as well as ionised phase. This is followed by a parameter space study to understand the relationship between the radio jet properties and the outflow properties, motivated by predictions from jet-ISM simulations. Finally, Section 5.6 concludes this chapter and discusses the results from the broader perspective of AGN feedback, while also speculating a possible evolutionary sequence of AGN feedback due to the evolution of the low-power jets as they progress through the galaxy-ISM.

The values of the cosmological parameters used are $H_0 = 70$ km s^{-1} Mpc^{-1}, $\Omega_M = 0.3$ and $\Omega_\Lambda = 0.7$. In this cosmology, 1 arcsec corresponds to 1.84 kpc for the redshift of $z = 0.1$ (i.e., the average redshift of the galaxies studied here). When referred to, the radio spectral index, α, is defined using $S_\nu \propto \nu^\alpha$.

5.2 Sample selection and data

Section 5.2.1, describes the sample selection used for this study and thereafter the methods to obtain science-ready data products, are outlined in Section 5.2.2.

5.2.1 Sample Selection

To select the sample of targets for this analysis, a comparison of all 42 targets from QFeedS was done based on the largest linear size of their radio structures ($\mathrm{LLS_{radio}}$) and their [O III] luminosities, as shown in Figure 5.1. The $\mathrm{LLS_{radio}}$ is a quantitative measure of the projected radio size of the sources (from Jarvis et al. 2021). The LLS values are measured using the VLA C-band data at 6 GHz ($\sim$1 arcsec resolution). For completeness, the $\mathrm{LLS_{radio}}$ values of five of the targets from Jarvis et al. 2019, are also shown using grey stars. In this earlier study, these measurements were made using slightly different data products, in which the radio image construction parameters were optimised to draw out the extended radio structures for the individual targets.

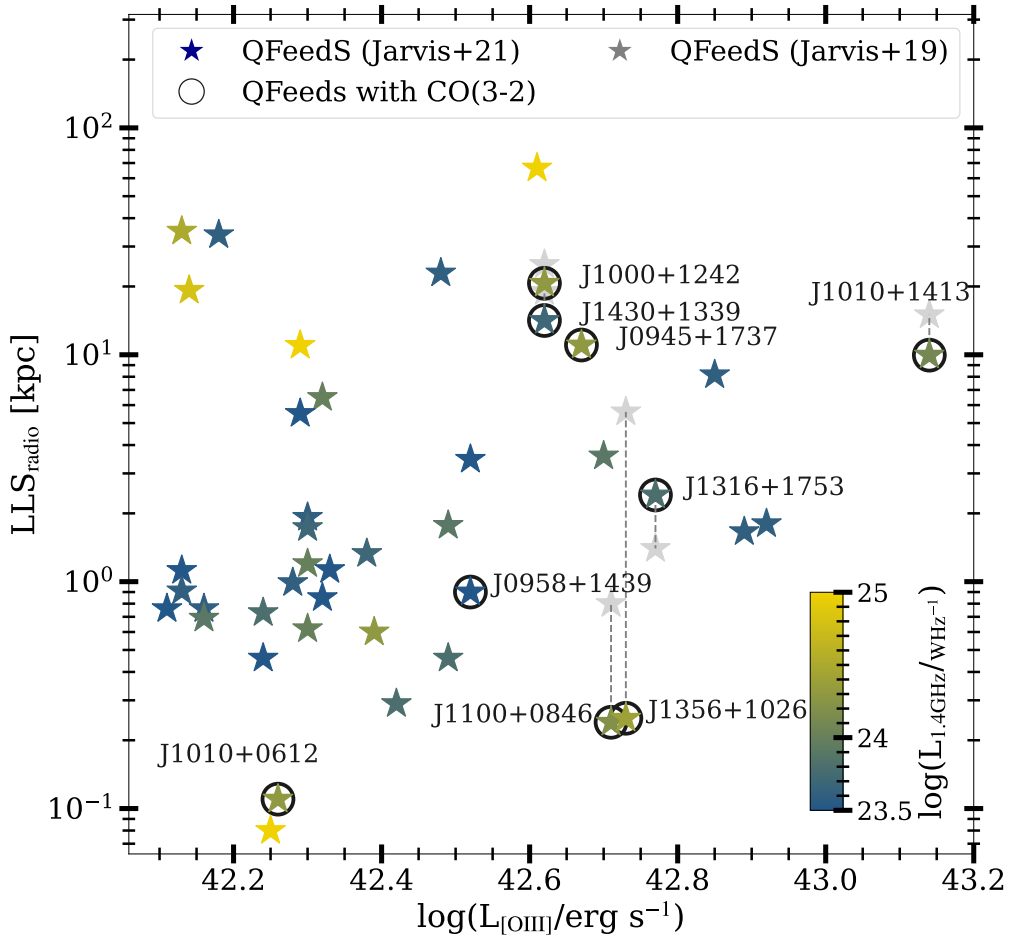

Figure 5.1: Largest linear size of radio structures (LLS_{radio}) versus [O III] luminosity for the parent sample of 42 QFeedS targets, colour-coded by their 1.4 GHz radio luminosity (Jarvis et al. 2021). The 9/42 QFeedS targets with the required CO(3–2) ALMA data are highlighted with a black circle. Additionally, the LLS_{radio} sizes from Jarvis et al. (2019) are shown using grey stars and are joined to their counterparts with dashed grey lines. The 9 targets are selected as such to have data available in the same wavelengths for comparison (see Section 5.2.1). Table 5.1 presents further details on the 9 targets.

In the later study (Jarvis et al. 2021), a more consistent approach was used to produce the radio images for all 42 targets, using consistent imaging parameters. For clarity, the LLS values estimated in both studies are listed in Table 5.1.

With the objective of performing a multi-phase analysis, the targets with data available in radio, molecular, and ionised phases were selected. Since only 9/42 targets (encircled in black) have the required molecular phase data available in the form of CO (3–2) emission from ALMA, these were chosen as the final sample. All 9 targets also have available MUSE data (see Section 5.2.2). The 9 selected quasars are labeled in the figure and Table 5.1 provides an overview of their properties, namely, positions, redshifts, luminosities (bolometric, radio, [OIII]) and largest linear scales of the radio structures.

5.2.2 Data Reduction

As briefly mentioned above, I have combined the following available datasets for the selected targets for a multi-phase overview:

- ALMA, for the molecular gas information based on the CO (3–2) emission line;
- MUSE, for the stellar kinematics and for the ionised gas information utilising the [OIII] emission line;
- VLA, for the radio continuum emission at 6 GHz.

The methods outlined in Section 4.2 have been used to obtain the reduced data products in each case, but now expanding to the 9 targets used in this work.

Briefly, for the VLA data, the C-Band images at 6 GHz were used at low-resolution (LR) and high-resolution (HR). In each of the figures in this chapter, the contours from both low- and high-resolution radio images are shown, which helps visualise the variation of the radio continuum. The LR images have an average major axis beam size of $\sim$1 arcsec while the HR images have ~ 0.2 arcsec (i.e. ~ 2 kpc and 0.5 kpc, respectively, at $z = 0.1$).

To obtain the ionised gas kinematics and stellar kinematics, I use the data obtained with the MUSE instrument. The final MUSE stacked cubes were obtained from the ESO archive[2] using a combination of the proposals 0103.B-0071 (PI: C. Harrison), 0102.B-107 (PI: Sartori) and 0104.B-0476 (PI: G. Venturi). For the stellar kinematics, I employed the GIST[3] (Bittner et al. 2019) pipeline which implements stellar continuum fitting to obtain stellar velocity and stellar velocity dispersion (see Section 3.4.3).

Finally, the ALMA data are reduced following the steps illustrated in Section 4.2.2. All 9 targets were observed in the same ALMA band, covering the CO (3–2) emission. 7/9 datacubes are obtained from the ALMA project 2018.1.01767.S (PI: A.P. Thomson). For the other two, archival data is used; i.e., J1430+1339 is obtained from the observing programme 2016.1.01535.S (PI: G. Lansbury) and J1356+1026 is obtained from 2012.1.00797.S (PI: J. Greene). The details of the datasets for the former two programmes can be found in Section 4.2.2. Noting that the datacubes for targets, J0945+1737, J1000+1242, J1010+1413, and J1430+1339 are exactly the same as that used Chapter 4; for J0958+1439, J1010+0612, J1100+0846, and J1316+1753, the same data reduction was employed as the observational set up was also the same across all these targets of the programme 2018.1.01767.S. The major axis of the synthesised beam sizes of these data cubes range from $0.32 - 0.70$ arcsec. The exception is, J0958+1439, for which the final data cube has a beam size of 1.2×1.0 arcsec. Using a higher resolution (smaller beam) in the cleaning stages did not recover any significant emissions for the target. However, on using a weighting scheme to favor the large-scale structures, significant emissions were detected (as shown in Figure 5.2).

[2] http://archive.eso.org/scienceportal/
[3] https://abittner.gitlab.io/thegistpipeline/

For the target J1356+1026, the observations were performed in Band-7, with a field-of-view of 21 arcsec. The spectral setup of the observation had a total band-width of 2 GHz corresponding to a channel width of 15 $\mathrm{km\,s^{-1}}$(or 15.63 MHz). Fresh data calibration was carried out using ALMA CASA version 6.4.3 to obtain the data product similar to the others. The resulting angular resolution of the observation was $\sim 0.6 \times 0.3$ arcsec.

Table 5.1: Study targets and their properties: (1) quasar name; (2) redshift; (3) and (4) optical Right Ascension and Declination positions from SDSS (DR7: Abazajian et al. 2009) in the format hh:mm:ss.ss and dd:mm:ss.s, respectively. Values in (5)-(7) are from Jarvis et al. (2019): (5) bolometric AGN luminosity; (6) [O III] luminosity; (7) 1.4 GHz radio luminosity; and (8) largest linear size measured for the radio structures (LLS_{radio}) as estimated through a uniquely catered and a uniform approach following Jarvis et al. (2021) and Jarvis et al. (2019), respectively.

Quasar	z (SDSS)	RA (J2000)	Dec (J2000)	$\log(L_{bol})$ [erg s^{-1}]	$\log(L_{[OIII]})$ [erg s^{-1}]	$\log(L_{1.4GHz})$ [W Hz^{-1}]	LLS_{radio} [kpc]
(1)	(2)	(3)	(4)	(5)	(6)	(7)	(8)
J0945+1737*	0.1281	09:45:21.30	+17:37:53.2	45.70	42.66	24.3	11.04/11.00
J0958+1439	0.1091	09:58:16.88	+14:39:23.7	45.20	42.51	23.5	0.9/0.9
J1000+1242*	0.1479	10:00:13.14	+12:42:26.2	45.30	42.61	24.2	20.66/25
J1010+0612	0.0982	10:10:43.36	+06:12:01.4	45.30	42.25	24.4	0.11/-
J1010+1413*	0.1992	10:10:22.95	+14:13:00.9	46.20	43.13	24.0	9.96/15
J1100+0846	0.1004	11:00:12.38	+08:46:16.3	46.00	42.70	24.2	0.24/0.8
J1316+1753†	0.1504	13:16:42.90	+17:53:32.5	44.40	42.76	23.8	2.41/1.4
J1356+1026	0.1233	13:56:46.10	+10:26:09.0	45.20	42.72	24.4	0.25/5.6
J1430+1339*	0.0852	14:30:29.88	+13:39:12.0	45.50	42.61	23.7	14.16/19

†Target studied in Chapter 3

*Targets studied in Chapter 4

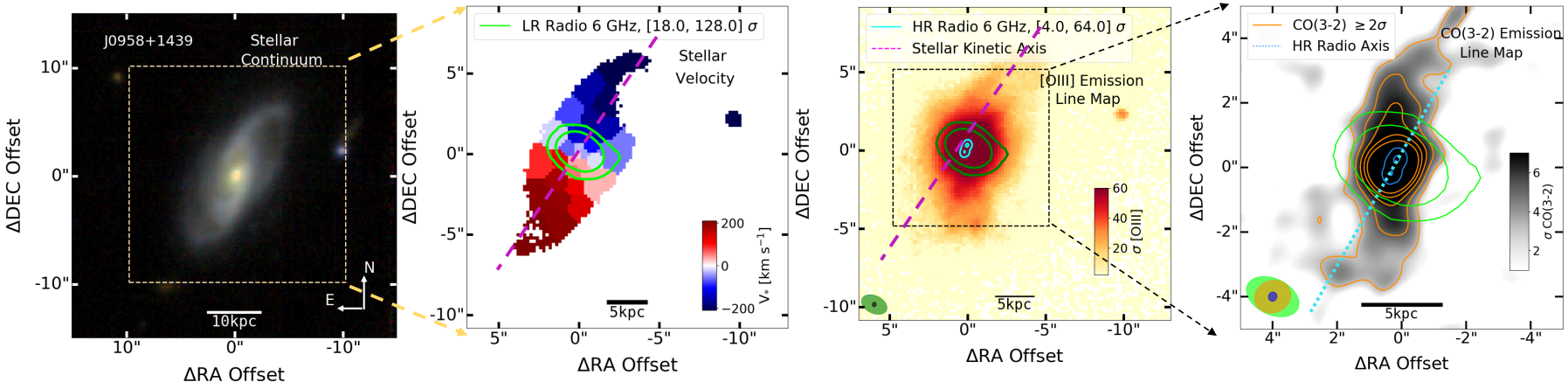

Figure 5.2: A multi-phase overview of the targets, with each row representing a unique target, this panel: J0958+1439. For each target, the ***first column*** shows the 3-color stellar continuum image integrated over continuum ranges as indicated in Table 5.2. The target name is indicated to the top-left in this panel. The arrows at the bottom-right show the North and East orientation of the target in the sky. The dashed-golden box, when shown indicates the region from which the stellar and ionised gas kinematics are extracted in the subsequent panels. A scale bar at the bottom represents 10 kpc spatial extent. In the ***second column***, the stellar velocity is shown in Voronoi bins as described in Section 5.3. The green contours represent a low-resolution radio continuum at 6 GHz at the levels as indicated in the individual legends. The dashed magenta line represents the major stellar kinematic axis. The bottom scale bar now represents 5 kpc distance. In the ***third panel***, the [OIII] emission map is shown with the emission levels normalised by the signal-to-noise level of the image as shown in the color bar. In addition to the green contours (that are same as the previous column), there are also blue contours showing the radio continuum emission at 6 GHz from high-resolution VLA images. The bottom-left shows the beams of both the low- and the high-resolution VLA images in green and blue contours, respectively. The dashed black box shows the extent over which the CO emission is obtained in the next panel. In the ***fourth-panel***, the CO (3–2) emission line map, extracted from ALMA data, is shown. The orange contours trace the CO-emission at levels as indicated in the individual panels. The emission map is also normalised for the noise in the CO-cube and the levels are as indicated in the color bar. The light blue, dotted line shows the alignment with the radio jet axis. In addition to the two radio beams, the ALMA beam is also shown at bottom-left in this column in orange.

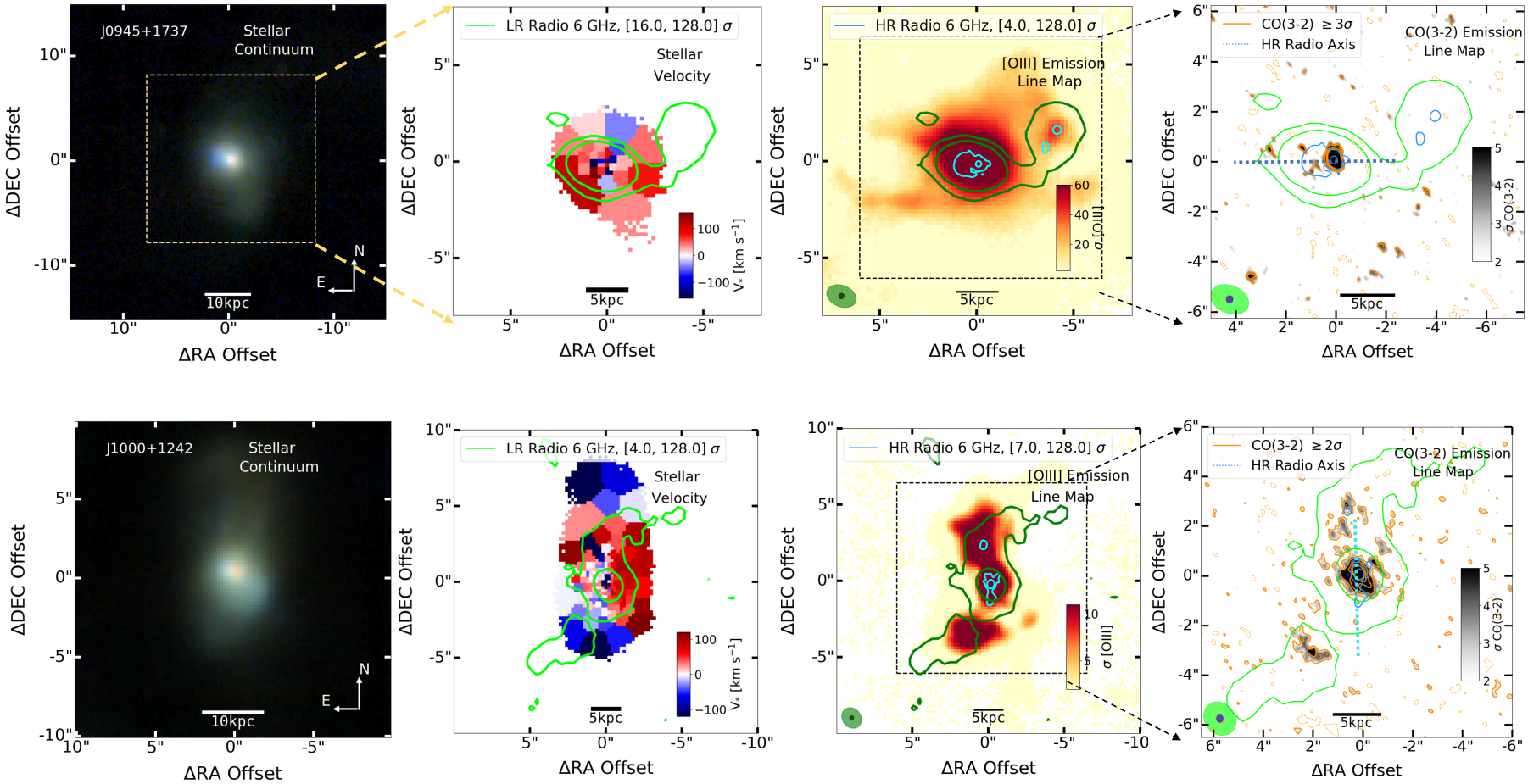

Figure 5.2: Figure caption as above, but for J0945+1737 (top row) and J1000+1242 (bottom row).

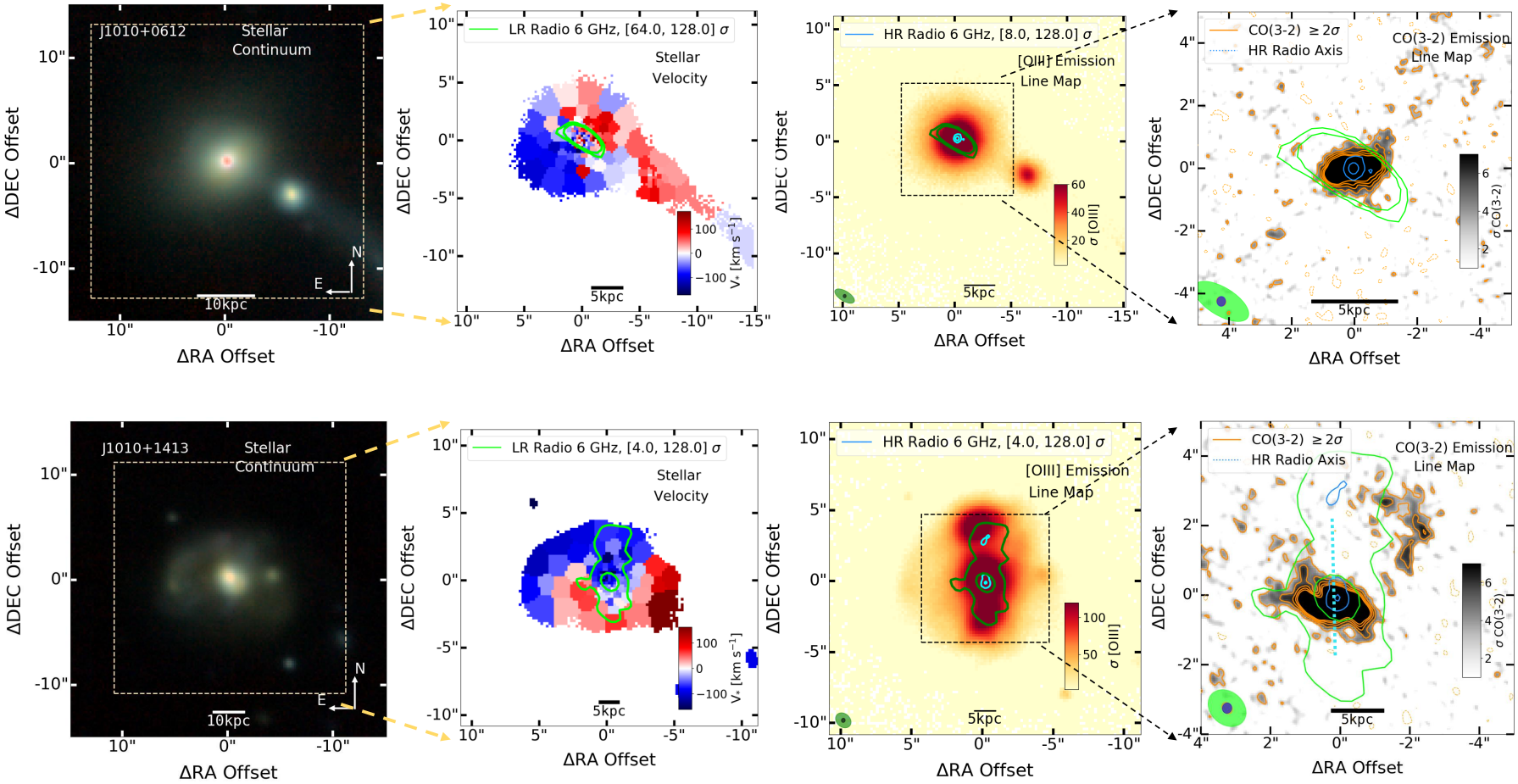

Figure 5.2: Figure caption as above, but for J1010+0612 (top row) and J1010+1413 (bottom row).

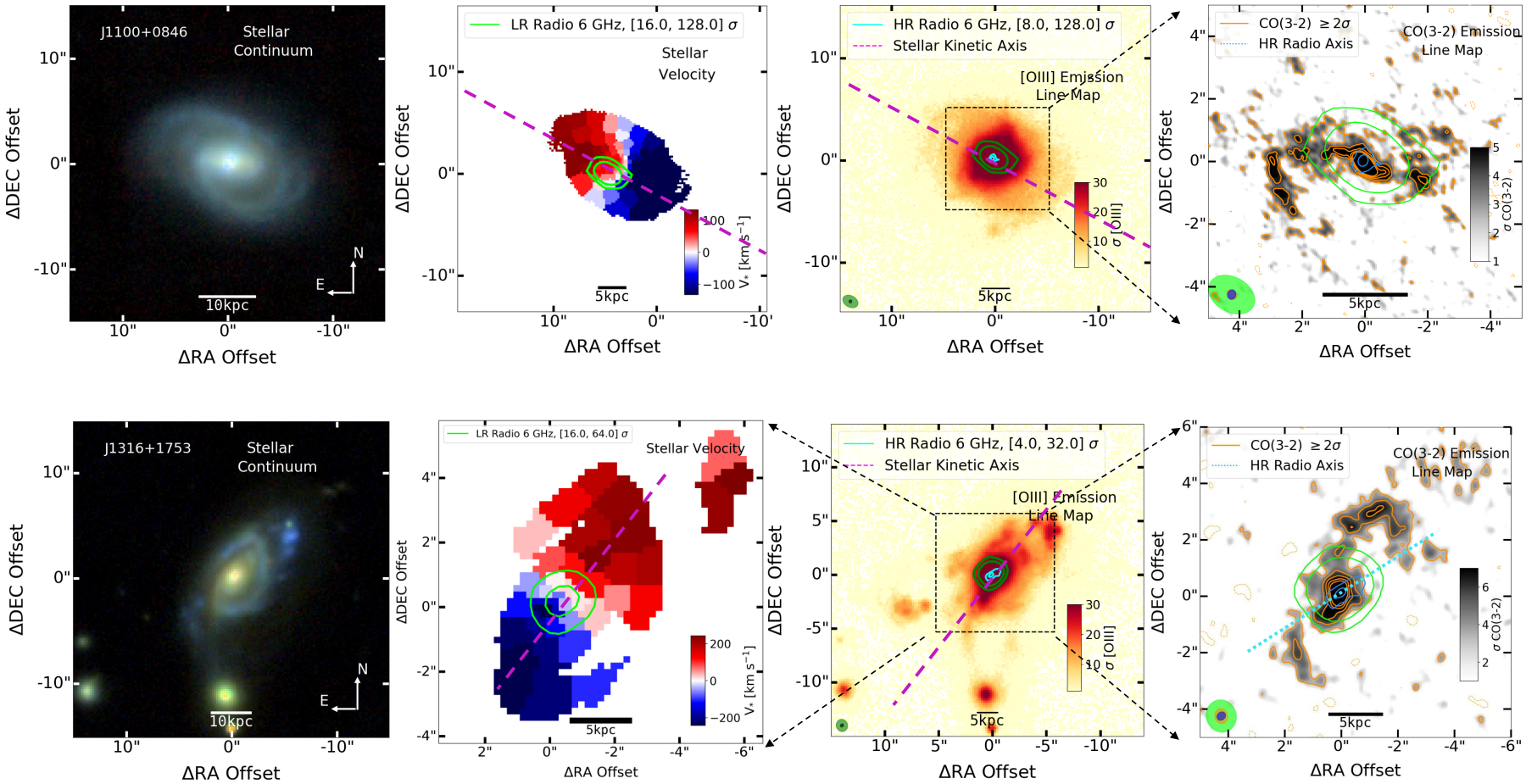

Figure 5.2: Figure caption as above, but for J1100+0846 (top row) and J1316+1753 (bottom row).

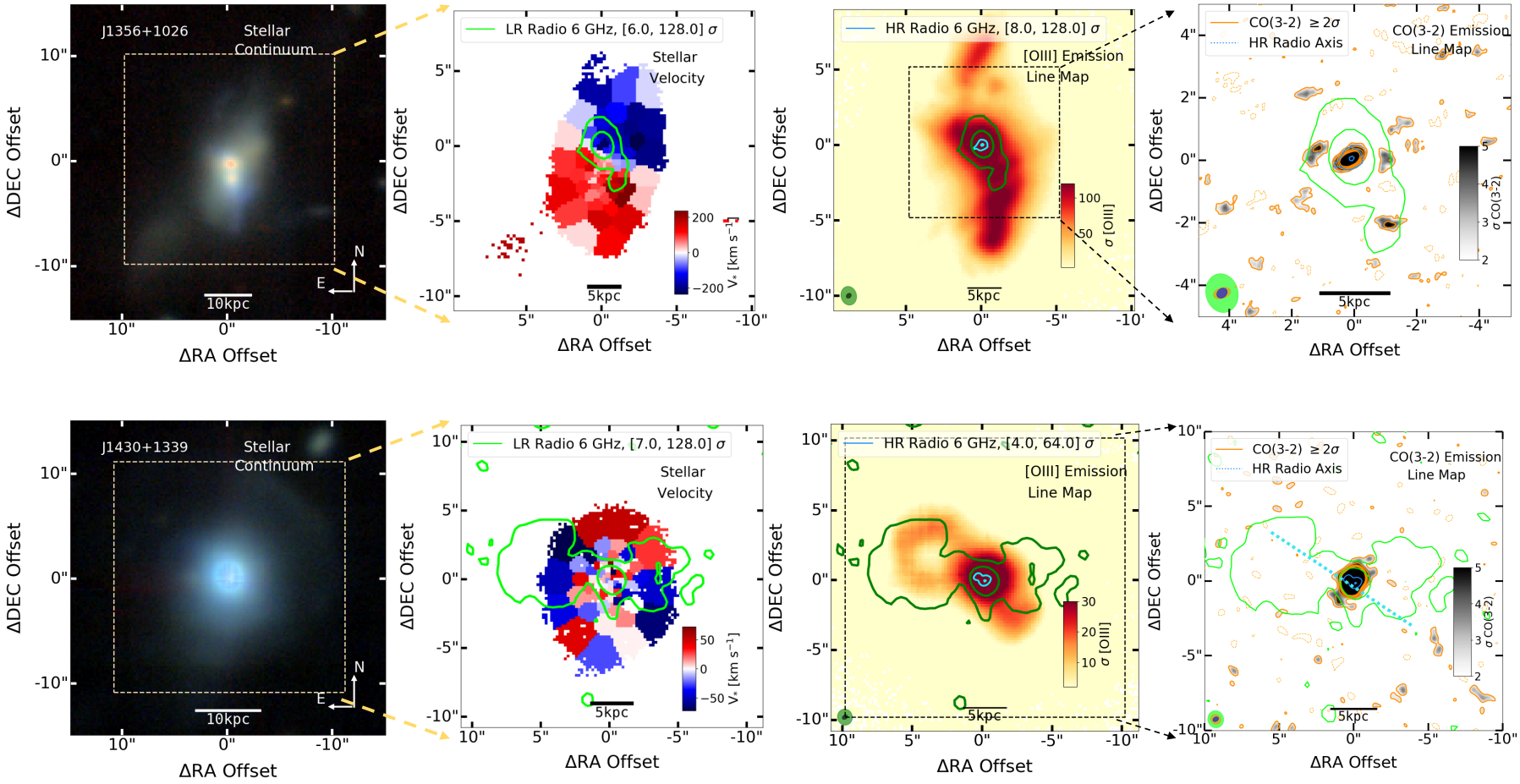

Figure 5.2: Figure caption as above, but for J1356+1026 (top row) and J1430+1339 (bottom row).

5.3 Multi-phase overview of the 9 selected targets

In this section, I qualitatively explore the 9 targets, based on their stellar emission (morphology and kinematics), the distribution of ionised gas (traced via [OIII]) and molecular gas (traced via CO(3–2)), and relate these properties to the radio structures observed in each target. This analysis will be used to guide the interpretation of the quantitative results on the gas kinematics presented in the following sections.

5.3.1 Methods to obtain the multi-phase properties

Figure 5.2 presents a multi-phase overview of the 9 targets studied in this chapter. Each row shows a different galaxy wherein from left-to-right, each column presents the following: (a) a three-color continuum image; (b) a map of the stellar velocity; (c) an emission line map of [OIII] to show the ionized gas distribution; and (d) an emission line map of CO (3–2) to show the molecular gas distribution. As detailed below, the first three columns are obtained using the MUSE datacubes, and the last column is obtained using the ALMA datacubes.

The galaxy continuum images were designed to trace the stellar emission (see first column in Figure 5.2). To obtain these, all emission lines were masked and three different line-free continuum ranges were selected from the overall galaxy spectra. The choice of the three continuum ranges was roughly to cover bluer (shorter) wavelengths, greener (middle) wavelengths, and redder (longer) wavelengths. The three continuum ranges for each galaxy are indicated in Table 5.2. Individual color images were obtained obtained from each of these wavelength bands and combined using `make_lupton_rgb` function of `astropy` library[4] to obtain a 3-color stellar continuum image.

To obtain the stellar velocity maps, firstly the GIST pipeline (Bittner et al. 2019) was employed following the steps outlined in detail in Section 3.4.3. However, briefly, each galaxy was first divided into Voronoi bins corresponding to a signal-to-noise ratio of 30 following the Voronoi tessellation routine (Cappellari & Copin 2003). Then from each bin, the combined spectra were extracted and all emission lines were masked. This was then followed by fitting the stellar continuum for each bin using the stellar templates from the XSL library (Arentsen et al. 2019; Gonneau et al. 2020) and employing the pPxF routine (Cappellari & Emsellem 2004; Cappellari 2017). GIST provides a pipeline to implement each of these steps and obtain for each galaxy bin a value for stellar velocity and stellar velocity dispersion. To obtain the systemic galaxy redshifts and total galaxy velocity dispersion values, I used the flux-weighted average over all the Voronoi bins. When possible (i.e., where the kinematics look rotation-dominated), the stellar velocity map is also used to obtain the galaxy's kinematic major axis as shown through a pink dashed line in the second and third column of Figure 5.2 .

To obtain the [OIII] emission line map (i.e. the third column in Figure 5.2), the MUSE cube was collapsed over a narrow wavelength range corresponding to the [OIII] emission. Care was taken to first subtract the continuum so a continuum-free emission line map could be obtained. A continuum of equivalent wavelength-width was subtracted from the [OIII] emission map. For a better image representation, the

[4] Astropy Collaboration et al. 2013, 2018

Table 5.2: Study targets and their stellar continuum properties: (1) quasar name; (2-4) wavelength bands used to create the 3-color images from blue, green and, red wavelength ranges, respectively; (5-6) systemic redshift estimated using the stellar velocity; and the stellar velocity dispersion obtained from the stellar continuum fits (see Section 5.3.1).

Quasar	Blue Range Å	Green Range Å	Red Range Å	z_*	σ_* [$\mathrm{km\,s^{-1}}$]
(1)	(2)	(3)	(4)	(5)	(6)
J0945+1737	[5100, 5120]	[6650, 6800]	[9230, 9300]	0.12840	162.74
J0958+1439	[4900, 5120]	[6680, 6800]	[7200, 7230]	0.10908	132.52
J1000+1242	[4760, 4880]	[6100, 6250]	[9150, 9280]	0.14787	173.47
J1010+0612	[4830, 5200]	[6640, 6750]	[9270, 9285]	0.09843	230.94
J1010+1413	[4950, 5170]	[6610, 6800]	[9260, 9290]	0.19877	271.63
J1100+0846	[4850, 5050]	[6720, 6775]	[9240, 9280]	0.10040	179.00
J1316+1753	[4740, 4830]	[6660, 6750]	[9170, 9280]	0.15004	241.24
J1356+1026	[5125, 5200]	[6680, 6800]	[9230, 9280]	0.12348	191.80
J1430+1339	[4900, 5050]	[6600, 6800]	[9020, 9250]	0.08507	182.80

emission line map was then normalized using the image's SNR between the velocity ranges as shown in the corresponding color bars. The image SNR was calculated by estimating the noise in the image after masking the central bright source. The black dashed box in this image represents the spatial extent of the molecular gas map, shown in the right-most column.

To obtain the CO (3–2) map (shown in the last column in Figure 5.2), a similar procedure to that used for [OIII] was followed but using the ALMA cube, collapsed over the CO (3–2) line. The orange contours show the CO (3–2) contours at levels as indicated in the legends in each panel. The beam corresponding to each observation is shown in orange at the bottom-left of the panels. This panel also shows the identified radio axis using a blue-dotted line. To obtain the radio axis, I joined the hotspots seen in the high-resolution radio emission and extrapolated this across the galaxy. Radio contours corresponding to low and high-resolution continuum emission at 6 GHz are shown using green and blue colors, respectively, in different panels. The beams corresponding to the VLA observations are shown in respective colors at the bottom-left of the emission line maps. The contour levels are indicated in the legend of each galaxy panel.

5.3.2 Results of the multi-phase overview of the 9 targets

Following from Figure 5.2 , a few features of the galaxy become apparent that I have summarised below, along with an overview of the relevant properties of each as known from the literature.

J0945+1737 shown in Figure 5.2 *second row*, doesn't show a clear disk-like structure from its stellar continuum (first column) and nor seems to have stellar kinematics dominated by rotation as seen through its stellar velocity plot (second column). It therefore has the appearance of an elliptical galaxy. Large radio structures can be seen to extend to about 2 kpc to the East and 11 kpc to the North-West. Closer to where the North-West radio lobe extends, an enhancement in [OIII] emission can be seen (see third column). Previous works have also confirmed complex ionised

gas kinematics in this region (see Harrison et al. 2014; Kang & Woo 2018; Jarvis et al. 2021). The [OIII] emission appears irregular and extends to ~ 15 kpc to the East. HST-observations of the source also confirm a single nucleus in continuum and an extended emission line region (Storchi-Bergmann et al. 2018). The molecular gas, on the contrary, appears, to be very compact, within the central few kpcs. No spatial alignment between the extended radio structures and the molecular gas are apparent. However, it is known to be a gas-rich, star-forming galaxy and is seen to be bright in CO (2–1) emission (Jarvis et al. 2020). Further, the source is known to host a warm-molecular gas outflow when studied with K-band near-infrared integral spectrograph (see Speranza et al. 2022).

J0958+1439 is presented in Figure 5.2 (*first row*). It is observed to be a beautiful spiral galaxy as seen from the stellar continuum (first column). The stellar velocity appears to have regular rotational dynamics ranging between ± 200 km s^{-1}. A stellar kinematic axis could be obtained as shown through a dashed pink line (see second column). The [OIII] emission appears to be roughly extending up to the galaxy disk scales (see third column). The low-resolution radio contours shown no structures; however, the high-resolution 6 GHz contours (shown as blue) reveal the presence of a double-sided radio jet, on $\lesssim 1$ kpc scales. This appears to be closely aligned into the galaxy disk, and the radio hotspots are clearly still within the molecular gas disk (fourth column). The molecular gas disk extends to similar scales, as seen in ionised gas phase, and the morphological major axis of the molecular gas disk is closely aligned to the radio jet axis (shown through a dashed blue line). Previous work revealed a spatial association between the location of the radio hot spots and kinematic line-splitting of the ionised [OIII] line-profile (see Harrison et al. 2014; Jarvis et al. 2019).

J1000+1242 is presented in Figure 5.2 *third row*. It appears to be an irregular galaxy from the stellar morphology (first panel), which is also evident from the irregular stellar velocity field (second panel) and a dominant kinematic axis could not be established. This target is likely to have undergone a merger. The ionised gas is spatially aligned with the radio structure towards the South-East (third panel). Interestingly, this is also seen in the molecular gas phase in the same region (fourth panel). Indeed, as discussed in Chapter 4, the molecular gas shows filamentary structures extending from a very compact central galaxy disk. The high-resolution radio contours appear to have none of the radio hotspots within the molecular gas disk. Therefore, the radio emission seems to already have escaped the galaxy disk.

J1010+0612 is presented in Figure 5.2 *fourth row*. This target appears to be an elliptical galaxy interacting with a stellar neighbour to the South West (first panel). The interaction is also apparent from the stellar continuum detected in the region connecting the main galaxy body with the neighbour through a tail-like structure to the South-West. The stellar velocities are irregular and a major kinematic axis could not be defined (second panel). Both the ionised (third panel) and molecular gas map (fourth panel) appear compact and do not show clear evident signs of interaction with the radio continuum emission. Indeed, the radio images show no extended structures from either the low- and high-resolution contours. An ionised gas outflow has been observed in previous studies using [OIII] emission and proposed to be due to a small-scale, unresolved radio jet (Villar Martín et al. 2014).

J1010+1413 is presented in Figure 5.2 *fifth row*. This source has been widely studied in literature and is suspected to have undergone a merger (see Goulding et al. 2019; Veres et al. 2021). Indeed, the 3-color continuum image (first panel) shows multiple stellar structures and a faint shell-like feature in the East that could be indicative of past-mergers. The stellar velocity also appears very similar to a merging system (second panel), and hence a rotational axis could not be established. Goulding et al. 2019 also suspects the presence of binary quasar arising from the merger using HST data. However, Veres et al. 2021 offers alternative explanations and challenges the proposed dual-AGN classification using VLBI data, which reveals only a single radio feature offset from the HST point sources.

The ionised gas morphology (third panel) shows a more North-South extension, contrary to the East-West stellar morphology. Furthermore, the ionised gas is spatially correlated to the radio emission, along the same axis. Towards the North, the high-resolution radio contour is bent, possibly due to an interaction with an ionised gas cloud in this location. Both the ionised and the molecular gas seem to be disturbed. The molecular gas (third panel) seems to also show the presence of filamentary structures that appear morphologically wrapping around the radio bubble, most strongly visible to the North-West of the central galaxy disk (see Chapter 4). Following from the high-resolution radio contours, a radio hot spot can be seen to be still within the molecular galaxy disk.

J1100+0846 is presented in Figure 5.2 *sixth row*. The continuum image reveals a beautiful barred spiral galaxy structure (first panel). The stellar velocity map (second panel) also appears as of an ordered rotating galaxy disk, which helped establish a major kinematic axis as shown through the dashed magenta line. The ionised gas emission is compact and featureless (third panel). This is also true of the radio emission, and hence a clear radio structure could not be identified. The molecular gas (fourth panel), on the other hand, shows a faint spiral arm structure, with molecular gas being seen in the central bar-like structure and extending in the arm North-Eastwards and in the arm South-Westwards.

J1316+1753 is presented in Figure 5.2 *seventh row*. It appears to be a spiral galaxy with a minor structure in the North-West showing the presence of stellar emissions (first panel). This source was the case-study that is already presented in Chapter 3. The blue spiral arms reveal the presence of younger stellar populations. The stellar velocity seems to be rotation-dominated and a major rotation axis could be established (second panel). The ionised gas, however, shows a very disturbed structure with gas clouds (third panel), likely due to the interaction of the AGN (Girdhar et al. 2022). The molecular gas appears to have a considerably different morphology to the ionised gas. The radio jet axis is very close to the major stellar rotational axis and the radio hot spots can be seen to be still within the molecular galaxy disk. An ionised and molecular gas outflow has been detected in this galaxy (see Girdhar et al. 2022) due to the close-inclination of the radio-jet (as seen through blue contours).

J1356+1026 is presented in Figure 5.2 *eight row*. It appears to be an irregular galaxy and the presence of two galactic nuclei, indicative of an ongoing merger, is evident in the 3-color image (first panel; also see Liu et al. 2010; Fu et al. 2011; Greene et al. 2012). Spatially-resolved spectroscopy has confirmed these to be two AGN

(Greene et al. 2012; Harrison et al. 2014). The stellar velocity shows a broad velocity gradient but is not ordered enough for a major kinematic axis to be established as a signature of rotation (second panel). The ionised gas follows a similar spatial direction to radio emission, but the ionised gas is much more extended (third panel). Indeed, the extended ionised gas to the South is known to be due to an expanding outflowing bubble, and some emission in the North that is identified to be an ionised tidal tail (Greene et al. 2012; Jarvis et al. 2019). The molecular gas (fourth panel), on the other hand, appears to be very compact with some molecular gas blobs around the East-West direction. These are likely associated with the previously identified molecular gas tidal tail to the West (see Sun et al. 2014). An intriguing molecular blob is also observed in the South, co-spatial with the radio bubble as shown through the green contours. These molecular gas structures are investigated in more detail in Section 5.4.

J1430+1339 is presented in Figure 5.2 *ninth row*. This target is well-studied in the literature and is also popularly known as the 'teacup galaxy', due to the shape of the ionised emission line region (Keel et al. 2017). Indeed, this is clearly visible in the [OIII] emission (third panel). The radio emission also traced this extended emission-line region, with an additional radio bubble seen to the West (see Harrison et al. 2015). Lansbury et al. 2018 confirms that the teacup is a highly obscured AGN with a radiatively dominated AGN. The high bolometric luminosity of the teacup galaxy contradicted the previously held understanding of it being a fading quasar. The 3-color stellar continuum image (first panel) looks like an elliptical galaxy with a shell-like feature that is indicative of previous mergers (also seen by Keel et al. 2015; Harrison et al. 2015). The stellar velocities (second panel) appear to be very unordered, further indicating a merger system and a kinematic axis could not be established. The molecular gas (fourth panel) seems to be laterally extended in the North-South direction, contrary to the morphology in other phases. A molecular gas outflow was detected using the CO (3–2) data for this galaxy in Chapter 4. An outflow has also been detected in the same direction using CO (2–1) observations of the teacup galaxy, extending to ~ 1 kpc perpendicular to the radio-jet (Ramos Almeida et al. 2021; Audibert et al. 2023). Using the high-resolution radio contours, a radio hotspot can be seen to be located within the molecular galaxy disk.

5.4 Interaction of radio lobes on the large scale

This section focuses on identifying any interaction between the radio lobes and the extended molecular gas structures if any, across all the 9 targets. A similar analysis was also performed in Chapter 4; however, there I only focussed on the four targets with LLS ≥ 10 kpc (see Figure 5.1). Here, I test if these extended molecular gas structures can also be found in the targets with more compact radio structures.

5.4.1 Methods to search for large-scale molecular structures

To search for molecular gas structures in a systematic way, I created emission line maps over 25 km s^{-1} velocity widths for each of the CO (3–2) datacubes. For every target, each velocity channel was then visually inspected for the presence of any CO (3–2) emission at a significance level of $\geq 5\sigma$ and which is morphologically and/or kinematically separated from the galaxy disk; where the galaxy 'disk' is defined as the

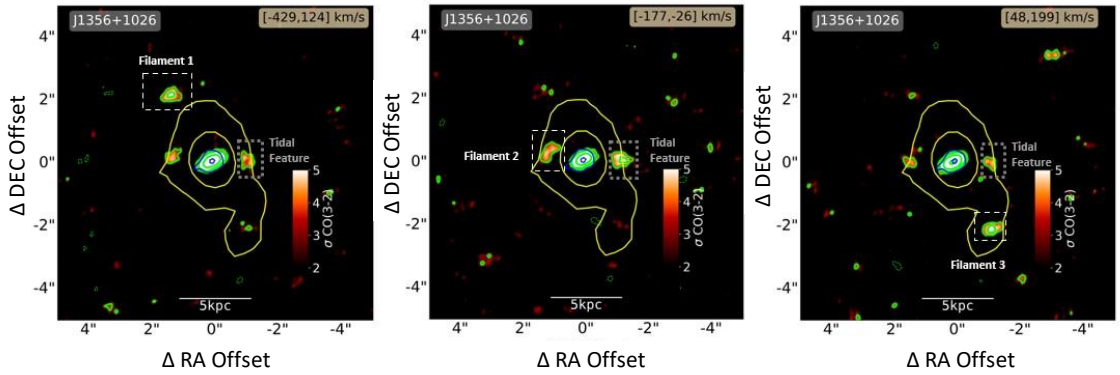

Figure 5.3: CO (3–2) emission-line maps integrated over specific velocity ranges (indicated in the top-right of each panel) to highlight the identified filaments (shown through dashed white boxes). The green contours are the CO (3–2) emission in these velocity ranges at $\geq 2\,\sigma$. The blue and yellow contours show the radio continuum emission at 6 GHz (from Jarvis et al. 2019). The radio contour levels are the same as in Figure 5.2. The dashed green contours indicate the $-3\,\sigma$ levels of CO(3–2) emission.

continuous emission structures seen in the central regions. A particular non-central structure was considered relevant for further analysis only when it was detected in more than one contiguous velocity channel, following the procedure defined in Section 4.3.1. The newly detected structures are shown in Figure 5.3) and discussed in the following section. The molecular gas structures are referred to as 'filaments' when they meet the above-mentioned criteria and show significant CO (3–2) emission (SNR ≥ 3) as explained below.

To extract the spectral properties of the molecular gas structures, I employed a Gaussian fitting routine for the emission-line profiles obtained from the region in consideration. The Bayesian inference criteria (BIC) was used to select between one, two, and three Gaussian components, needed to obtain the best fit to the CO (3–2) emission-line profiles. Hence, for the filaments, this fit was used to obtain the filament velocity ($V_{50,fil}$), the filament velocity dispersion (σ_{fil}), and filament flux ($S_{CO(3-2),fil}$). For the case when more than one Gaussian component was required to obtain a suitable fit to the emission line profile, W_{80} was estimated and converted to σ, by dividing by a factor of ~ 2.6. To estimate the molecular gas mass, the same procedure as outlined in Section 3.2.3 was implemented. Specifically, the integrated line flux for CO (3–2) was converted to CO (1–0) by assuming an integrated line flux ratios of 7.2 (Vantyghem et al. 2016). The conversion ratio was selected to be the same as used in Chapter 4 for consistent comparison. The CO (1–0) flux was then converted to molecular gas mass using equation 4.1.

For the CO properties at the whole galaxy level, the line emission was obtained over all CO-emitting regions, and for the filament properties, the emission was obtained from the dashed-white boxes shown in Figure 5.3. A comparison for the whole galaxy level, as well as filament properties is shown in Figure 5.5 with $\sigma_{mol,galaxy}$ (total galaxy) shown in the left-panel and $\sigma_{mol,fil}$ (individual filaments) in the right-panel. Their comparison with stellar velocity dispersion is discussed in the following section. All estimated spectral properties and the derived molecular mass for the newly observed filaments (see Section 5.4.2) are listed in Table 5.3. The filaments detected for the other two galaxies are shown in the previous chapter, precisely in Figures 4.11 and 4.12; and the associated properties are in Table 4.3.

Table 5.3: Measured properties for the filamentary molecular gas structures (see Section 5.4.1) extracted from within the dashed-white regions shown in Figure 5.3. The properties listed here are namely: (1) quasar name; (2) filament name; (3) velocity range used to identify the filaments (see Figure 5.3); (4) filament velocity ($V_{50,fil}$); (5) filament velocity dispersion (σ_{fil}); (6) filament flux, and (7) filament molecular mass.

Quasar	Filament	Velocity range [km s^{-1}]	$V_{50,fil}$ [km s^{-1}]	σ_{fil} [km s^{-1}]	$S_{CO(3-2);fil}$ [Jy]	M_{fil} $M_\odot$
(1)	(2)	(3)	(4)	(5)	(6)	(7)
J1356+1026	1	[-429,-124]	−4	357	1.54	8.82
	2	[-177,-26]	−43	212	1.19	8.71
	3	[48,199]	55	172	0.73	8.50

5.4.2 Results of molecular gas interaction with radio lobes

In this work, I searched for extended molecular gas structures in all nine targets. In addition to the case of J1000+1242 and J1010+1413, which are analysed in detail in Chapter 4, only one more target showed any evidence for such structures. This was J1356+1026, which shows 3 molecular gas structures located beyond the central gas disk, as shown in Figure 5.3 and the properties are listed in Table 5.3. In the narrow-band image of the target shown in Figure 5.2, along with the 3 identified filaments, another gas structure can be seen to the West of the galaxy center (shown enclosed in dotted grey color). However, this structure has not been attributed to be a filament, as defined here, since it is connected to the central galaxy disk. Indeed, this structure has previously been identified as a tidal feature (Sun et al. 2014). The continuous velocity slices in which the tidal tail is observed, are shown in the appendix Section 5.11.

Across the whole sample studied here, I have found that 3/9 targets show extended molecular gas structures. It is interesting that all three sources have a radio structure extending beyond the molecular gas disc.

For the other 6 targets, namely, J0945+1737[5], J0958+1439, J1010+0612, J1100+0846, J1316+1753, and J1430+1339, no such molecular gas filaments were observed. I now go on to further explore the properties of the molecular gas filaments that have been identified, following the approach taken in Chapter 4.

The main aim of this analysis is to understand if the presence of the molecular filaments is connected to the properties of the radio structures. In Figure 5.4, we compare their molecular and radio properties. Here, along y-axis the largest linear projected length of the radio structures, LLS_{radio} normalized against the size of the molecular galaxy disk is plotted. To obtain the size of the central molecular gas disk, I used the emission line maps of the CO (3–2) emission as shown in the right-most panel of Figure 5.2. On fitting a 2D Gaussian to the surface brightness maps of the CO (3–2) emission, I estimated the size of the molecular gas disk corresponding to the FWHM (major axis of the 2D Gaussian). Using this size-ratio helps to differentiate the quasars that have radio emission extending beyond the galaxy disk and those with the radio emission still *within* the galaxy disk, i.e., those with LLS_{radio}/CO

[5]While certain gas blobs are also visible for the case of J0945+1737 in the collapsed narrow-band image (see Figure 5.2), they weren't seen in contiguous velocity slices at a $\geq 5\,\sigma$ limit. Further, a morphological association with radio bubbles was also not apparent.

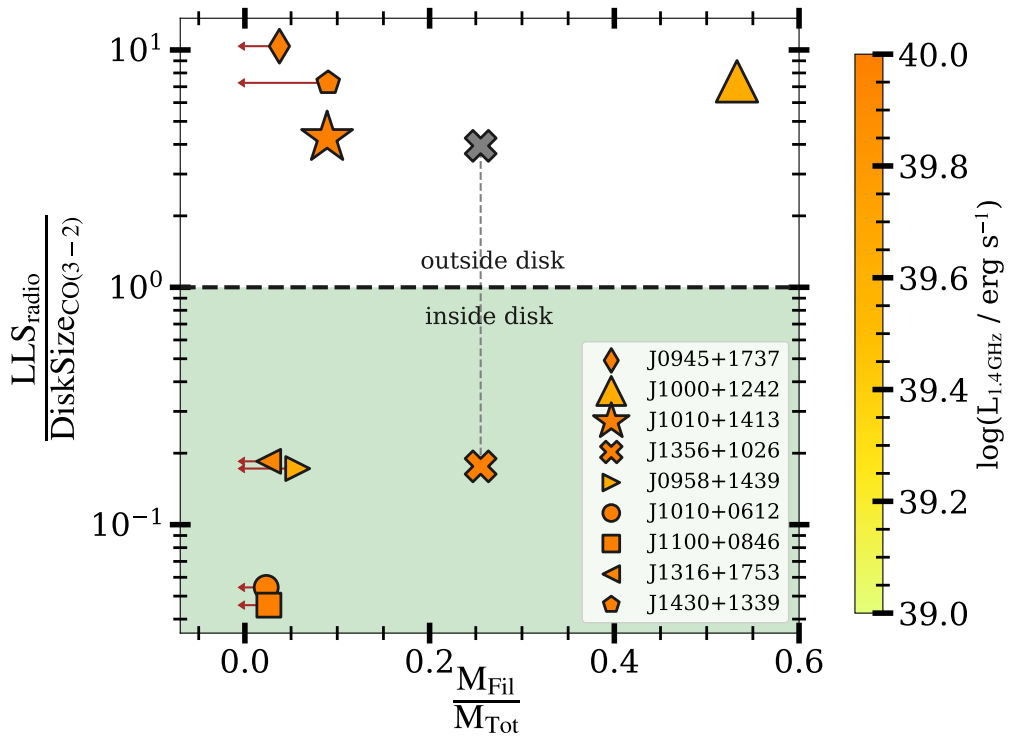

Figure 5.4: Ratio of molecular gas in filaments to the total molecular gas as a function of the ratio of the largest linear radio size (in terms of LLS_{radio}) to the galaxy disk size identified in CO (3–2) for the respective targets. Fraction of filament mass to the total mass is shown for the targets where the filaments were spotted, namely, J1000+1242, J1010+1413, and J1356+1026. Where the filaments are not observed (see Section 5.4), upper limits are estimated and shown for the targets instead. The symbols are as in the legend. The data points are colour-coded by the radio luminosity of the galaxies at 1.4 GHz ($\log(L_{1.4\,GHz}/\,erg\,s^{-1})$). The green, shaded region corresponds to the region within the galaxy disk, also marked through a dashed black line.

disk size ≤ 1 (see green shaded area in Figure 5.4). A visual inspection of the data, reveals this is an appropriate diagnostic to distinguish between these scenarios (see Figure 5.2).

Figure 5.4 quantitatively confirms that four of the targets have compact radio emission, i.e., the radio structures do not extend beyond the molecular gas disk. These are namely, J0958+1439, J1010+0612, J1100+0846, and J1316+1753, and can be seen in the shaded green region in Figure 5.4 for $LLS_{radio}/\text{Disk Size}_{CO(3-2)} < 1$. On the other hand, 5 targets (J0945+1737, J1000+1242, J1010+1413, J1356+1026, and J1430+1339) have radio emission extending beyond their molecular gas disks. The ambiguous case of J1356+1026, depends on the choice of radio image used to make this quantitative measurement. In addition to the LLS_{radio} measurement from Jarvis et al. (2021) (shown as a coloured symbol), the measurement from Jarvis et al. (2019) is also shown using a grey-filled symbol.[6] The radio images in Jarvis et al. (2019) were obtained using image processing parameters catered to individual sources with the aim of extracting their radio structures, while the latter study uses a more uniform approach. The latter hence misses the low surface brightness radio

[6]For all the other 8 targets, using the measurements from Jarvis et al. (2019) does not change their position on the plot significantly and hence only their measurements from Jarvis et al. (2021) are shown here (i.e., orange-filled symbols).

bubble seen in J1356+1026, which forms an elongated radio structure. Hence the Jarvis et al. (2019) measurements are most relevant for this study as they reveal the extended radio structures that are also observed by Villar Martín et al. (2021).

Of the five sources with radio structures beyond the disk, three show molecular gas structures, located beyond the disk - but none of those with radio structures within the disk have such structures.

To quantify the significance of these extended molecular gas structures further, the x-axis, of Figure 5.4, shows the ratio of the molecular gas mass observed in filaments with respect to the total molecular gas mass in the galaxy system. Following Chapter 4, J1000+1242 and J1010+1413 have 9% and 53% of their total mass in the extended filamentary structures. Additionally, for the case of J1356+1026, 26% molecular gas mass was observed in the form of filaments. Since the other 6 targets do not show any such filamentary structures, I have estimated the upper limits for the mass ratio. To obtain the upper mass limits, for any filaments that may exist in the other galaxy systems, I assumed them to be equivalent in flux to the faintest detected filament, i.e. filament 3 of J1010+1413. I estimated a ratio of this filament flux to the total flux in the individual galaxy systems and scaled it by the noise associated to the respective datacubes of the target in consideration. The resulting estimated upper limits are shown as brown arrows in the figure.

Filamentary molecular gas structures wrapped around radio bubbles have been observed in the case of Bright Cluster Galaxies (BCGs; see Russell et al. 2016; Tremblay et al. 2018; Russell et al. 2019; Tamhane et al. 2022). I have used the same BCG comparison sample (from Russell et al. 2019; Tamhane et al. 2022) as used in Chapter 4 to put the properties of the filaments detected in our radio-quiet quasars in an overall context of the BCGs (see Section 4.4.2). To understand the origin of these filaments, following Section 5.4.2, the velocity dispersion of the molecular gas in the filaments was obtained. This was then compared to the stellar velocity dispersion obtained from the GIST pipeline as mentioned in Section 5.2.2. In the right panel, the individual filaments are compared based on their velocity dispersion, wherein $\sigma_{\rm mol,filament}$ is estimated from the spectra extracted only over the filamentary regions (as also shown with a white-dashed box in Figure 5.3). The main addition from Chapter 4, therefore, is including the structures found in J1356+1026.

The comparison of the velocity dispersion in the molecular phase versus the stellar dispersion is shown in Figure 5.5. In the right panel of the figure, the three filaments for J1356+1026 are represented using cross symbols and can be seen to sit much higher than all of the other filaments, i.e., even higher than the filaments seen in BCGs. This might suggest a different origin of these filaments. Further suggestion that these structures may have a different origin to the other targets (and to the BCGs), comes from their relative lack of alignment with the radio emission in J1356+1026, compared to that seen for the cases of J1000+1242 and J1010+1413. Only filament 1 shows a clear spatial alignment with the extended radio structure, but this is also the filament with the most extreme velocity dispersion. In the left panel of the same figure, the galaxy-wide velocity dispersion for J1356+1026 is compared with the four galaxies analyzed in Chapter 4 and with the BCG sample. Unlike the majority of the galaxies in that plot, J1356+1026 shows a much higher molecular gas velocity dispersion than as compared to the stellar velocity dispersion.

This may indicate more turbulent molecular gas in J1356+1026, or the presence of CO-emission from multiple kinematic components, i.e., the central galaxy, the filaments, and the tidal arm in this case.

In summary, the targets that have small radio structures, **do not** show extended molecular gas structures whereas 3/5 quasars with extended radio structures **do show the presence** of these. Across the 9 targets, 6 have $< 10\%$ of their total molecular gas mass located in the molecular gas structures located outside of the main molecular gas disks (as estimated from their upper mass limits). The three targets that show the presence of these molecular gas structures display a range of $10-50\%$ mass fractions in these. As also discussed in Chapter 4, all of this tends to a possible association between the extended radio lobes and these molecular gas structures, potentially with the radio lobes lifting this gas (as is also observed in BCGs) as a potential feedback effect, causing them to be seen apparently as being wrapped around the radio lobes. However, this interpretation is less clear for the case of J1356+1026 as the velocity dispersion of the detected molecular gas structures for this target is significantly higher than those detected in the former targets, and further, the radio alignment is not so straightforward. Hence, the extended molecular gas structures are only seen in 3/5 targets where the radio structures are also extended on similar scales. However, it is unclear why the other two targets with large radio lobes do not show the presence of these filaments, namely in the case of J0945+1737, and J1430+1339. J0945+1737 clearly shows an irregular radio morphology, that of a bent-radio jet, making its interpretation not very straightforward. On the contrary, J1430+1339 does have extended radio lobes along with radio hotspots still within molecular disk. As it happens, even in the BCGs, not all the sources show the presence of such molecular gas structures. A larger sample of 'radio quiet' quasars with large radio structures will need to be observed to further understand the prevalence of these structures, and establish the interaction of the radio lobes (see Chapter 6).

In the following section, I explore the small-scale interaction of radio jets, specifically, for the radio structures that may still be within the galaxy disk.

5.5 Interaction of radio jets on the central scales

Observationally, AGN feedback has been seen to influence the distribution of molecular gas in the central kpc of the galaxies (e.g. in Rosario et al. 2019; García-Burillo et al. 2021; Girdhar et al. 2022). Additionally, the higher Eddington ratios as seen in quasars might also lead to higher concentrations of molecular gas in the central regions of galaxy. These factors make it an interesting avenue to investigate the central regions of the galaxy and through a systematic approach to look for outflows and check for their impact at the central and possibly at the wider galaxy scales. Characterizing the multi-phase properties of these systems, can help understand how the radio structures interact with the multi-phase outflows and which outflow phase dominates on different scales. Hence, in this section, I look into identifying any signatures of outflows across the different phases with a focus on if the jet-ISM interactions in the central regions could be associated to these.

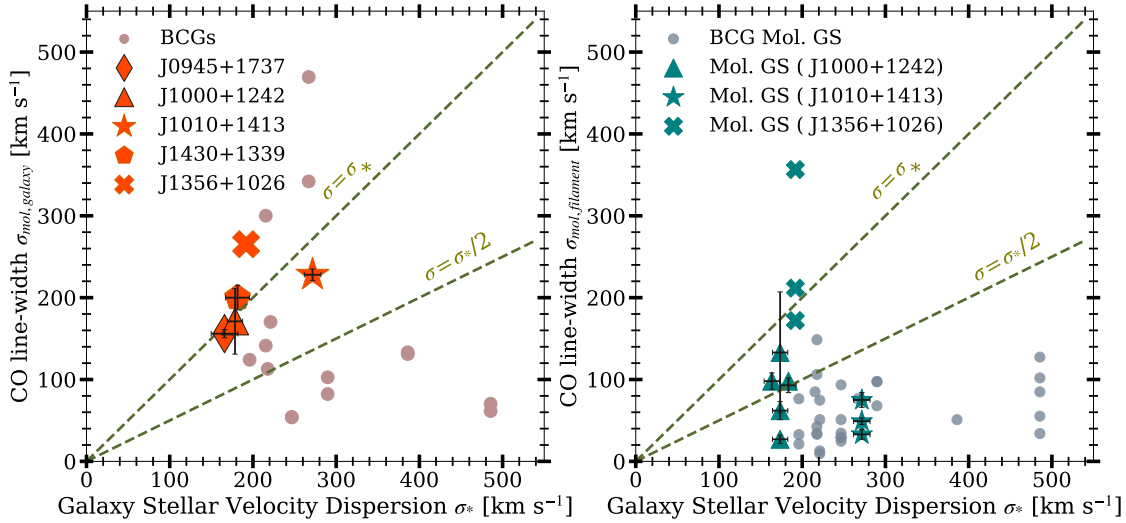

Figure 5.5: A comparison of the stellar velocity dispersion (σ_*) with *Left:* the galaxy-wide molecular velocity dispersion($\sigma_{\rm mol,galaxy}$), and *Right:* the molecular velocity dispersion for the molecular gas filaments ($\sigma_{\rm mol,filaments}$). Unique symbols are used for each of the quasars studied in this work as indicated in the legend on the top-left. The BCGs showing such similar filamentary structures are also shown in the panels using circular markers (Russell et al. 2019). The two dashed lines in each panel correspond to the ratio of $\sigma_{\rm mol} : \sigma_*$ at 1:1 and 1:0.5.

All the 9 quasars studied here are known to host broad and fast-moving ionised gas outflows, with velocities reaching 1000 km s^{-1}, and extending to $\gtrsim$1–10 kpc (see Harrison et al. 2014, 2015; Ramos Almeida et al. 2017; Jarvis et al. 2019; Speranza et al. 2022; Venturi et al. 2023; Ulivi et al. in prep.). Further, Mullaney et al. (2013) performed a spectral fit to the [OIII] emission line profiles of these sources using a narrow and a broad Gaussian component to conclude that each of the sources required a broad Gaussian component of a significant width, i.e., FWHM $\geq$ 800 km s^{-1}. This also formed the motivation to study these quasars as a parent sample for a prior study before the Quasar Feedback Survey in Jarvis et al. (2019). Four of these nine quasars, namely, J0945+1737, J1000+1242, J1010+1413, and J1430+1339, studied in Chapter 4, revealed the presence of molecular gas outflows on very central scales ($\sim$ a few kpc). Motivated by finding central outflows in the four galaxies studied in Chapter 4, a search for the presence of central molecular gas outflows in all 9 quasars is conducted here.

5.5.1 Searching for the central molecular gas outflows

As a first step, I extracted the spectra from the central 4 arcsec × 4 arcsec region for both the ionised and molecular gas. For this study, I have used the [OIII] emisison from MUSE as a tracer for ionised gas and the CO (3–2) emission from ALMA as a tracer of the molecular gas. For the extracted emission, the spectral fitting routine was followed for both phases, i.e., successively a fit was obtained using one, two, and three Gaussian components (see Section 5.4.1). For each phase, the final fit was statistically chosen using the BIC parameter. The line profiles and the respective spectral fits are shown in *panels e and f* of Figure 5.6 for quasar J1430+1339, and for the remaining quasars at the end, in appendix Section 5.7.

For both the ionised and molecular gas, the central $4 \times 4\,\mathrm{arcsec}^2$ region was explored and divided up into spatial units of $0.4 \times 0.4\,\mathrm{arcsec}^2$. Since the spaxel size for ALMA is roughly 0.05 arcsec, to obtain a spatial unit of 0.4 arcsec, the region accounts for groups of 8×8 spaxels. Similarly, using MUSE's spaxel size of 0.2 arcsec, groups of 2×2 spaxels were created. The pixel map for ALMA is shown in *panel d*, of Figure 5.6, with the spaxel grid labeled with y-coordinates on the left side and x-coordinates on the top. From each spatial unit, the line emission was obtained and fitted following the same procedure as above. A spectral fit was identified to be associated to a molecular outflow when following the BIC parameter, more than 1 Gaussian component was needed to obtain a fit, and a significantly broad Gaussian component was observed, from visual inspection. The spaxels where such fits were observed, are shown in magenta color in the pixel map. Examples of the spectra and the fits in these magenta spaxels are shown in *panels e1 and e2* of Figure 5.6 for the molecular gas emission and in *panels f1 and f2* for the ionised gas emission from the same spaxels. Single and multiple Gaussian components (not attributed to outflows) are indicated using light and dark blue colors, respectively. The spaxels rejected due to low SNR, i.e., ≤ 3, are shown using grey colors.

Using the spectral fitting, I obtained the kinematic maps of these quasars for their molecular gas velocity and velocity dispersion. In spatial units requiring multiple Gaussian fits, the non-parametric approach was used to obtain V_{50} as a measure of the bulk CO velocity and W_{80} to obtain the velocity width as a tracer of the dispersion of the gas in that region. The molecular kinematic maps are shown in *panels b and c*, for W_{80} and V_{50}, respectively, in Figure 5.6 for J1430+1339. The other targets are represented in Figures 5.12 to 5.19.

5.5.2 Analysing the properties of the molecular gas outflows

Figure 5.6 presents a kinematic overview of the quasar J1430+1339 in the top row; and a summary of the detection of the central outflow and its comparison to the ionised gas phase in the bottom row. For the [OIII] emission-line profiles extracted from the 4 arcsec × 4 arcsec region, a broad Gaussian component was always required to obtain the best fit as seen for J1430+1339 in *panel f* of Figure 5.6 and for the other 8 quasars in the respective panels of Figure 5.12 to 5.19. This is also expected since all 9 were previously known to host ionised gas outflows.

Following the methods described in Section 5.5.1, gas outflows were also searched for in the molecular gas phase using the CO (3–2) emission. At the 4 arcsec × 4 arcsec level, except for the case of J0958+1439 and J1000+1242, none of the other quasars showed clear spectral evidence for the presence of a central outflow (see *panel e*; Figure 5.6). Precisely, in the case of J1010+0612, J1010+1413, J1100+0846, J1316+1753, and J1430+1339, two clear narrow kinematic components were observed in the emission line profile at this scale, potentially arising from the rotational motion of the molecular gas in the galaxy disk.

Further, looking at the more resolved, spaxel-level, as would have been expected for the ionised gas, broad Gaussian components were detected in almost each of the spaxels in the central region. However, this was quite unlike the case of the spaxel fits for the molecular gas. On inspecting each of the individual spaxel fits by eye, a clear broad Gaussian component was detected only in a few spaxels along with one or two

narrow Gaussian components. These were then highlighted in the pixel grid map using magenta color as shown in *panel d* of Figure 5.6. Hence, when observed on a more spatially resolved scale, all 9 quasars showed the presence of centrally compact, broad gas outflows in the molecular phase. As an example, two spectral emissions and the corresponding fits are shown for the magenta pixels in *panels e1 and e2* for the molecular gas; and in *panels f1 and f2* for the same corresponding pixels in the ionised gas. The light blue color in the pixel map indicates that one Gaussian component was sufficient for the spectral fit and the dark blue color indicates the presence of multiple (two or three) Gaussian components.

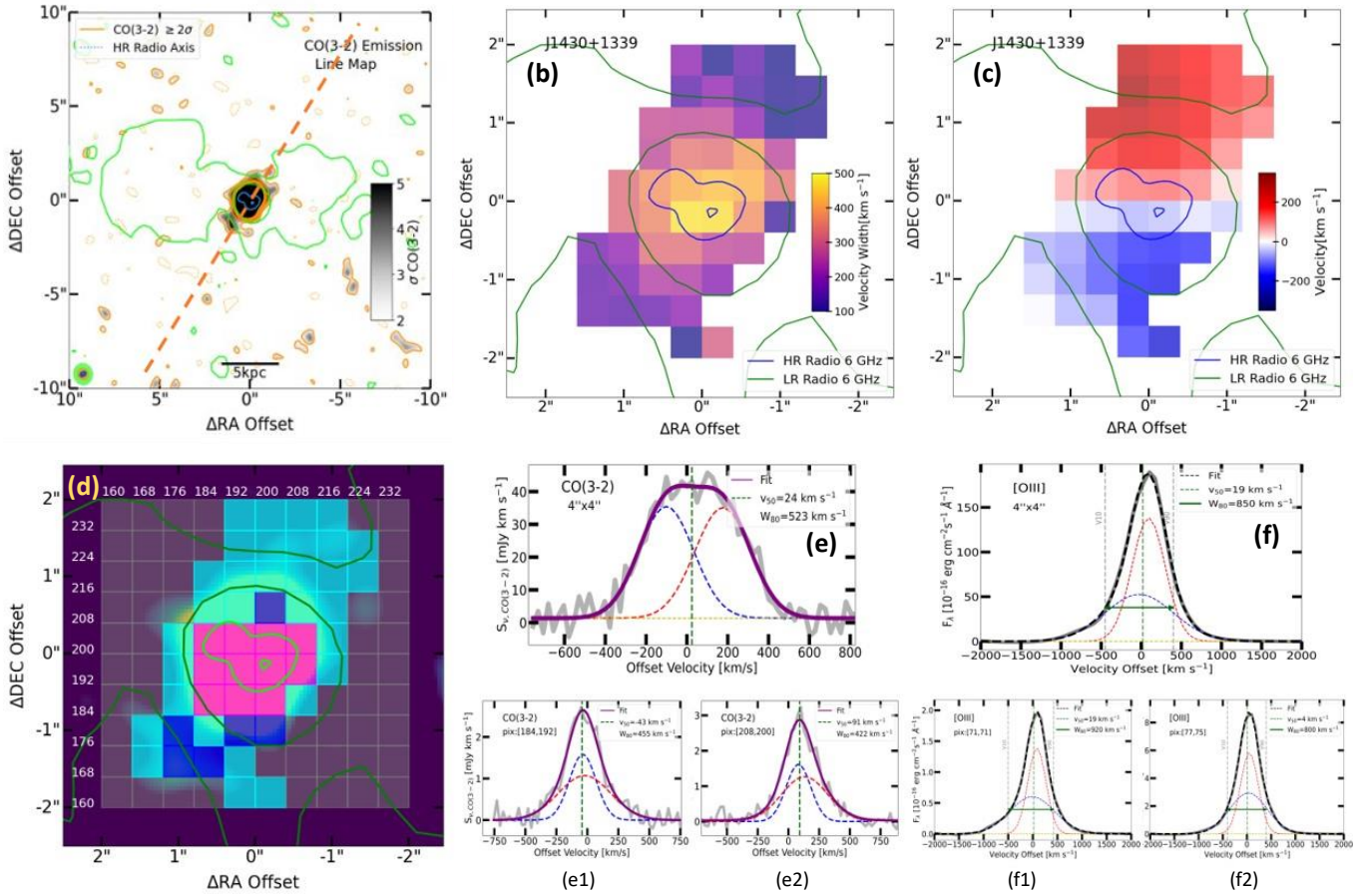

Figure 5.6: For **J1430+1339**, a kinematic overview (*top row*) and detection of central multi-phase outflows (*bottom row*). **Panel (a)**: shows the CO (3–2) narrowband image (see Figure 5.2) with the dashed-orange line indicating the morphological position angle for the molecular gas disk. **Panels (b) and (c)**: represents the kinematic maps within the central $4 \times 4\,\mathrm{arcsec}^{22}$ of the velocity width (W_{80}) and of bulk molecular gas velocity (V_{50}), respectively. The green and blue contours indicate the low- and high-resolution radio continuum emission at 6 GHz. Levels same as indicated in Figure 5.2. **Panel (d)** shows the pixel grid map overlaid on the CO (3–2) emission. This grid is used to show the division of the central region into individual spaxel units (~ 0.4 arcsec). The color coding is to indicate the Gaussian fits for the molecular emission line profile. The magenta spaxels indicate the presence of broad Gaussian component used as a mark for central molecular outflows; and the light and dark blue spaxels indicate one or more Gaussian components in the fits respectively. **Panels (e) and (f)**: show the emission line spectra for CO (3–2) gas and [OIII] gas, respectively over the entire $4{\times}4\,\mathrm{arcsec}^2$ area. **Panels (e1), (e2) and (f1), (f2)**: respectively show example fits from two magenta spaxels showing the presence of broad central outflows in molecular as well as ionised gas.

The detection of molecular gas outflows along with ionised gas outflows in these radio-quiet quasar host galaxies hence motivated a study of their comparisons and drivers. In the following sections, this work tries to address the following questions:

- How do the different phases (ionised and molecular) compare in the observed outflows?
- Do the molecular outflow properties depend on the radio jet property and/or the disk-jet orientation?
- Is the fraction of outflowing gas in the different phases dependent on the host galaxy properties and/or the radio jet properties?

Comparing the different phases in the central gas outflows

In order to compare the molecular and ionised gas phases in the same regions, only the spectral fits from the magenta spaxels (from Figure 5.6 and Figures 5.12 – 5.19) were used for both the phases for a consistent comparison. Hence, for the regions where molecular gas outflows were detected (i.e. the magenta spaxels), I also obtained the spectral fits for the ionised gas. For each galaxy, an average of the velocity-width was obtained across these spaxels in each phase. For the averaging, a flux-weighted approach was used and W_{80} was used as the parameter to obtain the velocity-width. The average velocity-widths (i.e., $W_{80,Avg.}$) were then compared across the two phases, as shown in Figure 5.7. Each quasar is represented by a star, as labeled next to the data point, and is color-coded by its bolometric AGN luminosity. Dashed-orange lines indicate different velocity-width ratios between the phases as indicated next to them. As can be seen in Figure 5.7, the ionised gas can be observed to be more turbulent for the case of all quasars, i.e., [OIII] $W_{80,Avg.} \geq \mathbf{2}\times$ CO (3–2) $W_{80,Avg.}$, except for J1356+1026 (for which the factor is $\sim$1.5). For the majority, i.e., 7/9 quasars, the ionised gas velocity widths **2 – 5 times broader** than the molecular gas widths. J1010+0612 further sits on the extreme with 5 times broader ionised gas velocity as compared to the molecular gas velocity. However, there is no clear trend observed with bolometric luminosity.

Spatially, the ionised gas outflows are detected to extend throughout the investigated region of 4×4 arcsec^2, using which a lower spatial limit for the ionised gas outflows can be assumed, i.e., $R_{outf,ion} \geq 4$ arcsec. On the contrary, the molecular gas outflows are detected in very compact central regions shown through the magenta spaxels. Across the 9 targets, these show a spatial extent of $\sim 0.8 - 1.6$ arcsec, which translates to a physical scale of $R_{outf,mol} \sim 1.5 - 3$ kpc (using the average z$\sim$0.1). This is consistent with the finding in Chapter 3, where J1316+1753 was observed to have three times more disturbed and three times more spatially extended ionised gas phase in comparison to the molecular gas outflow.

Impact on the star-forming material as a function of jet properties

Since molecular gas serves as the fuel for galaxy growth through star-formation, the subsequent step was to analyse the impact on the molecular gas phase in particular. Consequently, in this section, I have looked into the amount of molecular gas

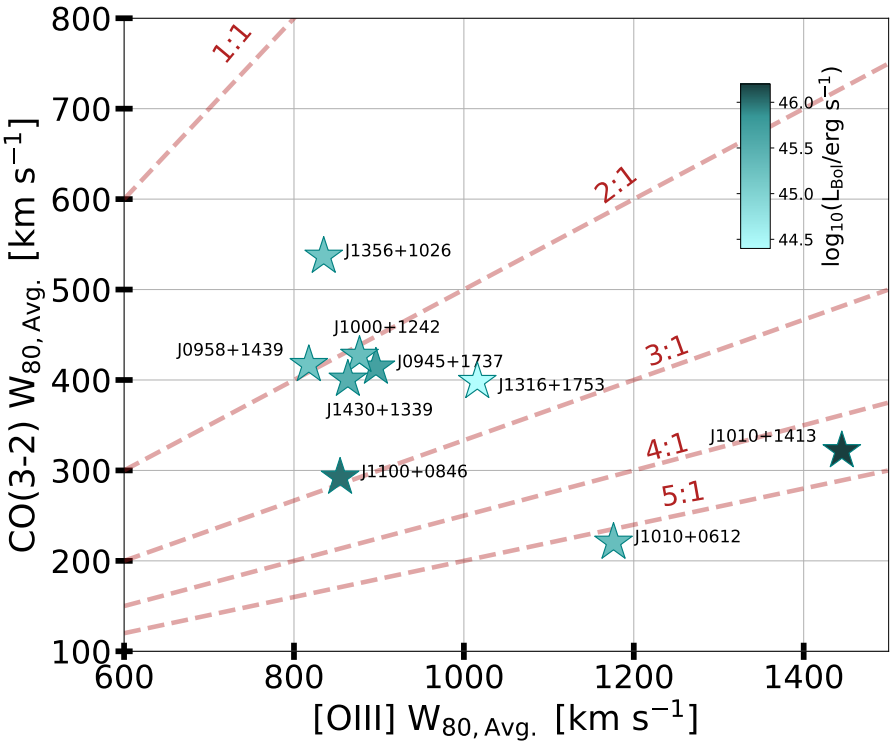

Figure 5.7: A Comparison of the velocity-widths across the different phases for the observed central outflows. Along x-axis, the $W_{80,Avg.}$ from the [OIII] emission line profile across the magenta spaxels (from Figure 5.6 and Figures 5.12 – 5.19) is plotted. In comparison, along the y-axis, the CO (3–2) $W_{80,Avg.}$, is shown. The data points are color-coded with their bolometric AGN luminosity (L_{Bol}) as indicated in the color map. Dashed orange lines are shown to divide the parameter space into regions corresponding to different ratios between the velocity widths of the two phases.

displaced across the sample as a function of the radio jet properties. For this the following parameters are taken into account in particular: (i) the largest extent of the radio structure; (ii) whether the radio hotspots are within the galaxy disk or not; (iii) the relative orientation of the radio jet with respect to the molecular gas disk; (iv) and the radio jet power. With the motivation to test the first two factors, in Figure 5.8, along the x-axis is the ratio of the largest projected radio size of the detected radio structures for each galaxy (LLS_{radio}), as a ratio with the CO disk size (as estimated in Section 5.4.2). Along the y-axis, I have shown the ratio of the flux in the broad component in the magenta spaxels to the total flux within the same spaxels for the molecular gas. Further, the red-dashed line shows the distinction of the radio structures being within the galaxy disk (towards the left), or extending outside (towards the right) based on the low-resolution radio structures. Additionally, if any hotspots were observed to be present within the galaxy disk, from the high-resolution radio structures, then an additional orange square is indicated for those data points. As can be seen in Figure 5.8, in the regions where these molecular gas outflows are identified (indicated by magenta spaxels), a fraction of 50 – 90 % of flux is seen to be in the outflows as compared to the total gas flux in the regions corresponding to the magenta spaxels. While this is a significant flux fraction in those regions, an obvious relation between the spatial extent of the radio structures and the amount of flux in the broad component was not evident.

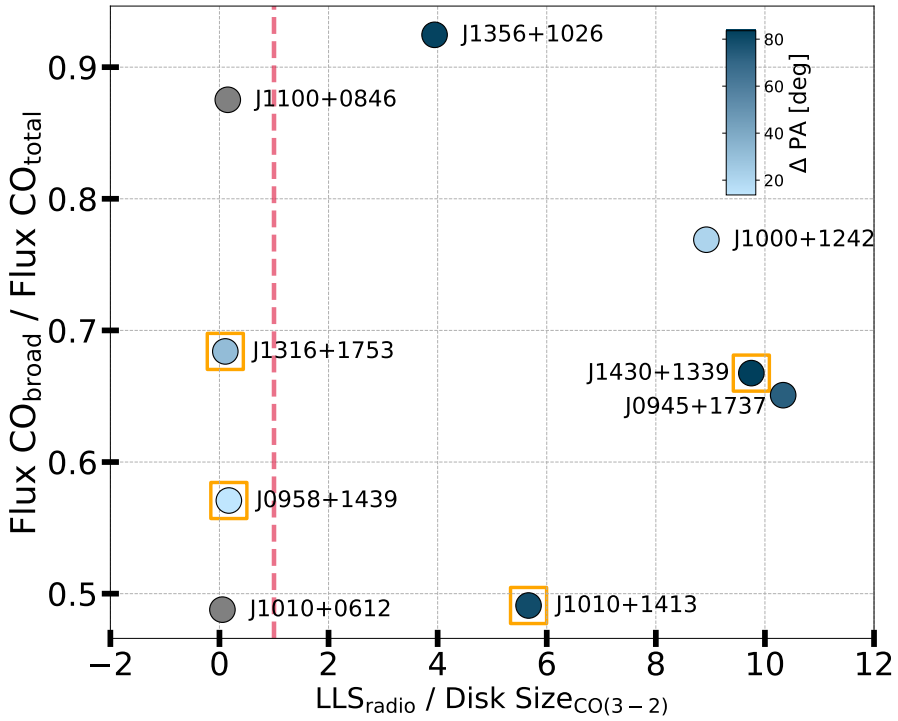

Figure 5.8: Studying the impact on the star-forming material as a function of the jet properties. Along the y-axis, the ratio of broad-to-total CO (3–2) flux is shown across the magenta pixels. Along the x-axis, the largest projected radio structure extent is plotted normalised against the CO disk size. This is to identify the radio structures extending beyond the CO galaxy disk, or to the right of the red-dash line representing LLS$_{radio}$/ CO Disk Size ≥ 1. The data points are color-coded with the misalignment (Δ PA) between the radio and CO position angle as indicated through the color bar. The two targets where PA$_{radio}$ could not be obtained due to resolution limits are filled with grey. Additionally for those targets where radio hotspots were observed to be within the galaxy disk as identified with the high-resolution radio structures (see blue contours in Figure 5.2), an additional orange square has been shown.

The data points in Figure 5.8 have been color-coded to represent the difference in the position angle between the morphological major axis of the radio emission (PA$_{radio}$) and the morphological major axis of the molecular gas disk (PA$_{CO}$), also known as misalignment. The radio position angle values are used from the Jarvis et al. (2019) study where the major radio axis is obtained by joining the two radio peaks in the radio emission and then confirmed using a 2D Gaussian fit. For the case of J1010+0612, and J1100+0846, I do not use a PA estimate since these two targets have largely unresolved radio emissions. To obtain the morphological major axis for the molecular gas, a 2D Gaussian fit was done on the CO (3–2) narrow-band images and is shown through dashed-orange lines in *panel a* in Figure 5.6. Having the two morphological position angles, the misalignment was obtained following the relation as below from Harrison (2017):

$$\Delta\,\mathrm{PA} = \Psi = sin\,(\mathrm{PA_{CO}} - \mathrm{PA_{radio}}) \tag{5.1}$$

A comparison of this misalignment with respect to the ratio of the molecular gas flux in the disturbed component to the total molecular gas flux is shown in Figure 5.8 through the color-coded data points. Since simulations predict a significant impact of the jet when the inclination angles are seen to be lower; a lack of trend here was unanticipated.

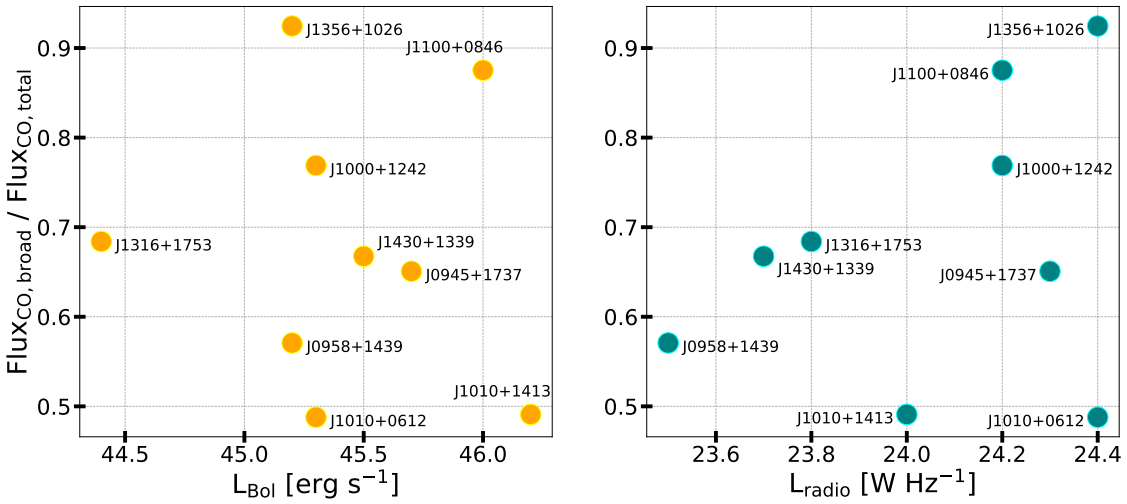

Figure 5.9: Analysing the dominant driver of the molecular gas outflow by comparing the flux in the broad component of the molecular emission line fit against different luminosity drivers. Along y-axis, the ratio of broad to total CO (3–2) is shown for the magenta spaxels where the outflow is detected. This is compared with the radiative power using the bolometric AGN luminosity on the left and the kinetic jet power derived from the radio luminosity on the right.

I also looked into whether the amount of molecular gas being driven in the molecular gas outflows could be scaled as a function of the bolometric AGN Luminosity or the kinetic energy of the jet. A scaling with AGN luminosities has been observed for ionised and molecular gas outflows in literature (e.g. see Wylezalek et al. 2020; Cicone et al. 2014). This motivated the search for understanding the driving mechanism of the molecular gas outflows. In Figure 5.9, the fraction of molecular gas flux in the outflow versus the total molecular gas flux in the magenta spaxels (from Figures 5.6 and 5.12 – 5.19) is plotted. Firstly, it is compared against the available radiative power, as shown using the bolometric AGN Luminosity (L_{bol}; in the left-panel); and secondly, with respect to the kinetic jet power (P_{jet} in the right-panel). The L_{bol} and radio flux densities are used from Jarvis et al. (2019). For obtaining the kinetic jet-powers, the radio core flux density at 5.2 GHz was used (corresponding to HR:A in that work). This was then converted to the corresponding radio core luminosity for each quasar, using the spectral index estimated for the associated radio core. By applying the relation from Merloni & Heinz (2007), i.e., Equation 3.1, the kinetic jet powers were then calculated. While a clear relation can not be seen in terms of the bolometric AGN Luminosity, it is interesting that the three targets with the highest fraction of the molecular gas within an outflow, are also the three of those with the highest powered jets. This might tentatively suggest that the jet is capable of coupling better with the ISM and higher jet powers are causing more molecular gas to be removed. However, the parameter space covered by this sample, in terms of jet power, is very small (1 order of magnitude), and a wider sample would be required to confirm any such trends.

Fraction of disturbed gas as a function of host galaxy properties

Having compared how the ionised and molecular gas phases compared with each other, the next objective was to understand what could be the main driver of this multi-phase outflow. Towards this end, I have studied the variation of the fraction of the flux in the multiple phases in the outflow, with respect to the property of

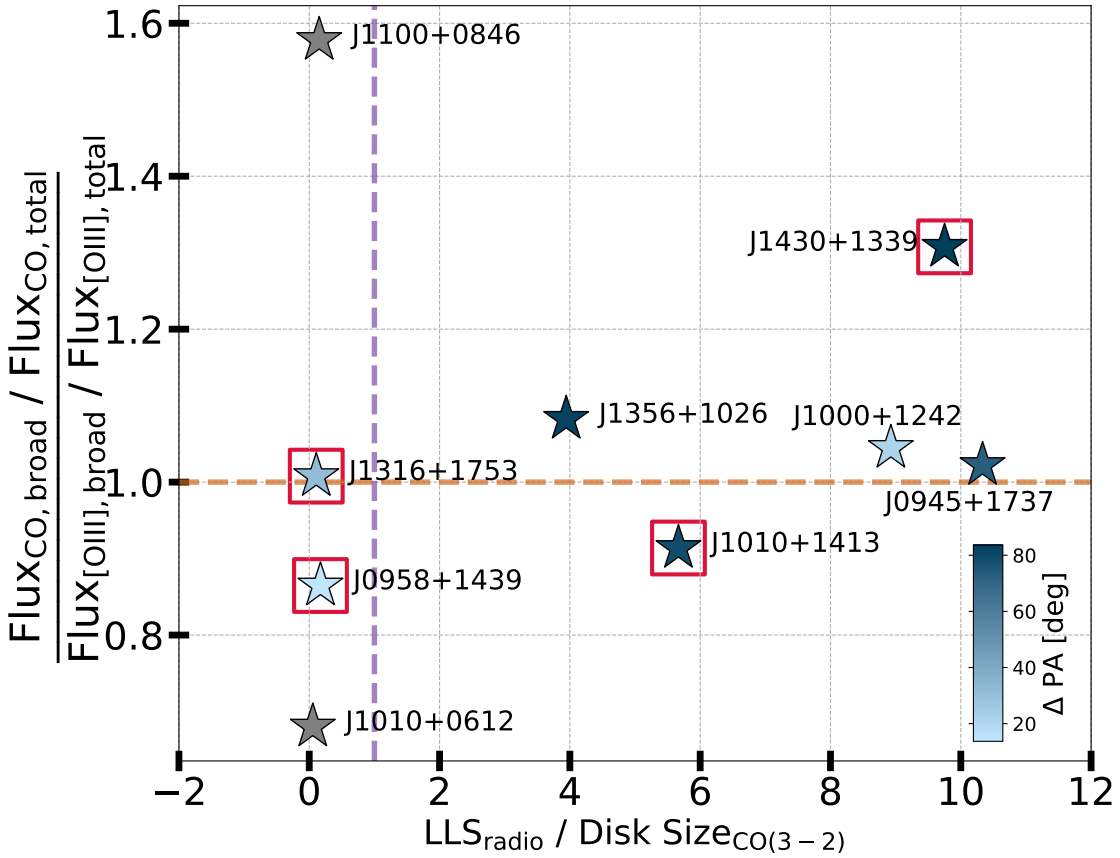

Figure 5.10: Comparison of the flux in the central outflows across the multiple phases. Along the y-axis, the ratio of broad-to-total CO (3–2) flux fraction is plotted in comparison to the broad-to-total [OIII] flux fraction, for the magenta spaxels (from Figure 5.6 and Figures 5.12 – 5.19) where the molecular gas outflows are detected. Along the x-axis, the largest projected radio structure extent is plotted normalised against the CO disk size. The data points are color-coded with the misalignment (Δ PA) between the radio and CO position angle as indicated through the color bar. The two targets where $\mathrm{PA_{radio}}$ could not be obtained due to resolution limits are filled with grey. Additionally, for those targets where radio hotspots were observed to be within the galaxy disk as identified with the high-resolution radio structures, an additional red square has been shown.

the radio jets in the galaxy. For a comprehensive picture, I have also taken the host galaxy properties into account. For example, instead of comparing with just the extent of radio structure, i.e. $\mathrm{LLS_{radio}}$, I have normalised this quantity by the molecular gas disk size. This helps to normalise the radio jet property with respect to the host galaxy across the entire sample for a consistent comparison. I obtained the fraction of flux in the broad Gaussian component against the total flux under the fit, across all the magenta pixels. I compared this value in CO as well as [OIII] phase along the y-axis in Figure 5.10. Following Figure 5.8, the disturbed flux fraction across multiple phases is then plotted against the $\mathrm{LLS_{radio}}$/CO disk Size, and is color-coded as per Δ PA. A lack of trend seen here is an interesting find given simulations predict a stronger fraction of the molecular gas phase to be impacted as opposed to the warmer phases; particularly in cases when the radio jets are ploughing through gas disks with low inclination angles. Following from the jet-ISM simulations (for e.g. Mukherjee et al. 2018b; Tanner & Weaver 2022); it is expected that if the jet is more inclined into the galaxy disk (i.e., lower misalignment), it can result in much stronger outflows being launched and a higher content of multi-phase gas in the outflow. However, a strong dependence on the misalignment measured

using projected position angles is not apparent. However, this doesn't account for sky projections. Another interesting observation here is that for most of the galaxies, the amount of flux within the broad component is seen to be quite similar across the two phases, i.e., the ratio of the broad-flux-fraction in the two phases is between $\sim 0.8-1.2$ for 6/9 targets and between $0.7-1.6$ across the entire sample. This is a captivating result since while the molecular gas outflows are not observed to extend as farther as the ionised counterparts, the fractional amount of disturbed gas in both phases is observed to be the same when studied within the same spatial regions.

5.6 Conclusions and Implications

AGN feedback can happen through a myriad of physical processes acting at very different temporal and spatial scales. For example, radio jets grow within a cocoon or bubble of hot gas. Both the jets and the pressure bubble are capable of interacting with, and impacting upon, the ISM through the transfer of momentum and energy. While on the central galaxy scales (≤ 5 kpc), fast and multi-phase gas outflows may be produced due to jet-ISM interactions; on the larger scales (≥ 10 kpc), as the jet propagates, the interaction with the bubble of plasma may take over causing pushing/lifting of molecular gas (see Morganti et al. 2023). Indeed, simulations have come to suggest an evolutionary feedback sequence due to the radio jets as they themselves evolve and propagate through the galaxy ISM (also see Mukherjee et al. 2016). In other words, depending on the phase of the radio jet in its evolution cycle, it may interact with the host galaxy in varying ways thus causing feedback on its host galaxy through different physical mechanisms.

Motivated by these ideas, in this chapter, I have analysed how jets may interact with the multi-phase ISM on small scales ($\lesssim 3$ kpc) and on larger scales (≥ 10 kpc). Further, as a test of theoretical predictions, I have explored the properties of the multi-phase outflows in regard to the different host galaxy and jet properties. For this study, I have analysed 9 type 2 'radio quiet' quasars, at $z \leq 0.2$, that were selected from the Quasar Feedback Survey (Jarvis et al. 2021) with available emission line data from ALMA for CO (3–2) (to study the molecular gas) and from MUSE (to study ionised gas with [OIII] and stellar kinematics). Additionally, archival, high-resolution VLA data at 6 GHz was used to study the low-power radio jets detected in all 9 quasars (Jarvis et al. 2019). The 9 targets were selected to be bright (in terms of their bright [OIII] luminosities), with broad line widths ($\mathrm{FWHM}_{[\mathrm{OIII}]} \geq 800$ km s^{-1}), and moderate radio luminosities (see Figure 5.1). Further, all 9 have been found to be gas-rich and star-forming (see Jarvis et al. 2020). The main conclusions from this chapter are summarised as follows:

- **A range of stellar morphologies are observed across the targets (see Figure 5.2)** Despite the uniform pre-selection in AGN properties and the sample being consistently gas-rich and star-forming, the 9 targets were observed to display a wide range of morphologies, based on the stellar morphologies and kinematics. Particularly, ordered rotating spiral disk-like structures were observed for J0958+1439, J1100+0846, and J1316+1753; irregular morphologies potentially arising from ongoing mergers and/or other interactions were

observed for J1000+1242 and J1010+1413; and finally elliptical morphologies arising from late stage mergers were observed for J0945+1737, J1010+0612, J1356+1026 and J1430+1339.

- **Interactions observed at large-scales between the radio lobes and molecular gas (see Figures 5.3,5.4,5.5)** Large-scale (≥ 10 kpc) interactions between radio lobes and detected molecular gas structures (consisting of $9-53$ % of the total molecular gas mass) are observed in 3/9 studied targets (Figures 5.3 and 5.4). These 3 targets (namely, J1000+1242, J1010+1413, and J1356+1026) are among the 5 that show radio structures extending to scales beyond the molecular gas disks (Figure 5.4). None of the targets that only have compact radio structures, within the molecular gas disk, show such interactions. The filaments observed in J1000+1242 and J1010+1413 had very similar properties (i.e., velocity widths, radial extent, mass outflow rate, kinetic power) to the filaments detected in the case of BCGs (see Figure 5.5 and Chapter 4). It could be that these interactions which are often observed to be related to 'radio loud' BCGs with giant radio lobes; could be happening for at least a subset of quasars hosting low-power radio jets. For the molecular gas structures detected for J1356+1026, the physical interpretation of the structures is less clear.

- **Ubiquitous multi-phase outflows observed across all 9 quasars on $\sim 1.6-3$ kpc scales (see Figure 5.6, and Figures 5.12 – 5.19**) Traced via broad CO emission-line components, molecular gas outflows were detected in all 9 quasars. These are only clearly identified in the central galaxy regions. When searched for on galaxy-wide scales (i.e., $\gtrsim 4$ arcsec; or ~ 7.4 kpc), the previously-know ionised gas outflows were seen in all 9; however, no molecular outflows are clearly detected in these galaxy-scale emission-line profiles. Hence, molecular gas outflows in this sample, do not dominate at global scales.

- **Molecular gas outflows seen to be compact and 2 –5 times slower than the ionised gas outflows (see Figures 5.7 and 5.10)** The molecular gas outflows in all 9 targets are more compact (≤ 5 times less-extended) than the ionised gas outflows (see Figures 5.6, and 5.12–5.19). Comparing their velocity-widths, the molecular gas outflows are found to be $2-5$ times slower than their ionised counterparts in the same spatial regions (Figure 5.7). However, in the same spatial regions, the fractional flux contribution of the broad components is seen to be comparable across the two phases, i.e., $\sim 0.8-1.2$ times (Figure 5.10).

- **No clear outflow trends seen based on the relative location and orientation of the jets and host galaxies (see Figures 5.7, 5.8, 5.9, 5.10**) Simulations of jet-ISM interactions predict a strong dependency on the radio properties: i.e., stronger multi-phase outflows are expected when the radio sources are seen to be more inclined, or more confined, and hence still within the galaxy disk (Mukherjee et al. 2018b; Tanner & Weaver 2022; Meenakshi et al. 2022). However, such trends are not observed for the sample studied in this chapter (see Figures 5.8 and 5.10). Nor did we find molecular gas outflows to become relatively more dominant, compared to the ionised phase, if the jet was more confined within the disk (Figure 5.10). However, the highest

fractional contribution of the outflow to the total molecular gas is seen in the 3 of the sources with the most luminous radio power and hence the highest jet power (Figure 5.9, right-panel).

Across the sample studied here, molecular and ionized gas outflows are seen to be ubiquitous and the radio jets are observed to be interacting with the multi-phase ISM at both small and large scales through different mechanisms. However, these interactions did not seem to show the trends that were expected from the jet-ISM simulations. This could be due to the bias in our sample selection since it was pre-selected to have ionised gas outflows which limits our interpretations of the multi-phase analysis. The sample also only covers a relatively narrow range in radio jet powers. Further, there are also challenges in estimating properties like jet power and jet inclination angles and these measurements are susceptible to assumptions that have stronger effects, especially in the cases where the radio structures are not resolved. These challenges could introduce a scatter in the explored trends. These reasons warrant a larger sample, free of pre-selection biases that would greatly help to obtain quantitative comparisons with simulations (see Chapter 6).

Despite the limited sample, this work shows that radio jets may have a relevant role in the feedback processes through different physical mechanisms panning out at different spatial scales in 'radio quiet' quasars. Through the observations of this chapter, this work challenges the quintessential approach to label AGN-driven central outflows as 'quasar feedback' and attribute jet-related feedback only to radio-loud galaxies; and demonstrates how low-power jets residing in quasar host galaxies, could also be causing remarkable jet-associated feedback on their hosts.

5.7 Appendix to the Chapter

5.7.1 Tidal arm in J1356+1026

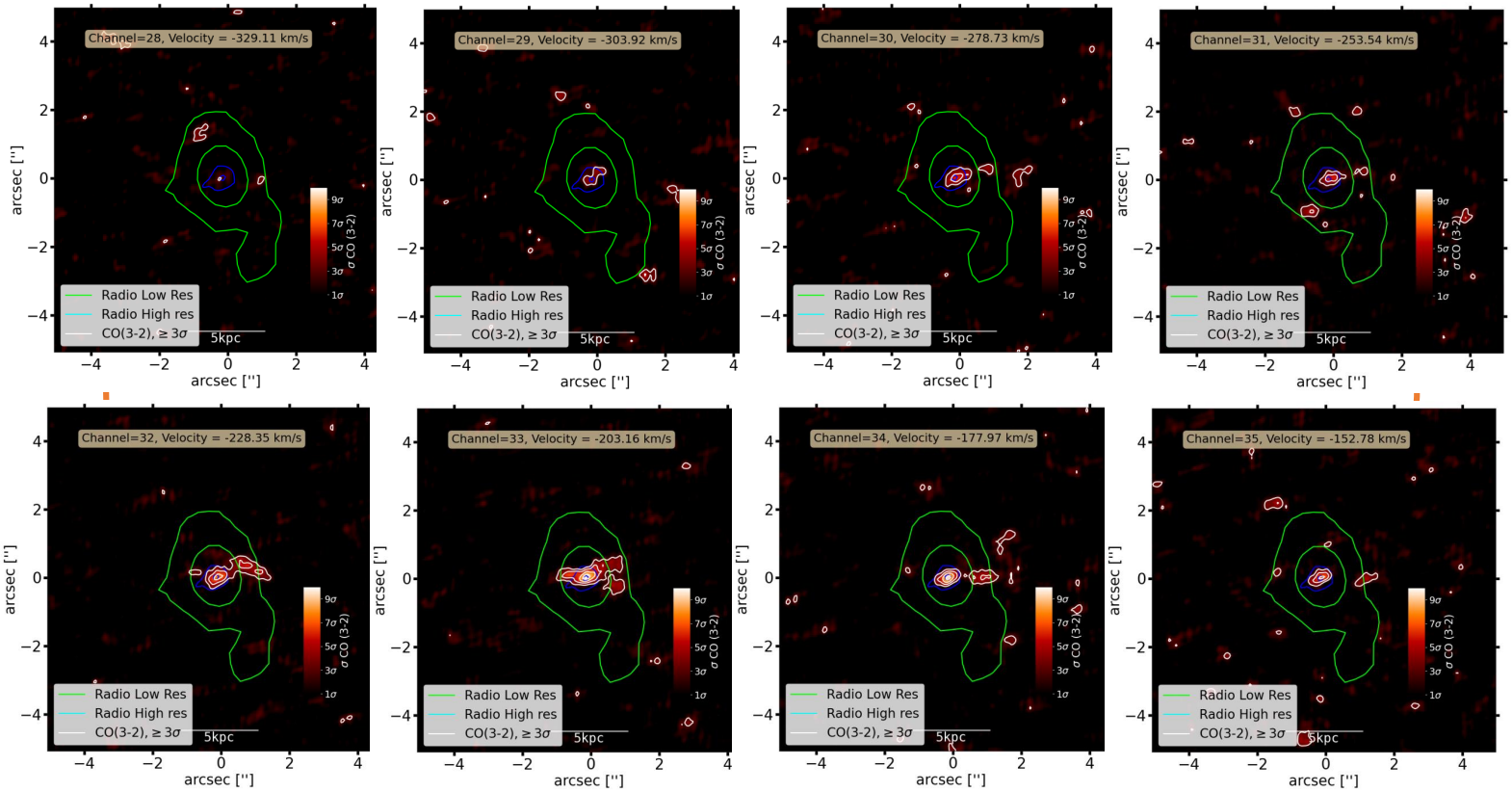

Figure 5.11: CO (3–2) emission-line maps corresponding to velocity channels from $[-329, -153]$ km s^{-1}(also indicated in the top-right of each panel). The subsequent images show the tidal arm detected to the West of the central galaxy disk in CO (3–2) emission as is also observed by Sun et al. (2014). The white contours are the CO (3–2) emission in these velocity ranges at $\geq 3\,\sigma$. The blue and green contours show the radio continuum emission at 6 GHz in high- and low-resolution respectively. The radio contour levels are the same as in Figure 5.2.

5.7.2 Kinematic multi-phase overview of the entire target sample

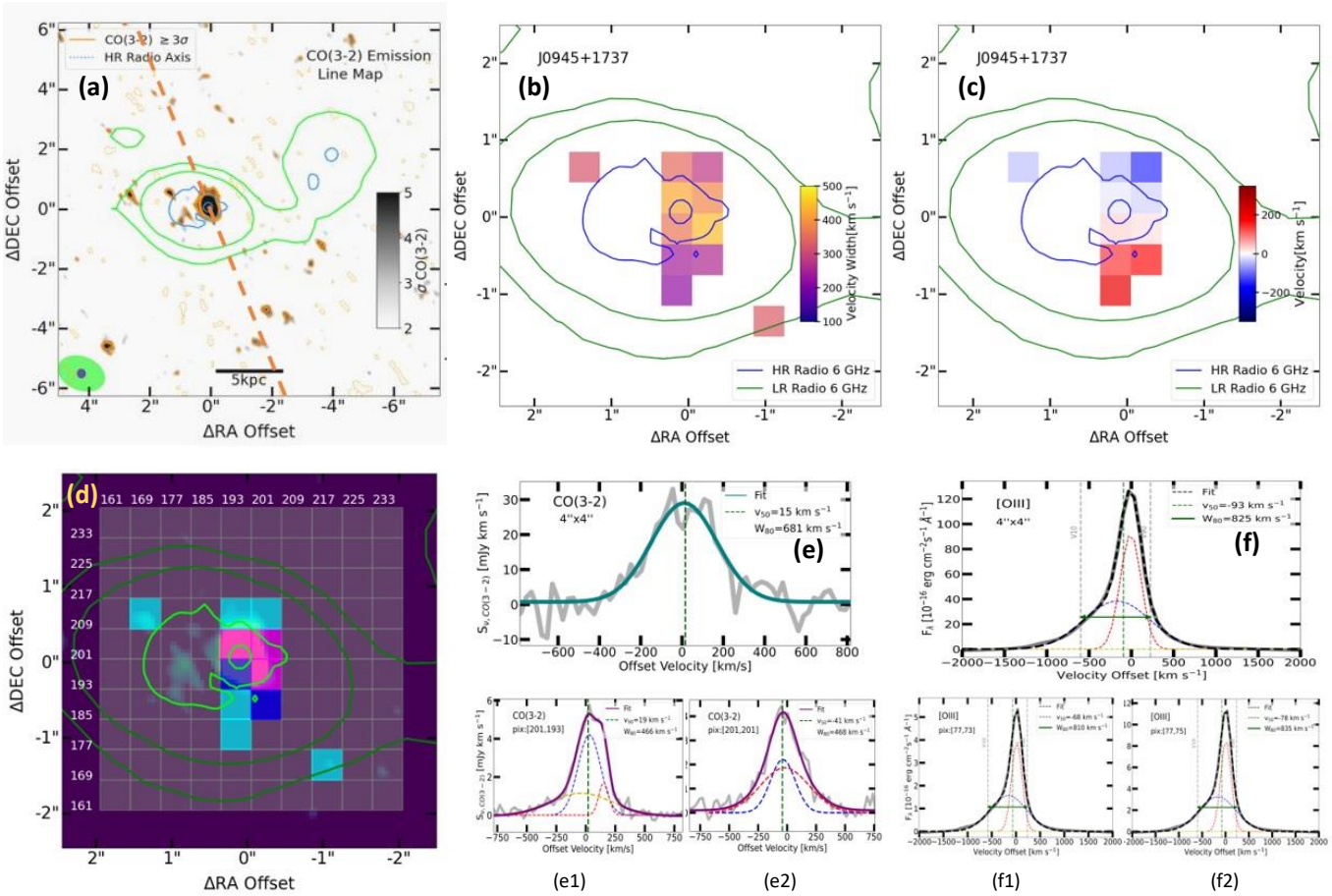

Figure 5.12: For **J0945+1737**, description same as Figure 5.6.

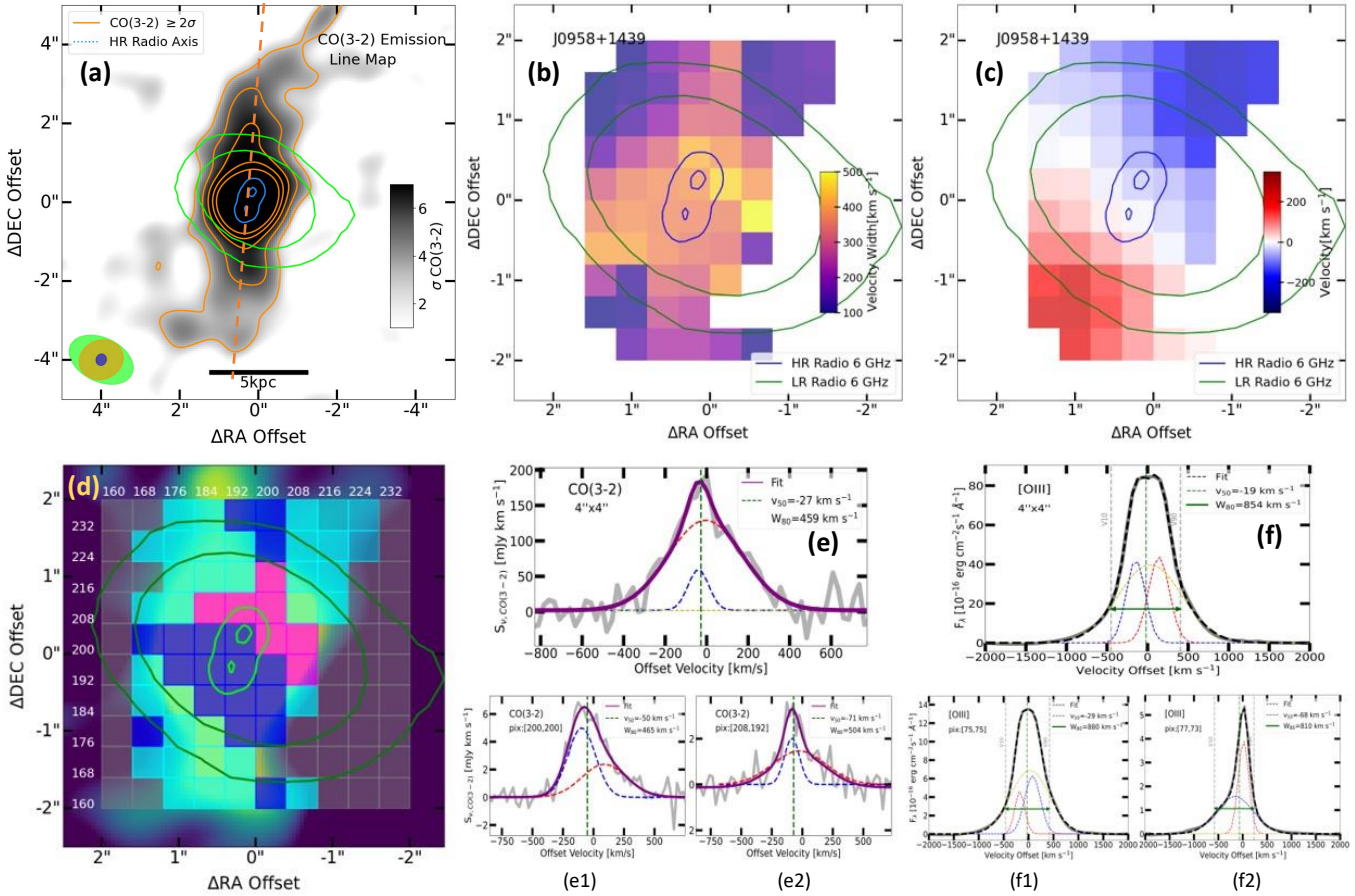

Figure 5.13: For **J0958+1439**, description same as Figure 5.6.

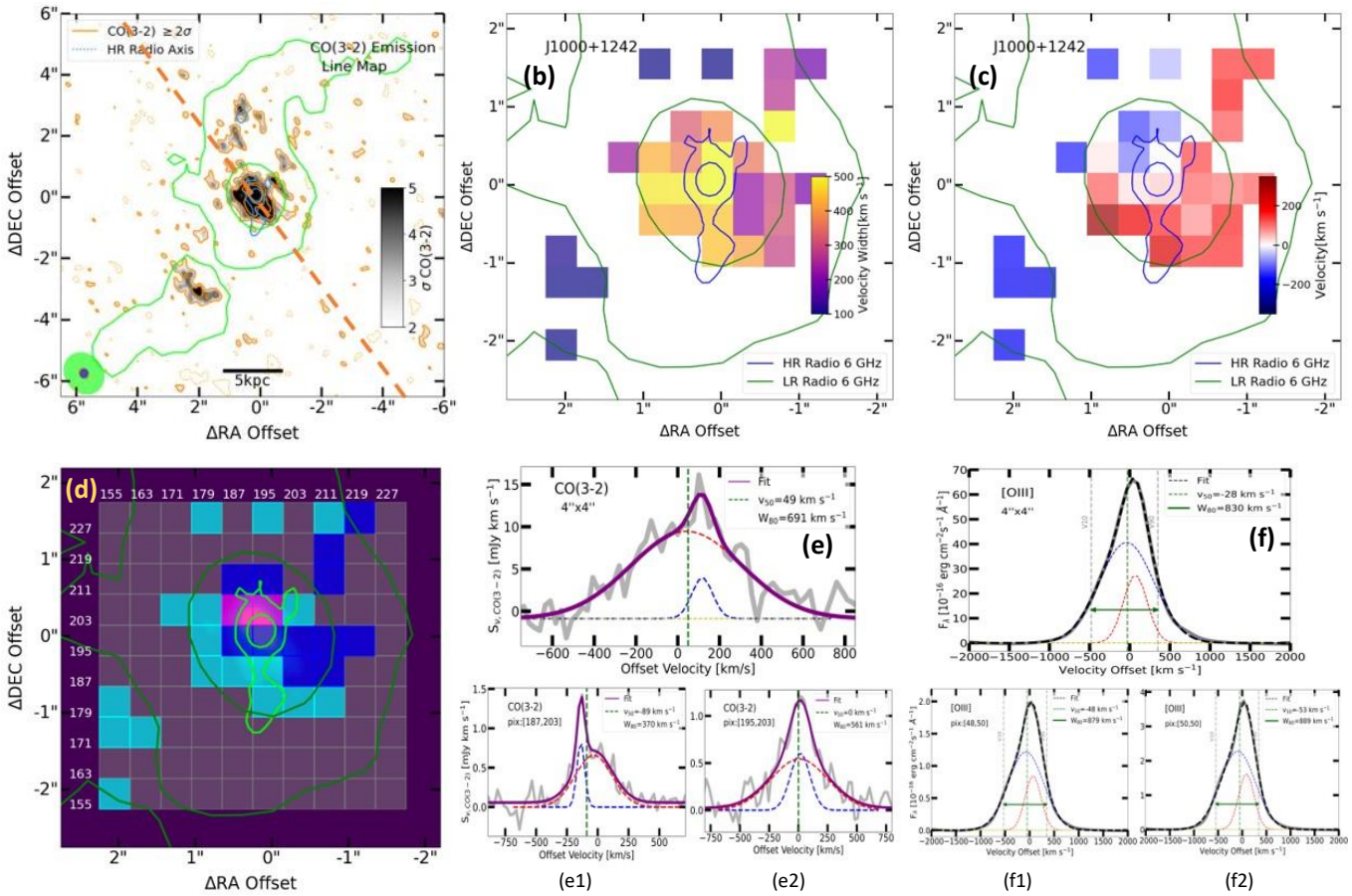

Figure 5.14: For **J1000+1242**, description same as Figure 5.6.

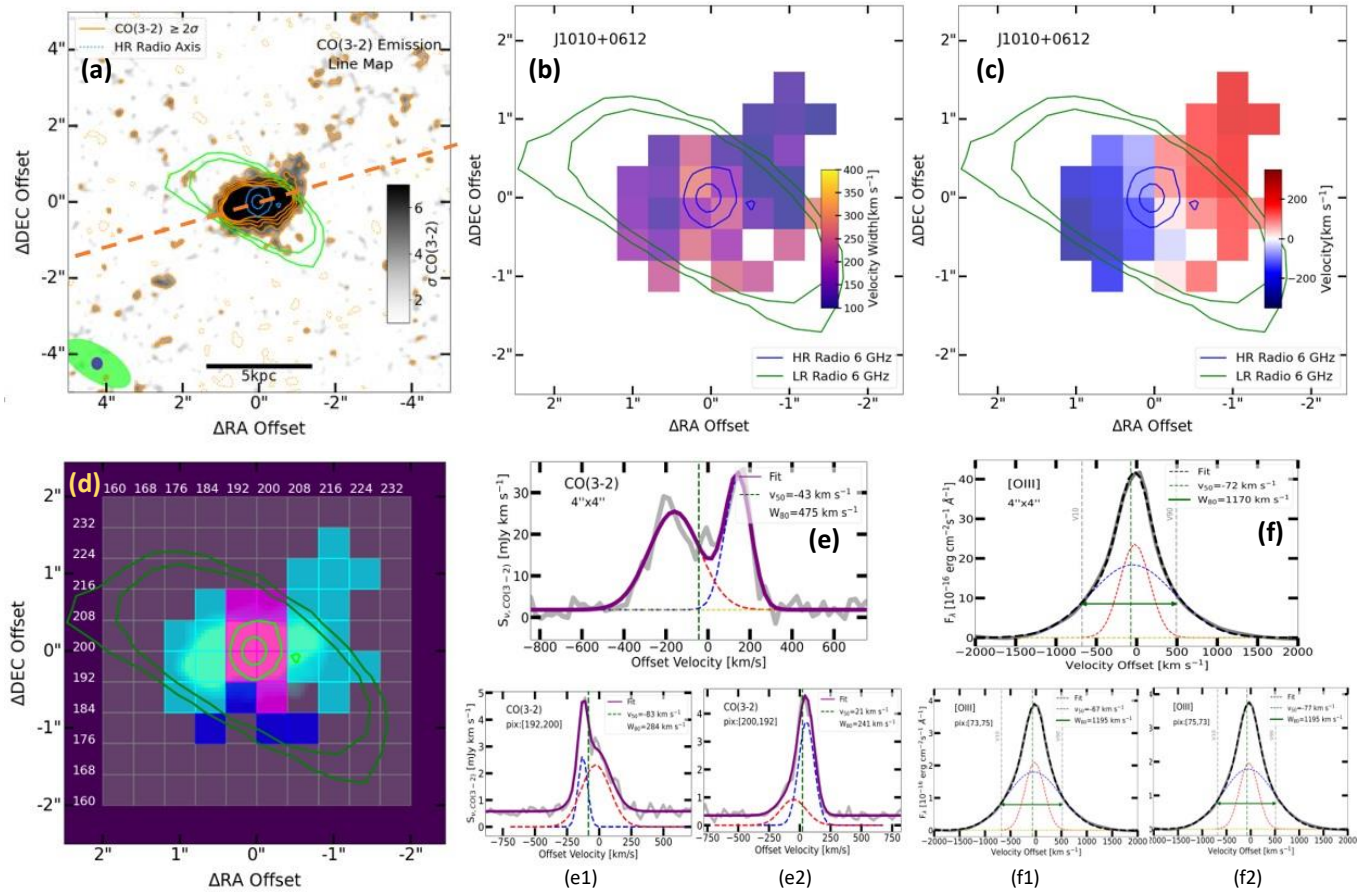

Figure 5.15: For **J1010+0612**, description same as Figure 5.6.

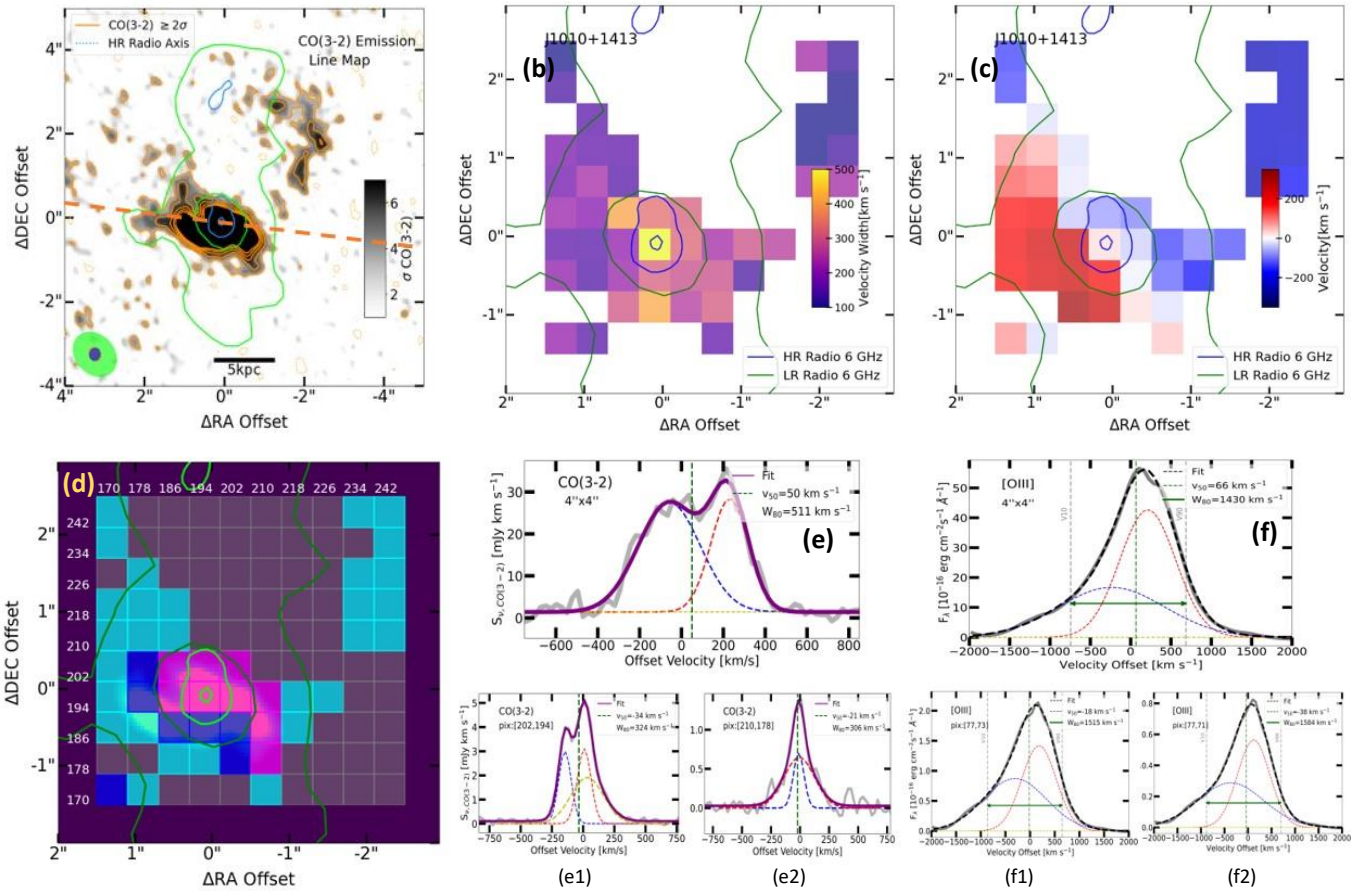

Figure 5.16: For **J1010+1413**, description same as Figure 5.6.

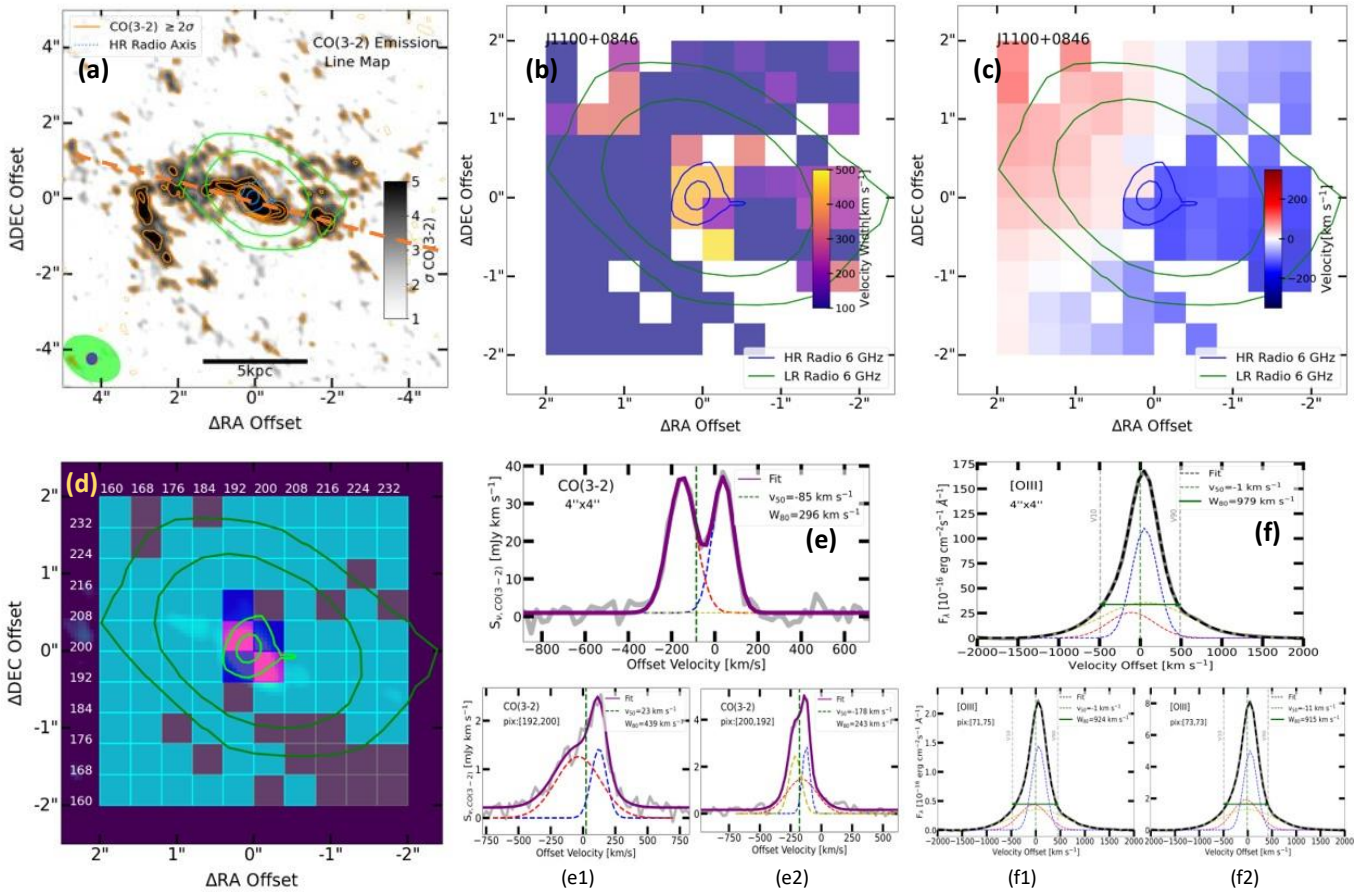

Figure 5.17: For **J1100+0846**, description same as Figure 5.6.

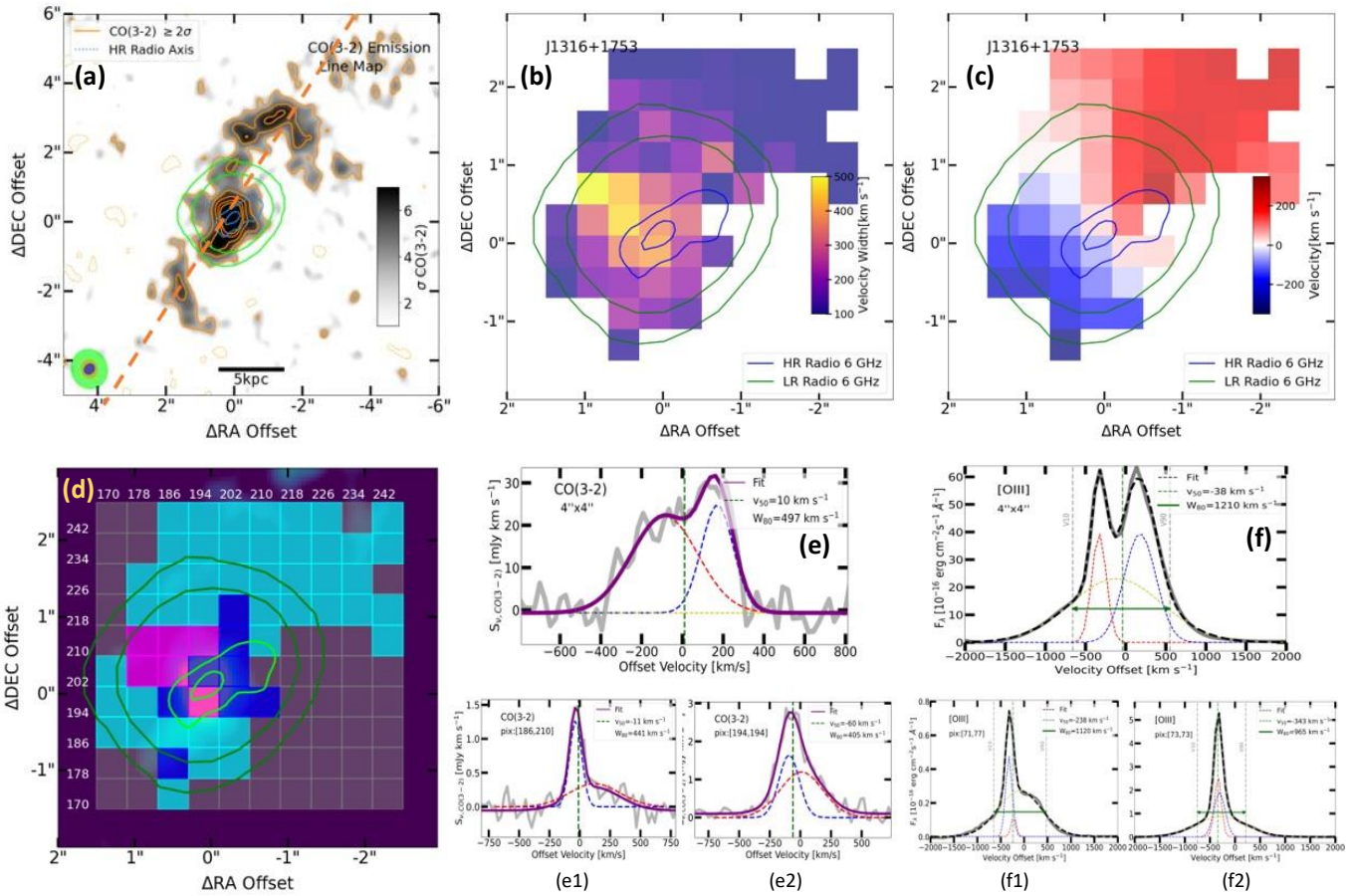

Figure 5.18: For **J1316+1753**, description same as Figure 5.6.

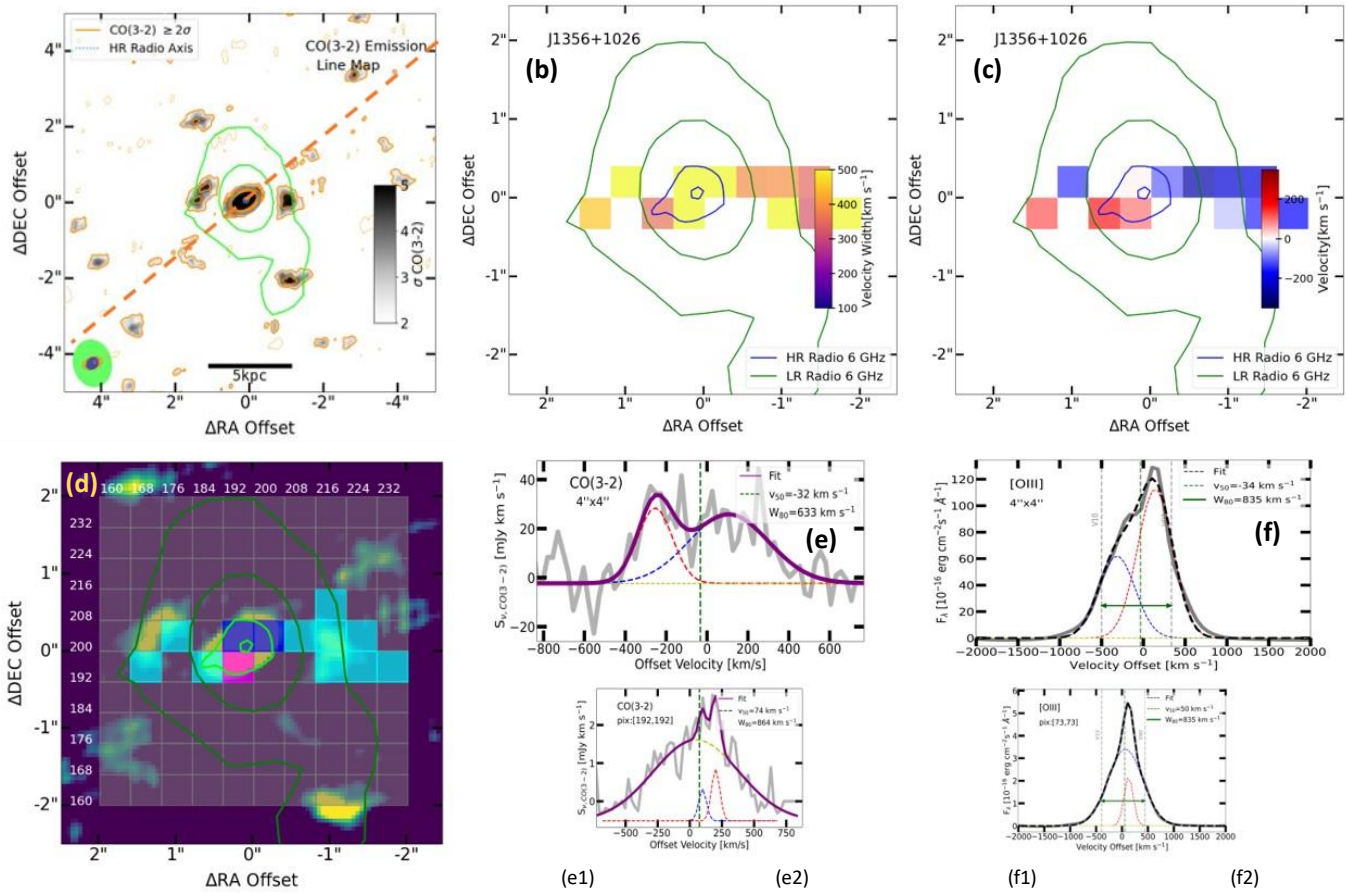

Figure 5.19: For **J1356+1026**, description same as Figure 5.6.

Chapter

6 Summary and Future Work

Active galactic nuclei (AGN) are fundamental in galaxy formation models to explain the properties of massive galaxies and their central supermassive black holes (see Section 1.4 e.g., reviews in Cattaneo & Best 2009; Harrison 2017). However, the observational evidence for the role of the most powerful AGN(i.e., quasars; $L_{\rm AGN} \gtrsim 10^{45}\,{\rm erg\,s^{-1}}$) remains controversial. This thesis has presented observational experiments, combining data from multiple facilities (see Chapter 2), to tackle the open questions around how galaxies are influenced by AGN (see Chapter 1). The work in this thesis presents evidence for how radio-quiet quasars hosting compact and low-power radio jets are capable of causing significant turbulence and galactic scale outflows in the host galaxies.

In this chapter, I first summarise the main conclusions of the work in this PhD thesis (in Section 6.1). This is followed by some questions that still remain open after this work. To answer these questions, I then provide an illustration of ongoing projects, including those that are based on the data from my two successful telescope proposals from Astrosat, and NOEMA (The Northern Extended Millimeter Array), as the PI and Co-PI, respectively (Section 6.2). Finally, this chapter concludes the thesis by discussing the broader direction I expect this research to take over the next decade and beyond, noting the upcoming facilities that would aid this field of astrophysical research (Section 6.3).

6.1 Summary of the work in this thesis

This thesis has aimed to advance the understanding in the field of quasar feedback on its host galaxy, particularly by characterizing the multiphase outflows and their impact on their hosts. Throughout its chapters, the thesis has focussed on 9, $z < 0.2$ Type-2 quasars, from the parent sample of the Quasar Feedback Survey (introduced in Section 1.7), and having AGN luminosities ideal for studying the outflows (i.e., L_* equivalent to that observed at cosmic epoch, where the quasars as well as the AGN driven outflows are seen to be prevalent). This helps establish the impact of jets/outflows beyond the local Universe (where low-power systems dominate) but with a spatial accuracy not possible at high-z (where equivalent quasars are prevalent). All the 9 targets are also observed to be radio-quiet by the traditional radio criteria and have modest radio luminosities ($L_{1.4\rm GHz} = 10^{23.3-24.4}\,{\rm W\,Hz^{-1}}$). This provides for an interesting dataset of sources where feedback would have been traditionally considered to be caused by radiative processes. However, this thesis reveals the importance of comparing the multi-phase gas properties in detail to high-resolution radio imaging to challenge this assumption. Across the chapters, the ionised gas

phase is traced primarily using the [OIII] transition from MUSE data (see Section 2.1.2); and the molecular gas phase is studied using ALMA (see Section 2.2.1), specifically focusing on the CO (3–2) emission.

The primary open questions that this thesis tries to address are broadly:

- Which is the dominant mechanism for driving the outflows/turbulence in the interstellar medium of the quasar host galaxies (e.g. jets/disk winds/radiation)?
- What impact do these multiphase outflows have on their host galaxies?
- How does the AGN feedback vary with the radio properties?

Chapter 3 performs a single source case study to address each of these questions, followed by Chapter 4 and Chapter 5 that are aimed at assessing the impact of the feedback on the host galaxies on the wider sample; and its dependence on the properties of the radio jets. Following these, the main conclusions from each chapter are summarised below.

6.1.1 Main conclusions from Chapter 3

Chapter 3 is based on the case study of one target from QFeedS, J1316+1753, at $z = 0.15$. This target exhibits a broad [OIII] emission-line profile (FWHM$\sim$ $1300\,\mathrm{km\,s^{-1}}$) and is one of the most luminous in QFeedS based on its [OIII] luminosity ($L_{[OIII]} = 10^{42.8}\,\mathrm{erg\,s^{-1}}$). VLA radio data had revealed the presence of a compact, low-power radio jet (i.e., $\sim 1\,\mathrm{kpc}$ projected size and $P_{jet} = 10^{44}\,\mathrm{erg\,s^{-1}}$). Importantly, this jet is also observed to be inclined with respect to the galaxy disc at a very low inclination angle ($\sim 5°$). In this thesis, the ALMA data of this target was used to map the molecular gas properties from CO(3–2) in addition to using the MUSE data for mapping the stellar kinematics as well as ionised gas properties. The kinematic analysis revealed ongoing jet-ISM interactions with enhanced velocities in the multi-phase ISM at the jet hotspots. Multi-phase turbulent gas was also observed in this galaxy being driven perpendicular to the galaxy disc in both the ionised and the molecular gas phase. This was also consistent with the predictions from simulations of the jet-ISM interactions which suggested that jets inclined into the disk, even if low in power are capable of causing significant effects to the host galaxy. The molecular component of the outflow was seen to be three times less extended and three times less disturbed (in terms of velocity dispersion) as compared to the ionised counterpart. The regions of the outflows also show a higher electron density as determined with the [SII] emission. Finally, strong spatial connections were revealed between the jets and the stellar properties with a close alignment seen between the position angle of the stellar bulge with respect to the jet axis. This could be a possible hint of the presence of positive feedback induced by the jet in the galaxy ISM.

This work provides strong observational evidence of the feedback power that inclined low-power jets may have. This is especially noteworthy for the case of this source because while the energy output is dominated by the bolometric radiative luminosity of the AGN, the kinetic energy from the jet is observed to cause an outflow and more significant turbulence. This is particularly notable since this chapter presents the observation of a process that has previously only been associated with less

bolometrically luminous systems and/or with those with more powerful jets. This result hence forms the foundation to study the jet feedback in low-power quasars in the subsequent chapters.

6.1.2 Main conclusions from Chapter 4

Chapter 4 lends further evidence to the significance of jet feedback in radio-quiet galaxies. This chapter focuses on the study of the molecular gas properties in four z<0.2 quasars from the QFeedS sample, namely, J0945+1737, J1000+1242, J1010+1413, and J1430+1339. To search for radio lobe interactions with the gas on larger scales than the molecular gas disks, the four galaxies with projected radio sizes $\geq 10\,\mathrm{kpc}$ were selected, specifically defined as radio largest linear sizes ($\mathrm{LLS_{radio}}$). The four targets have bolometric and radio luminosities in the range of $\mathrm{L_{bol}} \sim 10^{45.5-46.7}\,\mathrm{erg\,s^{-1}}$; $\mathrm{L_{1.4\,GHz}} \sim 10^{23.7-24.3}\,\mathrm{W\,Hz^{-1}}$, respectively. The kinematics and spatial distribution of the CO (3–2) emitting molecular gas were studied using the ALMA data, and compared with the radio continuum emission observed with VLA at 6 GHz. Filamentary molecular gas structures were identified in two out of the four targets, namely, in J1000+1242 and J1010+1413, with $\sim 9\,\%$ and $\sim 53\,\%$ of the total molecular mass located in these structures. These filaments are observed to extend from $5-13\,\mathrm{kpc}$, but with modest velocities of $|\,100-340|\,\mathrm{km\,s^{-1}}$. Further, their velocity dispersion values were observed to be relatively narrow, i.e. $\sigma_{\mathrm{fil}} = 30-135\,\mathrm{km\,s^{-1}}$, compared to the galaxies as a whole ($170-230\ \mathrm{km\,s^{-1}}$). The mass fractions seen in the filament are in agreement with those predicted by simulations for low-power radio jets (see Mukherjee et al. 2016). It is intriguing how similar the filament properties are to those filaments that are more commonly seen in bright cluster galaxies (BCGs) powered by strong radio jets, and hence predominantly classified as radio-loud. The mass outflow rates and kinetic powers are seen to be in agreement for the radio-quiet targets studied in this chapter and the BCG sample; despite the different orders of the jet kinetic powers. The other two targets, namely J0945+1737 and J1430+1339 did not show any such extended molecular gas filaments, however, an upper limit of 4% and 9% was estimated, respectively.

In addition to the large-scale molecular filaments, the analyses in this chapter revealed the presence of central broad molecular outflows in all 4 of the studied galaxies. These outflows are observed to be centrally concentrated (at around $0.6-1.6\,\mathrm{kpc}$), but show the presence of broad velocity wings reaching up to $440\,\mathrm{km\,s^{-1}}$. These molecular outflows have properties comparable to an archival sample of star-burst and AGN galaxies (at typically lower $\mathrm{L_{bol}}$). Following from Chapter 3, this further lends support to the presence of molecular gas outflows arising due to interactions of low-power radio jets seen to be present in all four targets. The presence of both the physical mechanisms, i.e. filamentary molecular gas structures at the large scales and broad outflows at the central scales, in the same targets hints at a possible evolutionary sequence of low-power radio jets where they might cause broad but less-extended outflows in the central regions due to jet-ISM interactions, and then proceeding to larger scales causing a gentler pushing around of molecular gas seen as wrapped around the radio bubbles.

A limitation of this chapter in investigating both the small- and large-scale feedback mechanisms on the molecular gas was the pre-selection of large (≥ 10 kpc) radio structures. Therefore, the study sample is expanded in the following chapter to look for possible signatures of the two physical mechanisms in the overall 9 targets and assimilate a possible evolutionary sequence of the radio jets.

6.1.3 Main conclusions from Chapter 5

Chapter 5 expands the study from the previous chapter to a larger sample of 9 quasars from Quasar Feedback Survey with the dataset to enable a multi-phase study. All 9 quasars are 'radio quiet' and host low-power radio jets. While the 9 targets were pre-selected to have similar optical and radio luminosities, and at similar redshifts ($z \sim 0.1$), they interestingly display a variety of host galaxy stellar morphologies. The availability of MUSE data enabled a study of stellar kinematics and morphology that revealed an ordered disk-like morphology in 3/9 targets, an irregular morphology arising from potential ongoing mergers in 2/9, and elliptical morphologies in the remaining 4. While the sample was selected to have ionised gas outflows; molecular gas outflows were also observed to be ubiquitous across all 9. However, the molecular gas outflows were not detected on galaxy-wide scales, and undertaking a spatially-resolved approach helped detect them on compact scales (≤ 3 kpc); which were observed to be approximately $4-5$ times less extended than the ionized gas outflows. Further, comparing the velocity widths of the emission lines only within the regions where molecular gas outflows were detected, showed that the ionised gas outflows were $2-5$ times faster than the molecular gas. However, within the same regions, the fractional flux contribution of the outflow to the overall emission in those regions was found to be comparable (i.e., $0.8-1.2$) for both phases.

In this chapter, I have also searched for the presence of extended molecular gas structures beyond the galaxy disk and for any signs of interaction with the radio lobes, across all 9 targets. This builds on Chapter 4, where such features were only searched for in sources with radio structures beyond 10 kpc. Only 3/9 targets, i.e., only 1 new target (J1356+1026) revealed the presence of such molecular gas structures extending outside of the molecular gas disk. Interestingly, these molecular gas structures were only observed for the 3/5 targets that also had radio structures extending at such scales. This reveals that they are uniquely associated with the larger-scale radio emission. Finally, in this chapter, motivated by predictions from simulations, I have also looked for trends with respect to the host galaxy and jet properties. Specifically, the relative inclination and size of the jets and molecular gas disks. However, no such trends were clearly observed. However, the three targets with the highest broad molecular flux fractions are also the three with the highest radio jet powers; suggesting a potentially stronger contribution from the kinetic jet powers in the removal of molecular gas from the host galaxy. As discussed below, a larger and less biased sample would be required to draw more definitive conclusions on the relationship between multi-phase outflow properties and the jet and/or host galaxy ISM properties.

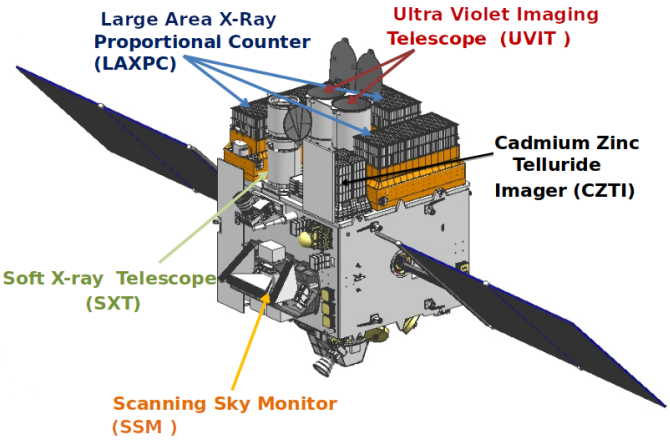

Figure 6.1: A schematic representation of the Astrosat satellite with the placement of UVIT at the top. *Image Credit: Astrobrowse Archive.*

6.2 Ongoing and Future Work

This thesis has demonstrated the importance of jet-ISM interactions in even radiatively powerful AGN (i.e., quasars). The multi-phase (ionised and molecular) gas can be strongly influenced by low-power jets in quasars, in a similar manner as previously observed in AGN where the jets are more dominant in the total energy output.

Some questions however still remain to be addressed and have motivated ongoing and future work, as summarised below. The specific areas of interest are:

1) To understand the potential direct impact by the AGN on the *star formation* in their host galaxies, as opposed to just the star-forming material investigated thus far. This motivated a successful Astrosat proposal to map the UV emission in the QFeedS galaxies to trace the younger stellar populations (see Section 6.2.1; PI: A. Girdhar).

2) The molecular gas analysis in the above chapters has been biased to targets with known ionised outflows, which may also prejudice the conclusions. This has further motivated two successful proposals to study the molecular gas using NOEMA (see section 6.2.2; co-PI: A. Girdhar and S. Molyneux) and secondly using ALMA (see Section 6.2.3; PI: C. M. Harrison; co-I: A. Girdhar).

3) The initial selection of 42 targets for QFeedS, has a radio luminosity constraint of $L_{1.4GHz} \geq 10^{23.5}\,W\,Hz^{-1}$. This biases the sample to intermediate radio luminosities, thereby excluding the quasars with lower radio luminosities. This therefore motivated a successful VLA proposal to extend the data sample to the lower radio luminosities (see Section 6.2.4; P.I. A. Njeri; co-I: A. Girdhar).

Table 6.1: The proposed targets for observation with UVIT onboard the Astrosat with their properties, in priority order: (1) Target number; (2) quasar name; (3) target redshift (4) the magnitude of the target in the Far-UV band; (5) Requested exposure time for each target (in seconds); (6) the observation date status as of present.

Target	Name	z	$m_{AB,FUV}$	Requested Exposure Time [s]	Observation Status
(1)	(2)	(3)	(4)	(5)	(6)
TO1	J1000+1242	0.15	19.540	12600	N.A.
TO2	J1010+1413	0.20	19.878	11300	N.A.
TO3	J1356+1026	0.12	18.420	3900	27 June 20
TO4	J1430+1339	0.09	17.632	1900	27 June 20
TO5	J0945+1737	0.13	19.683	14200	N.A.

6.2.1 Studying the UV emission in quasars from Astrosat data

To establish the role of quasars in galaxy evolution, the impact of multiphase AGN outflows on star formation is imperative to be accounted for. This calls for observational evidence to understand the impact of the outflows on the ISM properties and star formation in their host galaxies. Various theoretical models have shown how jets could suppress or regulate the star formation in the host galaxy by introducing turbulence in the ISM or causing multi-phase outflows (see Nesvadba et al. 2010, 2011; Alatalo et al. 2015; Mukherjee et al. 2018b). On the contrary, studies have also shown jet-induced positive feedback being driven by the shocks caused by the jets thereby inducing star formation from both theoretical (e.g., Gaibler et al. 2012; Bieri et al. 2016; Fragile et al. 2017) and observational perspectives (e.g., Bicknell et al. 2000; Salomé et al. 2015; Lacy et al. 2017). Hence, it is not well understood how these collimated radio jets may interact with the galaxy ISM. Simulations have also shown that both the gas distribution and star formation can be affected up to kilo-parsecs away by a jet. Having combined the radio imaging with MUSE and ALMA data to identify and characterize jets and spatially resolve the multi-phase interstellar medium (ISM) at $\lesssim$kpc resolution (see Chapter 3-5), the next goal is to connect the physics of the gas with the star-formation over the entire galactic structures.

This formed the basis of the proposal to obtain for the first time, high spatial-resolution UV observations for the five quasars with the strongest evidence of outflows and jet-ISM interactions. All five targets were confirmed to have strong GALEX (NASA's Galaxy Evolution Explorer; Martin et al. 2005) detections. Astrosat's spatial resolution ~ 5 kpc (corresponding to UVIT's FWHM resolution of < 1.8", at an average redshift of $z = 0.2$) will help obtain observations with 3 times better spatial resolution than GALEX. UV emission provides a good tracer to study the young star-forming regions, produced by the hottest most massive stars. Therefore, spatially-resolved UV emission will help obtain the distribution of young star-forming regions and compare to the spatial distribution of the radio emission, further helping to identify signatures of positive or negative feedback due to the jets and/or outflows. These targets are listed in Table 6.1.

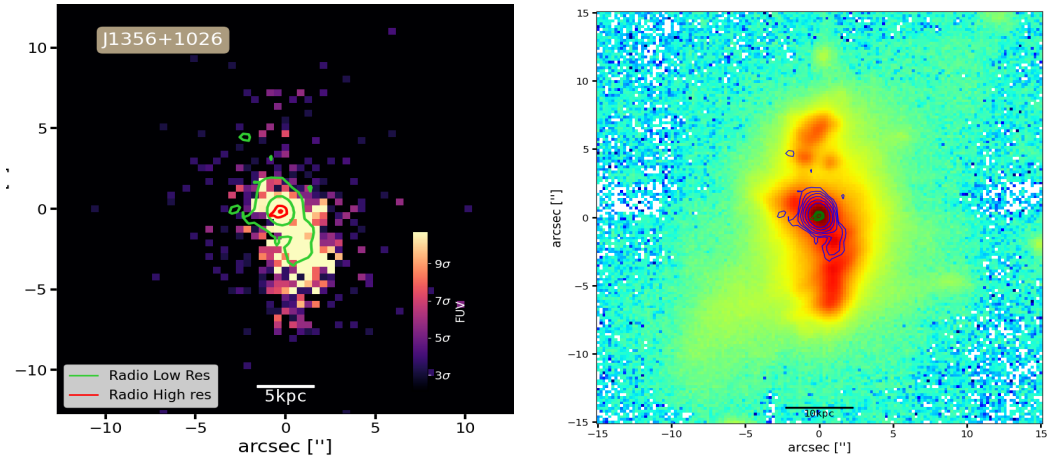

Figure 6.2: J1356+1026: *Left-Panel:* Far-UV emission, as observed by UVIT with the radio emission, overlaid as contours in green and red. *Right-Panel:* [OIII] emission image from MUSE data cube with the same radio contours overlaid to compare with the UV data for the same target.

Astrosat

Astrosat (Agrawal, 2006; Singh et al., 2014) is India's first space telescope, launched by the Indian Space Research Organisation (ISRO) and covering multi-wavelength observations in UV, optical, and X-ray bands simultaneously. The satellite is designed in a way that it has several co-aligned instruments and hence is capable of observing the targeted celestial body in multiple wavelengths simultaneously by passing the light through different filters. Astrosat currently resides at an orbit of 650 km above Earth, inclined at an angle of 6° to the equator. The satellite is managed from a ground-based spacecraft control centre called ISRO Telemetry, Tracking, and Command Network (ISTRAC), in Bengaluru, India. Of the various science objectives that Astrosat caters to, the one that is of main interest to this work is to utilise the observations in ultra-violet regimes to detect young stellar populations in the quasars from the QFeedS sample.

Figure 6.1 shows a schematic representation of Astrosat with the placement of the different instruments, including the Ultra Violet Imaging Telescope (UVIT; Kumar et al. 2012; Subramaniam et al. 2016) on Astrosat. UVIT is primarily an imaging instrument observing in three channels simultaneously FUV (130-180 nm), NUV (200-330 nm), and VIS (320-550 nm), with a field of view of 28 arcmin. Further, the two ultraviolet channels have gratings that provide low-resolution, slitless spectroscopy (spectral resolution ~ 100).

UVIT proposal status and plans

The observations were requested in the A09 cycle of Astrosat, during which the Near-UV instrument was out of function and hence the galaxies were only observed in FUV. Further, while the proposal was highly ranked and accepted for full observation, the pandemic caused the observations and data processing to be severely delayed which led to only two of the targets being observed in the end.

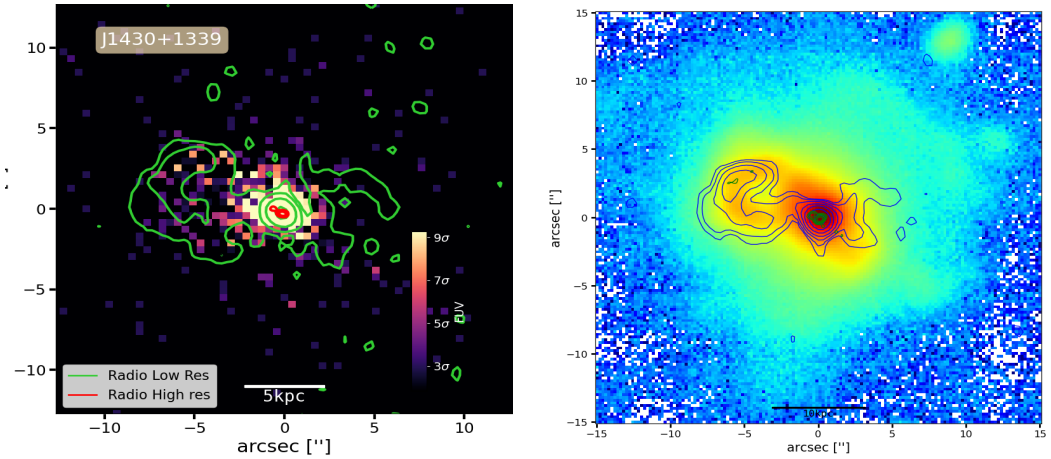

Figure 6.3: J1430+1339: *Left-Panel:* Far-UV emission, as observed by UVIT with the radio emission, overlaid as contours in green and red. *Right-Panel:* [OIII] emission image from MUSE data cube with the same radio contours overlaid to compare with the UV data for the same target.

The primary goal of this study is to establish the impact of the jets and outflows that have been previously identified in the proposed targets (see previous chapters). For a multiphase overview, the observations will be combined with the MUSE data, ALMA data, and the multi-frequency radio observations from VLA of the same targets. UV observations are crucial to obtain a complete census on the young star-forming regions, particularly in AGN host galaxies, where Hα alone can be quite ambiguous and is only an indirect tracer (e.g., see Lansbury et al. 2020). Therefore, spatially-resolved UV measurements will be the key tracer to map the star formation inside our systems; without having to solely depend on Hα which may often be dominated by the emissions due to the powerful AGN radiation. Using SED fitting, it has already been established that the UV emission in these targets is dominated by young stellar populations (Jarvis et al., 2019).

Figures 6.2 and 6.3 show preliminary images of the FUV emission obtained from Astrosat for J1356+1026 and J1430+1339, respectively, in comparison to the radio continuum emission from VLA (shown as overlaid contours) and the [OIII] emission obtained from MUSE. These figures show FUV emission to be co-spatial to the ionized gas and radio continuum, especially in the very central regions. This could help trace the presence of young stellar populations which have indeed also been detected in the 'handle' of the teacup galaxy (see Venturi et al. 2023).

These UV observations will further help to obtain quantitative estimates when performing the analysis as detailed below:

1) Mapping the spatial distribution of the UV emission. Using the UV morphology and comparing it to the spatially-resolved emission-line ratio diagnostics from the IFS data, will help to reliably disentangle AGN and stellar origin for the UV emission (following Figures 6.2 and 6.3). Towards this, spatially-resolved soft X-ray emissions are also available for the two observed targets (J1356+1026 and J1430+1339; e.g., see Greene et al. 2012; Lansbury et al. 2018) that will help provide an additional constraint on recent star-formation.

2) Constructing spatially-resolved maps of young stellar populations and making the unprecedented comparison to the jets/outflow interaction regions. Since all the targets have spatially resolved Balmer-decrement measurements from MUSE data, it is possible to correct the UV measurements for local extinction. Combining the UVIT photometry with the spectroscopic MUSE data will help derive the star formation histories and their resolved maps (following George et al. 2019; Lansbury et al. 2020).

3) Consequently, establishing the impact of outflows/jets on the host-galaxy star formation. For example, by searching for regions where jets/outflows have locally enhanced star formation (e.g., due to the compression of gas by the jets) and/or star formation cavities (potentially resulting due to the outflows; following George et al. 2019).

Overall, by placing these results into the context of the parent population (Figure 1.8) of the QFeedS sample, this analysis will provide some of the strongest determination yet on the direct impact upon star-formation by quasars.

6.2.2 Studying the molecular gas outflows and radio jet interactions from NOEMA data

NOEMA

The Northern Extended Millimeter Array (NOEMA) is a powerful radio interferometer observing at millimeter wavelengths and is run by the research institute IRAM (Institut de radioastronomie millimétrique). It works on similar working principles as ALMA (see Section 2.2.1), but instead consists of twelve 15-metre antennas that are capable of expanding to baselines of up to 1.7 km. At the maximum baseline, NOEMA can obtain an angular resolution of about 0.1 arcsecond at 350 GHz, thus serving as an excellent observatory to obtain high-resolution observations of the molecular clouds in distant galaxies. NOEMA is also part of the Event Horizon Telescope that helped obtain the image of the SMBHs at the centre of M87 and our galaxy (see Figure 1.1).

Radio jet interaction with the molecular gas

For a complete understanding of the interactions between the supermassive black holes and their host galaxies, multiphase observations are needed. This work focuses on the analysis of the molecular gas since this gas phase is responsible for fuelling the SMBH as well as for promoting star formation activity in the host galaxy. All the 9 targets studied in this thesis reveal radio jets either in young and/or evolved stages. Chapter 4 has looked into the efficiency of coupling and the interaction between these radio jets and the molecular gas in the galaxy ISM in detail at different galaxy scales, i.e., at smaller scales in the central galaxy regions ($\sim$kpc scales) and also at more extended scales with the radio lobes (≥ 10 kpc scales). This NOEMA project extends a similar analysis on two more targets, namely, J1108+0659 and J1016+0028, from QFeedS (in addition to the 9 studied in this thesis). Importantly, these two targets were not pre-selected to have broad [OIII] emission in their SDSS spectra, unlike the former 9 targets.

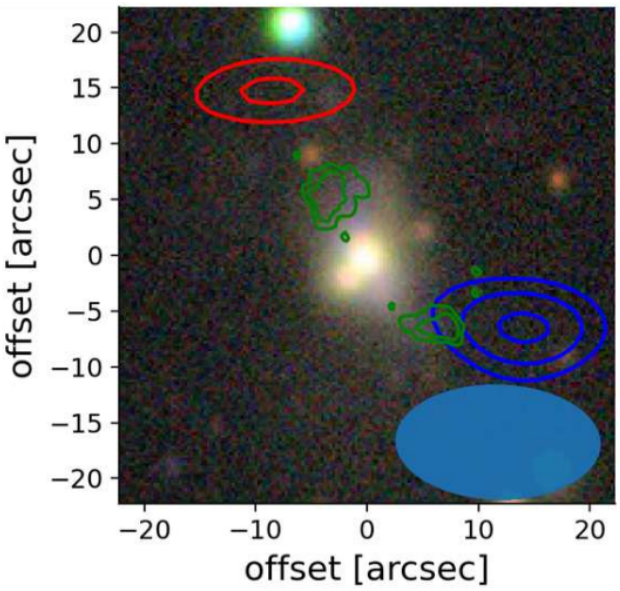

Figure 6.4: The CO (1–0) contours observed with ACA shown in red and blue corresponding to the redshifted and blue-shifted velocities at the levels of [3,4,5] σ_{CO}. VLA low-resolution radio contours at 6 GHz, shown in green at contour levels [8,16]σ. ACA data helped to detect the presence of molecular gas behind the radio lobes. The NOEMA observations will help confirm the presence of molecular gas along with improved sensitivity of detection.

The two targets for this proposal had available CO (1–0) transition data from the ACA telescope (Molyneux et al., submitted). ACA data for J1108+0659 shows evidence of a broad central molecular outflow along with the presence of a young compact radio jet. ACA data for J1016+0028 shows evidence for extended strong radio lobes with molecular gas concentrations behind the lobes, see Figure 6.4. These two targets were proposed for high-resolution interferometric observations using NOEMA and have been successfully observed. These data will help capitalize on ancillary multi-wavelength data for these two targets thereby helping the understanding of the processes at play in these targets. The two targets are listed in Table 6.2.

The Band 1 observations obtained with NOEMA have a five times higher resolution than the previously available observations with ACA. The improved resolution of J1108+0659 will hence help to identify the precise location of the molecular gas outflow in the target and its properties in comparison to the other phases. The observations for J1016+0028 will also greatly aid in identifying if the molecular gas around the radio lobes is wrapped similarly to that observed in the case of targets studied in Chapter 4 of this thesis. Hence, these observations with the available MUSE data will form a natural extension to the analysis in Chapter 3 and will help further the understanding of the evolutionary sequence of the radio jet and its interaction with the molecular gas.

6.2.3 Expanding the multiwavelength sample

This thesis has revealed important feedback processes observed to be happening in a sample of 9 of the 42 ‘radio quiet’ quasars from the Quasar Feedback Survey. While different feedback processes are observed in a subsample of the 9 quasars, it naturally indicates the need to expand the sample of study. Having multiwavelength data

Table 6.2: The proposed targets for observation with NOEMA with their properties as follows: (1) quasar name; (2) quasar redshift from SDSS DR7 (3) and (4) Right Ascension and Declination of the targets as per J2000 epoch; (5) their radio luminosity; (6) their [OIII] luminosity; where (5) and (6) are from Jarvis et al. 2021.

Quasar	z	RA (J2000)	Dec (J2000)	$\log(L_{1.4GHz})$ /[W Hz^{-1}]	$\log(L_{[OIII]})$ /[erg s^{-1}]
(1)	(2)	(3)	(4)	(5)	(6)
J1016+0028	0.116	10:16:53.82	+00:28:57.1	23.6	42.18
J1108+0659	0.181	11:08:51.03	+06:59:01.4	24.0	42.32

available for all targets will enable the multiwavelength analysis as followed in this thesis on a larger sample. Hence, in order to explore the prevalence and relevance of the different feedback processes across a larger sample, my collaborators and I have proposed further observations of the QFeedS targets. Based on the kinematic analysis, comparing to stellar kinematics performed in this thesis and following rotation models in other works (see e.g. Ramos Almeida et al. 2021; Audibert et al. 2023), molecular outflows have been detected in 90% of the targets. Further, the previous chapters build on the interaction seen between the radio structures and the multiphase gas. This calls for expanding the analysis to the other QFeedS targets that do not have equivalent molecular gas data. Towards this aim, in cycle 10 of ALMA, we have successfully proposed, the remaining 8 targets, with available ionised gas data, but no molecular gas data, for observation in the CO (3–2) emission. The proposal has been accepted and will be scheduled for observation in the coming term. A uniform analysis over the sample of these 17 quasars will help form a more comprehensive understanding of how the molecular gas is interacting with the radio structures at different scales and phases; and if the molecular gas outflows are as prevalent as their ionised counterparts (Jarvis et al. 2019). Further, including the 8 targets will help extend the analysis to targets that are not pre-selected based on their broad [OIII] widths, unlike the 9 analysed in this thesis. This will also aid in placing the radio-quiet quasars in a more concrete comparison against the predominantly radio-loud BCGs and will help form an unbiased understanding of what drives the efficiency of kinetic coupling in radio-quiet quasars.

6.2.4 Pushing to fainter radio systems

Another extension of this study will be into the lower luminosity radio regime. The vast majority ($\sim 90\%$) of the radio quasars are observed at moderate luminosities ($L_{1.4GHz} \leq 10^{25}$ W Hz^{-1}; Zakamska et al. 2004). However, the Quasar Feedback Survey is limited by a radio luminosity cut at $L_{1.4GHz} = 10^{23.45}$ W Hz^{-1}, at $z \sim 0.2$ (as shown by the dotted grey line in Figure 6.5). This limits the understanding of how representative the observations are of the entire quasar population. In particular, for the prevalence and importance of radio jets. Hence, to assess the prevalence of the feedback processes in the radio-quiet galaxies and to better understand the dominant driving mechanism of these feedback processes, observations catering to the lower radio luminosities are needed. This requirement has been successfully met with an accepted proposal submitted to VLA to expand QFeedS to lower luminosity regimes, removing this previously restricting radio luminosity cut.

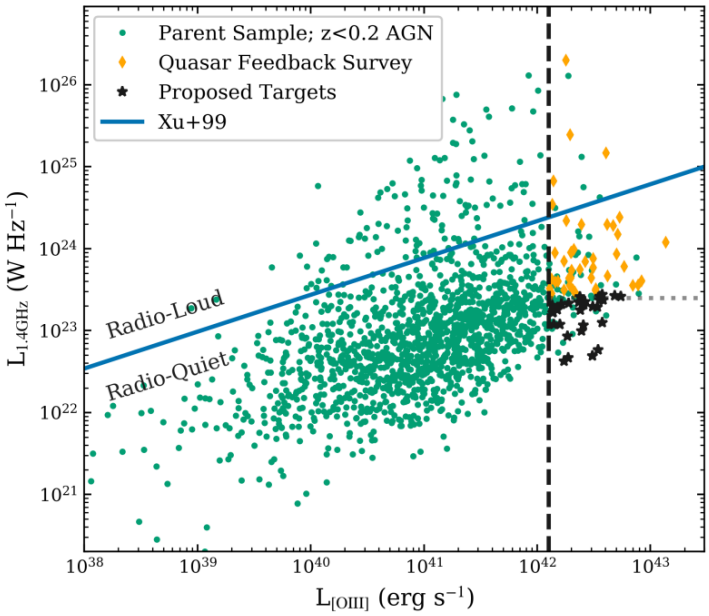

Figure 6.5: Radio luminosity ($L_{1.4GHz}$) vs. [OIII] Luminosity for the parent sample of all AGN at $z < 0.2$ from Mullaney et al. (2013) (in green). The dashed vertical black line shows the threshold of the quasar luminosity at $L_{[OIII]} \geq 10^{42.1}$ erg s^{-1}. The 42 quasars from the Quasar Feedback Survey are shown as orange diamonds above the radio luminosity cut of $L_{1.4GHz} \geq 10^{23.5}$ W Hz^{-1}. The 28 new targets extending this analysis to lower radio luminosities are shown as black stars. The light blue line indicates the 'radio loud' and 'radio quiet' boundary following the traditional classification criteria from Xu et al. (1999).

As shown in Figure 6.5, 28 targets have been selected for observation that have the same parameters as QFeedS, i.e., AGN with $z < 0.2$, and $L_{[OIII]} \geq 10^{42.1}$ erg s^{-1}, but all with 1.4 GHz luminosities lower than $10^{23.5}$ W Hz^{-1}.

6.3 Onwards to the next decade

The main open questions that I have tried to address in this thesis are as follows:

- If and how radio jets drive outflows and turbulence in quasar host galaxies?
- What impact do these outflows have their host galaxies?

This thesis has tried to address both the above questions using targets from the Quasar Feedback Survey to study the impact of radio jets on their host galaxies.

The Quasar Feedback Survey was designed from the SDSS survey to study the targets at $z \leq 0.2$. Being limited by the redshift, the goal was to obtain high-resolution spatial data to study the jet-ISM interactions at sub-kpc scales. This was met by using the modern interferometric and integral field unit spectral facilities which helped to dive into the very central regions of the galaxy while still maintaining a viable sensitivity. Further, the targets were selected to have bolometric luminosities comparable to the typical AGN luminosities expected in galaxies at cosmic noon, where the quasar outflows are the most prevalent. However, the sample still does not serve as a direct

tracer of the feedback processes at cosmic noon, where the bulk of black hole growth has occurred. The next decade, with the current and future surveys and facilities will open up the possibility to achieve this.

The next generation of radio facilities such as the Square Kilometer Array (SKA; Weltman et al. 2020), its precursor telescopes (e.g., MeerKAT; Jonas & MeerKAT Team 2016), and the Next Generation Very Large Array (ngVLA; Murphy et al. 2018; Selina et al. 2018) will help us obtain deeper radio observations thus improving the sensitivity to dive deeper into the radio quite cosmic dawn era, $z = 1$–2. These facilities are expected to provide a unique sensitivity, resolution, and frequency coverage for imaging at sub-kpc resolutions of radio data in distant galaxies. In addition to the estimates of molecular gas velocity field and velocity dispersion, in faint regions from ALMA; these radio observations will enable an unprecedented study of the weaker radio jets and their impact on these galaxies with higher AGN activity, thus also tremendously helping the understanding of star formation at higher redshifts.

The James Webb Space Telescope (JWST; Gardner et al. 2006) is already opening a new domain giving us the possibility to trace the ionised component of the outflows using [OIII], and the warm molecular gas with H_2 transitions in the mid-infrared. JWST will further enable a high-resolution multi-phase, and spatially-resolved characterisation of cosmic noon AGN outflows (e.g. Lai et al. 2022; Perna et al. 2023). Further, the upcoming near-infrared multi-object spectrographs such as MOONS (Multi-Object Optical and Near-infrared Spectrograph; Cirasuolo et al. 2014) on VLT, PFS (Prime Focus Spectrograph; Takada et al. 2014) on Subaru, will be transformational for the visible and near-infrared spectral regimes. MOONS and PFS will provide rest-frame optical spectroscopy for ~ 1 million galaxies and AGN at cosmic noon, thus providing statistical samples of spectroscopic data to characterise outflows and their relevance across different populations (following the works at $z < 1$ by e.g. Mullaney et al. 2013; Zakamska & Greene 2014. With HARMONI (High Angular Resolution Monolithic Optical and Near-infrared Integral field spectrograph; Thatte et al. 2021) on ELT, the combination of improved spectral and spatial resolutions with adaptive optics will aid similar multi-wavelength follow-up studies, like QFeedS, but at higher redshifts and test for the significance of the AGN-outflows at those redshifts. Whilst ALMA will still be effective for tracing molecular gas kinematics, HARMONI will open up the option to trace ionised gas kinematics and stellar kinematics at high sensitivity and spatial resolution in a similar manner to that achieved with MUSE for $z \leq 0.2$ quasars in this thesis. These facilities will transform our understanding with statistical samples and individual case studies of the relevance of different feedback mechanisms and ultimately their effect on the quasar host galaxies, during the most important epoch of galaxy and black hole growth.

Chapter

Supplementary Plots from Chapter Three

7

7.1 Spectral Fits for all Voronoi Bins

In the following section, we show all the spectral fits from each of the Voronoi bin for the

- ionised gas fits: [OIII];
- molecular gas fits: CO (3–2);
- stellar continuum fits.

The galaxy, J1316+1753, is divided in a total of 41 Vornoi bins as defined in Section 3.2 and shown in Appendix A of the paper. Here, in Figure 7.1-7.37, we show the fits for bins associated to the galaxy: 0-37 as below. We skip Bin 2 as the fits associated to it are already in the main paper (in Figure 2). The bins 38-40 are associated to the companion galaxy and are not used for any estimates but are shown here for completeness in Figure 7.38-7.40. Please note, for some Voronoi bins, the CO SNR was < 5 and hence not used for our analysis and subsequently, for these bins the CO-fits are not shown (namely Bins 10, 14, 24, 29, 40).

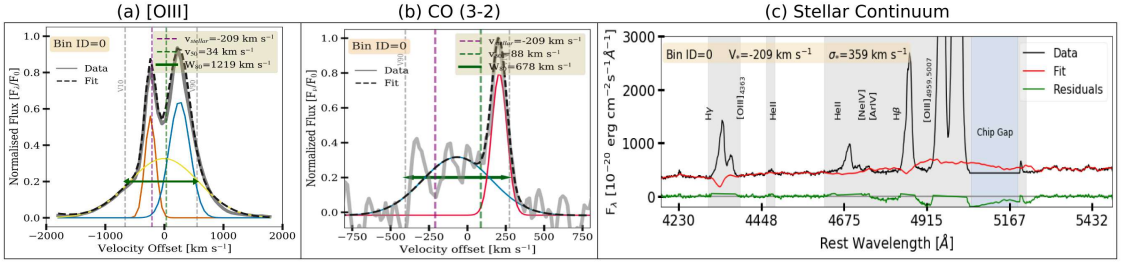

Figure 7.1: Bin 0: Examples of our emission-line and stellar continuum fits to the MUSE and ALMA data. *(a) Left:* [OIII] emission-line profile (grey curve) and our best fit (dashed black curve), as well as the three individual Gaussian components (for bins 0-33; and two components thereafter for bin 34-40) used to construct the total fit (yellow, blue and orange curves). *(b) Centre:* CO(3–2) emission-line profile (grey curve), with the best fit (dashed black curve) and the two Gaussian components that make up the total fit (blue and red curves). In both panels we indicate the non-parametric values obtained from our analyses: v_{50} (dashed green line) to trace the bulk velocity and, W_{80} (green arrows) to trace the velocity dispersion, which is the velocity width between v_{10} and v_{90} (vertical dashed grey lines). *(c) Right:* Spectra (black curve), presented across the wavelength range used to obtain the stellar continuum fits (red curve) for estimating the stellar kinematics (see Section 3.2). Wavelength regions excluded from the fits (due to strong emission lines and the instrumental chip gap) are highlighted with shaded regions. The fit residuals are shown as green curves.

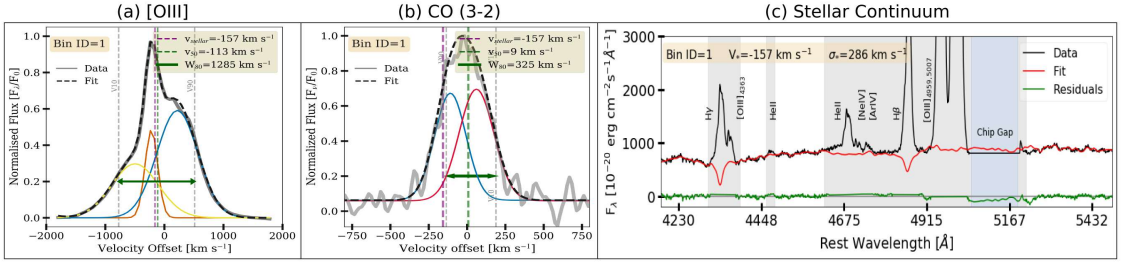

Figure 7.2: Bin 1: Description same as in Figure 7.1.

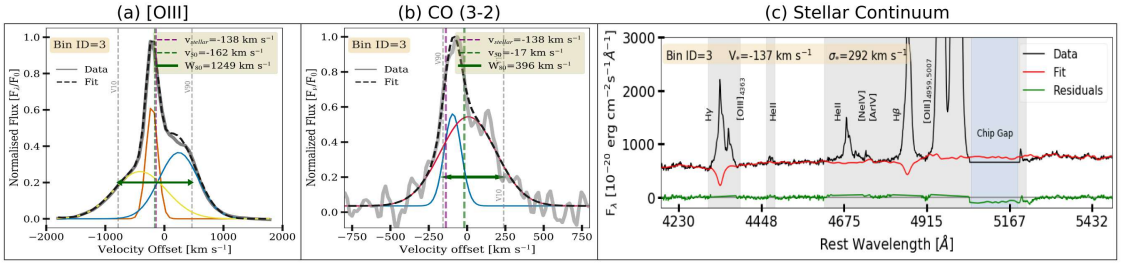

Figure 7.3: Bin 3: Description same as in Figure 7.1.

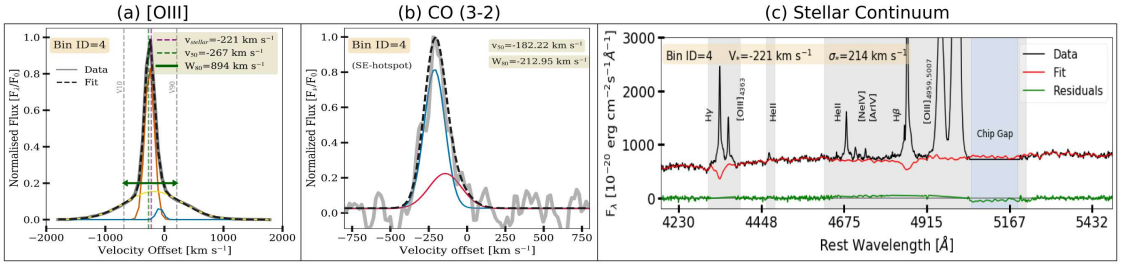

Figure 7.4: Bin 4: Description same as in Figure 7.1.

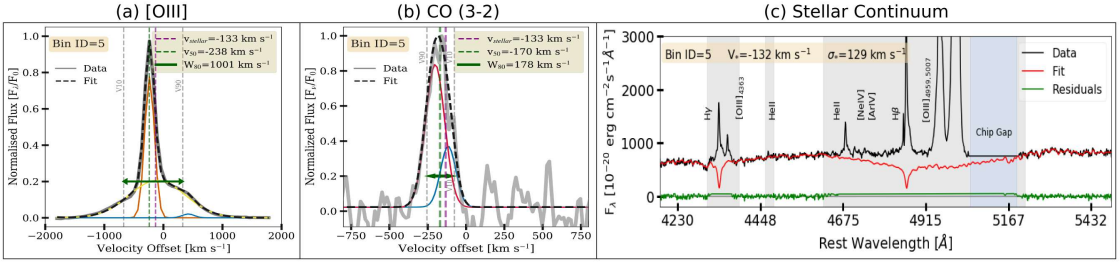

Figure 7.5: Bin 5: Description same as in Figure 7.1.

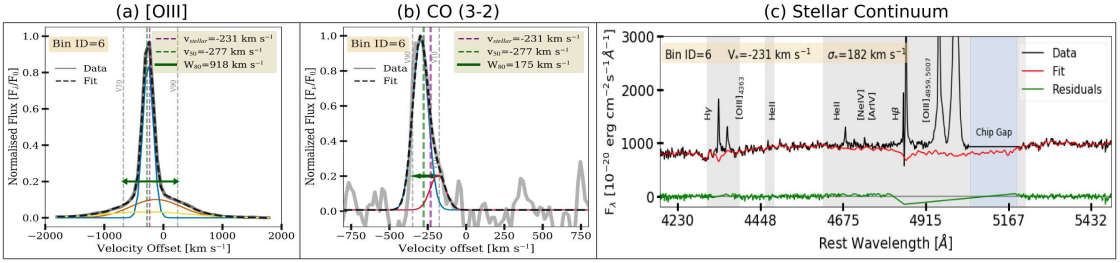

Figure 7.6: Bin 6: Description same as in Figure 7.1.

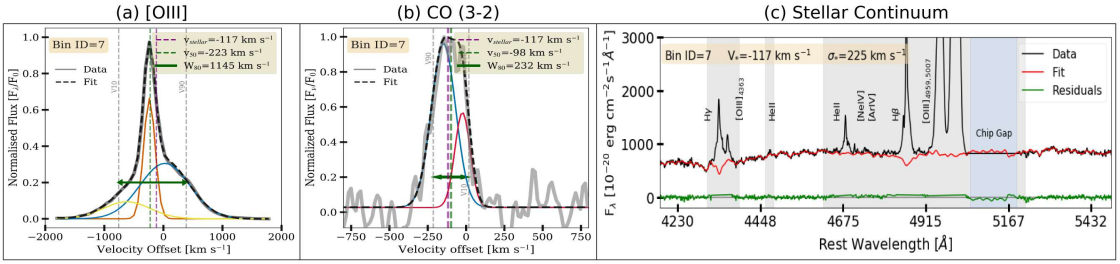

Figure 7.7: Bin 7: Description same as in Figure 7.1.

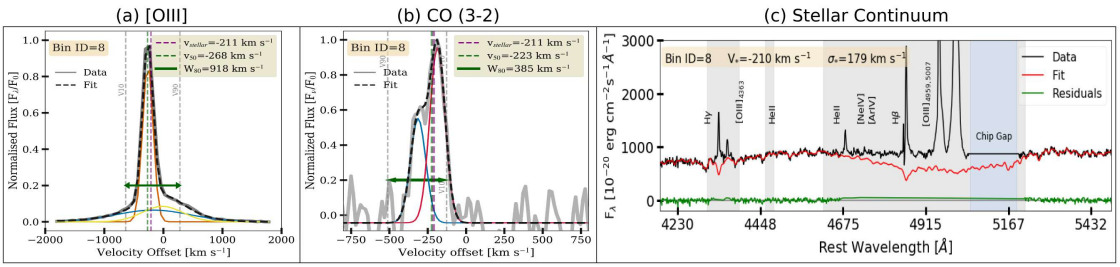

Figure 7.8: Bin 8: Description same as in Figure 7.1.

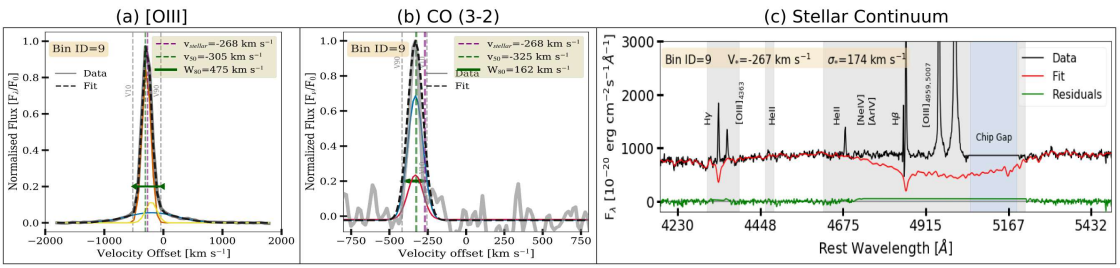

Figure 7.9: Bin 9: Description same as in Figure 7.1.

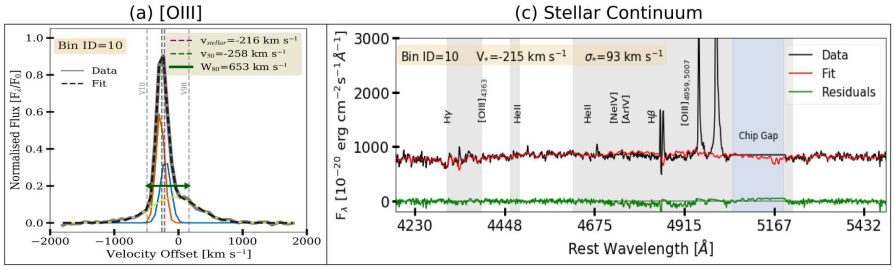

Figure 7.10: Bin 10: Description same as in Figure 7.1.

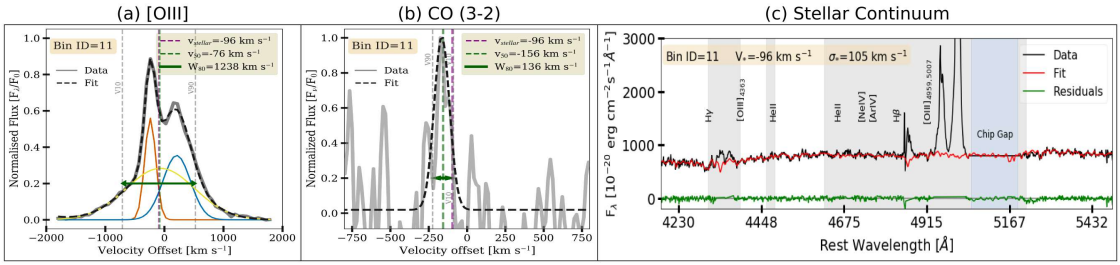

Figure 7.11: Bin 11: Description same as in Figure 7.1.

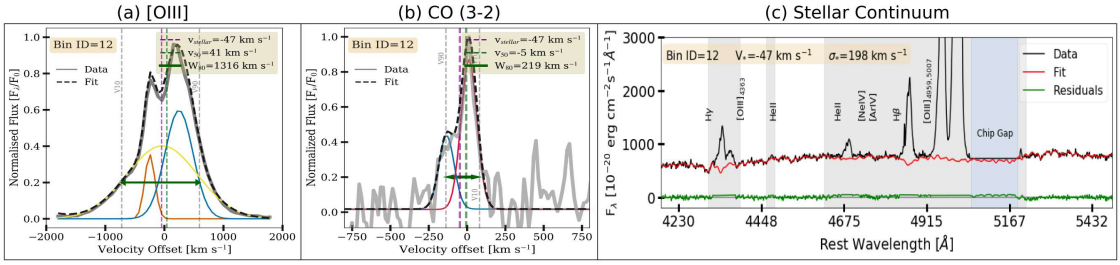

Figure 7.12: Bin 12: Description same as in Figure 7.1.

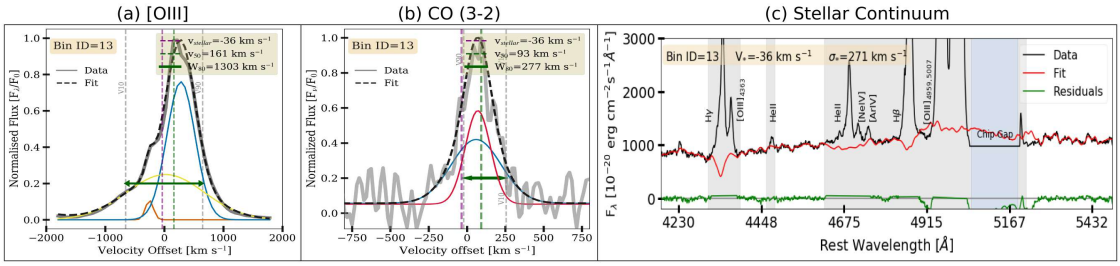

Figure 7.13: Bin 13: Description same as in Figure 7.1.

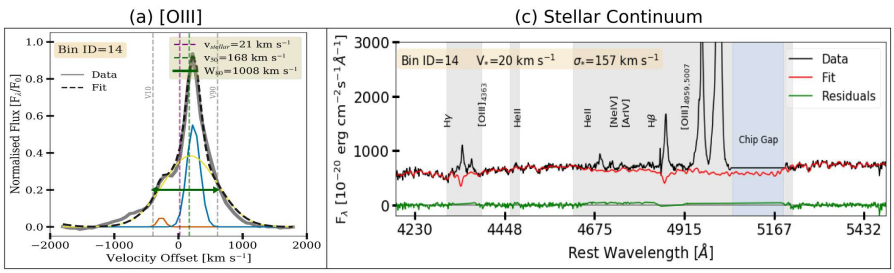

Figure 7.14: Bin 14: Description same as in Figure 7.1.

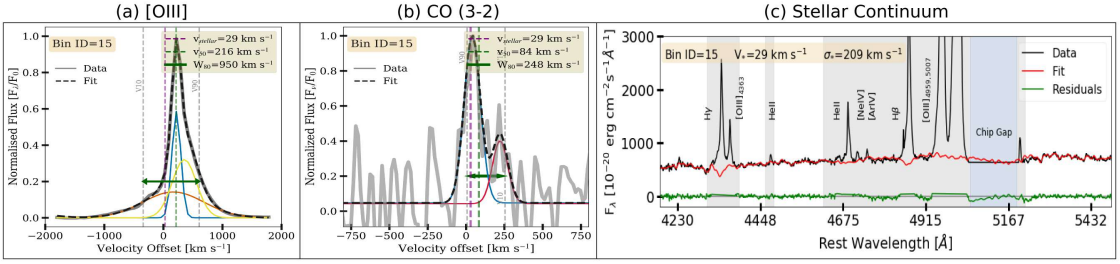

Figure 7.15: Bin 15: Description same as in Figure 7.1.

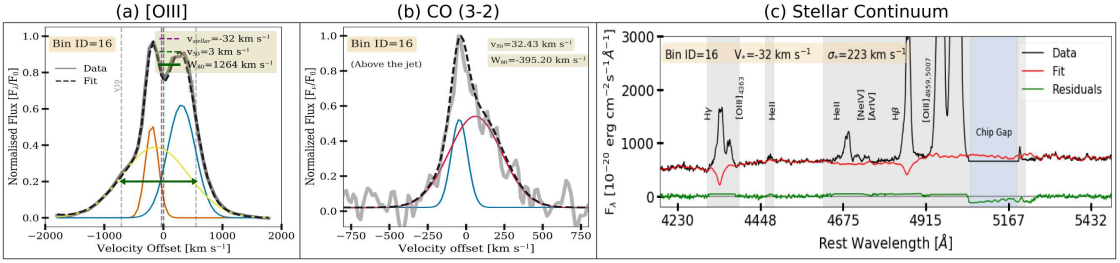

Figure 7.16: Bin 16: Description same as in Figure 7.1.

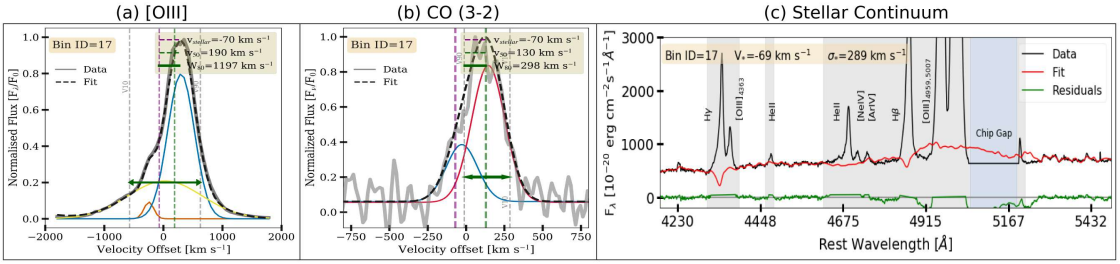

Figure 7.17: Bin 17: Description same as in Figure 7.1.

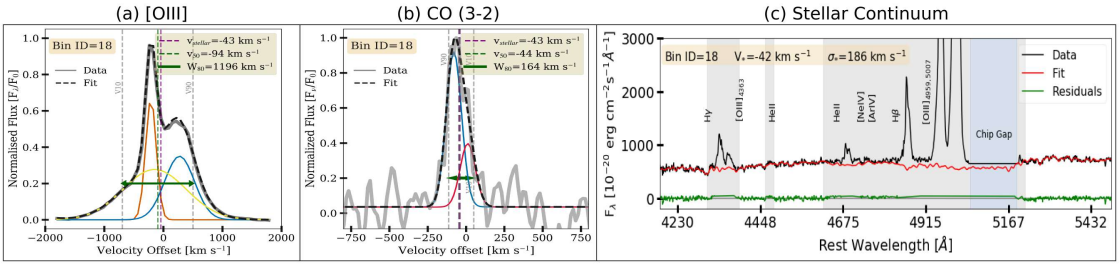

Figure 7.18: Bin 18: Description same as in Figure 7.1.

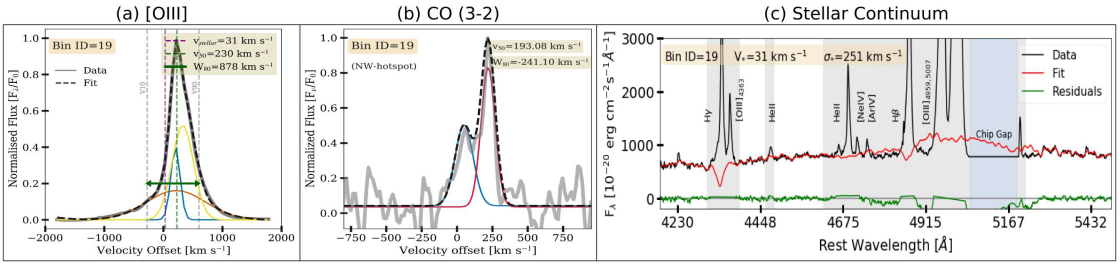

Figure 7.19: Bin 19: Description same as in Figure 7.1.

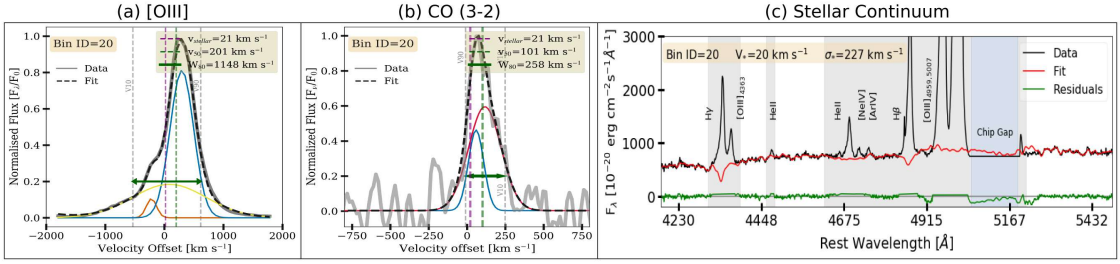

Figure 7.20: Bin 20: Description same as in Figure 7.1.

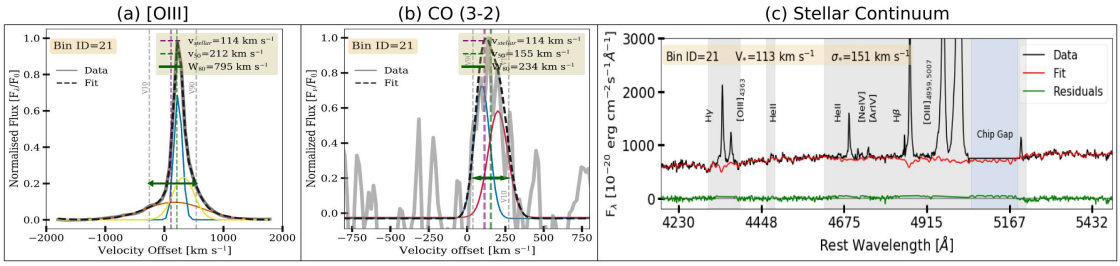

Figure 7.21: Bin 21: Description same as in Figure 7.1.

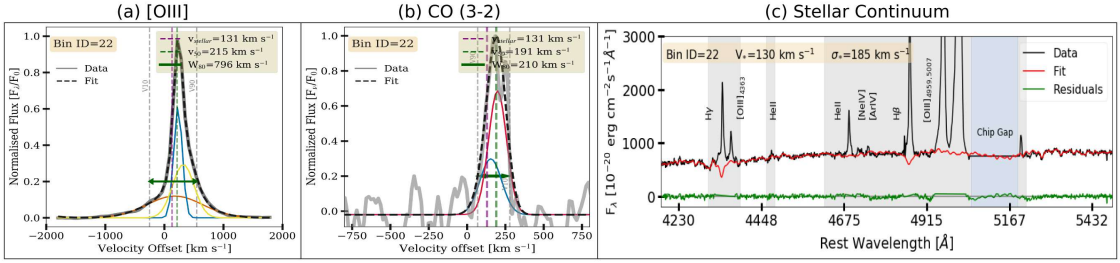

Figure 7.22: Bin 22: Description same as in Figure 7.1.

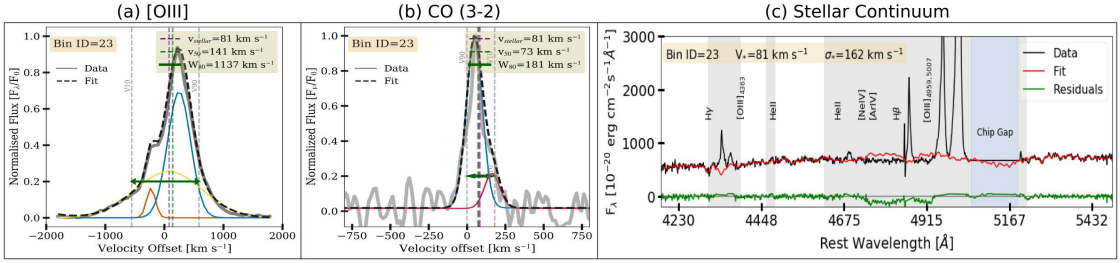

Figure 7.23: Bin 23: Description same as in Figure 7.1.

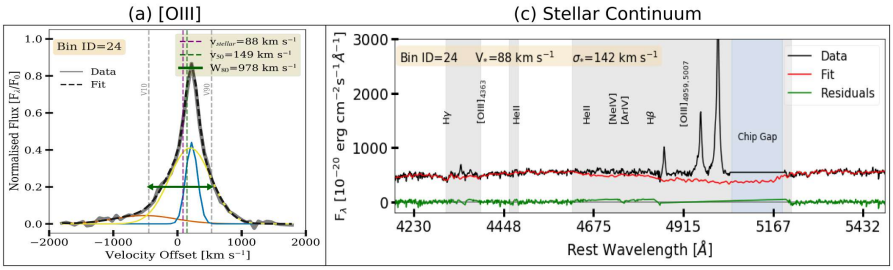

Figure 7.24: Bin 24: Description same as in Figure 7.1.

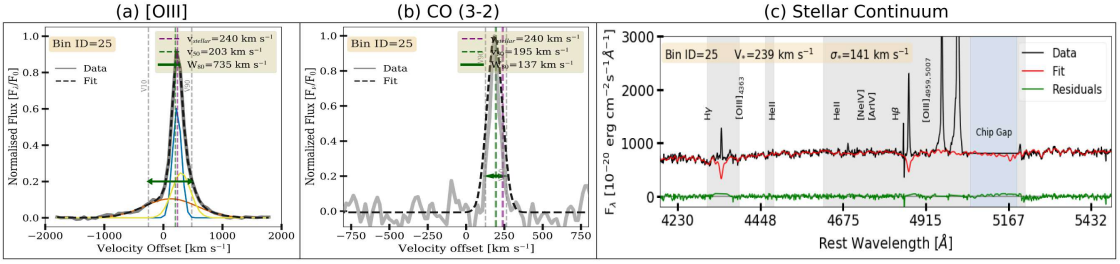

Figure 7.25: Bin 25: Description same as in Figure 7.1.

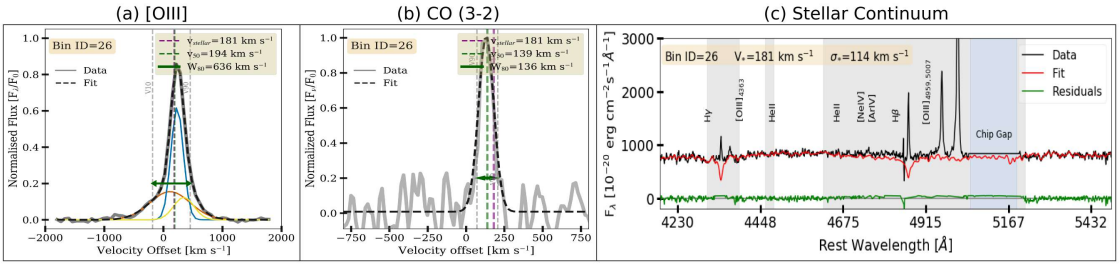

Figure 7.26: Bin 26: Description same as in Figure 7.1.

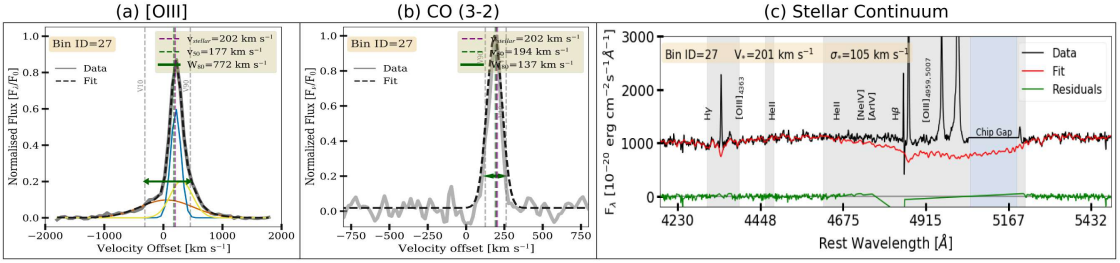

Figure 7.27: Bin 27: Description same as in Figure 7.1.

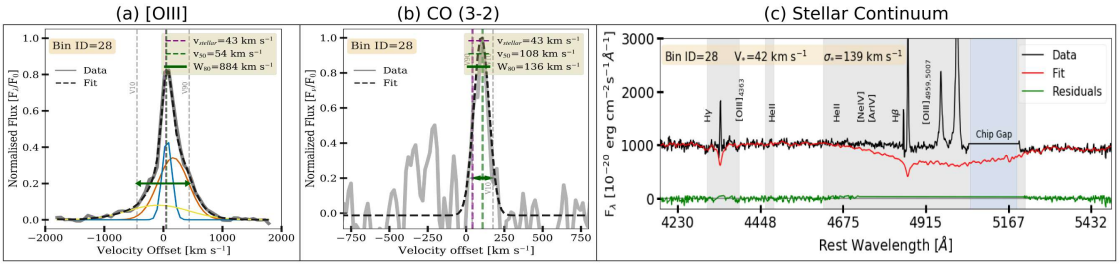

Figure 7.28: Bin 28: Description same as in Figure 7.1.

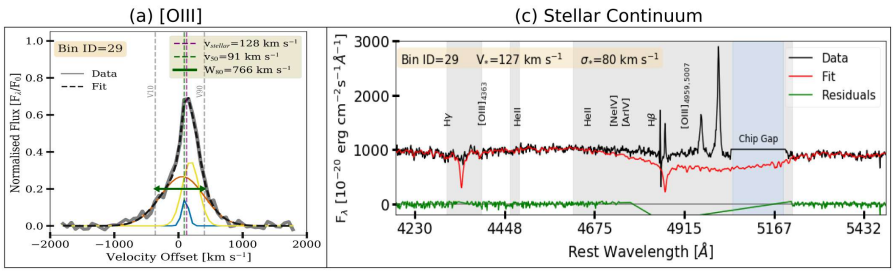

Figure 7.29: Bin 29: Description same as in Figure 7.1.

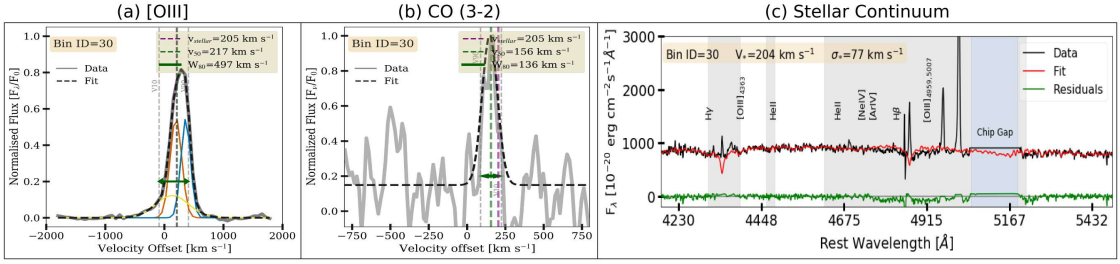

Figure 7.30: Bin 30: Description same as in Figure 7.1.

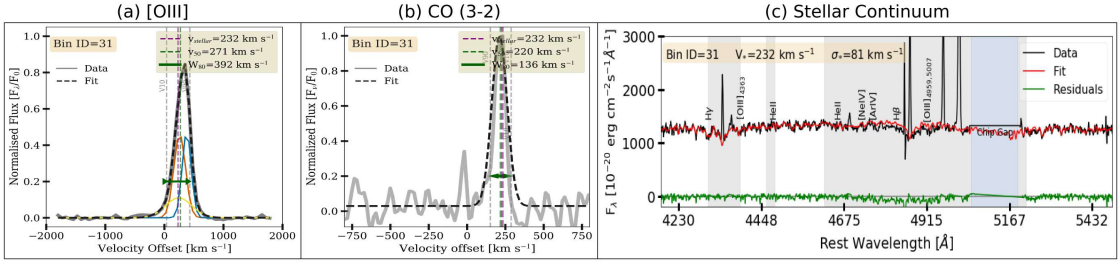

Figure 7.31: Bin 31: Description same as in Figure 7.1.

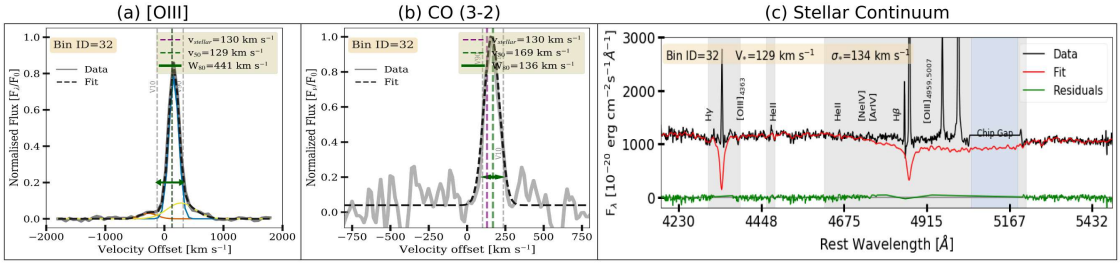

Figure 7.32: Bin 32: Description same as in Figure 7.1.

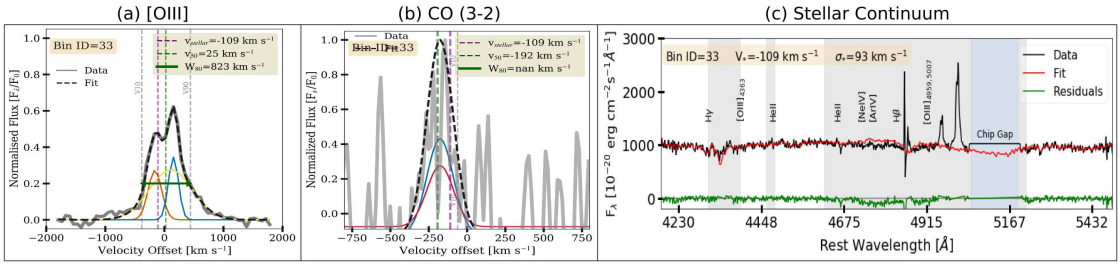

Figure 7.33: Bin 33: Description same as in Figure 7.1.

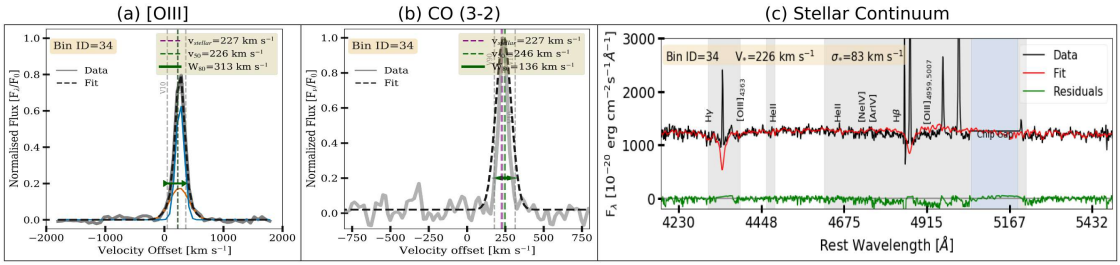

Figure 7.34: Bin 34: Description same as in Figure 7.1.

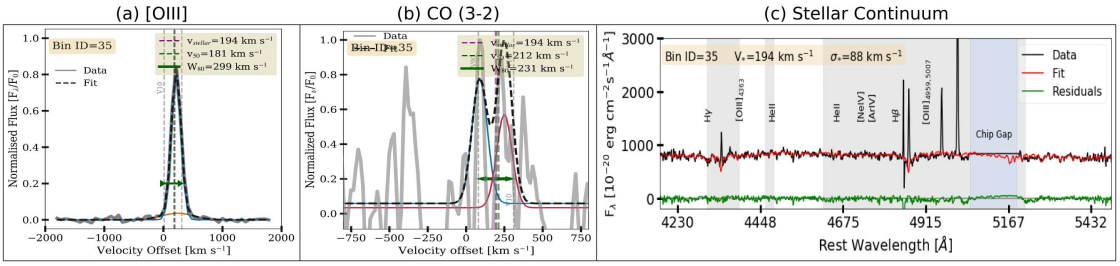

Figure 7.35: Bin 35: Description same as in Figure 7.1.

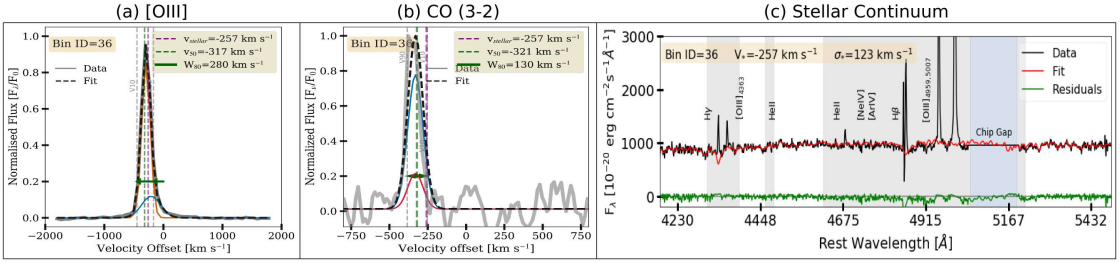

Figure 7.36: Bin 36: Description same as in Figure 7.1.

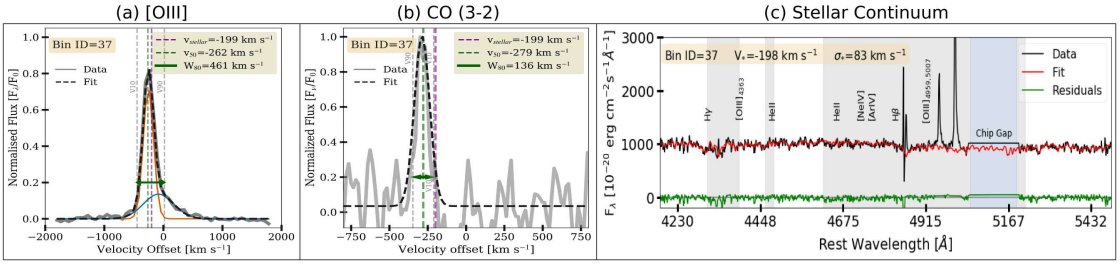

Figure 7.37: Bin 37: Description same as in Figure 7.1.

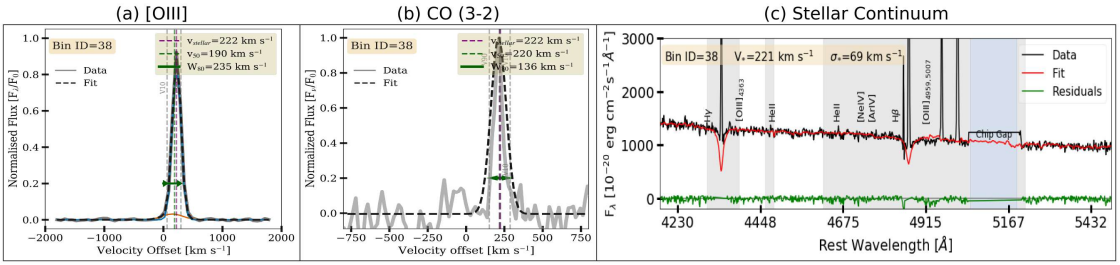

Figure 7.38: Bin 38: Description same as in Figure 7.1.

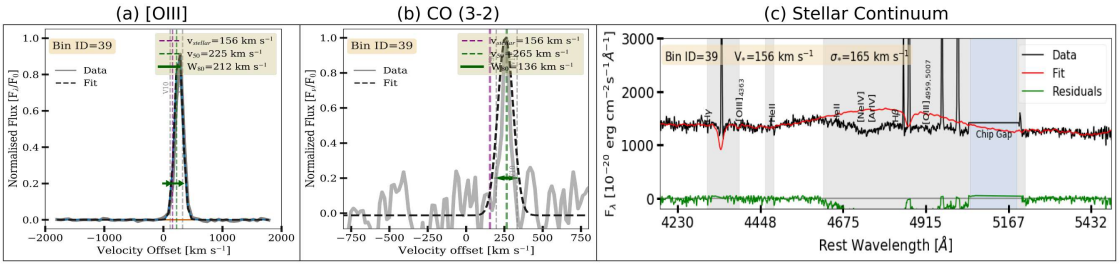

Figure 7.39: Bin 39: Description same as in Figure 7.1.

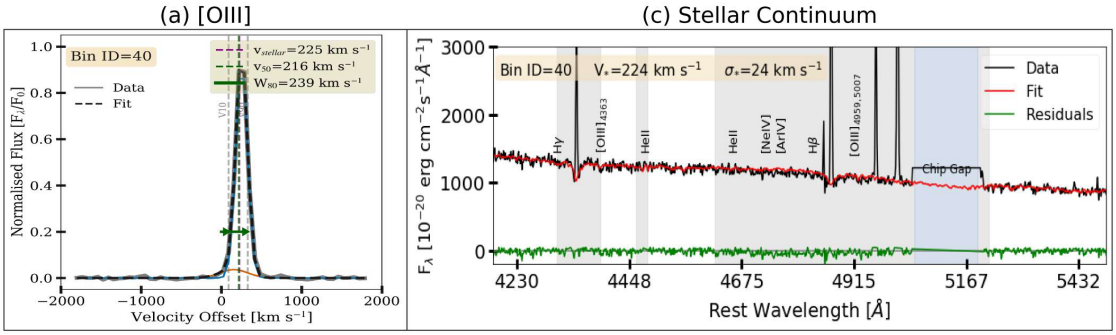

Figure 7.40: Bin 40: Description same as in Figure 7.1.

Chapter

Bibliography

Aalto S., et al., 2016, A&A, 590, A73

Abazajian K. N., et al., 2009, ApJS, 182, 543

Agrawal P. C., 2006, Advances in Space Research, 38, 2989

Aird J., et al., 2010, MNRAS, 401, 2531

Akaike H., 1974, IEEE Transactions on Automatic Control, 19, 716

Alatalo K., et al., 2011, ApJ, 735, 88

Alatalo K., et al., 2015, ApJ, 798, 31

Alexander D. M., Hickox R. C., 2012, New A Rev., 56, 93

Alexander D. M., Swinbank A. M., Smail I., McDermid R., Nesvadba N. P. H., 2010, MNRAS, 402, 2211

Alexandroff R. M., Zakamska N. L., van Velzen S., Greene J. E., Strauss M. A., 2016, MNRAS, 463, 3056

Almeida I., Nemmen R., Riffel R., 2023, arXiv e-prints, p. arXiv:2303.00826

An T., Baan W. A., 2012, ApJ, 760, 77

Antonucci R., 1993, ARA&A, 31, 473

Arav N., Xu X., Miller T., Kriss G. A., Plesha R., 2020, ApJS, 247, 37

Arentsen A., et al., 2019, A&A, 627, A138

Astropy Collaboration et al., 2013, A&A, 558, A33

Astropy Collaboration et al., 2018, AJ, 156, 123

Audibert A., et al., 2023, arXiv e-prints, p. arXiv:2302.13884

Baade W., Minkowski R., 1954, ApJ, 119, 206

Bacon R., et al., 2010, in McLean I. S., Ramsay S. K., Takami H., eds, Society of Photo-Optical Instrumentation Engineers (SPIE) Conference Series Vol. 7735, Ground-based and Airborne Instrumentation for Astronomy III. p. 773508, doi:10.1117/12.856027

Bacon R., Piqueras L., Conseil S., Richard J., Shepherd M., 2016, MPDAF: MUSE Python Data Analysis Framework (ascl:1611.003)

Bacon R., et al., 2017, A&A, 608, A1

Baldwin J. A., Phillips M. M., Terlevich R., 1981, PASP, 93, 5

Balmaverde B., Capetti A., Marconi A., Venturi G., 2018, A&A, 612, A19

Balmaverde B., et al., 2022, A&A, 662, A23

Baron D., Netzer H., 2019, MNRAS, 486, 4290

Baron D., Poznanski D., 2017, MNRAS, 465, 4530

Benson A. J., Frenk C. S., Baugh C. M., Cole S., Lacey C. G., 2003, MNRAS, 343, 679

Best P. N., Heckman T. M., 2012, MNRAS, 421, 1569

Bicay M. D., Kojoian G., Seal J., Dickinson D. F., Malkan M. A., 1995, ApJS, 98, 369

Bicknell G. V., Sutherland R. S., van Breugel W. J. M., Dopita M. A., Dey A., Miley G. K., 2000, ApJ, 540, 678

Bicknell G. V., Mukherjee D., Wagner A. Y., Sutherland R. S., Nesvadba N. P. H., 2018, MNRAS, 475, 3493

Bieri R., Dubois Y., Silk J., Mamon G. A., Gaibler V., 2016, MNRAS, 455, 4166

Bieri R., Dubois Y., Rosdahl J., Wagner A., Silk J., Mamon G. A., 2017, MNRAS, 464, 1854

Binney J., Tabor G., 1995, MNRAS, 276, 663

Bittner A., et al., 2019, A&A, 628, A117

Bittner A., et al., 2020, A&A, 643, A65

Blandford R. D., Königl A., 1979, ApJ, 232, 34

Bluck A. F. L., et al., 2020, MNRAS, 499, 230

Bolatto A. D., Wolfire M., Leroy A. K., 2013, ARA&A, 51, 207

Booth C. M., Schaye J., 2010, MNRAS, 405, L1

Boroson T., 2005, AJ, 130, 381

Boroson T. A., Green R. F., 1992, ApJS, 80, 109

Bourne M. A., Zubovas K., Nayakshin S., 2015, MNRAS, 453, 1829

Bower R. G., Benson A. J., Malbon R., Helly J. C., Frenk C. S., Baugh C. M., Cole S., Lacey C. G., 2006, MNRAS, 370, 645

Bower R. G., McCarthy I. G., Benson A. J., 2008, MNRAS, 390, 1399

Bower R. G., Benson A. J., Crain R. A., 2012, MNRAS, 422, 2816

Boyle B. J., Shanks T., Croom S. M., Smith R. J., Miller L., Loaring N., Heymans C., 2000, MNRAS, 317, 1014

Bradley L., et al., 2020, astropy/photutils: 1.0.0, doi:10.5281/zenodo.4044744, `https://doi.org/10.5281/zenodo.4044744`

Brinchmann J., Charlot S., White S. D. M., Tremonti C., Kauffmann G., Heckman T., Brinkmann J., 2004, MNRAS, 351, 1151

Brusa M., et al., 2015, MNRAS, 446, 2394

Burbridge G. R., 1963, in Radio Astronomy Today. pp 168–177

Capetti A., et al., 2022, A&A, 657, A114

Cappellari M., 2017, MNRAS, 466, 798

Cappellari M., Copin Y., 2003, MNRAS, 342, 345

Cappellari M., Emsellem E., 2004, PASP, 116, 138

Carilli C. L., Walter F., 2013, ARA&A, 51, 105

Carniani S., et al., 2015, A&A, 580, A102

Cattaneo A., Best P. N., 2009, MNRAS, 395, 518

Choi E., Somerville R. S., Ostriker J. P., Naab T., Hirschmann M., 2018, ApJ, 866, 91

Churazov E., Sunyaev R., Forman W., Böhringer H., 2002, MNRAS, 332, 729

Churazov E., Sazonov S., Sunyaev R., Forman W., Jones C., Böhringer H., 2005, MNRAS, 363, L91

Cicone C., et al., 2014, A&A, 562, A21

Cicone C., Brusa M., Ramos Almeida C., Cresci G., Husemann B., Mainieri V., 2018, Nature Astronomy, 2, 176

Cicone C., et al., 2021, arXiv e-prints, p. arXiv:2109.02269

Ciotti L., Ostriker J. P., 1997, ApJ, 487, L105

Cirasuolo M., Celotti A., Magliocchetti M., Danese L., 2003, MNRAS, 346, 447

Cirasuolo M., et al., 2014, in Ramsay S. K., McLean I. S., Takami H., eds, Society of Photo-Optical Instrumentation Engineers (SPIE) Conference Series Vol. 9147, Ground-based and Airborne Instrumentation for Astronomy V. p. 91470N, doi:10.1117/12.2056012

Circosta C., et al., 2021, A&A, 646, A96

Collet C., et al., 2016, A&A, 586, A152

Combes F., et al., 2013, A&A, 558, A124

Combes F., et al., 2014, A&A, 565, A97

Comerón S., Knapen J. H., Ramos Almeida C., Watkins A. E., 2021, A&A, 645, A130

Condon J. J., Cotton W. D., Greisen E. W., Yin Q. F., Perley R. A., Taylor G. B., Broderick J. J., 1998, AJ, 115, 1693

Costa T., Sijacki D., Haehnelt M. G., 2014, MNRAS, 444, 2355

Costa T., Sijacki D., Haehnelt M. G., 2015, MNRAS, 448, L30

Costa T., Rosdahl J., Sijacki D., Haehnelt M. G., 2018, MNRAS, 479, 2079

Costa T., Pakmor R., Springel V., 2020, MNRAS, 497, 5229

Couto G. S., Storchi-Bergmann T., Siemiginowska A., Riffel R. A., Morganti R., 2020, MNRAS, 497, 5103

Crain R. A., et al., 2015, MNRAS, 450, 1937

Crenshaw D. M., Kraemer S. B., George I. M., 2003, ARA&A, 41, 117

Cresci G., Maiolino R., 2018, Nature Astronomy, 2, 179

Cresci G., et al., 2015, A&A, 582, A63

Croton D. J., et al., 2006, MNRAS, 365, 11

Curtis H. D., 1918, Publications of Lick Observatory, 13, 9

Dall'Agnol de Oliveira B., Storchi-Bergmann T., Morganti R., Riffel R. A., Ramakrishnan V., 2023, MNRAS, 522, 3753

Dasyra K. M., Combes F., Oosterloo T., Oonk J. B. R., Morganti R., Salomé P., Vlahakis N., 2016, A&A, 595, L7

Davé R., Anglés-Alcázar D., Narayanan D., Li Q., Rafieferantsoa M. H., Appleby S., 2019, MNRAS, 486, 2827

David L. P., et al., 2014, in American Astronomical Society Meeting Abstracts #224. p. 417.08

Davies R., et al., 2020, MNRAS, 498, 4150

Debuhr J., Quataert E., Ma C.-P., 2012, MNRAS, 420, 2221

Decataldo D., Pallottini A., Ferrara A., Vallini L., Gallerani S., 2019, MNRAS, 487, 3377

Delvecchio I., et al., 2014, MNRAS, 439, 2736

Dimitrijević M. S., Popović L. Č., Kovačević J., Dačić M., Ilić D., 2007, MNRAS, 374, 1181

Disney M. J., Wall J. V., 1977, MNRAS, 179, 235

Dressler A., 1989, in Osterbrock D. E., Miller J. S., eds, Vol. 134, Active Galactic Nuclei. p. 217

Dubois Y., Gavazzi R., Peirani S., Silk J., 2013, MNRAS, 433, 3297

Dugan Z., Bryan S., Gaibler V., Silk J., Haas M., 2014, ApJ, 796, 113

Dugan Z., Gaibler V., Silk J., 2017, ApJ, 844, 37

Event Horizon Telescope Collaboration et al., 2021a, ApJ, 910, L12

Event Horizon Telescope Collaboration et al., 2021b, ApJ, 910, L13

Event Horizon Telescope Collaboration et al., 2022a, ApJ, 930, L12

Event Horizon Telescope Collaboration et al., 2022b, ApJ, 930, L13

Event Horizon Telescope Collaboration et al., 2022c, ApJ, 930, L14

Event Horizon Telescope Collaboration et al., 2022d, ApJ, 930, L15

Event Horizon Telescope Collaboration et al., 2022e, ApJ, 930, L16

Event Horizon Telescope Collaboration et al., 2022f, ApJ, 930, L17

Fabian A. C., 2012, ARA&A, 50, 455

Fabian A. C., et al., 2000, MNRAS, 318, L65

Falcón-Barroso J., et al., 2006, MNRAS, 369, 529

Faucher-Giguère C.-A., Quataert E., 2012, MNRAS, 425, 605

Federrath C., Klessen R. S., 2012, ApJ, 761, 156

Feldman F. R., Weedman D. W., Balzano V. A., Ramsey L. W., 1982, ApJ, 256, 427

Fernández-Ontiveros J. A., et al., 2020, A&A, 633, A127

Ferrarese L., Merritt D., 2000, ApJ, 539, L9

Feruglio C., Maiolino R., Piconcelli E., Menci N., Aussel H., Lamastra A., Fiore F., 2010, A&A, 518, L155

Finlez C., Nagar N. M., Storchi-Bergmann T., Schnorr-Müller A., Riffel R. A., Lena D., Mundell C. G., Elvis M. S., 2018, MNRAS, 479, 3892

Fiore F., et al., 2017, A&A, 601, A143

Fischer T. C., Johnson M. C., Secrest N. J., Crenshaw D. M., Kraemer S. B., 2023, ApJ, 953, 87

Fluetsch A., et al., 2019, MNRAS, 483, 4586

Fluetsch A., et al., 2021, MNRAS, 505, 5753

Förster Schreiber N. M., et al., 2019, ApJ, 875, 21

Fragile P. C., Anninos P., Croft S., Lacy M., Witry J. W. L., 2017, ApJ, 850, 171

Fu H., Stockton A., 2009, ApJ, 690, 953

Fu H., Myers A. D., Djorgovski S. G., Yan L., 2011, ApJ, 733, 103

Gabor J. M., Bournaud F., 2014, MNRAS, 441, 1615

Gadotti D. A., et al., 2020, A&A, 643, A14

Gaibler V., Khochfar S., Krause M., Silk J., 2012, MNRAS, 425, 438

Gallagher R., Maiolino R., Belfiore F., Drory N., Riffel R., Riffel R. A., 2019, MNRAS, 485, 3409

Gallimore J. F., Axon D. J., O'Dea C. P., Baum S. A., Pedlar A., 2006, AJ, 132, 546

Ganguly R., Brotherton M. S., 2008, ApJ, 672, 102

García-Burillo S., et al., 2014, A&A, 567, A125

García-Burillo S., et al., 2019, A&A, 632, A61

García-Burillo S., et al., 2021, A&A, 652, A98

Gardner J. P., et al., 2006, Space Sci. Rev., 123, 485

Gaspari M., Brighenti F., D'Ercole A., Melioli C., 2011, MNRAS, 415, 1549

Gebhardt K., et al., 2000, ApJ, 539, L13

George K., et al., 2019, MNRAS, 487, 3102

Ghisellini G., 2013, in European Physical Journal Web of Conferences. p. 05001 (`arXiv:1309.4772`), doi:10.1051/epjconf/20136105001

Ghisellini G., Padovani P., Celotti A., Maraschi L., 1993, ApJ, 407, 65

Gilmozzi R., Spyromilio J., 2007, The Messenger, 127, 11

Girdhar A., et al., 2022, Monthly Notices of the Royal Astronomical Society, 512, 1608

Girdhar A., et al., 2023, Monthly Notices of the Royal Astronomical Society, p. stad3453

Glover S. C. O., Federrath C., Mac Low M. M., Klessen R. S., 2010, MNRAS, 404, 2

Gonneau A., et al., 2020, A&A, 634, A133

Goulding A. D., Pardo K., Greene J. E., Mingarelli C. M. F., Nyland K., Strauss M. A., 2019, ApJ, 879, L21

Granato G. L., De Zotti G., Silva L., Bressan A., Danese L., 2004, ApJ, 600, 580

Greene J. E., Zakamska N. L., Smith P. S., 2012, ApJ, 746, 86

Greenstein J. L., 1963, Nature, 197, 1041

Griffith M. R., Wright A. E., Burke B. F., Ekers R. D., 1994, ApJS, 90, 179

Griffith M. R., Wright A. E., Burke B. F., Ekers R. D., 1995, ApJS, 97, 347

Gültekin K., et al., 2009, ApJ, 698, 198

Gürkan G., et al., 2018, MNRAS, 475, 3010

Gürkan G., et al., 2019, A&A, 622, A11

Hardcastle M. J., Croston J. H., 2020, New A Rev., 88, 101539

Häring N., Rix H.-W., 2004, ApJ, 604, L89

Harris C. R., et al., 2020, Nature, 585, 357

Harrison C. M., 2017, Nature Astronomy, 1, 0165

Harrison C. M., et al., 2012, MNRAS, 426, 1073

Harrison C. M., Alexander D. M., Mullaney J. R., Swinbank A. M., 2014, MNRAS, 441, 3306

Harrison C. M., Thomson A. P., Alexander D. M., Bauer F. E., Edge A. C., Hogan M. T., Mullaney J. R., Swinbank A. M., 2015, ApJ, 800, 45

Harrison C. M., Costa T., Tadhunter C. N., Flütsch A., Kakkad D., Perna M., Vietri G., 2018a, Nature Astronomy, 2, 198

Harrison C. M., Costa T., Tadhunter C. N., Flütsch A., Kakkad D., Perna M., Vietri G., 2018b, Nature Astronomy, 2, 198

Hecht E., 2001, Optics 4th edition

Heckman T. M., Miley G. K., van Breugel W. J. M., Butcher H. R., 1981, ApJ, 247, 403

Heckman T. M., Miley G. K., Green R. F., 1984, ApJ, 281, 525

Heckman T. M., Kauffmann G., Brinchmann J., Charlot S., Tremonti C., White S. D. M., 2004, ApJ, 613, 109

Helou G., Madore B. F., Schmitz M., Bicay M. D., Wu X., Bennett J., 1991, in Albrecht M. A., Egret D., eds, Astrophysics and Space Science Library Vol. 171, Databases and On-line Data in Astronomy. pp 89–106, doi:10.1007/978-94-011-3250-3_10

Henriques B. M. B., White S. D. M., Thomas P. A., Angulo R., Guo Q., Lemson G., Springel V., Overzier R., 2015, MNRAS, 451, 2663

Herrera-Camus R., et al., 2020, A&A, 635, A47

Hewett P. C., Foltz C. B., Chaffee F. H., 1993, ApJ, 406, L43

Hirschmann M., Dolag K., Saro A., Bachmann L., Borgani S., Burkert A., 2014, MNRAS, 442, 2304

Hogan M. T., et al., 2015, MNRAS, 453, 1223

Hogan M. T., et al., 2017, ApJ, 851, 66

Hopkins P. F., Elvis M., 2010, MNRAS, 401, 7

Hopkins P. F., Hernquist L., Cox T. J., Di Matteo T., Robertson B., Springel V., 2006, ApJS, 163, 1

Hopkins P. F., Richards G. T., Hernquist L., 2007, ApJ, 654, 731

Hopkins P. F., Cox T. J., Hernquist L., Narayanan D., Hayward C. C., Murray N., 2013, MNRAS, 430, 1901

Hubble E. P., 1925, Popular Astronomy, 33, 252

Hubble E. P., 1926, ApJ, 64, 321

Hubble E., 1929, Proceedings of the National Academy of Science, 15, 168

Hubin N. N., Le Louarn M., Conzelmann R., Delabre B., Fedrigo E., Stuik R., 2004, in Bonaccini Calia D., Ellerbroek B. L., Ragazzoni R., eds, Society of Photo-Optical Instrumentation Engineers (SPIE) Conference Series Vol. 5490, Advancements in Adaptive Optics. pp 846–857, doi:10.1117/12.552943

Huggins W., Miller W. A., 1864, Philosophical Transactions of the Royal Society of London Series I, 154, 437

Hunter J. D., 2007, Computing in Science and Engineering, 9, 90

Husemann B., Wisotzki L., Sánchez S. F., Jahnke K., 2013, A&A, 549, A43

Husemann B., Scharwächter J., Bennert V. N., Mainieri V., Woo J. H., Kakkad D., 2016, A&A, 594, A44

Husemann B., et al., 2019, ApJ, 879, 75

Hwang H.-C., Zakamska N. L., Alexandroff R. M., Hamann F., Greene J. E., Perrotta S., Richards G. T., 2018, MNRAS, 477, 830

Ishibashi W., Fabian A. C., 2015, MNRAS, 451, 93

Ishibashi W., Fabian A. C., 2016, MNRAS, 457, 2864

Ishibashi W., Fabian A. C., Canning R. E. A., 2013, MNRAS, 431, 2350

Ishibashi W., Fabian A. C., Maiolino R., 2018, MNRAS, 476, 512

Jarvis M. E., et al., 2019, MNRAS, 485, 2710

Jarvis M. E., et al., 2020, MNRAS, 498, 1560

Jarvis M. E., et al., 2021, MNRAS, 503, 1780

Jiang Y.-F., Ciotti L., Ostriker J. P., Spitkovsky A., 2010, ApJ, 711, 125

Jonas J., MeerKAT Team 2016, in MeerKAT Science: On the Pathway to the SKA. p. 1, doi:10.22323/1.277.0001

Kakkad D., et al., 2017, MNRAS, 468, 4205

Kakkad D., et al., 2022, MNRAS, 511, 2105

Kakkad D., et al., 2023, MNRAS, 520, 5783

Kang D., Woo J.-H., 2018, ApJ, 864, 124

Kauffmann G., et al., 2003, MNRAS, 346, 1055

Keel W. C., et al., 2012, AJ, 144, 66

Keel W. C., et al., 2015, AJ, 149, 155

Keel W. C., et al., 2017, ApJ, 835, 256

Keel W. C., et al., 2019, MNRAS, 483, 4847

Kellermann K. I., Sramek R., Schmidt M., Shaffer D. B., Green R., 1989, AJ, 98, 1195

Khachikyan É. Y., Weedman D. W., 1971, Astrophysics, 7, 231

Kharb P., Shastri P., 2004, A&A, 425, 825

Kharb P., Das M., Paragi Z., Subramanian S., Chitta L. P., 2015, ApJ, 799, 161

Kharb P., Vaddi S., Sebastian B., Subramanian S., Das M., Paragi Z., 2019, ApJ, 871, 249

Kharb P., Subramanian S., Das M., Vaddi S., Paragi Z., 2021, arXiv e-prints, p. arXiv:2106.09304

King A., 2005, ApJ, 635, L121

King A. R., Pounds K. A., 2003, MNRAS, 345, 657

King A., Pounds K., 2015, ARA&A, 53, 115

Komossa S., Xu D., Zhou H., Storchi-Bergmann T., Binette L., 2008, ApJ, 680, 926

Kormendy J., 1993, in Beckman J., Colina L., Netzer H., eds, The Nearest Active Galaxies. pp 197–218

Kormendy J., Gebhardt K., 2001, in Wheeler J. C., Martel H., eds, American Institute of Physics Conference Series Vol. 586, 20th Texas Symposium on relativistic astrophysics. pp 363–381 (arXiv:astro-ph/0105230), doi:10.1063/1.1419581

Kormendy J., Ho L. C., 2013, ARA&A, 51, 511

Kormendy J., Richstone D., 1995, ARA&A, 33, 581

Kovacevic-Dojcinovic J., Popovic L., 2012, Journal of Physics Conference Series, 399, 2023

Kraft R. P., Forman W. R., Jones C., Murray S. S., Hardcastle M. J., Worrall D. M., 2002, ApJ, 569, 54

Kumar A., et al., 2012, in Takahashi T., Murray S. S., den Herder J.-W. A., eds, Society of Photo-Optical Instrumentation Engineers (SPIE) Conference Series Vol. 8443, Space Telescopes and Instrumentation 2012: Ultraviolet to Gamma Ray. p. 84431N (arXiv:1208.4670), doi:10.1117/12.924507

Lacey C. G., et al., 2016, MNRAS, 462, 3854

Lacy M., Croft S., Fragile C., Wood S., Nyland K., 2017, ApJ, 838, 146

Lai T. S. Y., et al., 2022, ApJ, 941, L36

Lansbury G. B., Jarvis M. E., Harrison C. M., Alexander D. M., Del Moro A., Edge A. C., Mullaney J. R., Thomson A. P., 2018, ApJ, 856, L1

Lansbury G. B., Banerji M., Fabian A. C., Temple M. J., 2020, MNRAS, 495, 2652

Leavitt H. S., 1908, Annals of Harvard College Observatory, 60, 87

Leavitt H. S., Pickering E. C., 1912, Harvard College Observatory Circular, 173, 1

Lemaître G., 1927, Annales de la Société Scientifique de Bruxelles, 47, 49

Liao M., Gu M., 2020, MNRAS, 491, 92

Lintott C. J., et al., 2009, MNRAS, 399, 129

Liske J., et al., 2008, MNRAS, 386, 1192

Liu X., Shen Y., Strauss M. A., Greene J. E., 2010, ApJ, 708, 427

Liu G., Zakamska N. L., Greene J. E., Nesvadba N. P. H., Liu X., 2013, MNRAS, 436, 2576

Lutz D., et al., 2020, A&A, 633, A134

Lynden-Bell D., 1969, Nature, 223, 690

Lyu Y., Liu X., 2016, MNRAS, 463, 24

Macfarlane C., et al., 2021, MNRAS, 506, 5888

Madau P., Dickinson M., 2014, ARA&A, 52, 415

Mainieri V., et al., 2011, A&A, 535, A80

Mainieri V., et al., 2021, The Messenger, 182, 45

Maiolino R., et al., 2017, Nature, 544, 202

Mandal A., Mukherjee D., Federrath C., Nesvadba N. P. H., Bicknell G. V., Wagner A. Y., Meenakshi M., 2021, arXiv e-prints, p. arXiv:2109.13654

Marconi A., Risaliti G., Gilli R., Hunt L. K., Maiolino R., Salvati M., 2004, MNRAS, 351, 169

Marinacci F., et al., 2018, MNRAS, 480, 5113

Martin D. C., et al., 2005, ApJ, 619, L1

Matthews T. A., Sandage A. R., 1963, ApJ, 138, 30

McCarthy I. G., et al., 2010, MNRAS, 406, 822

McCarthy I. G., Schaye J., Bower R. G., Ponman T. J., Booth C. M., Dalla Vecchia C., Springel V., 2011, MNRAS, 412, 1965

McMullin J. P., Waters B., Schiebel D., Young W., Golap K., 2007, in Shaw R. A., Hill F., Bell D. J., eds, Astronomical Society of the Pacific Conference Series Vol. 376, Astronomical Data Analysis Software and Systems XVI. p. 127

McNamara B. R., Nulsen P. E. J., 2007, ARA&A, 45, 117

McNamara B. R., Nulsen P. E. J., 2012, New Journal of Physics, 14, 055023

McNamara B. R., et al., 2000, ApJ, 534, L135

McNamara B. R., et al., 2014, ApJ, 785, 44

McNamara B. R., Russell H. R., Nulsen P. E. J., Hogan M. T., Fabian A. C., Pulido F., Edge A. C., 2016, ApJ, 830, 79

Meenakshi M., et al., 2022, MNRAS, 516, 766

Merloni A., Heinz S., 2007, MNRAS, 381, 589

Merritt D., Ferrarese L., 2001, ApJ, 547, 140

Mingozzi M., et al., 2019, A&A, 622, A146

Molyneux S. J., Harrison C. M., Jarvis M. E., 2019, A&A, 631, A132

Morganti R., 2017, Nature Astronomy, 1, 596

Morganti R., Oosterloo T., Tadhunter C. N., 2005, in Braun R., ed., Astronomical Society of the Pacific Conference Series Vol. 331, Extra-Planar Gas. p. 361 (`arXiv:astro-ph/0410222`)

Morganti R., Frieswijk W., Oonk R. J. B., Oosterloo T., Tadhunter C., 2013, A&A, 552, L4

Morganti R., Oosterloo T., Oonk J. B. R., Frieswijk W., Tadhunter C., 2015, A&A, 580, A1

Morganti R., Oosterloo T., Tadhunter C., Bernhard E. P., Oonk J. B. R., 2021, arXiv e-prints, p. arXiv:2109.13516

Morganti R., Murthy S., Guillard P., Oosterloo T., Garcia-Burillo S., 2023, Galaxies, 11

Moster B. P., Naab T., White S. D. M., 2013, MNRAS, 428, 3121

Muñoz Marín V. M., González Delgado R. M., Schmitt H. R., Cid Fernandes R., Pérez E., Storchi-Bergmann T., Heckman T., Leitherer C., 2007, AJ, 134, 648

Mukherjee D., Bicknell G. V., Sutherland R., Wagner A., 2016, MNRAS, 461, 967

Mukherjee D., Wagner A. Y., Bicknell G. V., Morganti R., Oosterloo T., Nesvadba N., Sutherland R. S., 2018a, MNRAS, 476, 80

Mukherjee D., Bicknell G. V., Wagner A. Y., Sutherland R. S., Silk J., 2018b, MNRAS, 479, 5544

Mullaney J. R., Alexander D. M., Fine S., Goulding A. D., Harrison C. M., Hickox R. C., 2013, MNRAS, 433, 622

Murphy E. J., et al., 2018, in Murphy E., ed., Astronomical Society of the Pacific Conference Series Vol. 517, Science with a Next Generation Very Large Array. p. 3 (arXiv:1810.07524), doi:10.48550/arXiv.1810.07524

Naiman J. P., et al., 2018, MNRAS, 477, 1206

Nayakshin S., Zubovas K., 2012, MNRAS, 427, 372

Nelson C. H., Whittle M., 1996, ApJ, 465, 96

Nelson D., et al., 2018, MNRAS, 475, 624

Nesvadba N. P. H., Lehnert M. D., Eisenhauer F., Gilbert A., Tecza M., Abuter R., 2006, ApJ, 650, 693

Nesvadba N. P. H., Lehnert M. D., De Breuck C., Gilbert A. M., van Breugel W., 2008, A&A, 491, 407

Nesvadba N. P. H., et al., 2010, A&A, 521, A65

Nesvadba N. P. H., Boulanger F., Lehnert M. D., Guillard P., Salome P., 2011, A&A, 536, L5

Nevin R., Comerford J. M., Müller-Sánchez F., Barrows R., Cooper M. C., 2018, MNRAS, 473, 2160

Nims J., Quataert E., Faucher-Giguère C.-A., 2015, MNRAS, 447, 3612

Olivares V., et al., 2019, A&A, 631, A22

Orr M. J. L., Browne I. W. A., 1982, MNRAS, 200, 1067

Osterbrock D. E., Ferland G. J., 2006, Astrophysics of gaseous nebulae and active galactic nuclei

Padovani P., et al., 2017, A&A Rev., 25, 2

Panessa F., Baldi R. D., Laor A., Padovani P., Behar E., McHardy I., 2019, Nature Astronomy, 3, 387

Pereira-Santaella M., et al., 2018, A&A, 616, A171

Perna M., Lanzuisi G., Brusa M., Cresci G., Mignoli M., 2017, A&A, 606, A96

Perna M., et al., 2018, A&A, 619, A90

Perna M., et al., 2023, arXiv e-prints, p. arXiv:2304.06756

Peterson B. M., 2003, in Collin S., Combes F., Shlosman I., eds, Astronomical Society of the Pacific Conference Series Vol. 290, Active Galactic Nuclei: From Central Engine to Host Galaxy. p. 43

Peterson B. M., 2006, in Alloin D., ed., , Vol. 693, Physics of Active Galactic Nuclei at all Scales. p. 77, doi:10.1007/3-540-34621-X_3

Pierce J. C. S., Tadhunter C. N., Morganti R., 2020, MNRAS, 494, 2053

Pillepich A., et al., 2018, MNRAS, 473, 4077

Pinna F., et al., 2019, A&A, 623, A19

Puchwein E., Sijacki D., Springel V., 2008, ApJ, 687, L53

Pulido F. A., et al., 2018, ApJ, 853, 177

Quilis V., Moore B., 2001, ApJ, 555, L95

Ramos Almeida C., Piqueras López J., Villar-Martín M., Bessiere P. S., 2017, MNRAS, 470, 964

Ramos Almeida C., et al., 2021, arXiv e-prints, p. arXiv:2111.13578

Rees M. J., 1984, in Brinkmann W., Truemper J., eds, X-ray and UV Emission from Active Galactic Nuclei. pp 138–151

Reyes R., et al., 2008, AJ, 136, 2373

Richards G. T., et al., 2006, AJ, 131, 2766

Riechers D. A., et al., 2011, ApJ, 739, L32

Riffel R. A., Storchi-Bergmann T., Riffel R., 2014, ApJ, 780, L24

Rigopoulou D., Kunze D., Lutz D., Genzel R., Moorwood A. F. M., 2002, A&A, 389, 374

Rosario D. J., Shields G. A., Taylor G. B., Salviander S., Smith K. L., 2010, ApJ, 716, 131

Rosario D. J., et al., 2018, MNRAS, 473, 5658

Rosario D. J., Togi A., Burtscher L., Davies R. I., Shimizu T. T., Lutz D., 2019, ApJ, 875, L8

Rose M., Tadhunter C., Ramos Almeida C., Rodríguez Zaurín J., Santoro F., Spence R., 2018, MNRAS, 474, 128

Rose T., et al., 2019, MNRAS, 485, 229

Rosse T. E. O., 1850, Philosophical Transactions of the Royal Society of London Series I, 140, 499

Roy N., et al., 2021, ApJ, 919, 145

Ruffa I., et al., 2019, MNRAS, 484, 4239

Rupke D. S. N., Veilleux S., 2011, ApJ, 729, L27

Rupke D. S. N., Veilleux S., 2013a, ApJ, 768, 75

Rupke D. S. N., Veilleux S., 2013b, ApJ, 775, L15

Rupke D. S., Veilleux S., Sanders D. B., 2005, ApJS, 160, 115

Rupke D. S. N., Gültekin K., Veilleux S., 2017, ApJ, 850, 40

Russell H. R., et al., 2016, MNRAS, 458, 3134

Russell H. R., et al., 2017, MNRAS, 472, 4024

Russell H. R., Fabian A. C., McNamara B. R., Miller J. M., Nulsen P. E. J., Piotrowska J. M., Reynolds C. S., 2018, MNRAS, 477, 3583

Russell H. R., et al., 2019, MNRAS, 490, 3025

Sabater J., et al., 2019, A&A, 622, A17

Saikia D. J., Kapahi V. K., 1982, Bulletin of the Astronomical Society of India, 10, 42

Salomé P., Combes F., 2004, A&A, 415, L1

Salomé Q., Salomé P., Combes F., 2015, A&A, 574, A34

Salpeter E. E., 1964, ApJ, 140, 796

Sandage A., 1989, JRASC, 83, 351

Santoro F., Tadhunter C., Baron D., Morganti R., Holt J., 2020, A&A, 644, A54

Sargent M. T., et al., 2014, ApJ, 793, 19

Schaye J., et al., 2015, MNRAS, 446, 521

Scheiner J., 1899, ApJ, 9, 149

Schmidt M., 1963, Nature, 197, 1040

Schmidt M., Green R. F., 1983, ApJ, 269, 352

Schmitt H. R., Donley J. L., Antonucci R. R. J., Hutchings J. B., Kinney A. L., 2003, ApJS, 148, 327

Scholtz J., et al., 2021, MNRAS, 505, 5469

Schwarz G., 1978, Annals of Statistics, 6, 461

Selina R. J., et al., 2018, in Murphy E., ed., Astronomical Society of the Pacific Conference Series Vol. 517, Science with a Next Generation Very Large Array. p. 15 (`arXiv:1810.08197`), doi:10.48550/arXiv.1810.08197

Shankar F., Weinberg D. H., Miralda-Escudé J., 2009, ApJ, 690, 20

Shapley H., 1918, PASP, 30, 42

Shi Y., Yu X., Mao S., Gu Q., Xia X., Chen Y., 2021, MNRAS, 507, 2423

Shih H.-Y., Rupke D. S. N., 2010, ApJ, 724, 1430

Shimizu T. T., et al., 2019, MNRAS, 490, 5860

Sijacki D., Springel V., Di Matteo T., Hernquist L., 2007, MNRAS, 380, 877

Silk J., Rees M. J., 1998a, A&A, 331, L1

Silk J., Rees M. J., 1998b, A&A, 331, L1

Silpa S., Kharb P., Harrison C. M., Girdhar A., Mukherjee D., Mainieri V., Jarvis M. E., 2022, MNRAS, 513, 4208

Singh K. P., et al., 2014, in Takahashi T., den Herder J.-W. A., Bautz M., eds, Society of Photo-Optical Instrumentation Engineers (SPIE) Conference Series Vol. 9144, Space Telescopes and Instrumentation 2014: Ultraviolet to Gamma Ray. p. 91441S, doi:10.1117/12.2062667

Slipher V. M., 1915, Popular Astronomy, 23, 21

Slipher V. M., 1917a, Lowell Observatory Bulletin, 3, 59

Slipher V. M., 1917b, The Observatory, 40, 304

Smith K. L., Shields G. A., Bonning E. W., McMullen C. C., Rosario D. J., Salviander S., 2010, ApJ, 716, 866

Solomon P. M., Vanden Bout P. A., 2005, ARA&A, 43, 677

Solomon P. M., Rivolo A. R., Barrett J., Yahil A., 1987, ApJ, 319, 730

Solomon P. M., Downes D., Radford S. J. E., Barrett J. W., 1997, ApJ, 478, 144

Soltan A., 1982, MNRAS, 200, 115

Somalwar J., Johnson S. D., Stern J., Goulding A. D., Greene J. E., Zakamska N. L., Alexandroff R. M., Chen H.-W., 2020, ApJ, 890, L28

Somerville R. S., Hopkins P. F., Cox T. J., Robertson B. E., Hernquist L., 2008, MNRAS, 391, 481

Speranza G., et al., 2022, A&A, 665, A55

Springel V., et al., 2018, MNRAS, 475, 676

Stockton A., 1976, ApJ, 205, L113

Storchi-Bergmann T., et al., 2018, ApJ, 868, 14

Stuik R., Tinbergen J., Joos F., Schmid H. M., 2005, in Adamson A., Aspin C., Davis C., Fujiyoshi T., eds, Astronomical Society of the Pacific Conference Series Vol. 343, Astronomical Polarimetry: Current Status and Future Directions. p. 94

Subramaniam A., et al., 2016, in den Herder J.-W. A., Takahashi T., Bautz M., eds, Society of Photo-Optical Instrumentation Engineers (SPIE) Conference Series Vol. 9905, Space Telescopes and Instrumentation 2016: Ultraviolet to Gamma Ray. p. 99051F (arXiv:1608.01073), doi:10.1117/12.2235271

Sun A.-L., Greene J. E., Zakamska N. L., Nesvadba N. P. H., 2014, ApJ, 790, 160

Sutherland R. S., Bicknell G. V., 2007, ApJS, 173, 37

Tadhunter C., Morganti R., Rose M., Oonk J. B. R., Oosterloo T., 2014, Nature, 511, 440

Takada M., et al., 2014, PASJ, 66, R1

Talbot R. Y., Bourne M. A., Sijacki D., 2021, MNRAS, 504, 3619

Talbot R. Y., Sijacki D., Bourne M. A., 2022, MNRAS, 514, 4535

Talbot R. Y., Sijacki D., Bourne M. A., 2023, arXiv e-prints, p. arXiv:2306.07316

Tamhane P. D., McNamara B. R., Russell H. R., Edge A. C., Fabian A. C., Nulsen P. E. J., Babyk I. V., 2022, MNRAS, 516, 861

Tanner R., Weaver K. A., 2022, AJ, 163, 134

Taylor P., Kobayashi C., 2015, MNRAS, 448, 1835

Thatte N., et al., 2021, The Messenger, 182, 7

Thompson A. R., Clark B. G., Wade C. M., Napier P. J., 1980, ApJS, 44, 151

Thompson T. A., Fabian A. C., Quataert E., Murray N., 2015, MNRAS, 449, 147

Tombesi F., Cappi M., Reeves J. N., Braito V., 2012, MNRAS, 422, L1

Tombesi F., Meléndez M., Veilleux S., Reeves J. N., González-Alfonso E., Reynolds C. S., 2015, Nature, 519, 436

Tremblay G. R., et al., 2016, Nature, 534, 218

Tremblay G. R., et al., 2018, ApJ, 865, 13

Tremonti C. A., et al., 2004, ApJ, 613, 898

Trumpler R. J., 1930, Lick Observatory Bulletin, 420, 154

Tully R. B., Fisher J. R., 1977, A&A, 500, 105

Ulvestad J. S., Wrobel J. M., Roy A. L., Wilson A. S., Falcke H., Krichbaum T. P., 1999, ApJ, 517, L81

Urry C. M., Padovani P., 1995, PASP, 107, 803

Vantyghem A. N., et al., 2016, ApJ, 832, 148

Veilleux S., Kim D. C., Sanders D. B., Mazzarella J. M., Soifer B. T., 1995, ApJS, 98, 171

Veilleux S., Cecil G., Bland-Hawthorn J., 2005, ARA&A, 43, 769

Veilleux S., et al., 2013, ApJ, 776, 27

Veilleux S., Maiolino R., Bolatto A. D., Aalto S., 2020, A&A Rev., 28, 2

Venturi G., et al., 2021a, A&A, 648, A17

Venturi G., et al., 2021b, A&A, 648, A17

Venturi G., et al., 2023, arXiv e-prints, p. arXiv:2309.02498

Veres P. M., Gabányi K. É., Frey S., Paragi Z., Kun E., An T., 2021, ApJ, 922, 99

Veron M. P., 1981, A&A, 100, 12

Villar Martín M., Emonts B., Humphrey A., Cabrera Lavers A., Binette L., 2014, MNRAS, 440, 3202

Villar-Martín M., Arribas S., Emonts B., Humphrey A., Tadhunter C., Bessiere P., Cabrera Lavers A., Ramos Almeida C., 2016, MNRAS, 460, 130

Villar-Martín M., et al., 2017, MNRAS, 472, 4659

Villar Martín M., Emonts B. H. C., Cabrera Lavers A., Bellocchi E., Alonso Herrero A., Humphrey A., Dall'Agnol de Oliveira B., Storchi-Bergmann T., 2021, A&A, 650, A84

Virtanen P., et al., 2020a, scipy/scipy: SciPy 1.5.3, Zenodo, doi:10.5281/zenodo.4100507

Virtanen P., et al., 2020b, Nature Methods, 17, 261

Vito F., et al., 2014, MNRAS, 441, 1059

Vogelsberger M., et al., 2014, Nature, 509, 177

Vrtilek J. M., 1985, ApJ, 294, 121

Wagner A. Y., Bicknell G. V., 2011, ApJ, 728, 29

Wagner A. Y., Bicknell G. V., Umemura M., 2012, ApJ, 757, 136

Wagner A. Y., Umemura M., Bicknell G. V., 2013, ApJ, 763, L18

Wang X., Loeb A., 2018, New A, 61, 95

Wang J., Mao Y. F., Wei J. Y., 2011, ApJ, 741, 50

Ward S. R., Harrison C. M., Costa T., Mainieri V., 2022, MNRAS, 514, 2936

Weedman D. W., 1970a, ApJ, 159, 405

Weedman D. W., 1970b, ApJ, 159, 405

Weedman D. W., 1976, QJRAS, 17, 227

Weedman D. W., 1977, ARA&A, 15, 69

Weijmans A.-M., et al., 2014, MNRAS, 444, 3340

Weilbacher P. M., Streicher O., Urrutia T., Pécontal-Rousset A., Jarno A., Bacon R., 2014, in Manset N., Forshay P., eds, Astronomical Society of the Pacific Conference Series Vol. 485, Astronomical Data Analysis Software and Systems XXIII. p. 451 (`arXiv:1507.00034`)

Weilbacher P. M., et al., 2020, A&A, 641, A28

Weiss A., Downes D., Walter F., Henkel C., 2007, in Baker A. J., Glenn J., Harris A. I., Mangum J. G., Yun M. S., eds, Astronomical Society of the Pacific Conference Series Vol. 375, From Z-Machines to ALMA: (Sub)Millimeter Spectroscopy of Galaxies. p. 25

Weiß A., Kovács A., Güsten R., Menten K. M., Schuller F., Siringo G., Kreysa E., 2008, A&A, 490, 77

Weltman A., et al., 2020, PASA, 37, e002

Whiteoak J. B., 1970, Astrophys. Lett., 5, 29

Whittle M., 1992, ApJ, 387, 109

Whittle M., Unger S. W., Pedlar A., Axon D. J., Meurs E. J. A., Ward M. J., 1988, in Kafatos M., ed., Supermassive Black Holes. p. 80

Wright A., Otrupcek R., 1990, PKS Catalog (1990, p. 0

Wylezalek D., Morganti R., 2018, Nature Astronomy, 2, 181

Wylezalek D., Flores A. M., Zakamska N. L., Greene J. E., Riffel R. A., 2020, MNRAS, 492, 4680

Xu D., Komossa S., 2009, ApJ, 705, L20

Xu C., Livio M., Baum S., 1999, AJ, 118, 1169

Yesuf H. M., Ho L. C., 2020, ApJ, 901, 42

Young T., 1804, Philosophical Transactions of the Royal Society of London, pp 1 – 16

Zakamska N. L., Greene J. E., 2014, MNRAS, 442, 784

Zakamska N. L., Strauss M. A., Heckman T. M., Ivezić Ž., Krolik J. H., 2004, AJ, 128, 1002

Zakamska N. L., et al., 2016, MNRAS, 455, 4191

Zel'dovich Y. B., Novikov I. D., 1964, Soviet Physics Doklady, 9, 246

Zhang K., Dong X.-B., Wang T.-G., Gaskell C. M., 2011, ApJ, 737, 71

Zinger E., et al., 2020, MNRAS, 499, 768

Zovaro H. R. M., Sharp R., Nesvadba N. P. H., Bicknell G. V., Mukherjee D., Wagner A. Y., Groves B., Krishna S., 2019, MNRAS, 484, 3393

Zubovas K., King A. R., 2012, in Chartas G., Hamann F., Leighly K. M., eds, Astronomical Society of the Pacific Conference Series Vol. 460, AGN Winds in Charleston. p. 235 (`arXiv:1201.3540`), doi:10.48550/arXiv.1201.3540

Zubovas K., King A. R., 2014, MNRAS, 439, 400

Zubovas K., Nayakshin S., King A., Wilkinson M., 2013, MNRAS, 433, 3079

do Nascimento J. C., et al., 2019, MNRAS, 486, 5075

van der Vlugt D., Costa T., 2019, MNRAS, 490, 4918

Publications List

During the duration of the PhD, the author has undertaken the following work as the primary author which also inspires the thesis chapters 3 and 4:

- Girdhar A., Harrison C. M., Mainieri V., Bittner A., Costa T., Kharb P., Mukherjee D., Arrigoni Battaia F., Alexander D. M., Calistro Rivera G., Circosta C., De Breuck C., Edge A. C., Farina E. P., Kakkad D., Lansbury G. B., Molyneux S. J., Mullaney J. R., Silpa S., Thomson A. P., Ward S. R.; *Monthly Notices of the Royal Astronomical Society, Volume 512, Issue 2, May 2022, Pages 1608-1628*; **Multi-phase outflows, turbulence and evidence for feedback caused by low power radio jets inclined into the galaxy disk**

- Girdhar A., Harrison C. M. Mainieri V., Fernández Aranda R., Alexander D. M., Arrigoni Battaia F., Bianchin M., Calistro Rivera G., Circosta C., Costa T., Edge A. C., Farina E. P., Kakkad D., Kharb P., Molyneux S.J., Mukherjee D., Njeri A., Silpa S., Venturi G., Ward S. R.; *Monthly Notices of the Royal Astronomical Society, 2023, in press.*; **Molecular gas around radio lobes and in central outflows reveals dual feedback effects in 'radio quiet' quasars**

In addition to the work presented in this thesis, the author has also either worked on, or been involved in the following works:

- Harrison C. M., Zanella A., Girdhar A.; *Communicating Astronomy for Public Journal; in press*; **Evaluation and insights from a sonification-based planetarium show intended for improving inclusivity**

- Harrison C. M., Girdhar A., Ward S. R. Ward; *IAU Symposium 378 Conference Proceedings "Black Hole Winds at all Scales"*; July 2023; **Establishing the impact of luminous AGN with multi-wavelength observations and simulations**

- Venturi G., Treister E., Finlez C., D'Ago G., Bauer F., Harrison C. M., Ramos Almeida C., Revalski M., Ricci F., Sartori L. F., Girdhar A., Keel W. C., Tubín, D.; *accepted for publication in Astronomy & Astrophysics journal*; September 2023; **Complex AGN feedback in the Teacup galaxy. A powerful ionised galactic outflow, jet-ISM interaction, and evidence for AGN-triggered star formation in a giant bubble**

- Trayford James W., Harrison C. M., Hinz R. C., Kavanagh Blatt M., Dougherty S., Girdhar A.; *RAS Techniques and Instruments Journal*; January 2023; **Inspecting spectra with sound: proof-of-concept and extension to datacubes**

- Girdhar A.; *Hypatia Colloquium 2022: Early Career Astronomer series at ESO*; October 2022; **Quasar Feedback Survey – the impact of jets and multi-phase outflows on their host galaxies**

- Silpa S., Kharb P., Harrison C. M., Girdhar A., Mukherjee D., Mainieri V., Jarvis M. E.; *Monthly Notices of Royal Astronomical Society*; Volume 513; Issue 3; July 2022; **The Quasar Feedback Survey: revealing the interplay of jets, winds, and emission-line gas in type 2 quasars with radio polarization**

- Jarvis M. E., Harrison C. M., Mainieri V., Alexander D. M., Arrigoni Battaia, F., Calistro Rivera G., Circosta C., Costa T., De Breuck C., Edge A. C., Girdhar A., Kakkad D., Kharb P., Lansbury G. B., Molyneux S. J., Mukherjee D., Mullaney J. R., Farina E. P., Silpa S., Thomson A. P., Ward S.R.; *Monthly Notices of Royal Astronomical Society*; Volume 503; Issue 2; May 2021; **The quasar feedback survey: discovering hidden Radio-AGN and their connection to the host galaxy ionized gas**

Chapter

Acknowledgements

"A blue fly, if it clings to the tail of a thoroughbred horse, can travel ten thousand miles, and the green ivy that twines around the tall pine can grow to a thousand feet." – Nichiren Daishonin

In essence, I have felt like this throughout my PhD journey, thanks to the incredible support of my PhD supervisors, *Dr. Chris Harrison* and *Dr. Vincenzo Mainieri*. I feel immensely grateful to have had Chris and Vincenzo as my PhD supervisors. They have undoubtedly been the best PhD supervisors one could ask for. They have helped me expand my horizons way beyond what I could have imagined. I somehow got extremely lucky there when they picked me out of the pool of the 300+ applicants! Thank you for supervising me with such painstaking efforts, and checking on me every single week. I am quite aware this couldn't have been easy over these 4 years. But I hope you know how deeply I value the efforts you've put in to build my research career and I hope to make you both proud; that will truly be my way of conveying how immensely grateful I feel for this opportunity. You have both been profoundly compassionate in your supervising approach, and this has greatly enabled my growth. The Ph.D. had its own challenges and the pandemic didn't make it easier for anyone, but despite all, thank you for never giving up on me and encouraging me week after week! To *Vincenzo*, I'll be deeply grateful for your continued mentorship and care, especially during my time at ESO. Thank you for your wisdom and the bright cheer you always bring along, and thank you for your guidance and continued support. Thank you for looking after my growth in your own way.

In various ways, *Chris* has been a mentor for me, patiently training me and helping me fulfill the goals I set out for. I am and will be eternally grateful for it. Thank you for enabling excellent opportunities for me, for always making time for me, for your guidance that helped me grow as a researcher, as an educator, as a communicator, and as a person, and for always reminding me of my potential and giving me confidence in my own unrealized possibilities. I am grateful to have expanded my Astronomy endeavors to tie up with Audio Universe, I have deeply enjoyed each of the associated activities. My year at Newcastle has been a boost to my career and has enabled me to understand what I'd like to take up as a lifelong pursuit, and I owe a lot of it to you.

There are many people who have enabled, supported, and dearly loved me and made this journey possible. As I come to the threshold of my educational career, preparing myself to step out to make hopefully valuable contributions to society, I'd like to take a moment to thank the people who have a role in bringing me this far.

Let me start with those I hold the most dearest and who make me what I am. My earliest scientific encounters have been with my *Aai*; going to the labs with you and watching you conduct experiments as I got my own set of specimens to play with; and coming back home and reporting all the 'tasks' I did in the lab to *Papa*, have been the most exciting memories from that age. *(Yes, I had an academic career as a child as well, where I worked with my Ma, and reported to my Papa!)* Having had the privilege to be raised by such parents, and having seen my Mum pursue her Ph.D. with me running around and possibly bothering her, has been my guiding motivation to persevere. Thank you for being such excellent role models! *Ma and Pa*, I have missed you so much in these years, thank you for all that you do, and keep doing, and all the sacrifices you make. And thank you for the care with which you have made me capable and always guided me. I would never have enough words to express your value in my life, but I am committed to keep working towards paying this gratitude throughout. *Ananya*, despite being a younger sister, you've been my pillar; and a

crucial support that has helped me feel assured of everyone's well-being back home, which has helped me stay focussed on building my life here. You've been my support through tough times in these years and I feel grateful and proud of how you've become a friend to me and have grown up to take charge while evolving into a wonderful person yourself. I hope to be that support to you now as you start your journey, and fully believe you'll be fantastic! To *Malte*, so extremely grateful that our paths met at ESO! Thank you for ensuring I am laughing like crazy in no time whenever you see me stressed; for standing strong with me throughout, and for these long repeated trips you made in this last year to take care of me and support me, especially during the thesis submission time and the stressful periods of defence preparation. Thank you for being my family here away from home; and for standing with me through and through. I am so grateful and hope to do my best to be the same for you.
To you four, it has been difficult to be away from you all, but thank you for never letting me feel alone for a single day and for reorienting me through life's difficulties.

I'd also like to thank *Dr. Daisaku Ikeda*, who has been an incredible idol with his 400+ academic honors and honorary doctorates and through his own life. Thank you for always inspiring me to believe in myself, to have big dreams, and to go after them. And thank you for creating this wonderful society such that whichever country I went to, I found a Buddhist group! To all in the Buddhist groups in Delhi, Pisa, Innsbruck, Padova, Belgrade, Munich, and Newcastle: thank you for supporting me, I am deeply grateful to you all, thanks for always holding my back and being my Soka family! *Mansi di, Navina Aunty, Anjali Di, Ankur*, thank you for pushing me to apply abroad and believing I was capable of getting a scholarship. That really set off my journey! *Sophie, Esther, Peggy, Caro*, thank you for looking after me and sustaining me through difficult times.

Going a bit further back, I'd like to thank *Ms. Rimika Banerjee Sadhu, Ms. Sadhana Saxena*, and *Ms. Bhawna Sachdev* for investing time and care that I learned well and had a great start in my high school. Thank you for being great examples that helped me enjoy Physics and coding from then on. Thanks also to *Prof. Dr. Sumitra Mohanty* for creating the opportunities for me to succeed during my Bachelor's, and to *Prof. Dr. Nirmal Patel*, for welcoming us, and supporting us as we dreamily arrived for our research projects at NASA. And also to you both for writing my very many reference letters. A special thanks to *Prof. Dr. Andrea Ferrara*, for welcoming me at Pisa and supporting me with funding to start my research journey. A big thank you to the Astromundus scholarship and all the professors and staff who supported me in Innsbruck, Padova, and Belgrade, especially *Dr. Marco Gullieuszik*, and *Dr. Bianca Poggianti* for supervising my research endeavors during my Master's, and *Prof. Dr. Francine Marleau* for her references for my PhD applications. A special thanks to *Prof. Dr. Tijana Prodanvić, Prof. Dr. Dragana Illić*, and *Dr. Sladjana*, who were amazing professors and tutors at Belgrade. In your caring and warm ways, and through your struggles and stories, you encouraged me for a Ph.D. and inspired a love to study AGN in me!

I'd also like to thank Prof. Dr. *Andreas Burkert* for his support as my supervisor and making time for my PhD progress updates and discussions. To all on my thesis committee, thank you for making time and taking care I was progressing well. I'd also like to thank all the collaborators in QFeedS and on the telescope proposals who have helped with their constructive comments. I'd also like to thank the excellent staff at ESO and Newcastle University who have time and again sparked my astrophysical curiosities; and to the institutes themselves who have funded my PhD and enabled various opportunities across the many countries I have been fortunate to visit and talk about my research. A special thanks to Nelma, for continuing to support my PhD journey with her ever-helpful demeanour.

Through these four years, I have met some wonderful people who have supported me in various ways, a big thanks to the new friends I made and to the ones that kept supporting me: *Sonali, Miranda, Mrunmayee, Neha, Avinash, Isabella, Svea, Hitesh, Olena, Taïssir, Divya, Varun, Samuel, Ricchi, Vicky, Devang, Houda*, and all those whose names I haven't been mindful enough to remember; thanks for being there folks; I have truly enjoyed our chats, coffees, lunches, dances, and dinners! Your support has sustained me through these years! To *Katja and Silvia*, it has been an absolute honour being the student rep at ESO with you both and being fearless for standing up for the right things and bringing about changes in the system for the better!

To everyone, thank you for making the Ph.D. journey one that I could truly feel proud of. And hey everyone, I am finally submitting my Ph.D. thesis now!